Structure-properties correlation in hybrid perovskite for photovoltaics

Aicha Asma Medjahed

To cite this version:

Aicha Asma Medjahed. Structure-properties correlation in hybrid perovskite for photovoltaics. Material chemistry. Université Grenoble Alpes [2020-..], 2021. English. NNT : 2021GRALV029 . tel-03365012

HAL Id: tel-03365012
https://theses.hal.science/tel-03365012

Submitted on 5 Oct 2021

Université
Grenoble Alpes

THÈSE

Pour obtenir le grade de

DOCTEUR DE L'UNIVERSITE GRENOBLE ALPES

Spécialité : **Chimie Physique Moléculaire et Structurale**

Arrêté ministériel : 25 mai 2016

Présentée par

Aicha Asma MEDJAHED

Thèse dirigée par **Peter REISS**, ingénieur-chercheur CEA et
co-encadrée par **Stéphanie POUGET,** ingénieur-chercheur CEA

préparée au sein du **Laboratoire Systèmes Moléculaires et Nano Matériaux pour l'Energie et la Santé (SyMMES)**
et du **Laboratoire Modélisation et Exploration des Matériaux (MEM)**
dans **l'École Doctorale Chimie et Sciences du Vivant**

Corrélation structure-propriétés dans les matériaux pérovskites hybrides pour le photovoltaïque

Structure-properties correlation in hybrid perovskites for photovoltaics

Thèse soutenue publiquement le **21 mai 2021**,
devant le jury composé de :

Mme. Emmanuelle DELEPORTE
PROFESSEURE, ENS Paris Saclay, Rapporteur
M. Constantinos C. STOUMPOS
PROFESSEUR ASSOCIE, Université de Crète, Rapporteur
M. Antoine LETOUBLON
MAITRE DE CONFERENCES, INSA Rennes, Examinateur
M. Olivier ISNARD
PROFESSEUR, UGA, Président
M. David DJURADO
DIRECTEUR DE RECHERCHE CNRS, SyMMES, Invité

Acknowledgments / Remerciements

De manière tout à fait ironique, les premières lignes croisées par le lecteur, celles-ci, sont les toutes dernières que j'ajoute au document, non sans beaucoup de nostalgie. Le manuscrit porte mon nom, mais une thèse n'est jamais l'affaire d'une seule personne. Ainsi, ce qui suit tend à rendre hommage à toutes les personnes qui ont contribué de près comme de loin à l'achèvement de ce travail. L'écriture de ces remerciements m'oblige à faire défiler devant mes yeux ces quatre dernières années afin d'espérer n'oublier personne, ce qui n'est pas aisé tant l'épopée de la thèse fut riche en rencontres, en émotions, en apprentissages, en désillusions et en émerveillements.

Tout d'abord, aux membres de mon jury de thèse. Un grand merci au Pr. Olivier Isnard d'avoir accepté de présider mon jury de thèse, de m'avoir rencontré pour discuter de la thèse avant la soutenance ainsi que pour les conseils. I felt honoured and lucky to have Pr. Costas Stoumpos in my jury as a reviewer of the manuscript despite his undoubtedly busy schedule. Thank you for the great discussion we had during and after the defence, may we have the opportunity to further collaborate in the coming years. Enfin, merci au Pr. Emmanuelle Deleporte d'avoir accepté de rapporter mon travail et au Dr. Antoine Letoublon de l'avoir examiné. Je compléterai mes remerciements à ces deux personnes un peu plus loin dans cette section. To all jury members, thank you for your interest in my work, I feel lucky to be able to say that I enjoy my PhD defence thanks to the very interesting scientific discussion we had.

Evidemment, je remercie tout particulièrement mes encadrants de thèse : Dr. Peter Reiss, Dr. David Djurado et Dr. Stéphanie Pouget. Merci de m'avoir fait confiance après ce stage de M2, malgré la fracture de la cheville au bout d'une semaine de stage et mon retour clopinant au laboratoire. Peter, tu es le premier avec qui je me suis entretenu, merci d'avoir tout de suite compris que je correspondais plus à un autre de tes sujets de recherche que celui sur lequel j'ai postulé, tu ne t'es pas trompé. Merci de m'avoir fait confiance par la suite, de m'avoir laissé libre dans mes choix d'études tout en répondant présent quand j'avais des questions. David, sans être officiellement mon encadrant, j'ai toujours pu compter sur ton aide, ton regard extérieur et tes grandes connaissances. Merci pour ton intérêt et tes encouragements de toute heure. Je garde en tête les souvenirs de nos nuits sur ID01, à regarder naitre puis rapidement mourir cette «Insaisissable Pérovskite» (tous droits réservés à D. Djurado) mais aussi et surtout ton regard et ta passion pour la science et les matériaux. J'espère garder une flamme aussi vive que la tienne après une carrière aussi fascinante que celle que tu as eu. Enfin, Stéphanie, mon mentor. Dans sa conférence sur les pérovskites (celle qu'on a revu un trop grand nombre de fois sur Youtube pour pouvoir l'assumer), M. Glazer parle fièrement de son «arbre généalogique scientifique». Je peux dire sans rougir que je suis chanceuse de t'avoir dans le mien, de descendre directement de toi scientifiquement parlant. Merci pour ta patience, pour ta confiance en moi qui a très souvent été supérieure à celle que je m'accordais. Merci de m'avoir expliqué, parfois à plusieurs reprises, les subtilités de la diffraction et de la science des matériaux, de m'avoir appris une petite partie de tout ce que tu sais. Merci d'avoir toujours trouvé du temps pour moi, de m'avoir laissé vagabonder et explorer sur les diffractos du laboratoire. Aussi, pour toutes ces discussions durant lesquelles nous avons refait le monde autour d'un thé, d'un plateau repas à H2 ou autre et qui m'ont tant appris, tu l'auras compris : merci pour tout. A tous les trois, on se l'est déjà dit mais je l'écris ici : gardons contact.

Ce travail n'aurait pas été le même sans les personnes avec qui j'ai eu la chance de collaborer de près. Dr. Pia Dally, je me souviendrai très longtemps de toutes ces heures que l'on a passé à faire varier la température des échantillons et à guetter ces fameux doubles pics, ou de la chorégraphie que l'on a mis en place pour les études in-situ pour que les échantillons ne «voient pas trop longtemps l'air». Sans toi et tous les échantillons que tu n'as jamais hésité à fabriquer, une bonne partie de ces travaux et notre papier n'auraient pas pu exister, merci pour cette belle collaboration.

Dr Tao Zhou, ces quelques lignes n'arriveront jamais à traduire l'admiration que je te porte. Ta force de travail, tes connaissances, ta gentillesse, ton écoute, ta disponibilité et ta patience ont fait de nos manip' sur ID01 et du traitement de données une partie très enrichissante et stimulante de la thèse. Merci de m'avoir accueilli à l'ESRF le temps de quelques semaines pour mieux comprendre les subtilités du FFDXM, ainsi que pour toutes les heures, souvent tardives mais toujours passionnantes, que nous avons passé ensemble sur les données.

Dr. Mathilde Bouchard, qui m'a introduite au monde des pérovskites hybrides halogénées et des couches minces spin-coatées. Dr. Dmitry Aldakov, pour les discussions et les échanges durant les groupes meeting ou tes conseils quand je venais te chercher dans ton bureau. Dr. Jérôme Faure-Vincent, pour ces moments passés à se creuser la tête pour mettre des contacts électriques sur mes mini-monocristaux irréguliers ou mes couches minces. A Bernard Mongellaz, qui n'a jamais dit non pour m'aider quand les diffractos étaient en rade, ou quand il fallait adapter un environnement échantillon ou encore m'aider sur un montage farfelu sur les diffractomètres. Merci à tous.

J'ai eu la chance d'effectuer ma thèse entre deux laboratoires, le STEP et le SGX, dans lesquels j'ai trouvé des personnes toujours prêtes à me conseiller, me rebooster ou juste partager un café et de la bonne humeur. Un grand merci à toute la grande équipe du STEP : Dr. Pascale Chenevier, Dr. Renaud Demadrille, Dr. Benjmain Grevin, Yann Kervella, Dr. Cyrille Aumaitre, Céline Rivaux (mais quel bonheur de te croiser au laboratoire cette dernière année !), Emilie Dubard, Dr. Hakima Mendil-Jakani (1, 2, 3, VIVA L'ALGERIE, merci pour ta bonne humeur), Dr. Laurent Gonon, Dr. Vincent Mareau et Dr. Frédéric Chandezon. Merci au SGX où je me suis sentie comme à la maison: Dr. Edith Bellet-Amalric, Bernard Mongellaz, Dr. Arnaud DeGeyer, Dr. Stéphane Lequien et Dr. Jacques Pécaut (oui oui, je t'ai mis au SGX, tu ne m'en voudras pas !).

Au personnel chercheur de l'INAC avec qui j'ai eu la chance d'échanger, un grand merci. Je pense notamment à Dr. Joel Eymery, Dr. Samuel Tardif et Dr. Pascal Pochet. Un merci tout particulier à Charles Picot, Sarah et Rachelle Mauduit ; sans vous, j'aurai probablement étouffé sous le poids des démarches administratives, merci pour votre aide si précieuse.

Merci au Pr. Alain Ibanez et au Dr. Antoine Letoublon d'avoir fait partie de mon comité de suivi de thèse, d'avoir pris le temps, à trois reprises, de m'écouter parler de mes travaux, d'échanger et de me conseiller. Je retiens bien le conseil sur la confiance en soi.

Merci au Dr. Emmanuelle Deleporte et au Dr. Gaëlle Allard-Trippé de m'avoir accueilli pendant une semaine dans votre laboratoire pour apprendre votre art de faire croitre les monocristaux. Merci au GDR HPERO d'avoir financé la bourse de mobilité qui a rendu possible cette visite.

A tous mes collègues/amis non-permanents qui ont fait que cette thèse n'a pas été uniquement portée sur le travail : Caroline Keller (je te lègue la place de plus ancienne non-permanente au labo!), Dr. Davina Moodelly (et nos discussions dans les couloirs), Dr. Olivier Bardagot (merci encore pour cette chouette collaboration qui m'a fait voir plus loin que mes pérovskites !), Pavel Veyre, Dr. Christopher Berhaut (enfin un fan de Dr. Who !), Dr. Adrien Mery, Dr. Anthony Valero, Dr. Lydia Cabau (I miss so much our time together in Boston...), Valid Mwatati Mwalukuku, Johan Loitier, Fakourou Camara, Dr. Jiajiu Ye (a real pleasure to work and discuss with you about so many different subjects!), Yuze Li, Tuan Minh Dong, and Ranjana Yadav (you go get them girl!). Aux petits derniers arrivants du laboratoire: Nino Modesto, Guilhem Paradol et Louise Poutot (même si tu es déjà partie...), la relève est assurée et la bonne humeur entre non-permanents est sûre de perdurer. Un merci tout particulier à Baptiste Roselli (un Baptou toujours souriant), Claire Tougne (pour les petits mots sur les post-it et les dessins de chat) et Marc Dietrich (pour les fonds d'écrans incroyables et les petits coucous dans l'après-midi). Enfin, à Diana Zapata Dominguez, avec qui on a partagé un bureau pendant trois ans mais pas que (thés, pâtisseries, cours de P90X, de l'eau renversée sur le bureau à intervalles réguliers par ma faute et j'en passe...), un énorme merci. Qui sait, peut-être que l'on se retrouvera dans un même bureau dans les années à venir. Merci à tous les non-permanents pour les soirées folles, les cafés interminables du midi et les parties de cartes endiablées. Merci d'être tous venus pour me voir recevoir le titre de docteur et d'être restés fêter ça avec moi.

J'espère n'avoir oublié aucun collègue dans cette longue liste. Si tu ne trouves pas ton nom dans les lignes précédentes, sache que ce n'est qu'un fâcheux oubli. N'hésite pas à m'écrire, je t'emmène en terrasse pour me faire pardonner.

Avant d'en venir aux amis et à la famille, je souhaite ne pas remercier le Covid-19, qui a fait son apparition lors de ma dernière année de thèse, chamboulant quelque peu le programme mais surtout diminuant les chances de se croiser dans les couloirs et de discuter de science, ce qui, je trouve, est grandement néfaste à ce beau métier qu'est la recherche.

Sur une note plus personnelle, merci à tous mes amis qui m'ont soutenu, de près comme de loin durant ces années : à ceux avec qui on se suit depuis si longtemps : Celia, Mounir, Mehdi et Lynda. A celle qui a pris une place centrale dans ma vie, malgré ces quelques derniers mois difficiles, Lilia. A Samy. A mes copains Grenoblois, Alice et Jérémy, pour toutes ces soirées bouffe et films et nos Escape Game. Au meilleur binôme du monde, mon copain de coeur, Jérôme.

Un grand merci à toute ma belle-famille, les Ait-Mouloud, pour leur soutien, leurs encouragements et leur présence pendant cette thèse.

A un Ait-Mouloud en particulier, Amine. Merci pour ton amour, merci de m'avoir appris à reconnaitre quand il fallait que je m'arrête et d'être ma force tranquille dans la vie. Merci d'avoir été présent quand je rentrais le soir du travail excitée comme une puce et de m'avoir écouté parler de pérovskites et de rayons X pendant 4 ans. Merci aussi d'avoir toujours eu les mots quand ces mêmes pérovskites me mettaient à genoux. Je nous souhaite une longue route ensemble sur laquelle notre équipe restera aussi soudée qu'elle ne l'est actuellement voire plus.

A mes oncles et tantes, soutien de toujours, merci.

A mes petits (plus si petits que ça) frères, Raouf et Rémi. Merci pour votre amour, pour votre humour, merci d'être toujours là pour m'écouter, merci de m'avoir appris à prendre les choses moins au sérieux. La vie sans vous aurait été bien triste et monotone, je vous aime fort.

A maman, sans qui je ne serai pas là. Même s'il y a mon nom dessus, cette thèse est à 99.9999[...]999% la tienne. Merci d'avoir fait de nous ta priorité pendant si longtemps. Voilà où nous ont menées les leçons entre 12 et 14h sur la table de la cuisine. Merci d'avoir toujours été là, merci d'avoir choisi le CNED, merci de m'avoir toujours poussé et encouragé, d'avoir cru en moi. Merci d'avoir été et de continuer à être à l'écoute quel que soit ce que j'ai à dire, d'avoir toujours répondu présente.

A papa, mon plus grand fan. Merci pour ton amour de la première heure, merci d'avoir toujours cru en moi, de m'avoir toujours encouragée à être forte et indépendante. Merci pour les fiches de révisions d'histoire/géo, pour les entrainements sportifs le vendredi à 6h du matin. Merci pour les leçons de vie, les longues discussions, les heures que nous avons passé ensemble en voiture et pour tous les efforts que tu as fait sans laisser deviner ce que ça te coutait.

Papa, maman, sans vous, votre amour et vos sacrifices pour nous, rien n'aurait été possible. Je n'ai qu'un regret ; ne pas vous avoir eu à mes côtés pendant la soutenance, pas merci au covid. J'espère vous avoir rendu fiers. Je vous aime.

List of abbreviations

- AFM: Atomic Force Microscopy
- CTE: Coefficient of Thermal Expansion
- DMF: Dimethylformamide
- DMSO: Dimethylsulfoxide
- D.O.: $MAPbI_3$ thin layers obtained through Device Optimized protocol
- EDX: Energy Dispersive X-ray analysis
- FA^+: Formamidinium cation
- FFDXM: Full-Field Diffraction X-ray Microscopy
- FTO: Fluorine Doped Tin Oxide
- GBL: γ-butyrolactone
- H.C.: $MAPbI_3$ thin layers obtained through High Concentration protocol
- ITO: Indium Doped Tin Oxide
- L.C.: $MAPbI_3$ thin layers obtained through Low Concentration protocol
- MA^+: Methylammonium cation
- NMP: N-Methyl-2-Pyrrolidone
- NMR: Nuclear Magnetic Resonance
- NTE: Negative Thermal Expansion
- PDF: Pair Distribution Function
- PFM: Piezoresponse Force Microscopy
- RT: Room Temperature

- SEM: Scanning Electron Microscopy
- TEM: Transmission Electron Microscopy
- XRD: X-ray Diffraction

Table of contents

General introduction

As these lines are written, the Gregorian calendar indicates the year 2021. In fact, this system considers only a small part of the human history as a species, which starts several hundred thousand years ago. Recalling this fact helps to evaluate how incredibly recent our current way of life is. Since the industrial revolution at the end of the eighteenth century, society greatly transformed thanks to mechanization of the work. In less than three hundred years, agriculture was reformed, bigger cities were built, major scientific and technical advances were achieved. The modern society was built to follow one model: growth. After being relatively stable for more than 10 000 years, the size of the population started peaking with the industrial revolution, reaching unprecedented growth rate. The population size was estimated around 7.7 billion people in 2019, and United Nations projections predict the world population to reach 11 billion by the end of this century.[1] Economic growth is a dominant mantra of most of nowadays societies, and we have excelled at it: the global Gross Domestic Product (GDP) per capita was multiplied by 4 between 1950 and 2016 (adjusted to inflation).[2] Such economic growth has brought prosperity to billion, and our modern society entered the era of mass consumption.

Following this economic model, our energy needs have quickly increased. Between 1850 and 2019, global fossil fuel consumption has risen from ~570 TWH to ~ 137 000 TWH and, accordingly, the annual total CO_2 emissions exponentially climbed from ~ 200 000 million tons to ~ 37 billion tons, still increasing. As a direct consequence, over the same period, the global temperature on Earth has increased by ~ 1 °C[1], with now observable repercussions: twenty of the last twenty-two years have been the hottest on record, with more heat waves, glaciers melting faster. . ..[3] Climate change is real, and without immediate and decisive actions, the global temperature will continue rising, leading to more dramatic consequences. With the current climate policies undertaken worldwide, the global Earth temperature is predicted to rise by 2.8 to 3.2 °C by the end of the century, well above the limit targeted in the Paris Agreement.[4]

The answer to the problem of the climate change, which can be considered as *the* twenty-first century challenge, is the drastic reduction of our carbon footprint. The latter

---

[1] Unless specified otherwise, all the quantitative data was taken from ”Our World in Data” website (`https://ourworldindata.org`), accessed on 14/03/2021.

is not one-fold and multiple levels of actions need to be undertaken. Even though it seems unrealistic for the foreseeable future, a profound paradigm shift in our society is needed. The actual everlasting economic growth model relies on mass consumption which, combined with the population growth, explain the exponential rise of the CO_2 emissions. Whether change at that level will happen or not, the first step to cut down the effect of climate change is to swiftly and considerably decrease our use of fossil fuels as energy sources. Considering that the energy demand and supply accounts for 60 % of the total greenhouse gas emissions, the use of low-carbon, renewable energy sources such as the sun and the wind thanks to the adequate technology will help to decrease the carbon foot-print of the human activity.

In 2019, more than 80 % of the consumed energy was produced by fossil fuel, and only 15.7 % was generated by low carbon sources, mainly from nuclear and hydropower. Despite constant growth since 1920, renewable energies, which constitute endless, free and sustainable sources accounted only for 11.4 % of the energy consumption of 2019, and great room of improvement is ahead. The sun represents Earth's most abundant energy source, and huge efforts towards developing photovoltaic technologies have been undertaken by the scientific community over the past decades. Such efforts have led to notable improvement of the performances and observable reduction of the cost of photovoltaic modules. Silicon-based technology is the dominant one on the market, thanks to six decades of development, high efficiencies, long-term stability and steadily decreasing costs. Nonetheless, strong research efforts are also dedicated to several alternative technologies, targeting less energy-consuming fabrication processes, flexible and lighter solar cells as well as greater independence from Asia-located production. Among these emerging technologies, organic-inorganic hybrid halide perovskite solar cells, introduced ten years ago, have attracted great interest.

It is within this general context that the work of this PhD project was conducted. In hybrid halide perovskites, an organic cation occupies the center of an inorganic lead-halide cage. While this structure results in very promising properties for optoelectronic applications, the fundamental origins of these properties remain, to a large extent, elusive. This work aimed to study in details a number of the structural aspects of these materials, using X-Ray Diffraction (XRD) as the main experimental technique.

The **first chapter** presents a general overview of the context of this work and presents its objectives. The working principle of photovoltaic devices are briefly presented, together with the key optoelectronic properties of hybrid halide perovskites that led to their successful use in solar cells. Next, the major structural features of the large family of perovskite are given, followed by a more specific presentation of the structural aspects of hybrid halide perovskites. Finally, the main challenges the scientific community is currently facing in terms of understanding the structural features of these compounds and their relationship with their properties are presented.

The rest of the manuscript is divided into two independent parts.

The first part is devoted to the study of $MAPbI_3$ ($MA = CH_3NH_3$) thin layers, the first halide perovskite material used as an active layer in a solar cell. **Chapter 2** presents a detailed investigation of one of the $MAPbI_3$ crystallization mechanism in the presence of chlorine. In-situ XRD experiment allowed us to reveal the different steps of the crystallization through ion exchange from $MAPbCl_3$, and the impact on the microstructure of the resulting layers as well as the performances of the devices based on them. **Chapter 3** focuses on the $MAPbI_3$ thin films microstructure and more particularly on the peculiarity and variability of the texture which is observed. This behavior is shown to be related to the ferroelastic nature of the $MAPbI_3$ cubic-tetragonal phase transition.

The second part of this thesis is dedicated to the study of the impact of ion mixing on hybrid halide perovskites structural properties. Technological developments have led to the use of mixed cation and/or and mixed halide perovskite solid solutions as an active layer in solar cells, helping to reach increased efficiencies and long-term stability. Here, to understand the impact of ion substitution on the final compounds, each ion was substituted separately, and we investigated 3 solid solution families: mixed organic cation compounds $FA_{1-x}MA_xPbI_3$ (FA = formamidinium $CH(NH_2)_2$) and mixed halide compounds $MAPb(I_{1-x}Br_x)_3$ and $FAPb(I_{1-x}Br_x)_3$.

Chapter 4 is dedicated to the study of the properties of these systems at RT, presenting the evolution of the lattice parameters and band gap upon ion substitution. The effect of ion substitution on the polymorphism of FA-based compounds is also addressed. **Chapter 5** presents a temperature-dependent study of the mixed halide systems, monitoring the crystallographic changes in the compounds and thus giving acces to the temperature-composition phase diagram of the different families. Both chapters include a last part where a quinary compound used in high efficiency photovoltaic devices is studied in regard to the results obtained on the quaternary compounds.

A general conclusion summarizes the major results of this work and, finally, the perspectives and outlooks are discussed.

A description of the experimental methods is provided in the Appendix section, aiming to provide all the elements needed to reproduce the results presented here.

References

[1] *United Nations Climate Change Annual Report 2019*. 2019.

[2] Bolt et al. *The Maddison Project Database, version 2018 - www.ggdc.net/maddison*. 2018.

[3] World Meteorological Organization. *WMO statement on the state of the global climate in 2019*. en. 2019. ISBN: 978-92-63-11248-4 978-92-63-11233-0.

[4] *The Paris Agreement - UNFCCC*. 2014.

Chapter 1

Hybrid Halide Perovskites Photovoltaics : the latest wonder of a renowned family

Contents

1.1. Storming the photovoltaic field

1.1.1. Photovoltaic technologies

The general idea behind a working solar cell is to directly convert light into electricity. The story of the photovoltaic science starts in 1839, when 19 years old Edmond Becquerel discovered the photovoltaic effect. Various experimental observations followed, and Albert Einstein received the Nobel Prize in 1921 for his works explaining the photoelectric effect.[1] Later on, in 1941, Russel Ohl, in the frame of his work on the p-n junction, patented the modern solar cell.[2] Photovoltaic research started, and different technologies appeared.

Since the first report of a crystalline silicon-based solar device with a power conversion efficiency (PCE) of 6%,[3] the efficiency of this type of solar cells increased steadily over the years. As the fabrication cost decreased rapidly, this technology is the leading one on the market, accounting for 90% of the energy produced through photovoltaics.[4] Other inorganic semiconductors such as CdTe and CIGS (short for copper indium gallium diselenide) or GaAs were also developed over the years. Despite the long-term stability of the solar panels and the well-established fabrication process, all these technologies present several limitations. Ironically and despite the decreasing costs, the carbon-foot print of silicon based devices is high because, amongst other factors, of the high temperature process employed to fabricate the high-purity semi-conductor compounds needed (up to 1400 °C for single crystalline Si).[5] The obtained modules are rigid, opaque and rather heavy, limiting their range of applications. Moreover, the scarcity of the raw materials (such as Te) is a roadblock. These reasons lead scientists to develop novel approaches, comprising, among others, organic and hybrid organic/inorganic absorber materials.

An early breakthrough was the report, in 1990, of the first Dye-Sensitized Solar Cell (DSSC), in which, mimicking the photosynthesis process, an organic dye was used as light absorber compound.[6] The obtained modules can be light and semi-transparent. However, the best efficiencies are obtained with the use of liquid electrolytes, which are at the origin of a number of disadvantages in terms of device fabrication and stability.

In organic photovoltaics (OPV), the semi conducting materials responsible for solar light absorption are conjugated polymers or oligomers. Due to the solution processability of these compounds, OPV devices are easy to fabricate, cost-effective and potentially more environmentally friendly compared to inorganic technologies.[7] A different approach is using inorganic semiconductor nanocrystals (quantum dots), such as for example PbS or $CuInSe_2$ as the absorber material in different types of solar cell architectures.

Another breakthrough was achieved more recently, with the appearance of hybrid halide perovskite solar cells. While the initial report published in 2009 on the introduction of the organic-inorganic halide perovskite $CH_3NH_3PbI_3$ (= $MAPbI_3$ where MA = CH_3NH_3) in a DSSC went first unnoticed because of the poor stability of the system,[8] its use in a solid-state solar cell gave rise to a PCE exceeding 10% in 2012 and induced tremendous interest in the research community.[9] As of February 24th, 2021, using the keywords "hybrid perovskite solar" in Web of Science leads to 9 971 results, the oldest one appeared in 2009. Fueled by worldwide research interest, an impressive increase in the efficiency of these devices was achieved over the last decade; the highest PCE, as of now, being 25.5% is very close to the record efficiency of silicon (26.1%).

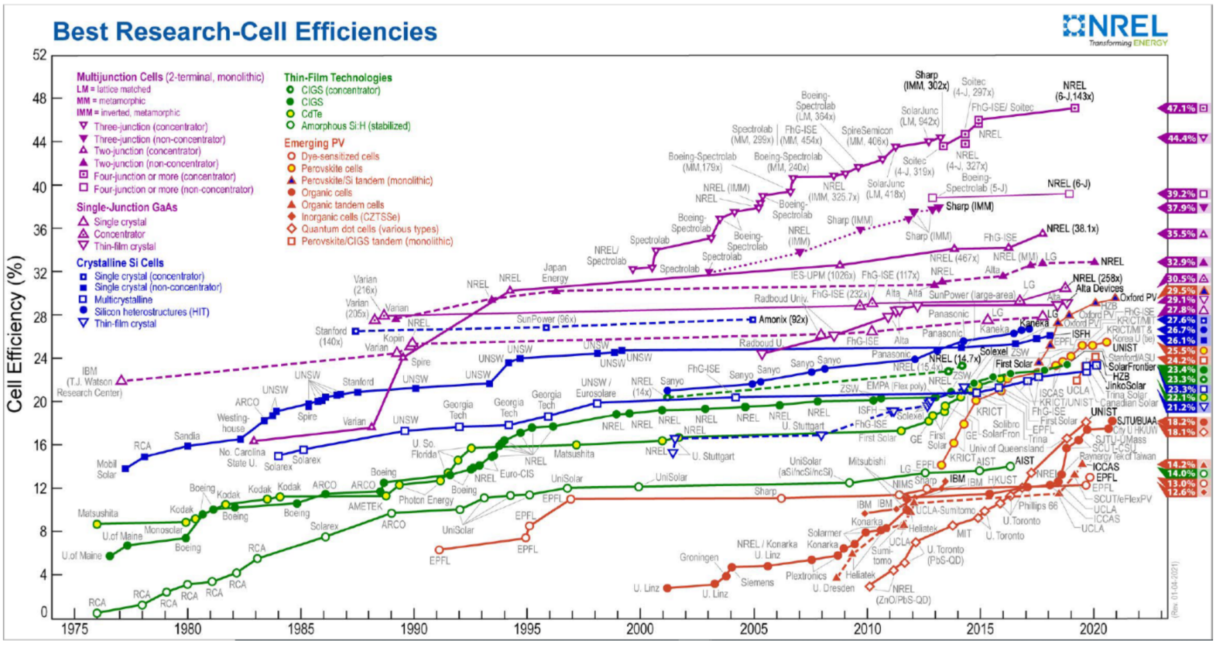

Figure 1.1: Record efficiency chart for the different solar cell technologies developed in research laboratories. Adapted from NREL (https://www.nrel.gov/pv/cell-efficiency.html), February 2021.

Photovoltaics is a fast growing domain, and to keep track of the multiple advances, "Progress in Photovoltaics" and the "Best research-cell efficiency chart" edited by the National Renewable Energy Laboratory (NREL), provide official, regularly up-dated and reliable status of the current progresses. The latter is reproduced in Figure 1.1, which is indeed a rather complicated graph to decipher. It summarizes the evolution of the record efficiency of the different technologies over the years, but one should keep in mind that it does not account for crucial parameters of real-life solar cells, such as device active area, long-term stability or production cost.. Nonetheless, the chart clearly demonstrates the much steeper rise of efficiency of halide perovskite solar cells as compared to that of silicon- or thin film technologies.

1.1.2. WORKING PRINCIPLE OF PEROVSKITE SOLAR CELLS

The general working principle of a perovskite solar cell can be roughly summarized in three major steps :

1. Photon absorption and exciton formation : when the incoming photon energy is equal or higher to the active material optical bandgap Eg, a valence band electron is promoted to the conduction band of the material, generating an electron-hole pair, called exciton. The absorption is limited by two factors : the absorption coefficient of the material (α) and its thickness (t), as defined in Beer-Lambert's law :

   $$I = I_0 e^{-\alpha t} \tag{1.1}$$

   with I the transmitted radiation intensity and I_0 the incident intensity. Even though a low absorption coefficient can be counterbalanced by increasing the thickness, this latter cannot be adjusted at will; it is limited by the exciton and carriers diffusion lengths.

2. Exciton diffusion and dissociation : The diffusion length L_D is governed by the exciton lifetime τ and the diffusion coefficient D according to the equation:

   $$L_D = \sqrt{D\tau} \tag{1.2}$$

   The exciton binding energy is dictated by the dielectric constant. In the materials with high dielectric constants, as it is the case for halide perovskites, the exciton binding energy is low, and RT thermal energy ($k_B T$ = 25.7 meV at 298 K) can be enough to instantly dissociate the excition into an electron and a hole, called the charge carriers.

3. Charge carrier diffusion and collection : Once created, the charge carriers diffuse within the material, driven by the difference of the work function of the materials contacting the active layer, to the corresponding electrode and are collected, generating the desired photocurrent. The presence of impurities or defects in the active material or at the interface with the other layers constituting the device, can act as

traps for the charge carriers, limiting their diffusion and thus the efficiency of the device..

Hence, we can already extract the semi-conducting material properties required for solar cells applications:

- Adapted bandgap to absorb the incoming photons (ideally 1.34 eV for a single junction).
- High absorption coefficient.
- High dielectric constants to weaken the exciton binding energy. Alternatively, long exciton lifetime and large diffusion coefficient.
- Low defect density to avoid charge trapping.

The parameters used to evaluate the efficiency of the photovoltaic devices are now briefly discussed. It quickly appeared that defining reliable testing conditions is of paramount importance. In particular, the results should not depend on the geographical position of the laboratory in which the solar cells are made. Hence, the device response to light is tested according to well defined experimental conditions: the irradiance spectrum is the same in all the labs, as defined by the International Electrotechnical Commission (IEC 60904-3, Ed. 2, 2008).

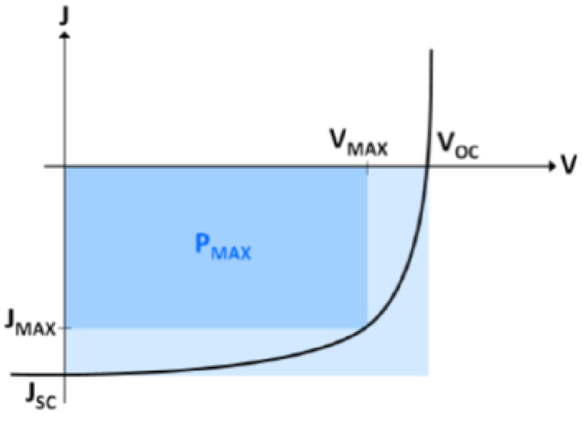

Figure 1.2: Typical solar J-V curve under illumination.

The devices are characterized under simulated solar light, by measuring current-voltage J-V curves (Figure 1.2). Four important parameters are extracted and used to quantify the efficiency of the working device. The open circuit voltage (V_{OC}) corresponds to the potential difference when no current flows and indicates the maximum voltage delivered by the solar cell. The short-circuit current density, J_{SC} is the current flowing through the solar cell under 0 V bias, characterizing the photocurrent. The fill factor (FF) is the ratio (between 0 and 100%) of the maximum power (P_M) over the product of J_{SC} and V_{OC}, as expressed in Equation 1.3, and characterizes, to simplify, the closeness to ideal behavior of the tested device.

$$FF = \frac{P_M}{J_{SC} \times V_{OC}} = \frac{J_{MAX} \times V_{MAX}}{J_{SC} \times V_{OC}} \tag{1.3}$$

Finally, the power conversion efficiency, PCE, corresponds to the ratio of the useful output to the input power, or, roughly, the percentage of received photons converted into electricity. It is calculated using the following equation:

$$PCE = \frac{P_{out}}{P_{in}} = \frac{P_{max}}{P_{light}} = \frac{J_{SC} \times V_{OC} \times FF}{P_{light}} \tag{1.4}$$

An important parameter for the commercialization of a technology is the long-term stability of the photovoltaic devices which are required to work for at least 25 years without significant degradation of their performance. Such time scales are not accessible during development, and it was agreed upon to perform accelerated tests. Hence, a device is considered to be sufficiently stable when the maximum PCE decay is not larger than 20% after being aged at 85 °C under continuous simulated solar light irradation (regulated spectrum) for 1000h.[10]

A more detailed, thorough and comprehensive text about the physics of solar cells can be found in the book by P. and U. Würfel.[11]

1.1.3. OPTOELECTRONIC PROPERTIES OF HYBRID HALIDE PEROVSKITES: THE SECRET BEHIND THE SUCCESS

As mentioned earlier, the efficiency of perovskite solar cells climbed from 10% to 25.5% between 2012 and 2020. Such improvement is quite impressive, and we propose now to briefly present the optoelectronic properties of these materials that led to such improvement :

- Direct and tunable bandgap. The optimal bandgap for photovoltaic applications is 1.35 eV. $MAPbI_3$ for example, presents a bandgap of ~ 1.55 eV, fairly close to the ideal value.[12] Compositional engineering allows tuning the bandgap.
- Hybrid halide perovskites present a high absorption coefficient $\alpha = 10^4 - 10^5 cm^{-1}$,[12] as shown in Figure 1.3, close to the absorption coefficient of GaAs and one order of magnitude higher than crystalline Silicon, as can be seen in Figure 1.3.

- High dielectric constant. In the case of $MAPbI_3$, the dielectric constant can reach the high value of $\epsilon = 70$[13] (in crystalline silicon: $\epsilon = 11.8$[14]). The exciton binding energy is thus very low and excitons are instantaneously dissociated at RT.[13]
- Ambipolar charge transport.
- Relatively low charge mobilities (between 20 and $160 cm^2V^{-1}s^{-1}$ in $MAPbI_3$.[15] However, the charge carriers have long diffusion lengths: up to 10 µm[16] or even 175 µm in single crystals.[17]
- Exceptionally long carrier lifetimes. In thin layers, the lifetimes range between hundreds of ns to several µs. It should be noted that such lifetimes can also be achieved in GaAs, but requiring much more complicated preparation conditions.[15]

The last two properties are particularly intriguing, considering that most of the devices reported in the literature are fabricated with polycrystalline perovskite thin layers, deposited by spin-coating and crystallized at relatively low temperatures (100 °C – more in subsection 1.3.1). Such fabrication protocols lead to very high defect densities, around $10^{16}\,\mathrm{cm}^{-1}$ in these polycrystalline thin films. In crystalline silicon, the defect density is around $10^{13} - 10^{14}\,\mathrm{cm}^{-1}$. Such a high defect density should lead to pronounced charge carrier recombination and charge trapping and hence decrease the optoelectronic performances of the devices. However, this is not the case, as these defects were found to be shallow, leading to the description of hybrid halide perovskites as “defect tolerant” materials.[18]

More details about the optoelectronic properties of the hybrid perovskites and the implications on the devices can be found in the comprehensive review of Egger.[15]

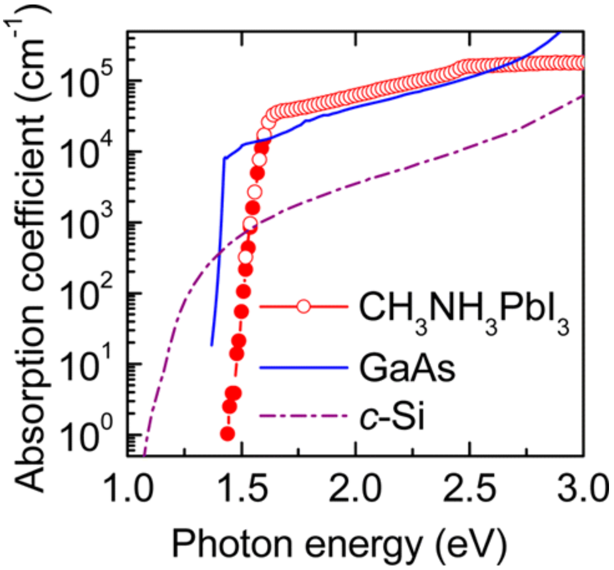

Figure 1.3: Absorption coefficient of a $MAPbI_3$ thin film compared with other typical photovoltaic materials : crystalline silicon and GaAs. Adapted from[12]

As mentioned above, the efficiency of perovskite solar cells increased rapidly during the last decade. The progress of the efficiencies is displayed in the left panel of Figure 1.4. To achieve such impressive increase, the used materials as well as the solar cells configuration evolved a lot. A recent comprehensive review by Jena *et al.* provides an extensive overview of the evolution of the device configuration, in addition to retracing the evolution of the major concerns of the scientific community over the years. The chart is reproduced in Figure 1.4.[19]

From this chart, we observe that the major concerns between 2016 and 2017 is the compositional engineering. $MAPbI_3$ was the first hybrid halide perovskite used in a solar device. However, its limitations appeared quickly, mostly due to its relatively low stability. Theoretical studies coupled with experimental works revealed that the use of a bigger organic cation, formamidinium ($CH(NH_2)_2 = FA^+$) in the inorganic cage could lead to higher efficiencies and increased stability. However, the photo-active phase $FAPbI_3$ is not stable at RT as it spontaneously transforms into a yellow, photo-inactive phase. In order to stabilize the photoactive phase, compositional engineering using a combination of organic and inorganic cations on the A-site of hybrid halide perovskites started in 2016, with the report of a device with enhanced stability.[20] The compound reported has a complex chemical formula: $Cs_x(MA_{0.17}FA_{0.83})_{100-x}Pb(I_{0.85}Br_{0.17})_3$, and it is concluded that alloying $FAPbI_3$ with two cations (Cs^+ and MA^+) and an additional halide (Br^-) increases the stability of its black phase. Shortly after, the rubidium cation was added to the already complex compound. This stabilization of the black phase was efficient and the interesting optoelectronic properties of $MAPbI_3$ were maintained, however, studies revealed ion segregation over time, as well as local compositional inhomogeneities. As a consequence, nowadays, the trend goes towards simplification of the structure, and currently, 5-components perovskites such as $Cs_xFA_{1-x}Pb(I_{1-y}Br_y)_3$ or $MA_xFA_{1-x}Pb(I_{1-y}Br_y)_3$ are widely used.

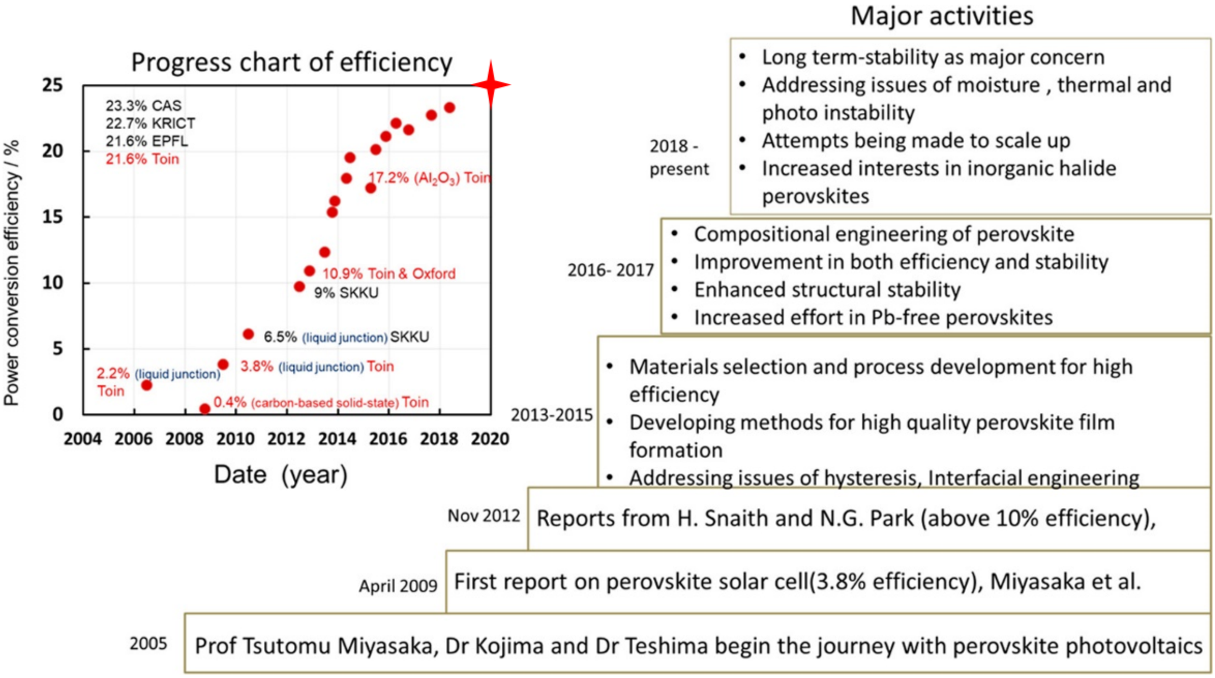

Figure 1.4: Major process in perovskite solar cells efficiencies (left) and major activities and concerns in the development of perovskite devices, as of 2019. Adapted from.[19] The red star in the left panel roughly indicates the record devices efficiencies reached in february 2021: 25.5%.

Finally, we would like to point out one of the last developments engaged in the last few years: the use of perovskite solar cells in tandem photovoltaic modules, that is, fabricating perovskite solar cell on top of another photovoltaic device, typically crystalline silicon, to enhance the absorption of visible or UV photons and increase their efficiencies. The bandgap tunability as well as the low temperature processability make halide perovskite a very promising candidate for these applications, as ideally a band gap of 1.7-1.8 eV is required for a material used in a tandem solar cell with a silicon subcell. Such devices have already achieved PCEs of 29.5%, illustrating the complementarity of different photovoltaic technologies.

1.1.4. LEAD TOXICITY AND APPLICATIONS BEYOND PHOTOVOLTAICS

From the very beginning, concerns about the presence of lead in these compounds have appeared. World Health organization classified lead as one of the ten most toxic substances for human health and environment. While some argue that the exposure to lead from large-scale perovskites modules could be lower than what we expected[21] or that the Pb content in the photovoltaic devices is relatively modest in comparison to existing technologies (banned lead gasoline, plumbing systems, soldering and paint),[22] the only real solution to this problem is the substitution of lead. It should be noted that in halide perovskites, lead occurs in its highly soluble Pb^{2+} form and thus generates a high risk of water pollution. Therefore, substantial efforts have been dedicated to obtain lead-free devices.

Substitution of lead by the lighter homologue tin is an obvious choice, however, it appears unsuccessful for now because of the easy oxidation of Sn^{2+} into Sn^{4+} which limits the PCE; likewise, the use of Ge^{2+} lead to low efficiencies. Lead-free double perovskites have also been used (typically $MA_3Bi_2I_9$) but, here again, the efficiency remained quite low. More information about the efforts towards lead-free perovskite solar cells can be found in.[19,23,24] The peculiar electronic structure of lead halide perovskites is at the heart of their impressive properties and in particular of their defect tolerance.[18] Despite considerable experimental and theoretical research efforts so far no Pb-free alternative could be found exhibiting similar features. It is intriguing to observe that similar efforts are made toward lead-free piezoelectric ceramic lead zirconate titanate (PZT), but here again, unsuccessfully.[25]

The outstanding optoelectronic properties of hybrid halide perovskite systems make them also attractive for a number of other applications such as X-ray detectors,[26] field effect transistors[18] or as light emitters due to their pure-color emission with high quantum yields when synthesized in form of colloidal nanocrystals.[27]

Before presenting the hybrid halide perovskites and some of their structural aspects, let us dive into the wonders of the extended perovskite structural family.

1.2. Perovskite structure: diving into infinite wonders

1.2.1. Crystal structure and stability conditions

When first heard of, the word “perovskite” can sound barbaric, hard to pronounce, with slight Russian-notes. Little is known then that it describes the crystal structure of the most abundant mineral on Earth $(Mg,Fe)SiO_3$, named bridgemanite after Percy Bridgman, Physics Nobel Prize recipient in 1946.[28] Further investigating the topic reveals that materials labelled as “perovskites” are met in everyday life thanks to their various properties, making them one of the most important class of materials in solid-state science.

In 1839, the German mineralogist Gustav Rose discovered the compound $CaTiO_3$, which he named perovskite after the Russian mineralogist Aleksevich von Perovski. The mineral eventually gave its name to a structural family of compounds which can be described by the general formula ABX_3. In the 1940's, the discovery of the dielectric and ferroelectric properties of $BaTiO_3$ attracted a great attention toward perovskite compounds, leading to the now recognized several hundreds of compounds described as perovskites.[29]

In a first approximation, perovskite materials can be considered as ionic structures described by the general ABX_3 formula, where A and B are cations and X is negatively charged. Hence, the first requirement for stabilizing a perovskite structure is the electrical neutrality. If q_i is the charge of the corresponding i ion, this condition can be written as :

$$q_a + q_b = -3q_x \tag{1.5}$$

A large number of perovskites are oxides: $X \equiv O^{2-}$ and A and B are inorganic cations with various charges, for instance the very famous $CaTiO_3$ ($q_A = 2$, $q_B = 4$) or $NaNbO_3$ ($q_A = 1$, $q_B = 5$) ... Halide perovskites, where $X = Cl^-, Br^-, I^-, F^-$ can be full inorganic or organic-inorganic hybrids. The latter, which will be the main focus of this thesis, have attracted growing interest in the last two decades. Less famous, nitride perovskites can also be formed, such as $ThTaN_3$ which exhibits promising thermopower properties.[30]

Since $CaTiO_3$ was found to adopt an orthorhombic structure at room temperature (RT),[31] it is the RT cubic structure of $SrTiO_3$ which was used to define the ideal perovskite structure, also called *aristotype phase*.[32] A very convenient way to visualize the structure is to define the cell with B cations at its origin. The A cations will occupy the cell center and the X anions will be located at the middle of the cube edges, as can be seen in Figure 1.5.a). The signature of the perovskite structure is the corner sharing BX_6-octahedra framework displayed in Figure 1.5.b). The A cation, positioned at the center of the cage formed by 8 corner sharing octahedra can also be described as the center of a cuboctahedral cage formed by the X anions (Figure 1.5.c).

The tolerance factor concept was developed early on, in 1928, by V. Goldschmidt is a simple tool, based on geometric considerations, to predict the geometric stability as well as distortions in oxide perovskites. Based on the assumption that cations are in contact with the anions, one can easily understand the steps in constructing this concept. A, B and X ions are adjacent along the cube edge and A and X ions are adjacent along a right triangle of $\sqrt{2}$ a hypotenuse length (cuboctahedron cage site), one can write:

$$2(r_x + r_b) = a \tag{1.6}$$

$$2(r_A + r_X) = \sqrt{2}a \tag{1.7}$$

Hence, the aristotype structure is stabilized for:

$$\frac{r_A + r_X}{r_X + r_B} = \sqrt{2} \tag{1.8}$$

This is nothing else but the famous tolerance factor t :

$$t = \frac{r_A + r_X}{\sqrt{2}(r_X + r_B)} \tag{1.9}$$

When $t = 1$, the ideal cubic structure is formed. Deviation from this value leads to distortion of the octahedral framework. Empirical studies showed that for oxide perovskites, in a range of t = 0.9-1, the cubic structure is stabilized. For t ranges between 0.71 and 0.9, a distorted lattice is stabilized with lower symmetry (tetragonal, orthorhombic...) whereas for t values higher than 1, hexagonal perovskites are formed (subsection 1.1.3).[33]

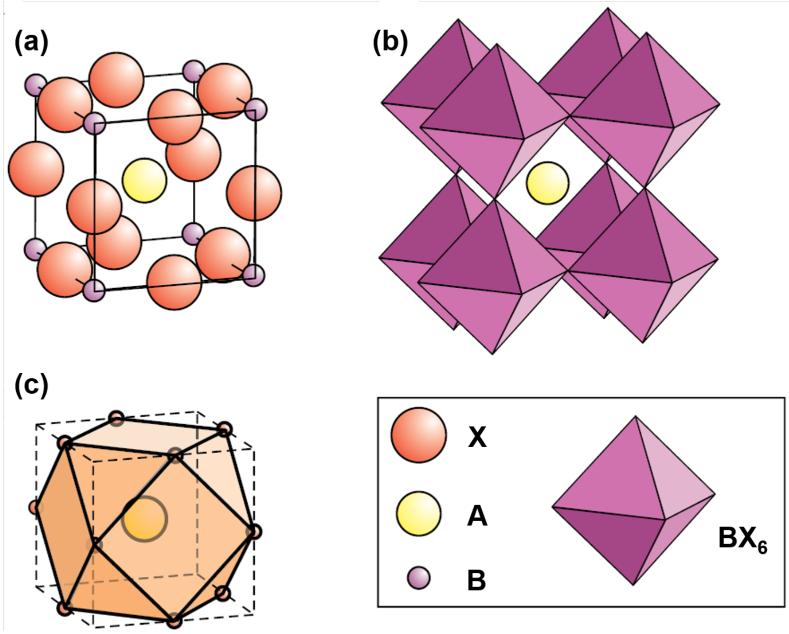

Figure 1.5: Perovskite aristotype cubic structure. (a) Cubic lattice with B atom at the cell origin. (b) BX_6 octahedra framework. (c) Cuboctahedral cage formed by the X ions with A ions site at the center. Adapted from.[29]

Later, an additional stability factor was defined, the octahedral factor μ, which characterize whether the B cation can fit in the octahedral hole lefts by the X anion sublattice. This factor is defined in Equation 1.10, and the ideal value of this unitless ratio was determined to be 0.41.

$$\mu = \frac{r_B}{r_X} \tag{1.10}$$

These two factors allow in a very simple way to predict the compatibility of a set of 3 ions to arrange in a perovskite structure. An amazing feature of the perovskite structure is its great flexibility and versatility in composition and a close correlation between the chemistry and the physical properties of these materials can be established. Perovskite materials can also be alloys, by introducing various amounts of different ions which would occupy the same A, B or X site. The most famous perovskite alloy is $\mathrm{Pb[Zr_xTi_{1-x}]O_3}$ which is used in various applications (sonars, capacitors. . .) thanks to its piezoelectric properties.[25]

Depending on the nature of the ions constituting the material, perovskites display an impressive set of different properties, such as pyroelectricity, semi and supra conductivity, colossal magnetoresistivity, magnetism in addition to ferro and piezoelectricity cited earlier. It is however important to highlight that for most of these properties to be observed, the material has to adopt tetragonal or lower symmetries. Wonders arise from breaking the cubic symmetry, and in perovskites, it can happen as a result of ion displacement, distortion and/or octahedral tilting, which are presented in the next section.

1.2.2. Where it gets interesting : displacement, distortion and octahedral tilting

Deviation from the aristotype structure is fundamental for the apparition of most of the well-known perovskite structural properties. Most often, it is the BX_6 octahedron which experiences modification of its ideal symmetry or stacking. The octahedra framework is largely considered as the root of the properties of the perovskites, which are modulated by the electronic configuration of the B atom, which is in turn affected by the surrounding X anions. The A cation cannot be ignored, but it is less responsive to the chemical manipulation that generates the physical properties. Three types of modifications can affect the BX_6 octahedron and thus the symmetry of the perovskite structure: distortion, ion displacement and octahedral tilting. All of these modifications are temperature and pressure dependent, such that a high temperature and/or pressure (the absolute values of which depend on the chemical composition of the perovskite), the cubic phase is favored. As temperature and/or pressure decreases, one or more of the above cited modifications arise.

Octahedral distortion can have two origins: disproportionation which is a change of cation valence ($2B^{n+} \rightarrow B^{n+1} + B^{n-1}$), leading to different cation sizes thus causing the octahedra to adjust through distortion. However, the most common effect in perovskite is the well-known Jahn-Teller effect (JTE). This principle states that polyatomic systems with electronic degenerate states are unstable, and distortion spontaneously happen to remove the degeneracy. Electronic degeneracy occurs for specific electronic configurations and ions that favor this effect are well known and called Jahn-Teller ions, the most famous being Cu^{2+}. This effect, which results from the interaction of the cation orbitals and the surrounding anions leads to an either elongated or compressed octahedron. The most well-known perovskite displaying such octahedral distortion is the compound $KCuF_3$.[34] More about the Jahn-Teller effect can be found in the article by Köppel, Yarkony and Barentzen.[35]

BX_6 octahedron can also experience B^{n+} cation displacement from the center of the octahedron. This phenomenon is attributed to the second order JTE, also called pseudo Jahn-Teller effect (PJTE), which explains that in polyatomic arrangements in which two or more states are not exactly degenerated but close in energy (pseudo-degeneracy), JTE is not removed but modified. In perovskite systems, this phenomenon is usually observed when the B ion is too small for the octahedral site, and results in cation displacement inside the octahedron. This displacement generates permanent electric dipole, leading to pyroelectric, ferro and anti-ferroelectric properties. Such cation displacement is observed in $BaTiO_3$, explaining its dielectric/ferroelectric properties. Text by Bersuker provides more information about pseudo Jahn-Teller effect.[36]

Finally, the last modification of the octahedral framework is tilting. Tilting usually happens when the A cation is too small for the cuboctahedral site, forcing the BX_6 arrangement to tilt to adjust. Here, the shape of the individual octahedron is not changed, it is the stacking of the octahedra which deviates from the ideal case. BX_6 octahedra are apex-linked, meaning that the tilt of one octahedron completely changes the arrangement of the octahedra in the perpendicular direction of this tilting. As tilting can occur simultaneously along the three directions and with different amplitudes, the resulting structures can often be quite complicated.

In 1972, Glazer rationalized all the possible octahedra tiltings in the perovskite structure, and developed a notation to translate these tiltings.[37] Starting from aristotype cubic perovskite crystal, three tilting directions are possible, corresponding to the cell direction (a, b and c), hence the notation uses three letters, each one corresponding to the direction around which the tilting occurs. For the ideal cubic structure, no tilting is observed in any of the three directions, and the Glazer notation in this case is $a^0a^0a^0$ (Figure 1.6.a). The a symbol is written in the three positions as the tilting amplitude is the same in the three cell directions, in this case, no tilting, as highlighted by the 0 exponent.

We consider, to start with, tilting around one direction only. When rotating around one direction, for example around c, the arrangement of the octahedra in the normal plane is affected, as can be clearly seen in Figure 1.6.b and Figure 1.6.c. When considering the adjacent layers stacked along the rotation axes, two scenarios are possible: both layers rotate in the same direction, making them indistinguishable from one another as it is the case in Figure 1.6.b or the two layers rotate in different directions along c as in Figure 1.6.c where the two layers can be distinguished. The notation corresponding to the first case would be $a^0a^0c^+$ whereas the second case will be noted $a^0a^0c^-$. The two first letters a with the 0 indices indicate that no tilting is observed around a and b cell directions, while the c letter indicates that the rotation occurs around the c direction. The + and – indices indicate that adjacent layers along the rotation axe tilt, respectively, in the same or in opposite directions.

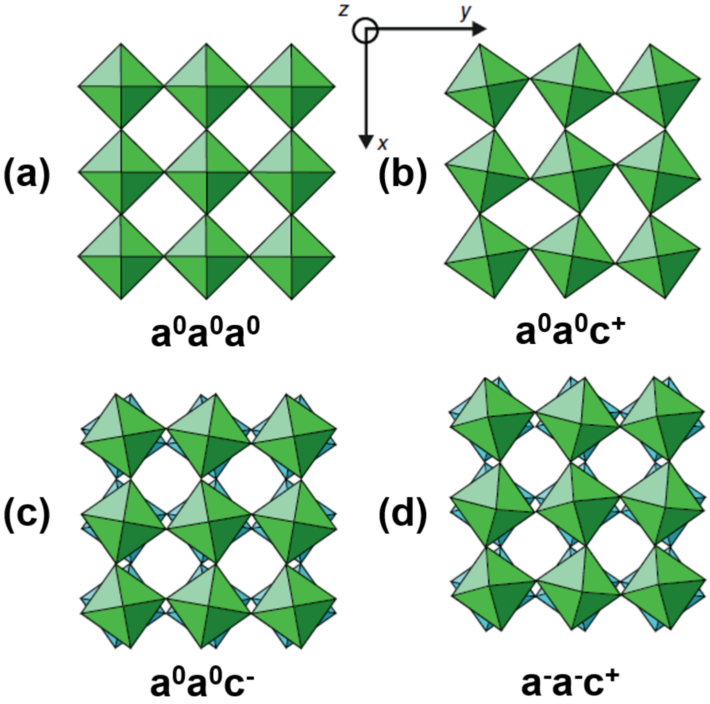

Figure 1.6: Illustration of different octahedra tiltings. (a) Aristotype cubic structure, no tilt. (b) and (c) one tilt along c direction, with in phase (b) and out-of-phase (c) tilting of two adjacent octahedra layers along c. (d) three tilts. Adapted from.[29]

When further introducing a second and a third rotation axes, the directions showing the same rotation amplitude would be indicated by the same letter. For example, in $a^-a^-c^+$ (Figure 1.6.d) where the octahedra are rotated around the three cell axes, the rotation amplitude around a and b directions is the same, with a different amplitude along c. This simple notation has been since widely used to describe the perovskite structure and tilting systems.

Developing this model, Glazer identified 23 possible tilt systems, which were later reduced to 15 possible systems by Howard and Stokes by symmetry arguments.[38] As mentioned earlier, octahedral tilting is favored when the A cation is too small for its site. However, these tilts are also experienced by many perovskites as the temperature and/or pressure is varied. The aristotype perovskite structure is described by the Pm-3m space group and is stable at high temperature and/or pressure. As temperature and/or pressure is lowered, the structure may experience tilting, leading to symmetry lowering. Here again by considering the group theory argument, Howard and Stokes listed the space group adopted by systems experiencing pure octahedral tilting, drawing the group-subgroup relationship induced by octahedral tilting, shown in Figure 1.7. It is however worth mentioning that this hierarchy is only valid for systems experiencing tilting solely, without considering the two other possible distortions experienced by the perovskites, which generate a different group-subgroup chart.

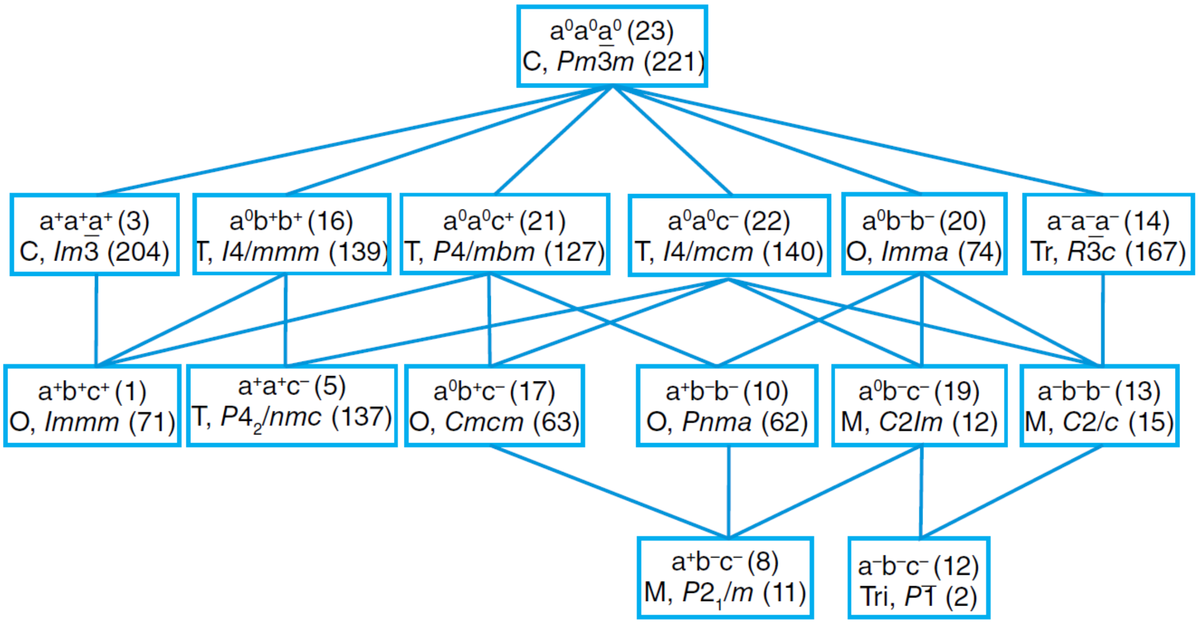

Figure 1.7: Group-subgroup hierarchy in perovskites displaying octahedral tilting solely. Developed by.[38]

The three modifications detailed above are not mutually exclusive and more than one of them can be observed in the same material. Moreover, these effects can be cooperative as they can add themselves, as well as non-cooperative. In the latter case, the effects might cancel out at the macroscopic level and nonetheless influence the microscopic properties of the perovskite.

1.2.3. HEXAGONAL PEROVSKITES

When the A cation is too large for its cuboctahedral site in the aristotype structure, in other words when $t > 1$, the favored structure is not cubic anymore but hexagonal, labelled as “hexagonal perovskite”. Cubic-packing of the octahedral refers to apex-sharing octahedra, as in the aristotype structure (Figure 1.8.c), and hexagonal packing describes face-sharing octahedra. A structure can exhibit purely hexagonal packing, as displayed in Figure 1.8.a, and can be described as column of face-sharing BX_6 octahedra, in which the A cation occupy the free space left between two consecutive chains.

Cubic packings can intercalate between the hexagonal layers, as illustrated by Figure 1.8.b. Theoretically, any linear combination of hexagonal and cubic stacking sequences is possible, creating a plethora of structures with more or less large cells. Furthermore, for the same number of hexagonal and cubic packings in one cell, different combinations of these packings can be formed, thus generating the impressive number of known hexagonal perovskite structures. To identify the different hexagonal structures, different notation systems exist, such as the ABC notation, the Zhdanov notation... Ramdsell notation remains the most used one. In this notation, the number of octahedron layers in one cell is reported next to a letter designating the symmetry of the cell : C for cubic, H for hexagonal, R for rhombohedral... Thus, the structure displaying purely hexagonal packing in Figure 1.8.a is labeled 2H, while the mixed structure in Figure 1.8.b is noted 4H and the cubic aristotype structure in Figure 1.8.c is labeled 3C.

The most famous hexagonal perovskites are $BaMO_3$ where M = Mn^{4+}, Co^{4+} or Ni^{4+}.[39]

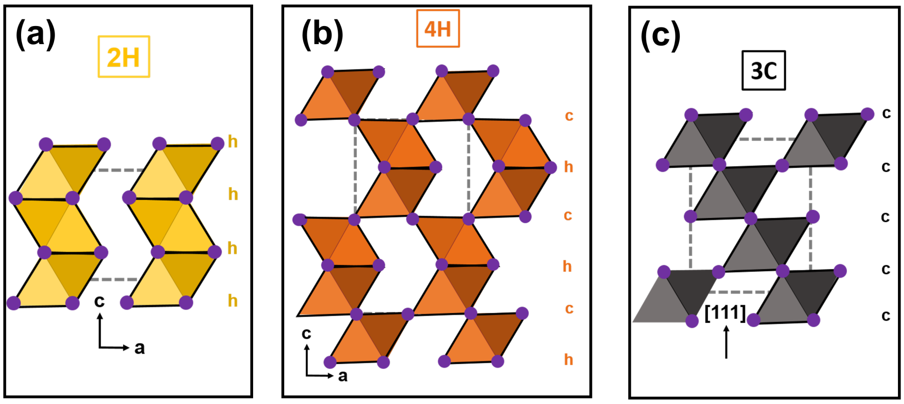

Figure 1.8: Schematic structures of (a) 2H and (b) 4H hexagonal polytypes projected along [110], (c) 3C cubic structure, visualized along [111] direction. For clarity, the A cation position is not displayed here. h and c letters refer to hexagonal or cubic packing, respectively.

High pressure favors high density packing, which results in the 3C cubic structure. It has been shown that upon increasing temperature/pressure, hexagonal perovskites can be transformed into the cubic structure, following different sequences, the most common one being 2H – 9R – 4H – 6H – 3C. These compounds, which have the same chemical formula but different crystallographic stackings are called polytypes. It has been shown that the different polytypes might exhibit different physical properties.[40]

Hexagonal structures can also be stabilized by ion vacancies. In this case, the name polytype should not apply as the chemical formula changes, but it has been widely used anyway. Moreover, changes in the material stoichiometry may change the hexagonal polytype, as it is the case in $BaMnO_3$ which adopts six different hexagonal perovskite structures as the anion deficiency increases and the chemical formula evolves from $BaMnO_3$

to $BaMnO_{2.5}$. These $BaMnO_3$ structures have been found to display interesting catalytic properties.[41] B cation vacancies also favors the hexagonal packing in compounds such as $SrCoO_3$, and such B-vacancies have shown interesting dielectric properties.[42]

1.2.4. Thermal expansion

The magnitude of the coefficient of thermal expansion (CTE) in many perovskites is closely related to the thermal behavior of BX_6 octahedra. The latter is in turn affected by the tilting and/or the bonding between B cation and the surrounding X anions. For example, thermal expansion can be anisotropic, with different expansion magnitudes depending on the crystallographic directions. In tetragonal $SrLaAlO_4$[1] for example, two different bond lengths between Al and O ions are observed inside the octahedron, resulting in different linear thermal expansion coefficients along the a and c tetragonal axis.[43] Such anisotropy can also be caused by magnetic and spin ordering with temperature.

A large number of perovskite compounds experience contraction as the temperature is increased, indicating a negative thermal expansion, noted NTE, at least for some temperature ranges. In many cases, this phenomenon is observed in crystals showing distortions (cation displacement for example) that lower the symmetry. As the temperature increases and the sample approaches the aristotype structure, the amplitude of the distortion decreases which can lead to a contraction along the corresponding cell direction. In some cases, the contraction along one direction can overweight the expansion along the other directions, leading to an overall contraction of the cell volume as the temperature increases. The most well-known example of this behavior is $PbTiO_3$, in which the Ti^{4+} displacement in the octahedron decreases as the temperature increases, leading to a contraction along c.[44] The same property can arise for compounds experiencing Jahn-Teller effect (JTE) and in which the octahedra are elongated: the increase in temperature decreases the amplitude of JTE leading to contraction along one direction. Finally, NTE has also been observed in compounds where continuous charge transfer happens, thus modifying the bonds lengths, as in $SrCu_3Fe_4O_{12}$.[45]

The CTE of many perovskites can be tuned through composition, by partial substitution of A, B or X ions. Considering that some perovskites display NTE while others experience positive thermal expansion, one can imagine that alloying two compounds with different thermal behavior could lead to a zero thermal expansion (ZTE) materials. These compounds which do not expand as the temperature rises are actively sought as they present major technological advantages in microelectronic devices but not only. As an example, ZTE was achieved when alloying $PbTiO_3$ and $Bi(Zn_{0.5}Ti_{0.5})O_3$.[46]

---

[1] The formula of this compound is different from the classical perovskite chemical formula ABX_3 as it adopts a structure described as "double perovskite" which is not detailed here. The same applies for $SrCu_3Fe_4O_{12}$ shown later on. However, both are still described as perovskites.

Additional information about the extended perovskite structural family can be found in the book by Tilley.[29]

1.2.5. Halide perovskites

The first halide perovskite material, $CsPbX_3$ ($X = I^-$, Br^-, Cl^-) was synthetized in 1893[47] but its perovskite structure was established only in 1958.[48] Since then, inorganic halide perovskites have shown interesting properties: large optical transmission domain, high resistivity, antiferromagnetism, piezoelectricity, photoluminescence. . . .[49]

The tolerance factor stability condition, initially defined for oxide perovskite was applied to halide compounds. An empirical systematic study on the stability of more than 180 systems based on geometry considerations extended the stability domains of halide perovskite to $0.813 < t < 1.107$.[49] It is however worth mentioning that as the charge of the halide is two times lower than oxygen, the overall Madelung electrostatic energy of the system is divided by four in comparison with oxide perovskites.[50] Moreover, as stated by Travis *et al.*, in the case of halides, which display lower electronegativity than oxides and greater chemical softness, considering the ions as hard, unpolarisable spheres is less valid than for oxides, questioning the applicability of the tolerance factor as defined for oxides.[51]

As explained earlier, the use of the once considered as a scientific curiosity compound $MAPbI_3$ in photovoltaic cells generated great interest in the scientific community, which, since 2012, produced a daunting number of papers. We will, in the following, introduce briefly the properties of hybrid perovskites that will be useful to understanding the results shown in this thesis.

1.3. Hybrid halide perovskites: general structural aspects and properties

Hybrid halide perovskites are a subclass of the larger perovskite structural family, hence, these compounds can be described using the same general principles as those introduced in the previous section. For example, the same tolerance factor concept can be used and remains fairly accurate, but it is important to keep in mind that other factors are ought to play a role which might be important but still needs to be further investigated. In the case of inorganic materials, the A cation can be in general considered as spherical, thus isotropic. However, in hybrid perovskites, the organic cation in the A site is no longer spherical and strong shape anisotropy may be observed, which is often accompanied by polarization effects and orientational disorder.[51] Moreover, while inorganic perovskites are mostly ionic structures, the introduction of the organic cation can lead to the formation of hydrogen bonds which might change the structure stability. The previous observation concerning the low charges of halide perovskites and the decreased Madelung energy is obviously still valid here.

Some of the above mentioned factors will be addressed in the following paragraphs, in the limit of what is known to date in this rather young and still growing field where a lot remains to be understood. This section will mainly focus on methylammonium (MA^+) and formamidinium (FA^+) lead halide perovskites, focusing on their general structural features, highlighting the common properties and the ones on which they differ. Discussions around tin-based hybrid halide perovskites will be introduced when needed to add comparison elements to these sections.

1.3.1. The easy synthesis of hybrid halide perovskites

One of the major advantages of hybrid halide perovskites is their simple preparation and low processing temperatures. In opposition to inorganic perovskites which are synthesized at high temperature (200 °C - 1200 °C[52]), crystalline hybrid halide perovskites can be obtained at temperatures lower than 150 °C and even at RT. This is also in stark contrast with the single crystalline silicon or GaAs which are obtained through high temperature melting methods, at temperatures as high as 1425 °C.

Vastly used as thin layers in laboratory solar cells, a plethora of deposition methods have been developed during the last 10 years. The most used technique is spin-coating of a liquid precursor solution, followed by an annealing step around 100 °C. The liquid precursor solution can be spin-coated in one-step when both PbX_2 and AX ($A = MA^+$ or FA^+ and $X = I$, Br, Cl) powders are dissolved together in a polar solvent, generally dimethylformamide (DMF). Alternatively, deposition can occur in two distinct steps in which the inorganic precursor is first deposited, before addition of the organic precursor, which can be dissolved and spin-coated or added in its vapor phase. Crystallization can also be achieved from vapor phase, through precursors evaporation or pulsed laser deposition methods, which can be tricky because of the highly volatile organic precursor that complicates the precise control of the evaporation parameters. The last years have also seen the rise of more scalable processes to achieve solar devices with larger areas, such as doctor blading, slot-die processes... Again, the number of publications and processing methods can be described as overwhelming, and summarizing all of them not the goal here. Very luckily, great reviews of these different fabrication methods now exist, and we can cite, among others, the papers by Dunlap-Shohl,[53] Dai,[54] Gao[55] and Park.[56] The latter is dedicated to scalable processing methods.

The growth of the materials in their single crystalline form is important for some applications, such as X-ray detection,[57] but is also a requirement for a number of fundamental studies aiming to better understand the intrinsic properties of the compounds. Initially, single crystals were grown from controlled temperature lowering of the solution precursors from 170 °C,[58] or by slow evaporation. A breakthrough in the growth of hybrid halide perovskites resulted from the two papers from O. Bark's team in 2015.[59,60] This team discovered that, in the right solvent, hybrid halide perovskites displayed an unusual inverse solubility trend, that is, as the temperature increased, instead of increasing as it generally is the case, the solubility of these materials tend to decrease (Figure 1.9.a and Figure 1.9.b). This property lead to the development of the crystal growth method called Inverse Temperature Crystallization (ITC) and large single crystals, with high crystalline quality, were grown within a few hours, and at low temperatures: between 80 and 120 °C. Various hybrid halide compounds were obtained through this method (Figure 1.9.c - Figure 1.9.h). Moreover, the process was adapted to obtain, amongst others, single crystals with controlled shape and thicknesses (Figure 1.9.d) through confined growth.[61,62,63] Such crystals have been introduced in solar devices recently, leading to efficiencies exceeding 21%.[64] Also, single crystals of solid solutions with multiple cations and anions have been grown.[65,66,67,68,69] However, it should be noted that only few of these reports gave quantitative proof of alloying by quantifying the final chemical composition of their samples. Recently, this approach has been extended to tin-based perovskites.[70] Here again, reviews on the numerous achievements in this field are available.[71,72]

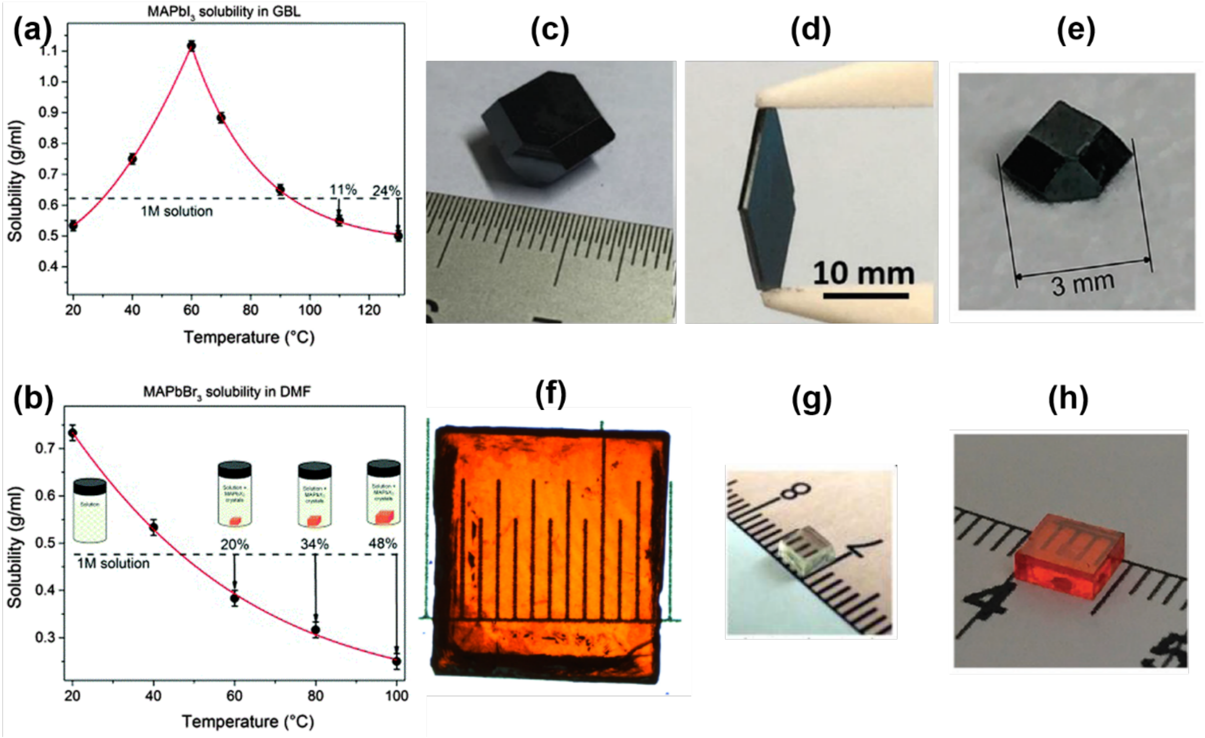

Figure 1.9: Inverse Temperature Crystallization (ITC) of hybrid halide perovskites. (a) and (b) Evolution with increasing temperature of the solubility of MAPI$_3$ and MAPbBr$_3$, respectively, in the appropriate solvent. (c)-(h) pictures of the single crystals obtained through ITC: (c) MAPbI$_3$ bulk and (a) shape controlled, (e) FAPbI$_3$, (f) MAPbBr$_3$, (g) MAPbCl$_3$ and (h) FAPbBr$_3$. (a), (b), (e) and (h) adapted from.[60] (c) and (d) adapted from.[63] (f) adapted from[57] and (g) adapted from.[73]

Finally, powder samples, less popular in this family of compounds, can be very helpful in understanding material properties. In previous reports, the most popular synthetic route to powders is through slow cooling of a stoichiometric precursor solution from 100 °C to RT.[74] Other authors have heated one precursors solution to around 100 °C and obtained the powder through solvent evaporation. In 2015, mechanosynthesis was found to be efficient to obtain crystalline powder samples. For this solid-state, solvent-free synthetic route, the precursor powders are ground at RT for at least 30 min using ball milling, leading to crystalline powders.[75,76] Recent works reported enhanced stability of the powders obtained through this method.[77]

1.3.2. THERMAL BEHAVIOR: PHASE TRANSITIONS AND EXPANSION COEFFICIENTS

Besides $MAPbI_3$, all hybrid halide perovskites of interest here, namely $MAPbBr_3$, $MAPbCl_3$ and $FAPbX_3$ ($X = I^-$, Br^-, Cl^-) adopt a cubic symmetry at RT, described by the space group Pm-3m. $MAPbI_3$ was found to be the only compound of this family to be tetragonal at RT. The tetragonal phase is now accepted as I4/mcm but it was initially largely debated. This aspect will be detailed in subsubsection 1.4.1.2 of this chapter. Before going any further, it is of high importance to precise here that in the case of $FAPbI_3$, the cubic phase is metastable at RT. The thermodynamically stable phase of this compounds is a hexagonal structure, similar to the hexagonal perovskites presented in subsection 1.2.3. The cubic structure can be temporarily stabilized at RT after heat treatment. The polymorphism of $FAPbI_3$ will be discussed in subsection 1.4.2 of this chapter as well as in chapter 4 of this manuscript.

The cubic lattice parameters and cubic-tetragonal phase transition temperature of the compounds of interest as found in the literature are gathered in Table 1.1 and Table 1.2. One can observe that substitution of the halogen leads to smaller lattice parameters in the following order $I^- > Br^- > Cl^-$ as expected by the smaller ionic radii in this same order. Moreover, the substitution of MA^+ by FA^+ leads to slightly bigger lattices, again in agreement with the greater size of the latter.

	$A^+ = MA^+$					
	$B^{2+} = Pb^{2+}$			$B^{2+} = Sn^{2+}$		
	X^-=I^- [78]	X^-=Br^- [79]	X^-=Cl^- [80,81]	X^-=I^- [82]	X^-=Br^- [80]	X^-=Cl^-
Cubic lattice parameters @ RT (Å)	6.306 (350 K)	5.929	5.865	6.309	5.916	-
Temperature cubic-tetragonal phase transition (K)	330	220	179	275	229	-
Tetragonal space-group	I4/mcm			-	-	-

Table 1.1: Cubic phase lattice parameter, temperature of cubic-tetragonal phase transition and tetragonal space group of selected MA-based halide perovskites.

	A^+=FA^+					
	B^{2+}=Pb^{2+}			B^{2+}=Sn^{2+}		
	X^-=I^- [83]	X^-=Br^- [84,85]	X^-=Cl^- [86]	X^-=I^- [84]	X^-=Br^-	X^-=Cl^-
Cubic lattice parameters @ RT (Å)	6.358	5.986	5.738	6.309	-	-
Temperature cubic-tetragonal phase transition	285	∼263	?	∼238	-	-
Tetragonal space-group	P4/mbm			P4/mbm	-	-

Table 1.2: Cubic phase lattice parameter, temperature of cubic-tetragonal phase transition and tetragonal space group of selected FA-based halide perovskites

The cubic-tetragonal transition temperature varies a lot, and the two tables seem to indicate that the smaller the halogen, the lower the transition temperature. It is also interesting to observe that the tetragonal phases of MA-based and FA-based compounds do not adopt the same symmetry. Tetragonal MA-based compounds crystallize in I4/mcm, which is described in Glazer notation as $a^0a^0c^-$ whereas FA-based compounds adopt a P4/mbm symmetry, noted $a^0a^0c^+$ according to Glazer's notation. In the former, two adjacent layers along c rotation in opposite directions along this axis while in the latter the layers experience in-phase rotation when the cubic-tetragonal phase transition occurs. Interatomic potential simulations seemed to indicate that larger A cations favor P4/mbm over I4/mcm symmetry.[87]

For almost all the compounds presented here which have been studied at low temperatures, further cooling leads to a tetragonal-orthorhombic Pnma phase transition. The only exception is $FAPbI_3$ for which, upon cooling, the tetragonal phase experiences a re-entrant phase transition to what seems to be a more disordered phase,[88,89] indicating a complex molecule-cage interaction in this compound. It is also worth mentioning that in its three crystallographic phases (cubic Pm-3m, tetragonal P4/mbm and orthorhombic Pnma), $FAPbBr_3$ remains pseudo-cubic, *i.e.*, with very similar a, b and c lattice parameters over the whole probed temperature range.[84,85]

For these compounds, in which non-spherical molecular cations occupy the A-site, to adopt a cubic symmetry, the organic cation has to display rotational disorder, which can either be static or dynamic.[78,85,86] As the temperature is decreased, the motion of the organic cation is found to slow down for all samples, but it is not clear yet whether the reduction of the motion of the organic cation influences the tilting of the inorganic cage or the other way around. Crystals such as these hybrids, which can be labelled as ”plastic crystals” because of their translation periodicity but orientational disorder,[90] are bound to experience a complex interplay between the motion of the molecular cations and the surrounding inorganic framework. Elements of discussion will be developped in the next section.

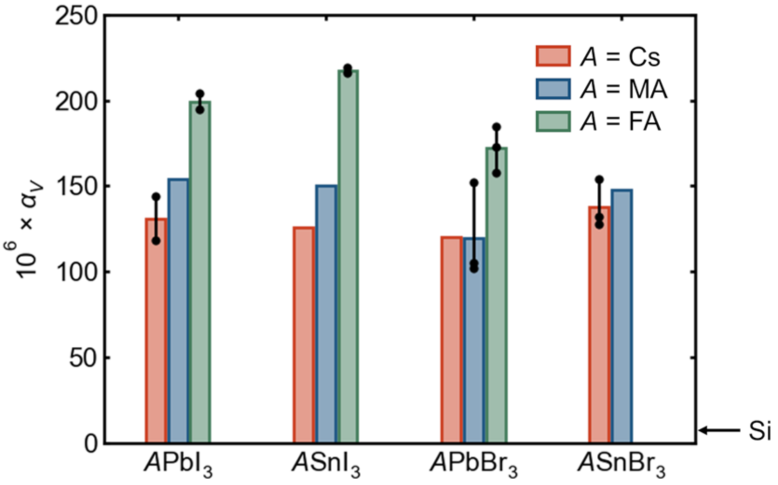

Figure 1.10: Volumetric thermal expansion coefficients α_V of various lead and tin, bromide and iodide perovskites. The value for crystalline Silicone is pointed for comparison. Adapated from.[91]

Before moving to the next section, we would like to point out a very interesting property observed in all these hybrid lead/tin perovskites: the enormous positive thermal expansion. Figure 1.10 was adapted from Fabini *et al.* which gathered all the reported volumetric CTE for the compounds of interest.[91] For comparison, the CTE of crystalline silicone is indicated on the graph. It is sticking to observe the huge values of volumetric CTE in hybrid halide perovskites. In fact, $FAPbI_3$ and $FASnI_3$ were found to exhibit the highest CTEs known for any 3D crystalline solids near RT.[58,84,91] This feature might, however, impact the devices in which these compounds are used, as repeated temperature cycling could lead to mechanical fatigue and cracking of the material.

The volumetric CTEs displayed in Figure 1.10 are positive, but it should be noted that directional negative thermal expansion (NTE) was observed in the tetragonal phase of some compounds ($MAPbI_3$ and $MAPbBr_3$ for instance). In other words, in tetragonal $MAPbI_3$ and $MAPbBr_3$ the c axis was found to contract while the a axis expands when the temperature is increased.[79,92,93] However, the rapid expansion along a counteracts the compression along c, leading, in the tetragonal structure, to positive volumetric CTEs.[78,94] Moreover, some of the compounds where no NTE is observed showed anisotropic expansion in the tetragonal phases.[83] As was discussed in subsection 1.2.4, these observations hint to complex local structures in the compounds.

1.3.3. The complex interplay between the inorganic lattice and the organic cations

The structure of the two molecular cations of interest in this discussion is shown in Figure 1.11 where the red arrow represents the electric dipole of the two molecules. It appears that MA^+ displays a larger permanent electric dipole than FA^+: 2.2 D in the former and 0.2 D in the latter.[95] It indicates that dipole-dipole interaction between the organic cation and the inorganic cage can arise, in addition to the electrostatic interaction, in the case of MA-based compounds but presumably in much less extent the case of FA-based because of its negligible electric dipole.

The role of the hydrogen bonds on the structural features of hybrid halide perovskites is a topic of intense debate and here also, a tremendous number of studies has appeared, but to this date, the question is not settled yet. Only nitrogen bound hydrogens are supposed to develop H-bonds with the halides, even though some papers have reported the formation of CH-X H-bonds.[96] These last results remain however controversial. As shown in Figure 1.11, the FA^+ cation can form 4 H-bonds, while 3 H-bonds can potentially arise from MA-based compounds. Through NMR experiments, Svane *et al.* determined, at RT, very weak hydrogen bonding energies for both MA and FA based lead perovskites: between 0.02 and 0.09 eV/H-bond. Moreover, no significant difference for the three halides in both systems has been observed.[95] These results indicate that, at least at RT and above, hydrogen bonds play little role in the interaction between the organic cation and the inorganic framework (thermal energy kBT = 25.7 meV at 298 K). At lower temperatures, some reports argued that the H-bonds are the driving forces of octahedral tilting during phase transitions[41,96,97] while others reported a more complex combination of entropy and H-bonding to cause the phase transitions.[50] The latter hypothesis is more coherent with the fact that for $MAPbI_3$, a cubic-tetragonal phase transition happens around 60 °C, a temperature at which no or very weak H-bonds are expected according to Svane *et al.*.[95]

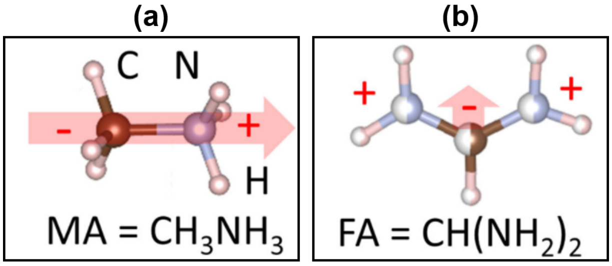

Figure 1.11: Structure of methylammonium (a) and formamidinium (b) cations. The red arrows represent the electric dipole. The carbon atom is represented in brown, the nitrogen in blue and the hydrogens in white. Adapted from[98]

The dynamics of the cations inside the inorganic cage have also to be considered. As mentioned earlier, the cations are fully disordered in the inorganic framework in the cubic symmetry. In the case of MA-based compounds, multiple studies have agreed that in the tetragonal phase, the molecular cations are partially disordered as they lost the degree of freedom around the 4-fold symmetry axis. Lowering the temperature leads to the transition into an orthorhombic symmetry where the organic cations are completely ordered in an antiferromagnetic fashion.[78,86,99] However, the picture seems to be a lot more complicated in FA-based compounds. In 2018, Weller's team published a neutron scattering study on $FAPbI_3$ where they observed, in the tetragonal phase, a dynamic disorder between preferred orientations of the organic cations, with thermal displacement parameters decreasing as the temperature is lowered. They concluded to a coupling between the dynamic mode of FA^+ cations and the inorganic framework.[89] The same year, Govinda *et al.* conducted dielectric measurements on $FAPbBr_3$ and $FAPbCl_3$ and compared the results with those obtained on the MA-based equivalents. The latter showed temperature-dependent dielectric constants, which drastically dropped in the orthorhombic phase, in agreement with the above mentioned ordering of the cations in this structure. However, the dielectric constants of FA-based compounds did not evolve with temperature in the probed range (300 – 140 K), and the authors concluded to a deep frozen state of the FA cations.[86]

However, the picture seems to be even more complicated than that. Combining NMR and dielectric constant measurements, Fabini *et al.* demonstrated that at RT, FA^+ and MA^+ in a PbI_3 inorganic cage display similar reorientation times. However, the reorientation times of FA^+ in $FAPbI_3$ shows a weaker dependence with temperature, in contrast to MA^+ cations in $MAPbI_3$. This studies shows that FA^+ cations keep considerable motion until 100K, even after the re-entrant phase transition mentioned earlier which is observed through scattering techniques around 140 K. Below 100 K, the cations experience glassy freezing. Scattering-based studies indicate that at these temperatures, no change in the inorganic framework happens. This study hints to a loss of correlation between the organic cations and the inorganic octahedra, and frustration of the organic cation in the octahedral framework is proposed to happen at low temperature.[100] Similar observations have been made on $FAPbBr_3$,[101] which does not display the re-entrant phase transition but for which low temperature glassy freezing was also reported.[101]

Another intriguing feature of these materials has to be mentioned: the observation of local, dynamic and anharmonic inorganic cage dynamics. A considerable number of reports have now emerged to show local distortions of the inorganic octahedra. Pair Distribution Function (PDF) experiments, which appeared to be a highly relevant for these studies, was performed on a number of different hybrid halide compounds ABX_3 ($A = MA^+, FA^+$; $B = Pb^{2+}, Sn^{2+}$ and $X = I^-, Br^-, Cl^-$) in the cubic phase and all led to the same conclusion. While the long-range pattern is satisfyingly reproduced using the cubic model, the short-range pattern is not well encountered when using this model. The measured data are correctly matched when using an orthorhombic phase, indicating lower local symmetry in the cubic lattices.[82,102,103,104,105] Taking these local tilting into account during theoretical calculations allowed some of the authors to reach an enhanced agreement between the calculated electronic structure and the measured one.[105] Moreover, temperature dependent Raman spectroscopy studies highlighted the liquid-like nature of the cubic lattice,[106,107] emphasizing the anharmonic nature of the inorganic lattice which cannot be considered as a rigid structure.

This part, in which the complex local and dynamic features of the hybrid halide perovskites were presented was designed to highlight some of the questions for which answers are still lacking: from the nature and the role of the H-bonds, to the tilting and distortions of the octahedra, but also the dynamics of the different cations in the different inorganic cages and the interplay between all these properties. It seemed important to me to add this part as, as precious it is to keep track of the advances made by the worldwide scientific community, it appears important to be aware of the questions which still needs our focus on, especially now that the field of these intriguing materials has existed for a little more than 10 years.

1.3.4. Mechanical properties: elastic softness and anisotropy

The relation between strain and stress is defined by Hooke's law as :

$$\epsilon = \mathbf{C}\,\sigma \;\; or \;\; \sigma = \mathbf{C}\,\epsilon \tag{1.11}$$

Where ϵ and σ are the strain and stress tensors, respectively, which are mediated by the elastic compliance S and elastic stiffness C tensors, related by $\mathbf{S} = \mathbf{C^{-1}}$.

In 2014, Feng used first principle calculations to estimate the elastic stiffness constants c_{ij} of different hybrid halide perovskites, including $MAPbBr_3$ and $MAPbI_3$, in their different crystal symmetries: cubic, tetragonal and orthorhombic.[108] Experimental values for cubic $MAPbBr_3$[109,110] and cubic $MAPbI_3$[111] were reported and confirmed the theoretical predictions. Some of the values are reported in Table 1.3. The first striking observation concerns the magnitude of these constants. In the order of a few hundreds of GPa in oxide perovskites,[112] these constants are a few tens of GPa in hybrid halide compounds. The elastic stiffness constants of Sn based perovskites appear to be higher than for their Pb-based counterparts, but the values remain notably smaller than for inorganic oxide structures. This observation illustrates the now well-known softness of the hybrid lead halide perovskites.

Elastic stiffness constants (in GPa)	c_{11}	c_{33}	c_{44}	c_{66}	c_{12}	c_{13}
Cubic $SrTiO_3$[112]	385	-	119	-	113	-
Cubic $MAPbBr_3$[111]	32.2	-	3.4	-	9.1	-
Cubic $MASnI_3$[108]	53.6	-	9.6	-	6.5	-
Cubic $MAPbI_3$[111]	21.8	-	7.3	-	11.3	-
Tetragonal $MAPbI_3$[108]	20.1	17.9	1.6	9.2	14.6	6.8

Table 1.3: Elastic constants (in GPa) of cubic $MAPbBr_3$ and $MASnI_3$, cubic and tetragonal $MAPbI_3$ compared with the elastic stiffness constant calculated for $SrTiO_3$.

Some oxide perovskites such as $BaTiO_3$ are known to exhibit anisotropic elastic properties.[113] In cubic $MAPbBr_3$, three previous reports demonstrated such anisotropy,[109,110,111] by calculating Young's modulus and Poisson's ratio from the elastic stiffness constants along different cubic directions [100], [110] and [111]. Young's modulus E measures the resistance of a material to being deformed elastically when stress is applied (the higher E, the stiffer the material). Poisson's ratio υ, which is dimensionless, measures the quotient of lateral contraction to longitudinal extension arising from the application of tensile stress. In isotropic media, υ values are expected to fall in the -1 – 0.5 range.[114] However, materials exhibiting anisotropic elastic properties can exhibit Poisson's ratio values higher than 0.5 along some crystallographic directions.[113] As the calculation was made only for cubic $MAPbBr_3$, we calculated the same constants for cubic $MAPbI_3$ and the result is shown in Table 1.4. Contrary to $MAPbBr_3$, cubic $MAPbI_3$ did not display such striking elastic anisotropy, in agreement with the predictions of Feng.[108]

	$E_{[100]}$ (GPa)	$E_{[110]}$ (GPa)	$E_{[111]}$ (GPa)	$\upsilon_{[100]}$	$\upsilon_{[110]}$	$\upsilon_{[111]}$
$MAPbBr_3$	28.2	11.4	9.6	0.22	0.41	0.39
$MAPbI_3$	14.1	17.4	18.8	0.34	0.28	0.30

Table 1.4: Anisotropic Young's modulus and Poisson's ratio for both $MAPbBr_3$ and $MAPbI_3$ along [100], [110] and [111] cubic directions.

For tetragonal $MAPbI_3$, to the best of our knowledge, no experimental work reported the values for the elastic stiffness constants and the values predicted by Feng.[108] From these values, Mante *et al.* evaluated the directional Poisson's ratio in the tetragonal $MAPbI_3$ structure. Very interestingly, a very high anisotropy was observed: for compression applied along the tetragonal [100] direction, they found Poisson's ratio along tetragonal [001] $\upsilon_{21} = 0.7$ and along [010] tetragonal direction $\upsilon_{31} = 0.1$.[93] The difference in the two values and the very strong 0.7 value points to the great elastic anisotropy of the $MAPbI_3$ tetragonal structure which, as a reminder, was weakly anisotropic in its cubic structure. However, we would like to point out that, our calculations, using the Poisson's ratio expressions for tetragonal crystals derived by Ballato[114] and the elastic constants reported by Feng[108] lead to the same 0.7 and 0.1 values, but we found the higher ratio along [001] direction and not [010] as reported by.[93]

1.4. Specific properties of MA and FA-based lead halide perovskites

1.4.1. $MAPbI_3$ thin layers

1.4.1.1. Crystallization of thin films

$MAPbI_3$ was the first hybrid perovskite material to be used as an active layer in solar devices. A large number of thin films fabrication procedures were developed,[53] each one of them allowing to reach slightly better layer quality, device performance or stability. With these different processes, a great number of studies of the crystallization mechanism of these layers were conducted, in order to eventually master the fabrication route, to reduce reproductibility problems and improve the devices. We will here present some of the crystallization paths identified for the one-step spin-coating process. During such a process, a precursor solution containing the lead halide and organic components is spin-coated on a substrate and subsequent annealing leads to crystallized $MAPbI_3$ thin layers.

A large number of teams fabricated $MAPbI_3$ thin layers through precursor solutions containing equimolar amounts of MAI and PbI_2 powders dissolved in polar DMF solvent. Different crystallization intermediates were identified for such solutions, for instance $(MA)_2DMF_2Pb_2I_6$ which crystallizes in a monoclinic $P2_1c$ space group and transforms into $MAPbI_3$ upon annealing.[115] This report also showed that the varying the relative proportions of the precursor powders leads to different intermediary phases with different structures. The one cited above was observed for stoichiometric conditions (1 MAI : 1 PbI_2). Yet, the most largely accepted intermediate reaction is the $MAPbI_3$-DMF complex, identified by Hoa *et al.*.[116] However, it was shown that this intermediate phase has a needle-like morphology, which results in films with large and numerous pinholes.[117] Two strategies were then developed to improve the morphology of the thin films. The first one, introduced by Chang *et al.*, consists of dripping an anti-solvent of the perovskite on the thin layer during the early stages of the spin-coating process. This anti-solvent, usually chlorobenzene, enhances the coverage of the thin layer on the substrate by “spreading” it..[118] The second method, introduced the same year by Jeon *et al.* consists in using a second solvent dimethylsulfoxide (DMSO) in addition to DMF,[119] and the formation of a CH_3NH_3I-PbI_2-DMSO intermediate phase was reported . The latter was found to slow the crystallization of $MAPbI_3$ by forming a smooth and extremely homogeneous thin layer, which, once converted, lead to $MAPbI_3$ with an enhanced morphology. It was shown that the adduct with DMSO has a lower formation enthalpy than the complex with DMF, explaining why, even though DMF is present in these solutions, it is the DMSO molecules that bond with the perovskite in solution.[115] Very recently, a study of the mechanism of this specific crystallization path showed that the driving force of the conversion is the evaporation of DMSO upon annealing.[120] The use of DMSO in the precursor solution was described as a milestone in the fabrication of perovskite thin films, and it has since been widely used to control the morphology of a variety of other perovskite thin films.[117] Very recently, Johansson *et al.* exposed an alternative process, where, instead of using DMF, the precursor powders are introduced in a poor solvent for perovskites, such as isopropanol, to induce the formation of a $MAPbI_3$ suspension. The thin layers obtained from the suspension appear as a porous framework and the devices they were integrated to displayed PCE = 18.9% with small hysteresis.[121] Interesting text gathering all these crystallization paths and more can be found.[55,117,122]

In 2013, Stranks *et al.*, reported $MAPbI_3$ thin layers with 10 times higher charge carrier diffusion lengths through the incorporation of Cl^- in the precursors solution.[123] Follow-up studies showed that Cl^- ions, incorporated by using $PbCl_2$ or MACl precursors, are not found, or in very small quantities in the final layer.[124,125] Studies revealed a great miscibility gap in $MAPb(I_{1-x}Clx)_3$ solid solutions for $2.2 > x > 98.7\%$ due to the large radii difference between I^- and Cl^-.[126] Whether the small traces of chlorine found by some papers in the thin layers are incorporated in $MAPbI_3$ crystal structure or only present at grain boundaries or acts as a passivation layer at the interface with the substrate has not been definitely elucidated. A large number of studies suggested that Cl^- disappears from the substrate due to the sublimation of MACl during the annealing at 100 °C and Unger *et al.* managed to confirm this sublimation.[124,125,127,128] Even if the presence of residual chlorine in the layers is still under debate, it is largely agreed upon that its introduction increases the carrier diffusion lengths, but also leads to the formation of larger grains, and a thin layer textured along [110] $MAPbI_3$ tetragonal direction.[117,129] However, little is known as of now about how Cl^- acts to lead to such an enhancement of the optoelectronic properties and crystallographic texture.

Here again, a lot of efforts have been dedicated to the identification of the different crystallization mechanisms behind the use of chlorine, but it seems more complicated than when using MAI and PbI_2. This question will be discussed in chapter 2 of this manuscript.

1.4.1.2. Ferroic properties and halogen migration

The perovskite structural family is well-known for frequently displaying ferroic and even multiferroic properties. In the case of hybrid halide perovskites, the question of ferroic properties has mostly been adressed in the case of $MAPbI_3$. As explained earlier, $MAPbI_3$ adopts a tetragonal structure at RT while all the other materials cited above are cubic, thus, at RT, $MAPbI_3$ is the only compound likely to display such properties. The assigned space group for tetragonal $MAPbI_3$ is I4/mcm. However, this space group was and still is, to date, under intense debate. In the early days of the perovskite based solar cells, $MAPbI_3$ at RT has falsely been described using Fmmm, I4/m or I4/22 symmetries due to supplementary reflections in single crystal XRD patterns observed by the authors. It now appears that it is crystal twinning that causes these additional diffraction spots.[130] The remaining question is now whether $MAPbI_3$ adopts the centrosymmetric I4/mcm or the non-centrosymmetric I4cm space groups in its tetragonal phase.

With the non-centrosymmetric space group, ferroelectricity in $MAPbI_3$ will be allowed. This property was proposed early on to explain the impressive optoelectronic properties of $MAPbI_3$, as the existence of a local internal electric field could assist charge separation and transport as well as reduce carriers recombination.[131] Many experimental reports have been dedicated to this question. While some papers reported the observation of ferroelectric switching,[132] some teams noted unusual shapes of polarization – electric field (P – E) loops,[133] and others failed to reproduce these observations.[134,135,136] However, all these papers share one common result: a response during Piezoresponse Force Microscopy (PFM) experiments, which probe the electromechanical properties of piezoelectric samples. Observing a response during these experiments would indicate that the sample is polar, thus justifying the description of RT $MAPbI_3$ in the I4cm space group.[131,134] However, for others, these experiments can easily be affected by differences in the local composition and electrostatic effects induced by iodine-atoms migration,[136] preventing the authors from making any conclusion. Moreover, Second Harmonic Generation which usually allows discriminating between polar and non-polar materials, remains non conclusive in the case of $MAPbI_3$.[137] Theoretical efforts have been conducted in this direction as well, but reports, here again, are contradictory.[138,139] Hence, the intense debate around the polarity of $MAPbI_3$ is still raging.

From the scattering experiments point of view, the two proposed space groups I4/mcm (non-polar) and I4cm (polar) lead to very similar patterns, without additional reflections or line splitting.[130] I4/mcm being the parent group of I4cm, we chose to use this space group in our work, keeping in mind that all of our results and discussions are valid for both space groups.

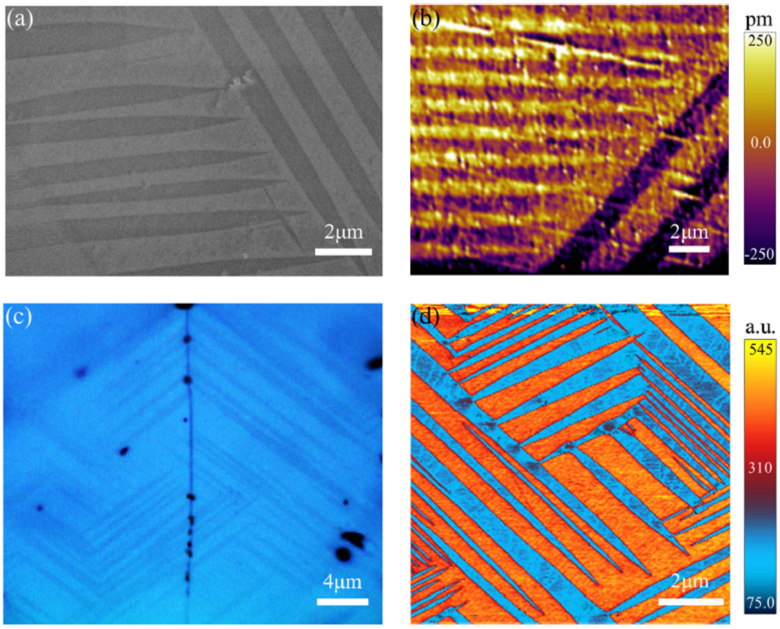

Figure 1.12: Stripped domains observed on $MAPbI_3$ crystals at RT revealed by (a) SEM, (b) AFM, (c) polarized microscopy and (d) PFM. Adapted from[140]

As mentioned earlier, similar PFM response was observed in all papers cited above. These experiments revealed stripe-structured domains within the perovskite grains at room temperature, as presented in Figure 1.12.d. While ferroelectricity in $MAPbI_3$ has yet to be demonstrated, the different domains are now largely accepted as ferroelastic twin domains.[135,140] Ferroelastic materials, very much like ferroelectrics or ferromagnets, present two or more equally stable states which can be switched through external stimuli. In the case of ferroelasticity, these states are twin domains, differing in terms of crystallographic orientation. Ferroelastic domains can be modulated by applying an external mechanical stress.[141] This property will be discussed in chapter 3 of this manuscript.

Quickly mentioned earlier, a few words will be now given about ion migration. Ion migration is a known phenomenon amongst oxide perovskites such as $SrTiO_3$ which can be described as an ionic conductor. Hybrid halide perovskites experience light and bias-induced ion migration. Polycrystalline perovskite thin layers can exhibit very high defect densities, up to $10^{16}\,\mathrm{cm}^{-3}$ which is orderd of magnetude higher than in classical inorganic semi-conductors (polycrystalline Si: 10^{13}-10^{14}). It has been shown that, albeit numerous, defects such as I^- and MA^+ vacancies are shallow and do not lead to charge carriers recombination. However, these intrinsic defects strongly participate to the ion migration observed in hybrid halide perovskites. This phenomena was found to be the main cause of the current-voltage hysteresis observed in perovskite solar cells. It also contributes to device degradation because of the charge accumulation in $MAPbI_3$-based devices. Ironically, this ion migration was also found to enhance the performances of the devices as the material can be considered as electronic and ionic conductor. It was also identified as the driving force of the self-healing observed on $MAPbI_3$ thin layers. The study of ion migration constitutes a field of research on its own, with a large number of reports published in the view of mastering these effects. A recent report gathers the major results obtained concerning this behavior.[18]

1.4.1.3. Stability issues

Briefly mentioned in the previous paragraph, ion migration observed in $MAPbI_3$ thin layers induces device degradation. However, it is not the only cause for the relatively low stability of $MAPbI_3$ containing solar cells. In addition to light and electric polarization which induce the harmful ion migration, exposure to humidity, oxygen and heat result in degradation of the compound. Water molecules were found to easily penetrate the perovskite structure, leading to the irreversible formation of a hydrate phase $MA_4PbI_6.2H_2O$ which eventually degrades into PbI_2, a well-known degradation product of $MAPbI_3$.[142,143] Concerning oxygen-induced degradation, it was found that O_2 quickly diffuses into the layer through iodide vacancies (remember the high density of defects in the polycrystalline layers) and traps electrons from the conduction band of the perovskite. Highly reactive O^{2-} is formed, leading to the deprotonation of MA^+ and thus degradation..[142] Finally, temperature can induce degradation through weakening of the Pb-I-Pb bonds and the sublimation of volatile CH_3NH_2 and HI.[144] Moreover, we highlighted earlier the extremely high thermal expansion coefficient of these compounds which can induce fatigue breaking when used in multi-stack architectured devices which experiences a large number of temperature cycles.

Finally, and more importantly, direct calorimetric measurements revealed that the formation enthalpy of $MAPbI_3$ from the binary precursors MAI and PbI_2 is positive and rather high: 34.5 kJ/mol. The formation enthalpies of $MAPbBr_3$ and $MAPbCl_3$ were evaluated at 6.7 and $-9\,\mathrm{kJ\,mol^{-1}}$, respectively. These results demonstrate that $MAPbI_3$ (and $MAPbBr_3$) are thermodynamically unstable, and they will spontaneously decompose, even when protected from all external parameters cited above.[145]

1.4.2. $FAPbI_3$: POLYMORPHISM, HEXAGONAL PHASE AND STABILIZATION OF THE CUBIC STRUCTURE

Theoretical calculation predicts cubic $FAPbI_3$ based device to show enhanced performances in comparison to $MAPbI_3$ based solar cells. The former displays a lower bandgap of 1.47 eV ($FAPbI_3$ is black) in comparison to the latter (1.55 eV), which is closer to the ideal value of 1.35 eV for photovoltaics. Moreover, $FAPbI_3$ exhibits greater thermal stability: it can be kept at 150 °C for several hours without degradation while $MAPbI_3$ turns into yellow PbI_2 in 30 min.[19] Furthermore, reduced ion migration has been observed on devices using $FAPbI_3$.[18] However, cubic $FAPbI_3$ (α-phase) is not stable at RT; it spontaneously and inevitably evolves into a hexagonal yellow phase. This structure, labelled $\delta - FAPbI_3$, corresponds to the 2H hexagonal structure in Ramsdell notation and consists of 1D chains of face-sharing $[PbI_6]^{4-}$ octahedral, linked through their interaction with the organic cation FA^+ (subsection 1.2.3.). Largely qualified as non-perovskite, it is worth reminding that such polymorphism is also observed in oxide perovskites and that their corresponding phases are labeled “hexagonal-perovskites” (subsection 1.2.3.).

In inorganic perovskites, high temperature and pressure are usually needed to induce transformation from hexagonal to cubic perovskites whereas for $FAPbI_3$ the hexagonal – cubic transition takes place around 150 °C.[27] The transition is reversible, and thermal treatment above 150 °C usually helps to stabilize the cubic phase at RT for a few hours up to a few days. Chen *et al.* suggested that the transition is entropy driven, forming a double-well potential geometry and that the momentary stabilization of the cubic phase at RT after thermal treatment is due to large thermal hysteresis.[61] DFT calculations estimated the formation enthalpy of the hexagonal phase to be lower by $\sim$70 meV per unit formula compared to the cubic phase, which is coherent with the spontaneous apparition of this yellow phase at RT.[61] Very recently, Tan *et al.* showed that unintentional shallow iodine interstitial defects introduced during the classical thin film fabrication process can accelerate the transition from the α-phase to the δ-structure.[146] Moreover, it was found that FA^+ is more hygroscopic than MA^+, leading to greater moisture sensitivity in $FAPbI_3$ than in $MAPbI_3$ where it was already a problem.[19]

In a 2020 report, Cordero showed that when $FAPbI_3$ is exposed to pressure as low as 0.6 GPa, notable color change is observed (Figure 1.13). Even though no XRD evidence of the formation of hexagonal polymorphs could be obtained (no peaks at the expected 4H, 6H… etc positions observed), the color change is an undeniable proof of the change in the octahedra connectivity in the compounds under pressure.[147]

In most reports, this polymorphism is explained by the large tolerance factor of $FAPbI_3$. However, it is worth mentioning that $FAPbBr_3$ and $FAPbCl_3$ exhibit even larger tolerance factor values because of smaller halogen ionic radii. In these compounds, no polymorphism is observed. This question will be further addressed in chapter 4.

Figure 1.13: Picture hexagonal δ-$FAPbI_3$ powder (yellow) and pressed pellet (0.6 GPa). Adapted from.[147]

Because of the superior device performances promised by this compound in its cubic phase, different strategies were developed to stabilize the cubic structure at RT.[27]

- Low dimensional materials : Nanocrystals of $FAPbI_3$ exhibited enhance stability at RT in their cubic phase compared to the bulk material. The high surface/volume ratio in nanocrystal generates compressive strain in the lattice. As the hexagonal phase displays larger cell volume, this compressive strain hinders the cubic-hexagonal phase transition. However, the long ligand chains at the surface of the molecules can hamper the charge transport and special care has to be given to the purification of the nanocrystals.
- Compositional engineering : organic cation and / or halide mixing to form solid solution appears to be an effective way to hinder the phase transition. More detailed discussion will be presented in the next paragraph.
- Dimensional engineering and use of additives: introduction of bulky cations leads to the formation of 2D/3D perovskites where the bandgap of the pure compound can be preserved while improving the stability. In the same way, the use of various additives during the fabrication of the devices, such as MACl or PbS helps stabilizing the cubic phase, because, in the case of the latter, of similar lattice parameters between the two materials, leading PbS to act as a template.

More about these stabilization methods can be found in texts by Masi *et al.*[27] and Fan *et al.*.[10]

1.4.3. MIXED ION COMPOUNDS

The biggest advantage of the perovskite structure is its chemical flexibility: a large number of compounds can be obtained, with different chemical compositions and properties, and the possibility to form alloys leads to an infinity of possibilities. Scientists mainly used the tolerance factor to obtain a first idea about the ability of the alloy to adopt a perovskite structure.

When Saliba *et al.* reported the enhanced stability and performance of devices containing multiple cations and halides,[20,148] the formation of hybrid halide perovskites solid solutions attracted a lot of interest and such compounds have been widely used since as a strategy to fabricate devices with high stability and performances (Figure 1.14.b). The tolerance factor has been used here again as a tool for predicting the ions that can be inserted in the APbX3 structure and stabilize the cubic structure (Figure 1.14.b). As explained earlier, pure $FAPbI_3$ is not stable in its cubic structure at RT and adopts a hexagonal arrangement. Cubic $CsPbI_3$ is not stable either at RT and prefers a non-perovskite orthorhombic phase and to recover the cubic structure, heating up to 300-360 °C is needed.[27]

Let us first discuss alloying the A perovskite site. Thanks to their close ionic radii, full solubility of $MAPbI_3$ and $FAPbI_3$ is possible. This family of compounds $FA_{1-x}MA_xPbI_3$ was intensively studied, and all the reports agreed that introducing around 20% of MA^+ in the $FAPbI_3$ lattice stabilizes the cubic structure. Higher thermal stability was also observed for these systems.[19] Facilitated by their simple preparation and stability, a number of reports about the fundamental properties of these compounds have emerged.[68,149,150,151] The solid solutions lattice parameters and bandgap were tuned by the composition between the values of pure $MAPbI_3$ and $FAPbI_3$, following Vegard's law. However, as FA^+ appears more hygroscopic than MA^+, the devices obtained with these materials suffered from poor long-term stability.

Introduction of Cs^+ into $MAPbI_3$ and $FAPbI_3$ lattices was also explored. However, because of the small ionic radii of Cs^+ in comparison with the organic molecules (Cs^+ = 167 pm, FA^+ = 253 pm and MA^+ = 217 pm[20]), full solubility cannot be expected. In both families, reports lead to different solubility limits for the introduction of Cs^+ in the two structures, between 10 and 25%, which seems to depend a lot on the synthetic path.[66,152,153,154,155,156] The other end of the composition (introduction of FA^+ or MA^+ in $CsPbI_3$ lattice) was not investigated. In the $Cs_xMA_{1-x}PbI_3$ family, the composition of the thin layers was found to be very different from the precursor solutions composition (2 times higher Cs^+ contents in the films) and the introduction of more than 0.9% Cs^+ leads to a rapid degradation of the thin films.[153] Hence, more efforts were dedicated to the incorporation of Cs^+ in $FAPbI_3$ which was more promising for the devices. Reports on the introduction of Cs^+ in $FAPbI_3$ showed increased structural, phase and thermal stability as well as higher moisture-resistance..[19] The understanding of the fundamental properties of Cs^+ containing compounds is still in its infancy.

In the early studies of solid-solution perovskites based devices, insertion of small Rb+ cations was also proposed. It now appears that this cation does not occupy the perovskite A site but is localized at the grain boundaries, playing the role of a passivation agent.[19]

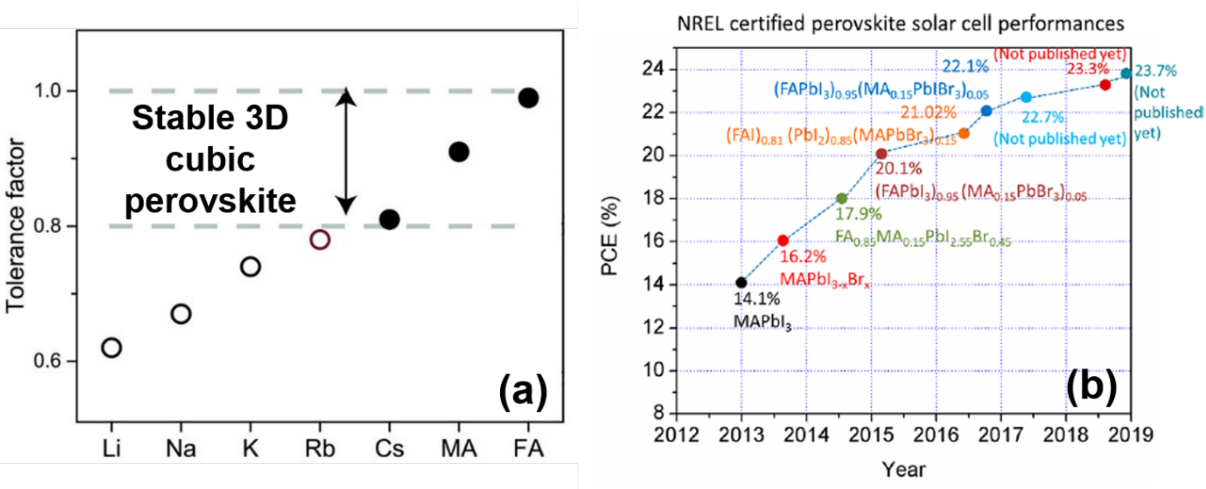

Figure 1.14: (a) Tolerance factor calculated for different A cations introduced in the $APbI_3$ perovskite structure. The stability domain used here and in the majority of the reported works is the one predicted for oxide perovskites. Adapted from.[20] (b) Known compositions of the perovskite materials used in the NREL photovoltaic efficiency chart, as of 2019. Adapted from.[19]

Alloys with mixed X site were also studied. As explained in subsubsection 1.4.1.1., poor solubility of Cl^- ions in $MAPbI_3$ was demonstrated. Substitution of iodide by bromide in $MAPbI_3$ led to contradictory results: a complete miscibility on the full range of bromide-iodide ratio on thin layers was obtained on thin layers[157,158] while powder samples have exhibited a large miscibility gap for Br contents between 29 and 92%.[79] Moreover, Marchenko *et al.* showed using a semi-empirical approach the existence of a large non-miscibility zone in the $MAPb(I_{1-x}Br_x)_3$ solid solutions which leads to a deviation from Vegard's law, confirming the results from Lehmann *et al.*.[159] Concerning the $FAPb(I_{1-x}Br_x)_3$ solid solutions, full solubility of the halides was predicted by theory,[160] however, experimental reports showed different results. To the best of our knowledge, all the investigations have been performed on thin layers. While some studies highlighted the presence of a miscibility gap between 30 and 50% of inserted bromide,[161,162] others have not commented the poor crystallinity of their samples in this same range of composition.[158,163] In both mixed halides systems, the introduction of Br^- allows to tune the bandgap, as Br-based compounds exhibit higher bandgap values ($\sim$2.2 eV for both $MAPbBr_3$ and $FAPbBr_3$). However, thin layers of these compounds suffered from light induced phase segregation.

Finally, compounds exhibiting both mixed A and X-sites have been most intensively used in solar devices. The majority of these compounds are formamidinium and iodide rich, as $FAPbI_3$ is the most promising compound for solar cells, despite the instability of the perovskite phase at RT. The composition of the phases is different from one team to another, but most of the devices use $FA_{1-x}MA_xPb(I_{1-y}Br_y)_3$ or $Cs_zFA_{1-z}Pb(I_{1-x}Br_x)_3$ compounds and very recently $Rb_zCs_xFA_{1-x-z}PbI_3$, which allow to obtain devices with high performances (more than 23% PCEs) and stability.[27] However, the fundamental properties of these compounds are not fully understood so far. Due to their complex composition, these materials exhibit local composition inhomogeneities. On the other hand, the information extracted from bulk measurements on thin layers describe an average behavior, and hence, the local properties can be very different from the average picture. The structure and how the different ions coordinate in the perovskite lattice lacks understanding.

1.5. Thesis motivations

As shown in this chapter, the efficiency of laboratory hybrid perovskite solar cells has quickly evolved during these last 10 years, becoming competitive with classical silicon-based solar cells. We highlighted that these compounds display very intriguing structural features, governing their optoelectronic properties, many of which not yet fully understood. In this thesis, we particularly focus on the structural properties using X-ray diffraction as our main tool.

Our work is divided into two main parts. The first one is devoted to $MAPbI_3$ thin layers. A large variability was observed in these systems, mainly in terms of structural properties and stability. Hence, we decided to investigate some of the factors leading to such differences, focusing on the crystallization path and on the strain experienced by the layers.

The second part was motivated by the need of understanding the structural properties of a complex solid solution material: $FA_{0.85}MA_{0.15}Pb(I_{0.85}Br_{0.15})_3$ which lead, in our team, to solar cells with high efficiencies (over 21 %). To do that, we fabricated quaternary compounds with mixed A or X site, and studied the influence of each ions on the intrinsic structural properties of the obtained perovskite, at RT but also on the structural phase transitions.

References

[1] A. Einstein. “Concerning an Heuristic Point of View Toward the Emission and Transformation of Light - Translation to English”. In: *Ann. Phys.* 17 (1905), p. 132.

[2] R. S. Ohl. “Light-sensitive electric device”. US2402662A. 1941.

[3] D. M. Chapin, C. S. Fuller, and G. L. Pearson. “A New Silicon p-n Junction Photocell for Converting Solar Radiation into Electrical Power”. en. In: *J. App. Phys.* 25 (1954), p. 676. DOI: `10.1063/1.1721711`.

[4] G. M. Wilson et al. “The 2020 photovoltaic technologies roadmap”. en. In: *J. Phys. D: Appl. Phys.* 53.49 (2020), p. 493001. DOI: `10.1088/1361-6463/ab9c6a`.

[5] A. Arcos-Vargas and L. Riviere. *Grid Parity and Carbon Footprint: An Analysis for Residential Solar Energy in the Mediterranean Area.* en. Ed. by A. Arcos-Vargas and L. Riviere. SpringerBriefs in Energy. Cham: Springer International Publishing, 2019. ISBN: 978-3-030-06064-0. DOI: `10.1007/978-3-030-06064-0_4`.

[6] B. O’Regan and M. Gratzelt. “A low-cost, high-efficiency solar cell based on dye-sensitized colloidal $Ti0_2$ films”. en. In: *Nature* 353 (1991), pp. 737–740. DOI: `10.1038/353737a0`.

[7] J. E. Carlé et al. “Overcoming the Scaling Lag for Polymer Solar Cells”. en. In: *Joule* 1.2 (2017), pp. 274–289. DOI: `10.1016/j.joule.2017.08.002`.

[8] A. Kojima et al. “Organometal Halide Perovskites as Visible-Light Sensitizers for Photovoltaic Cells”. en. In: *J. Am. Chem. Soc.* 131.17 (2009), pp. 6050–6051. DOI: `10.1021/ja809598r`.

[9] M. M. Lee et al. “Efficient Hybrid Solar Cells Based on Meso-Superstructured Organometal Halide Perovskites”. en. In: *Science* 338.6107 (2012), pp. 643–647. DOI: `10.1126/science.1228604`.

[10] Y. Fan et al. “Review of Stability Enhancement for Formamidinium-Based Perovskites”. en. In: *Solar RRL* 3.9 (2019), p. 1900215. DOI: `10.1002/solr.201900215`.

[11] P. Würfel and U. Würfel. *Physics of Solar Cells: From Basic Principles to Advanced Concepts.* Wiley-VCH Verlag GmbH & Co. KGaA. Weinheim, 2016.

[12] S. De Wolf et al. "Organometallic Halide Perovskites: Sharp Optical Absorption Edge and Its Relation to Photovoltaic Performance". en. In: *J. Phys. Chem. Lett.* 5.6 (2014), pp. 1035–1039. DOI: `10.1021/jz500279b`.

[13] B. Saparov and D. B. Mitzi. "Organic–Inorganic Perovskites: Structural Versatility for Functional Materials Design". In: *Chem. Rev.* 116.7 (2016), pp. 4558–4596. DOI: `10.1021/acs.chemrev.5b00715`.

[14] K. Al Abdullah, F. A. Alloush, and C. Salame. "Investigation of the Monocrystalline Silicon Solar Cell Physical Behavior after Thermal Stress by AC Impedance Spectra". en. In: *Energy Procedia* 50 (2014), pp. 30–40. DOI: `10.1016/j.egypro.2014.06.004`.

[15] D. A. Egger et al. "What Remains Unexplained about the Properties of Halide Perovskites?" en. In: *Adv. Mater.* 30.20 (2018), p. 1800691. DOI: `10.1002/adma.201800691`.

[16] V. Adinolfi et al. "The Electrical and Optical Properties of Organometal Halide Perovskites Relevant to Optoelectronic Performance". en. In: *Adv. Mater.* 30.1 (2018), p. 1700764. DOI: `https://doi.org/10.1002/adma.201700764`.

[17] Q. Dong et al. "Electron-hole diffusion lengths ¿ 175 μm in solution-grown $CH_3NH_3PbI_3$ single crystals". en. In: *Science* 347.6225 (2015), pp. 967–970. DOI: `10.1126/science.aaa5760`.

[18] T. Zhang, C. Hu, and S. Yang. "Ion Migration: A "Double-Edged Sword" for Halide-Perovskite-Based Electronic Devices". en. In: *Small Methods* 4.5 (2020), p. 1900552. DOI: `https://doi.org/10.1002/smtd.201900552`.

[19] A. K. Jena, A. Kulkarni, and T. Miyasaka. "Halide Perovskite Photovoltaics: Background, Status, and Future Prospects". en. In: *Chem. Rev.* 119.5 (2019), pp. 3036–3103. DOI: `10.1021/acs.chemrev.8b00539`.

[20] M. Saliba et al. "Incorporation of rubidium cations into perovskite solar cells improves photovoltaic performance". en. In: *Science* 354.6309 (2016), pp. 206–209. DOI: `10.1126/science.aah5557`.

[21] B. Hailegnaw et al. "Rain on Methylammonium Lead Iodide Based Perovskites: Possible Environmental Effects of Perovskite Solar Cells". en. In: *J. Phys. Chem. Lett.* 6.9 (2015), pp. 1543–1547. DOI: `10.1021/acs.jpclett.5b00504`.

[22] D. Fabini. "Quantifying the Potential for Lead Pollution from Halide Perovskite Photovoltaics". en. In: *J. Phys. Chem. Lett.* 6.18 (2015), pp. 3546–3548. DOI: `10.1021/acs.jpclett.5b01747`.

[23] N. Glück and T. Bein. "Prospects of lead-free perovskite-inspired materials for photovoltaic applications". en. In: *Energy Environ. Sci.* 13.12 (2020), pp. 4691–4716. DOI: `10.1039/D0EE01651A`.

[24] Po-Kai Kung et al. "Lead-Free Double Perovskites for Perovskite Solar Cells". en. In: *Solar RRL* 4.2 (2020), p. 1900306. DOI: `10.1002/solr.201900306`.

[25] P. K. Panda and B. Sahoo. “PZT to Lead Free Piezo Ceramics: A Review”. en. In: *Ferroelectrics* 474.1 (2015), pp. 128–143. DOI: `10.1080/00150193.2015.997146`.

[26] L. Gao and G. Yang. “Organic-Inorganic Halide Perovskites: From Crystallization of Polycrystalline Films to Solar Cell Applications”. en. In: *Solar RRL* 4.2 (2020), p. 1900200. DOI: `https://doi.org/10.1002/solr.201900200`.

[27] S. Masi, A. F. Gualdrón-Reyes, and I. Mora-Seró. “Stabilization of Black Perovskite Phase in $FAPbI_3$ and $CsPbI_3$”. en. In: *ACS Energy Lett.* 5.6 (2020), pp. 1974–1985. DOI: `10.1021/acsenergylett.0c00801`.

[28] T. Arimoto. “Phase relations of $MgSiO_3$-$FeSiO_3$ system up to 64 GPa and 2300 K using multianvil apparatus with sintered diamond anvils”. en. In: *Physics of the Earth and Planetary Interiors* 295 (2019), p. 106297. DOI: `10.1016/j.pepi.2019.106297`.

[29] R. J.D. Tilley. *Perovskites: structure-properties relationships.* Wiley. Wiley, 2016. ISBN: 978-1-118-93566-8.

[30] M.-C. Jung, K.-W. Lee, and W. E. Pickett. “Perovskite $ThTaN_3$: a Large Thermopower Topological Crystalline Insulator”. In: *Phys. Rev. B* 97.12 (2018), p. 121104. DOI: `10.1103/PhysRevB.97.121104`.

[31] H. Megaw. “Crystal structure of double oxides of the perovskite type”. In: *Proc. Phys. Soc.* 58.2 (1946), p. 133. DOI: `10.1088/0959-5309/58/2/301`.

[32] A. M. Glazer. “A brief history of tilts”. en. In: *Phase Transitions* 84.5-6 (2011), pp. 405–420. DOI: `10.1080/01411594.2010.544732`.

[33] L. M. Feng et al. “Formability of ABO_3 cubic perovskites”. en. In: *Journal of Physics and Chemistry of Solids* 69.4 (2008), pp. 967–974. DOI: `10.1016/j.jpcs.2007.11.007`.

[34] A. Okazaki and Y. Suemune. “The Crystal Structure of $KCuF_3$”. In: *Journal of the Physical Society of Japan* 16.2 (1961), pp. 176–183. DOI: `10.1143/JPSJ.16.176`.

[35] H. Köppel, D. R. Yarkony, and H. Barentzen. *The Jahn-Teller Effect. Fundamentals and Implications for Physics and Chemistry.* Springer. 2009. ISBN: 978-3-642-03431-2.

[36] I. B. Bersuker. “Pseudo-Jahn–Teller Effect—A Two-State Paradigm in Formation, Deformation, and Transformation of Molecular Systems and Solids”. en. In: *Chem. Rev.* 113.3 (2013), pp. 1351–1390. DOI: `10.1021/cr300279n`.

[37] A. M. Glazer. “The classification of tilted octahedra in perovskites”. In: *Acta Crystallographica Section By* 28.11 (1972), pp. 3384–3392. DOI: `10.1107/S0567740872007976`.

[38] C. J. Howard and H. T. Stokes. “Group-Theoretical Analysis of Octahedral Tilting in Perovskites”. en. In: *Acta Crystallographica Section B* 54.6 (1998), pp. 782–789. DOI: `10.1107/S0108768198004200`.

[39] B. L. Chamberland, A. W. Sleight, and J. F. Weiher. “Preparation and characterization of $BaMnO_3$ and $SrMnO_3$ polytypes”. In: *Journal of Solid State Chemistry* 1.3-4 (1970), pp. 506–511. DOI: `10.1016/0022-4596(70)90133-7`.

[40] J.-G. Cheng et al. “A New Perovskite Polytype in the High-Pressure Sequence of $BaIrO_3$”. en. In: *J. Am. Chem. Soc.* 131.21 (2009), pp. 7461–7469. DOI: `10.1021/ja901829e`.

[41] J.-H. Lee et al. “Resolving the Physical Origin of Octahedral Tilting in Halide Perovskites”. en. In: *Chem. Mater.* 28.12 (2016), pp. 4259–4266. DOI: `10.1021/acs.chemmater.6b00968`.

[42] X. Kuang et al. “Crystal structure, microwave dielectric properties and AC conductivity of B-cation deficient hexagonal perovskites $La_5M_xTi_{4-x}O_{15}$ (x = 0.5, 1; M = Zn, Mg, Ga, Al)”. en. In: *J. Mater. Chem.* 16.11 (2006), p. 1038. DOI: `10.1039/b513696b`.

[43] P. Byszewski et al. “Thermal properties of $CaNdAlO_4$ and $SrLaAlO_4$”. In: *Mat. Res. Bull.* 27 (1992), pp. 482–490. DOI: `10.1016/0025-5408(92)90026-V`.

[44] F. Wang et al. “First-principles study on negative thermal expansion of $PbTiO_3$”. en. In: *Appl. Phys. Lett.* 103.22 (2013), p. 221901. DOI: `10.1063/1.4833280`.

[45] I. Yamada et al. “Valence Transitions in Negative Thermal Expansion Material $SrCu_3Fe_4O_{12}$”. en. In: *Inorg. Chem.* 53.19 (2014), pp. 10563–10569. DOI: `10.1021/ic501665c`.

[46] J. Chen et al. “Zero Thermal Expansion in $PbTiO_3$-Based Perovskites”. en. In: *J. Am. Chem. Soc.* 130.4 (2008), pp. 1144–1145. DOI: `10.1021/ja7100278`.

[47] H. L. Wells. “Über die Cäsium- und Kalium-Bleihalogenide”. en. In: *Zeitschrift für anorganische Chemie* 3.1 (1893), pp. 195–210. DOI: `10.1002/zaac.18930030124`.

[48] C.N. Moller. “Crystal Structure and Photoconductivity of Cæsium Plumbohalides”. In: *Nature* 182 (1958), p. 1436. DOI: `10.1038/1821436a0`.

[49] C. Li et al. “Formability of ABX_3 (X = F, Cl, Br, I) halide perovskites”. en. In: *Acta Crystallographica Section B* 64.6 (2008), pp. 702–707. DOI: `10.1107/S0108768108032734`.

[50] G. Kieslich et al. “Hydrogen Bonding versus Entropy: Revealing the Underlying Thermodynamics of the Hybrid Organic–Inorganic Perovskite $CH_3NH_3PbBr_3$”. en. In: *Chem. Mater.* 30.24 (2018), pp. 8782–8788. DOI: `10.1021/acs.chemmater.8b03164`.

[51] W. Travis et al. “On the application of the tolerance factor to inorganic and hybrid halide perovskites: a revised system”. en. In: *Chem. Sci.* 7.7 (2016), pp. 4548–4556. DOI: `10.1039/C5SC04845A`.

[52] A. S. Bhalla, R. Guo, and R. Roy. “The perovskite structure - a review of its role in ceramic science and technology”. In: *Material Research Innovations* 4 (0200), pp. 3–26. DOI: `10.1007/s100190000062`.

[53] W. A. Dunlap-Shohl et al. “Synthetic Approaches for Halide Perovskite Thin Films”. en. In: *Chem. Rev.* 119.5 (2019), pp. 3193–3295. DOI: `10.1021/acs.chemrev.8b00318`.

[54] X. Dai, K. Xu, and F. Wei. “Recent progress in perovskite solar cells: the perovskite layer”. en. In: *Beilstein J. Nanotechnol.* 11 (2020), pp. 51–60. DOI: `10.3762/bjnano.11.5`.

[55] L. Gao and Q. Yan. “Recent Advances in Lead Halide Perovskites for Radiation Detectors”. en. In: *Solar RRL* 4.2 (2020), p. 1900210. DOI: `https://doi.org/10.1002/solr.201900210`.

[56] Nam-Gyu Park. “Research Direction toward Scalable, Stable, and High Efficiency Perovskite Solar Cells”. en. In: *Advanced Energy Materials* 10.13 (2020), p. 1903106. DOI: `https://doi.org/10.1002/aenm.201903106`.

[57] S Amari et al. “Optimization of the Growth Conditions for High Quality $CH_3NH_3PbBr_3$ Hybrid Perovskite Single Crystals”. en. In: *Crystal Growth & Design* 20.3 (2020), pp. 1665–1672. DOI: `10.1021/acs.cgd.9b01429`.

[58] C. Stoumpos, C. D. Malliakas, and M. G. Kanatzidis. “Semiconducting Tin and Lead Iodide Perovskites with Organic Cations: Phase Transitions, High Mobilities, and Near-Infrared Photoluminescent Properties”. en. In: *Inorg. Chem.* 52.15 (2013), pp. 9019–9038. DOI: `10.1021/ic401215x`.

[59] M. I. Saidaminov et al. “High-quality bulk hybrid perovskite single crystals within minutes by inverse temperature crystallization”. en. In: *Nature Communications* 6.1 (2015). DOI: `10.1038/ncomms8586`.

[60] M. I. Saidaminov et al. “Retrograde solubility of formamidinium and methylammonium lead halide perovskites enabling rapid single crystal growth”. en. In: *Chem. Commun.* 51.100 (2015), pp. 17658–17661. DOI: `10.1039/C5CC06916E`.

[61] Y.-X. Chen et al. “General Space-Confined On-Substrate Fabrication of Thickness-Adjustable Hybrid Perovskite Single-Crystalline Thin Films”. en. In: *J. Am. Chem. Soc.* 138.50 (2016), pp. 16196–16199. DOI: `10.1021/jacs.6b09388`.

[62] H.-S. Rao et al. “In Situ Growth of 120 cm2 $CH_3NH_3PbBr_3$ Perovskite Crystal Film on FTO Glass for Narrowband-Photodetectors”. en. In: *Adv. Mater.* 29.16 (2017), p. 1602639. DOI: `10.1002/adma.201602639`.

[63] Y. Liu et al. “Thinness- and Shape-Controlled Growth for Ultrathin Single-Crystalline Perovskite Wafers for Mass Production of Superior Photoelectronic Devices”. en. In: *Adv. Mater.* 28.41 (2016), pp. 9204–9209. DOI: `10.1002/adma.201601995`.

[64] Z. Chen et al. “Single-Crystal $MAPbI_3$ Perovskite Solar Cells Exceeding 21% Power Conversion Efficiency”. en. In: *ACS Energy Lett.* 4.6 (2019), pp. 1258–1259. DOI: `10.1021/acsenergylett.9b00847`.

[65] O. Nazarenko et al. “Single crystals of caesium formamidinium lead halide perovskites: solution growth and gamma dosimetry”. en. In: *NPG Asia Materials* 9.4 (2017), e373. DOI: `10.1038/am.2017.45`.

[66] S. Du et al. “Incorporation of Cesium Ions into $MA_{1-x}Cs_xPbI_3$ Single Crystals: Crystal Growth, Enhancement of Stability, and Optoelectronic Properties”. In: *J. Phys. Chem. Lett.* 9.19 (2018), pp. 5833–5839. DOI: `10.1021/acs.jpclett.8b02390`.

[67] Y. Huang et al. “The intrinsic properties of $FA_{1-x}MA_xPbI_3$ perovskite single crystals”. en. In: *J. Mater. Chem. A* 5.18 (2017), pp. 8537–8544. DOI: `10.1039/C7TA01441D`.

[68] W.-G. Li et al. “A formamidinium–methylammonium lead iodide perovskite single crystal exhibiting exceptional optoelectronic properties and long-term stability”. en. In: *J. Mater. Chem. A* 5.36 (2017), pp. 19431–19438. DOI: `10.1039/C7TA04608A`.

[69] L. Chen et al. “Toward Long-Term Stability: Single-Crystal Alloys of Cesium-Containing Mixed Cation and Mixed Halide Perovskite”. en. In: *J. Am. Chem. Soc.* 141.4 (2019), pp. 1665–1671. DOI: `10.1021/jacs.8b11610`.

[70] T. Sekimoto et al. “Inverse Temperature Crystallization of Formamidinium Tin Iodide: Indirect Transition State and Restriction of Cation Motion”. en. In: *Crystal Growth & Design* 20.2 (2020), pp. 874–883. DOI: `10.1021/acs.cgd.9b01262`.

[71] S. Li et al. “Metal Halide Perovskite Single Crystals: From Growth Process to Application”. en. In: *Crystals* 8.5 (2018), p. 220. DOI: `10.3390/cryst8050220`.

[72] Y.-L. Wang et al. “Rapid Growth of Halide Perovskite Single Crystals: From Methods to Optimization Control”. en. In: *Chinese Journal of Chemistry* 37.6 (2019), pp. 616–629. DOI: `https://doi.org/10.1002/cjoc.201900071`.

[73] G. Maculan et al. “$CH_3NH_3PbCl_3$ Single Crystals: Inverse Temperature Crystallization and Visible-Blind UV-Photodetector”. en. In: *J. Phys. Chem. Lett.* 6.19 (2015), pp. 3781–3786. DOI: `10.1021/acs.jpclett.5b01666`.

[74] A. Poglitsch and D. Weber. “Dynamic disorder in methylammoniumtrihalogenoplumbates (II) observed by millimeter-wave spectroscopy”. en. In: *The Journal of Chemical Physics* 87.11 (1987), pp. 6373–6378. DOI: `10.1063/1.453467`.

[75] D. Prochowicz et al. “Mechanosynthesis of the hybrid perovskite $CH_3NH_3PbI_3$: characterization and the corresponding solar cell efficiency”. en. In: *J. Mater. Chem. A* 3.41 (2015), pp. 20772–20777. DOI: `10.1039/C5TA04904K`.

[76] D. Prochowicz et al. “Mechanosynthesis of pure phase mixed-cation $MA_xFA_{1-x}PbI_3$ hybrid perovskites: photovoltaic performance and electrochemical properties”. en. In: *Sustainable Energy Fuels* 1.4 (2017), pp. 689–693. DOI: `10.1039/C7SE00094D`.

[77] C. A. López et al. “Enhanced stability in $CH_3NH_3PbI_3$ hybrid perovskite from mechano-chemical synthesis: structural, microstructural and optoelectronic characterization”. en. In: *Sci Rep* 10.1 (2020), p. 11228. DOI: `10.1038/s41598-020-68085-0`.

[78] P.S. Whitfield et al. "Structures, Phase Transitions and Tricritical Behavior of the Hybrid Perovskite Methyl Ammonium Lead Iodide". In: *Sci Rep* 6 (2016), p. 35685. DOI: `10.1038/srep35685`.

[79] F. Lehmann et al. "The phase diagram of a mixed halide (Br, I) hybrid perovskite obtained by synchrotron X-ray diffraction". en. In: *RSC Adv.* 9.20 (2019), pp. 11151–11159. DOI: `10.1039/C8RA09398A`.

[80] R. J. Worhatch et al. "Study of Local Structure in Selected Organic–Inorganic Perovskites in the Pm-3m Phase". en. In: *Chem. Mater.* 20.4 (2008), pp. 1272–1277. DOI: `10.1021/cm702668d`.

[81] H.-P. Hsu et al. "Structural, Photophysical, and Electronic Properties of $CH_3NH_3PbCl_3$ Single Crystals". en. In: *Sci Rep* 9.1 (2019), p. 13311. DOI: `10.1038/s41598-019-49926-z`.

[82] G. Laurita et al. "Chemical tuning of dynamic cation off-centering in the cubic phases of hybrid tin and lead halide perovskites". en. In: *Chem. Sci.* 8.8 (2017), pp. 5628–5635. DOI: `10.1039/C7SC01429E`.

[83] D. H. Fabini et al. "Dynamic Stereochemical Activity of the Sn^{2+} Lone Pair in Perovskite $CsSnBr_3$". en. In: *J. Am. Chem. Soc.* 138.36 (2016), pp. 11820–11832. DOI: `10.1021/jacs.6b06287`.

[84] E. C. Schueller et al. "Crystal Structure Evolution and Notable Thermal Expansion in Hybrid Perovskites Formamidinium Tin Iodide and Formamidinium Lead Bromide". In: *Inorg. Chem.* 57.2 (2018), pp. 695–701. DOI: `10.1021/acs.inorgchem.7b02576`.

[85] A. Franz et al. "The influence of deuteration on the crystal structure of hybrid halide perovskites: a temperature-dependent neutron diffraction study of $FAPbBr_3$". en. In: *Acta Crystallogr B Struct Sci Cryst Eng Mater* 76.2 (2020), pp. 267–274. DOI: `10.1107/S2052520620002620`.

[86] S. Govinda et al. "Critical Comparison of $FAPbX_3$ and $MAPbX_3$ (X = Br and Cl): How Do They Differ?" en. In: *J. Phys. Chem. C* 122.25 (2018), pp. 13758–13766. DOI: `10.1021/acs.jpcc.8b00602`.

[87] K. T. Butler. "The chemical forces underlying octahedral tilting in halide perovskites". en. In: *J. Mater. Chem. C* 6.44 (2018), pp. 12045–12051. DOI: `10.1039/C8TC02976H`.

[88] D. H. Fabini et al. "Reentrant Structural and Optical Properties and Large Positive Thermal Expansion in Perovskite Formamidinium Lead Iodide". en. In: *Angew. Chem.* 128.49 (2016), pp. 15618–15622. DOI: `10.1002/ange.201609538`.

[89] O. J. Weber et al. "Phase Behavior and Polymorphism of Formamidinium Lead Iodide". en. In: *Chem. Mater.* 30.11 (2018), pp. 3768–3778. DOI: `10.1021/acs.chemmater.8b00862`.

[90] J. Even, M. Carignano, and C. Katan. “Molecular disorder and translation/rotation coupling in the plastic crystal phase of hybrid perovskites”. In: *Nanoscale.* Themed Collection ”Perovskites at the nanoscale: from fundamentals to applications” 8.12 (2016), pp. 6222–6236. DOI: `10.1039/C5NR06386H`.

[91] D. H. Fabini, R. Seshadri, and M. G. Kanatzidis. “The underappreciated lone pair in halide perovskites underpins their unusual properties”. en. In: *MRS bulletin* 45 (2020), pp. 467–477. DOI: `10.1557/mrs.2020.142`.

[92] T. J. Jacobsson et al. “Determination of Thermal Expansion Coefficients and Locating the Temperature-Induced Phase Transition in Methylammonium Lead Perovskites Using X-ray Diffraction”. In: *Inorg. Chem.* 54.22 (2015), pp. 10678–10685. DOI: `10.1021/acs.inorgchem.5b01481`.

[93] P.-A. Mante et al. “Directional Negative Thermal Expansion and Large Poisson Ratio in $CH_3NH_3PbI_3$ Perovskite Revealed by Strong Coherent Shear Phonon Generation”. en. In: *J. Phys. Chem. Lett.* 9.12 (2018), pp. 3161–3166. DOI: `10.1021/acs.jpclett.8b01330`.

[94] J. Zhao et al. “Strained hybrid perovskite thin films and their impact on the intrinsic stability of perovskite solar cells”. en. In: *Sci. Adv.* 3.11 (2017), eaao5616. DOI: `10.1126/sciadv.aao5616`.

[95] K. L. Svane et al. “How Strong Is the Hydrogen Bond in Hybrid Perovskites?” en. In: *J. Phys. Chem. Lett.* 8.24 (2017), pp. 6154–6159. DOI: `10.1021/acs.jpclett.7b03106`.

[96] P. R. Varadwaj et al. “Significance of hydrogen bonding and other noncovalent interactions in determining octahedral tilting in the $CH_3NH_3PbI_3$ hybrid organic-inorganic halide perovskite solar cell semiconductor”. En. In: *Sci Rep* 9.1 (2019), p. 50. DOI: `10.1038/s41598-018-36218-1`.

[97] A. Varadwaj, P. R. Varadwaj, and K. Yamashita. “Hybrid organic–inorganic $CH_3NH_3PbI_3$ perovskite building blocks: Revealing ultra-strong hydrogen bonding and mulliken inner complexes and their implications in materials design”. en. In: *Journal of Computational Chemistry* 38.32 (2017), pp. 2802–2818. DOI: `https://doi.org/10.1002/jcc.25073`.

[98] F. Cordero et al. “Cation reorientation and octahedral tilting in the metal-organic perovskites MAPI and FAPI”. en. In: *Journal of Alloys and Compounds* 867 (2021), p. 158210. DOI: `10.1016/j.jallcom.2020.158210`.

[99] M. T. Weller et al. “Complete structure and cation orientation in the perovskite photovoltaic methylammonium lead iodide between 100 and 352 K”. en. In: *Chem. Commun.* 51.20 (2015), pp. 4180–4183. DOI: `10.1039/C4CC09944C`.

[100] D. H. Fabini et al. “Universal Dynamics of Molecular Reorientation in Hybrid Lead Iodide Perovskites”. en. In: *J. Am. Chem. Soc.* 139.46 (2017), pp. 16875–16884. DOI: `10.1021/jacs.7b09536`.

[101] E. M. Mozur et al. “Dynamical Phase Transitions and Cation Orientation-Dependent Photoconductivity in $CH(NH_2)_2PbBr_3$”. en. In: *ACS Materials Lett.* 1.2 (2019), pp. 260–264. DOI: `10.1021/acsmaterialslett.9b00209`.

[102] A. N. Beecher et al. “Direct Observation of Dynamic Symmetry Breaking above Room Temperature in Methylammonium Lead Iodide Perovskite”. en. In: *ACS Energy Lett.* 1.4 (2016), pp. 880–887. DOI: `10.1021/acsenergylett.6b00381`.

[103] A. Bernasconi and L. Malavasi. “Direct Evidence of Permanent Octahedra Distortion in $MAPbBr_3$ Hybrid Perovskite”. In: *ACS Energy Lett.* 2.4 (2017), pp. 863–868. DOI: `10.1021/acsenergylett.7b00139`.

[104] A. Bernasconi et al. “Ubiquitous Short-Range Distortion of Hybrid Perovskites and Hydrogen-Bonding Role: the $MAPbCl_3$ Case”. In: *J. Phys. Chem. C* 122.49 (2018), pp. 28265–28272. DOI: `10.1021/acs.jpcc.8b10086`.

[105] X.-.G Zhao et al. “Polymorphous nature of cubic halide perovskites”. en. In: *Phys. Rev. B* 101.15 (2020), p. 155137. DOI: `10.1103/PhysRevB.101.155137`.

[106] R. Sharma et al. “Elucidating the atomistic origin of anharmonicity in tetragonal $CH_3NH_3PbI_3$ with Raman scattering”. en. In: *Phys. Rev. Materials* 4.9 (2020), p. 092401. DOI: `10.1103/PhysRevMaterials.4.092401`.

[107] O. Yaffe et al. “Local Polar Fluctuations in Lead Halide Perovskite Crystals”. en. In: *Phys. Rev. Lett.* 118.13 (2017). DOI: `10.1103/PhysRevLett.118.136001`.

[108] J Feng. “Mechanical properties of hybrid organic-inorganic $CH_3NH_3BX_3$ (B = Sn, Pb; X = Br, I) perovskites for solar cell absorbers”. en. In: *APL Materials* 2.8 (2014), p. 081801. DOI: `10.1063/1.4885256`.

[109] A. Létoublon et al. “Elastic Constants, Optical Phonons, and Molecular Relaxations in the High Temperature Plastic Phase of the $CH_3NH_3PbBr_3$ Hybrid Perovskite”. en. In: *J. Phys. Chem. Lett.* 7.19 (2016), pp. 3776–3784. DOI: `10.1021/acs.jpclett.6b01709`.

[110] A. M. Lomonosov et al. “Exceptional elastic anisotropy of hybrid organic–inorganic perovskite $CH_3NH_3PbBr_3$ measured by laser ultrasonic technique”. en. In: *Phys. Status Solidi RRL* 10.8 (2016), pp. 606–612. DOI: `https://doi.org/10.1002/pssr.201600156`.

[111] A. C. Ferreira et al. “Elastic Softness of Hybrid Lead Halide Perovskites”. en. In: *Phys. Rev. Lett.* 121.8 (2018), p. 085502. DOI: `10.1103/PhysRevLett.121.085502`.

[112] Narasak Pandech, Kanoknan Sarasamak, and Sukit Limpijumnong. “Elastic properties of perovskite $A\mathrm{TiO}_3$ (A = Be, Mg, Ca, Sr, and Ba) and $\mathrm{Pb}B\mathrm{O}_3$ (B = Ti, Zr, and Hf): First principles calculations”. en. In: *Journal of Applied Physics* 117.17 (2015), p. 174108. DOI: `10.1063/1.4919837`.

[113] C. W. Huang et al. “Abnormal Poisson’s ratio and Linear Compressibility in Perovskite Materials”. In: *Adv. Mater.* 24.30 (2012), pp. 4170–4174. DOI: `https://doi.org/10.1002/adma.201104676`.

[114] A. Ballato. “Poisson’s Ratio for Tetragonal Crystals”. en. In: *IEEE Transactions on Ultrasonics, Ferroelectrics, and Frequency Control* 43.1 (1995), pp. 56–62. DOI: `10.1109/58.484463`.

[115] A. A. Petrov et al. “Crystal Structure of DMF-Intermediate Phases Uncovers the Link Between CH_3 NH_3PbI_3 Morphology and Precursor Stoichiometry”. en. In: *J. Phys. Chem. C* 121.38 (2017), pp. 20739–20743. DOI: `10.1021/acs.jpcc.7b08468`.

[116] F. Hao et al. “Controllable Perovskite Crystallization at a Gas–Solid Interface for Hole Conductor-Free Solar Cells with Steady Power Conversion Efficiency over 10%”. en. In: *J. Am. Chem. Soc.* 136.46 (2014), pp. 16411–16419. DOI: `10.1021/ja509245x`.

[117] H. Zhang, M. K. Nazeeruddin, and Wallace C. H. Choy. “Perovskite Photovoltaics: The Significant Role of Ligands in Film Formation, Passivation, and Stability”. en. In: *Adv. Mater.* 31.8 (2019), p. 1805702. DOI: `https://doi.org/10.1002/adma.201805702`.

[118] M. Xiao et al. “A Fast Deposition-Crystallization Procedure for Highly Efficient Lead Iodide Perovskite Thin-Film Solar Cells”. en. In: *Angew. Chem.* 126.37 (2014), pp. 10056–10061. DOI: `10.1002/ange.201405334`.

[119] N. J. Jeon et al. “Solvent engineering for high-performance inorganic–organic hybrid perovskite solar cells”. en. In: *Nature Materials* 13.9 (2014), pp. 897–903. DOI: `10.1038/nmat4014`.

[120] S. Chen et al. “Crystallization in one-step solution deposition of perovskite films: Upward or downward?” en. In: *Sci. Adv.* 7.4 (2021), eabb2412. DOI: `10.1126/sciadv.abb2412`.

[121] Malin B. Johansson et al. “Highly crystalline $MAPbI_3$ perovskite grain formation by irreversible poor-solvent diffusion aggregation, for efficient solar cell fabrication”. en. In: *Nano Energy* 78 (2020), p. 105346. DOI: `10.1016/j.nanoen.2020.105346`.

[122] H.-S. Kim, A. Hagfeldt, and N.-G. Park. “Morphological and compositional progress in halide perovskite solar cells”. en. In: *Chem. Commun.* 55.9 (2019), pp. 1192–1200. DOI: `10.1039/C8CC08653B`.

[123] S. D. Stranks et al. “Electron-Hole Diffusion Lengths Exceeding 1 Micrometer in an Organometal Trihalide Perovskite Absorber”. en. In: *Science* 342.6156 (2013), pp. 341–344. DOI: `10.1126/science.1243982`.

[124] E. L. Unger et al. “Chloride in Lead Chloride-Derived Organo-Metal Halides for Perovskite-Absorber Solar Cells”. In: *Chem. Mater.* 26.24 (2014), pp. 7158–7165. DOI: `10.1021/cm503828b`.

[125] S. Colella et al. “Elusive Presence of Chloride in Mixed Halide Perovskite Solar Cells”. en. In: *J. Phys. Chem. Lett.* 5.20 (2014), pp. 3532–3538. DOI: `10.1021/jz501869f`.

[126] A. Franz et al. “Determination of the miscibility gap in the solid solutions series of methylammonium lead iodide/chloride”. en. In: *Acta Crystallographica Section B* 74.5 (2018), pp. 445–449. DOI: `10.1107/S2052520618010764`.

[127] N. Yantara et al. “Unravelling the Effects of Cl Addition in Single Step $CH_3NH_3PbI_3$ Perovskite Solar Cells”. en. In: *Chem. Mater.* 27.7 (2015), pp. 2309–2314. DOI: `10.1021/cm502710r`.

[128] H. Yu et al. “The Role of Chlorine in the Formation Process of “$CH_3NH_3PbI_3 - xCl_x$” Perovskite”. en. In: *Adv. Funct. Mater.* 24.45 (2014), pp. 7102–7108. DOI: `https://doi.org/10.1002/adfm.201401872`.

[129] M. Bouchard et al. “Direct Evidence of Chlorine-Induced Preferential Crystalline Orientation in Methylammonium Lead Iodide Perovskites Grown on TiO_2”. en. In: *J. Phys. Chem. C* 121.14 (2017), pp. 7596–7602. DOI: `10.1021/acs.jpcc.6b11529`.

[130] J. Breternitz et al. “Role of the Iodide–Methylammonium Interaction in the Ferroelectricity of $CH_3NH_3PbI_3$”. en. In: *Angew. Chem. Int. Ed.* 59.1 (2020), pp. 424–428. DOI: `https://doi.org/10.1002/anie.201910599`.

[131] H. Röhm et al. “Ferroelectric Properties of Perovskite Thin Films and Their Implications for Solar Energy Conversion”. en. In: *Adv. Mater.* 31.26 (2019), p. 1806661. DOI: `https://doi.org/10.1002/adma.201806661`.

[132] L. M. Garten et al. “The existence and impact of persistent ferroelectric domains in $MAPbI_3$”. en. In: *Sci. Adv.* 5.1 (2019), eaas9311. DOI: `10.1126/sciadv.aas9311`.

[133] Z. Fan et al. “Ferroelectricity of $CH_3NH_3PbI_3$ Perovskite”. en. In: *J. Phys. Chem. Lett.* 6.7 (2015), pp. 1155–11661. DOI: `10.1021/acs.jpclett.5b00389`.

[134] I. M. Hermes et al. “Ferroelastic Fingerprints in Methylammonium Lead Iodide Perovskite”. en. In: *J. Phys. Chem. C* 120.10 (2016), pp. 5724–5731. DOI: `10.1021/acs.jpcc.5b11469`.

[135] E. Strelcov et al. “$CH_3NH_3PbI_3$ perovskites: Ferroelasticity revealed”. en. In: *Sci. Adv.* 3.4 (2017), e1602165. DOI: `10.1126/sciadv.1602165`.

[136] Y. Liu et al. “Dynamic behavior of $CH_3NH_3PbI_3$ perovskite twin domains”. en. In: *Appl. Phys. Lett.* 113.7 (2018), p. 072102. DOI: `10.1063/1.5041256`.

[137] P. Nandi et al. “Organic-inorganic hybrid lead halides as absorbers in perovskite solar cells: a debate on ferroelectricity”. en. In: *J. Phys. D: Appl. Phys.* 53.49 (2020), p. 493002. DOI: `10.1088/1361-6463/abb047`.

[138] S. M. Vorpahl et al. “Orientation of Ferroelectric Domains and Disappearance upon Heating Methylammonium Lead Triiodide Perovskite from Tetragonal to Cubic Phase”. en. In: *ACS Appl. Energy Mater.* 1.4 (2018), pp. 1534–1539. DOI: `10.1021/acsaem.7b00330`.

[139] K. Frohna et al. “Inversion symmetry and bulk Rashba effect in methylammonium lead iodide perovskite single crystals”. en. In: *Nat Commun* 9.1 (2018), p. 1829. DOI: `10.1038/s41467-018-04212-w`.

[140] B. Huang. “Ferroic domains regulate photocurrent in single-crystalline CH3NH3PbI3 films self-grown on FTO/TiO_2 substrate”. en. In: *npj Quantum Materials* 3 (2018), p. 30. DOI: `10.1038/s41535-018-0104-5`.

[141] K. Aizu. “Possible Species of “Ferroelastic” Crystals and of Simultaneously Ferroelectric and Ferroelastic Crystals”. In: *Journal of the Physical Society of Japan* 27.2 (1969), p. 1374. DOI: `10.1143/JPSJ.27.387`.

[142] C. C. Boyd et al. “Understanding Degradation Mechanisms and Improving Stability of Perovskite Photovoltaics”. en. In: *Chem. Rev.* 119.5 (2019), pp. 3418–3451. DOI: `10.1021/acs.chemrev.8b00336`.

[143] J. Yang and T. L. Kelly. “Decomposition and Cell Failure Mechanisms in Lead Halide Perovskite Solar Cells”. en. In: *Inorg. Chem.* 56.1 (2016), pp. 92–101. DOI: `10.1021/acs.inorgchem.6b01307`.

[144] H.-S. Kim, J.-Y. Seo, and N.-G. Park. “Material and Device Stability in Perovskite Solar Cells”. en. In: *ChemSusChem* 9.18 (2016), pp. 2528–2540. DOI: `10.1002/cssc.201600915`.

[145] G. P. Nagabhushana, Radha Shivaramaiah, and Alexandra Navrotsky. “Direct calorimetric verification of thermodynamic instability of lead halide hybrid perovskites”. In: *Proceedings of the National Academy of Sciences* 113.28 (2016), pp. 7717–7721.

[146] S. Tan et al. “Shallow Iodine Defects Accelerate the Degradation of a-Phase Formamidinium Perovskite”. en. In: *Joule* 4.11 (2020), pp. 2426–2442. DOI: `10.1016/j.joule.2020.08.016`.

[147] F. Cordero et al. “Influence of Temperature, Pressure, and Humidity on the Stabilities and Transition Kinetics of the Various Polymorphs of $FAPbI_3$”. en. In: *J. Phys. Chem. C* 124.42 (2020), pp. 22972–22980. DOI: `10.1021/acs.jpcc.0c06342`.

[148] M. Saliba et al. “Cesium-containing triple cation perovskite solar cells: improved stability, reproducibility and high efficiency”. en. In: *Energy Environ. Sci.* 9.6 (2016), pp. 1989–1997. DOI: `10.1039/C5EE03874J`.

[149] O. J. Weber, B. Charles, and M. T. Weller. “Phase behaviour and composition in the formamidinium–methylammonium hybrid lead iodide perovskite solid solution”. en. In: *J. Mater. Chem. A* 4.40 (2016), pp. 15375–15382. DOI: `10.1039/C6TA06607K`.

[150] A. Fransisco-Lopez et al. “Phase Diagram of Methylammonium/Formamidinium Lead Iodide Perovskite Solid Solutions from Temperature-Dependent Photoluminescence and Raman Spectroscopies”. en. In: *J. Phys. Chem. C* 124.6 (2020), pp. 3448–3458. DOI: `10.1021/acs.jpcc.9b10185`.

[151] A. Pisanu et al. “The $FA_{1-x}MA_xPbI_3$ System: Correlations among Stoichiometry Control, Crystal Structure, Optical Properties, and Phase Stability”. en. In: *J. Phys. Chem. C* 121.16 (2017), pp. 8746–8751. DOI: `10.1021/acs.jpcc.7b01250`.

[152] B. Charles et al. “Phase Behavior and Substitution Limit of Mixed Cesium-Formamidinium Lead Triiodide Perovskites”. en. In: *Chem. Mater.* 32.6 (2020), pp. 2282–2291. DOI: `10.1021/acs.chemmater.9b04032`.

[153] G. Niu. “Enhancement of thermal stability for perovskite solar cells through cesium doping”. en. In: *RSC Advances* 7 (2017), p. 17473. DOI: `10.1039/c6ra28501e`.

[154] D. J. Kubicki et al. “Phase Segregation in Cs-, Rb- and K-Doped Mixed-Cation $(\mathrm{MA})_x(\mathrm{FA})_{1-x}\mathrm{PbI}_3$ Hybrid Perovskites from Solid-State NMR”. en. In: *J. Am. Chem. Soc.* 139.40 (2017), pp. 14173–14180. DOI: `10.1021/jacs.7b07223`.

[155] R. Prasanna et al. “Band Gap Tuning via Lattice Contraction and Octahedral Tilting in Perovskite Materials for Photovoltaics”. en. In: *J. Am. Chem. Soc.* 139.32 (2017), pp. 11117–11124. DOI: `10.1021/jacs.7b04981`.

[156] Ralf G. Niemann et al. “Cs^+ incorporation into $\mathrm{CH_3NH_3PbI_3}$ perovskite: substitution limit and stability enhancement”. en. In: *J. Mater. Chem. A* 4.45 (2016), pp. 17819–17827. DOI: `10.1039/C6TA05869H`.

[157] J. H. Noh et al. “Chemical Management for Colorful, Efficient, and Stable Inorganic–Organic Hybrid Nanostructured Solar Cells”. en. In: *Nano Lett.* 13.4 (2013), pp. 1764–1769. DOI: `10.1021/nl400349b`.

[158] T. J. Jacobsson et al. “An exploration of the compositional space for mixed lead halogen perovskites for high efficiency solar cells”. en. In: *Energy Environ. Sci.* 9 (2016), pp. 1706–1724. DOI: `10.1039/C6EE00030D`.

[159] E. I. Marchenko et al. “Transferable Approach of Semi-Empirical Modeling of Disordered Mixed-Halide Hybrid Perovskites $\mathrm{CH_3NH_3Pb(I_{1-x}Br_x)_3}$: Prediction of Thermodynamic Properties, Phase Stability, and Deviations from Vegard’s Law”. en. In: *J. Phys. Chem. C* 123.42 (2019), pp. 26036–26040. DOI: `10.1021/acs.jpcc.9b08995`.

[160] Z. Muhammad et al. “Tunable relativistic quasiparticle electronic and excitonic behavior of the $\mathrm{FAPb(I_{1-x}Br_x)_3}$ alloy”. en. In: *Phys. Chem. Chem. Phys.* 22.21 (2020), pp. 11943–11955. DOI: `10.1039/D0CP00496K`.

[161] G. E. Eperon et al. “Formamidinium lead trihalide: a broadly tunable perovskite for efficient planar heterojunction solar cells”. en. In: *Energy Environ. Sci.* 7.3 (2014), p. 982. DOI: `10.1039/c3ee43822h`.

[162] W. Rehman et al. “Charge-Carrier Dynamics and Mobilities in Formamidinium Lead Mixed-Halide Perovskites”. In: *Adv. Mater.* 27.48 (2015), pp. 7938–7944. DOI: `10.1002/adma.201502969`.

[163] B. Slimi et al. “Synthesis and characterization of perovskite $\mathrm{FAPbBr_{3-x}I_x}$ thin films for solar cells”. en. In: *Monatsh Chem* 148.5 (2017), pp. 835–844. DOI: `10.1007/s00706-017-1958-0`.

Part I

MAPbI$_3$ thin layers : A detailed structural study

General context of the study and motivations

Thin layers of $MAPbI_3$ have attracted great interest in the scientific community since the first perovskite based solar cells. Plethora of synthetic methods have been developed over the years often only slightly different from one another but allowing better performances to be achieved.

A consensus has been reached regarding the highly beneficial effect of the use of chlorine in the fabrication process. In addition to enhancing the electrical properties of the films,[1] it increases the grain size and induces a preferential orientation along the tetragonal [110] $MAPbI_3$ direction.[2] However, the mechanism leading to this enhancement is still not understood, even more so as the presence of the chlorine in the final sample is not settled yet: reports showing the presence of traces quantity of chlorine in the layers were published while others did not observe this halogen in their films. However, even when identified in the sample, it is always in trace quantities, notably lower than the amounts introduced in the precursor solutions. This observation is in good agreement with the great miscibility gap demonstrated when attempting to form $MAPb(I_{1-x}Cl_x)_3$ solid solution.[3]

This part is mainly dedicated to the study of $MAPbI_3$ thin layers prepared in the presence of chlorine. All thin layers were prepared by spin coating a precursor solution on a glass/FTO/TiO_2 or glass/ITO/SiO_2 substrate and further thermal annealing at 100 °C. More details about the fabrication of the thin layers can be found in Appendix A.1. We had the opportunity to work on three types of thin layers, all obtained from the same precursors: MAI and $PbCl_2$, introduced in a 3:1 ratio, to satisfy the stoichiometry of the final structure $MAPbI_3$. All precursors where dissolved in dimethylformamide (DMF) solvent. The difference between these layers reside in the solubilization of the precursors, as shown in Figure I.15.a.

The first type of layers, labelled **Low Concentration, or L.C**., were obtained by using the protocol largely adopted in the literature.[1] In this protocol, both precursors are dissolved simultaneously in the solvent, leading to a molar concentration of lead atoms of 0.8 M. A clear and limpid solution is obtained. This concentration is however relatively low, especially in comparison with the concentration used to fabricate thin layers without Cl which proven their reproducibility.[2] Hence, in order to investigate the influence of the solution concentration, the **High Concentration (H.C.** in the following) layers were fabricated from a 1.6 M solution, in which both precursors were solubilized simultaneously. However, $PbCl_2$ was proven to display poor solubility in DMF,[4] leading to a turbid solution at room temperature (RT). The H.C. solution is thus heated at 70 °C to achieve full dissolution of the precursors, and the hot solution is used for the deposition process.

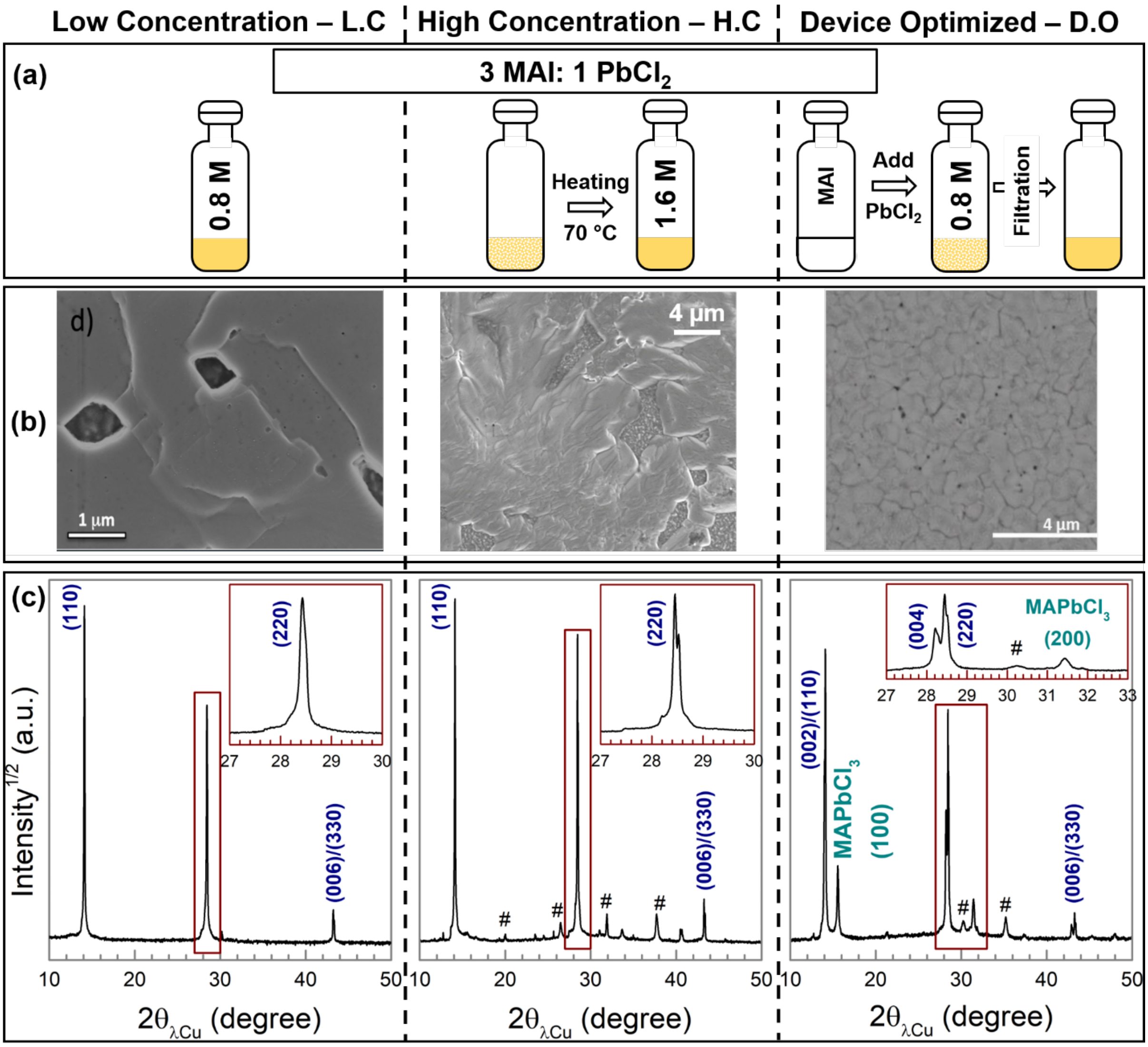

Figure I.15: Presentation of the three different layers used in this study: Low Concentration (L.C.), High Concentration (H.C) and Device optimized (D.O.). (a) Protocol of preparation of the precursor's solution. (b) SEM images of the three different layers. (c) Typical θ-2θ diffractogram of the three types of layers, with, in red, an enlarged view of the region identified by in the red square in the main pattern. # sign indicated the peaks of the substrate, FTO/TIO_2 or ITO/TiO_2.

The third and last protocol was studied in the frame of a collaboration with Dr. Pia Dally, a former PhD student at l'Institut National de l'Energie Solaire (INES), in Chambery, France. These layers were optimized by INES team to obtain the best solar cell performances and stability, hence the label **Device Optimized or D.O**. Here, the same concentration as L.C. layers is used, but the solubilization order of the precursors is different: MAI is pre-solubilized separately, and $PbCl_2$ is added in a second time. Interestingly and in contrast with the L.C. protocol, a turbid solution is obtained here, requiring an additional filtration step to obtain the clear solution used for spin coating. All the precursor solutions fabrication steps are illustrated in Figure I.15.a.

Figure I.15.b displays the SEM images of the three layers, showing large grains for L.C. and H.C. layers with a poor surface coverage for both layers, as it has been previously reported for thin layers obtained through similar protocols.[5,6,7,8] D.O. thin layers, on the other hand, displayed full surface coverage, with lateral grain size of around 800 nm. The thicknesses of the layers were estimated as 300, 500 and 300 nm for L.C, H.C and D.O. thin layers respectively.

$MAPbI_3$ crystallizes at RT in a tetragonal I4/mcm structure. $\theta/2\theta$ XRD patterns are displayed in Figure I.15.c.

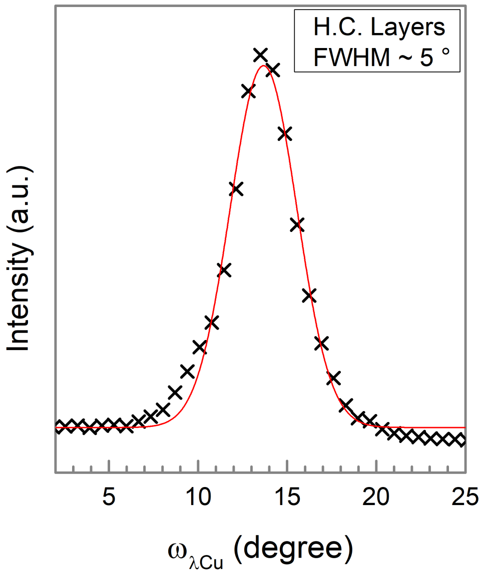

Figure I.16: Rocking curves around the (220) measured on a typical H.C. thin layer. The red curve corresponds to the Gaussian fit used to extract the mosaicity.

Two main striking features are observed from Figure I.15.b.

1. The presence of additional peaks in D.O. thin layers diffractograms. These peaks were identified as cubic $MAPbCl_3$ (h00) peaks. The observation of these peaks

is quite unexpected as the stoichiometry used in the precursor solution (3 MAI : 1 $PbCl_2$) would favor the formation of $MAPbI_3$. The presence of $MAPbCl_3$ in $MAPbI_3$ thin layers was reported in some previous studies.[9,10,11,12] At the time of our study, $MAPbCl_3$ was suspected to be a crystallization intermediate for $MAPbI_3$, but the mechanism behind such phenomenon was poorly understood. **Chapter 2 of this manuscript is dedicated to the investigation of the mechanism behind the ion exchange in D.O. thin layers**.

2. While L.C. and H.C. layers evidence a preferential orientation along the tetragonal [hh0] direction, as expected from the use of Cl in the precursors solution,[2] D.O. ones reveal a double texture along [00l] and [hh0] $MAPbI_3$ tetragonal directions. It has to be noted that this can be observed with L.C and H.C. samples but only rarely. Figure I.16 presents a rocking curve measured on the (220) $MAPbI_3$ reflection on H.C. thin layers, illustrating the texture of the layers. The mosaicity varied between 5 and 10 °, depending on the nature of the layer (L.C., H.C. or D.O.). Such texture was already reported in previous reports but rarely commented.[5,9,10,13] **The microstructure of** $MAPbI_3$ **thin layers and the formation of the double texture is addressed in chapter 3**.

Chapter 2

Crystallization mechanisms of $MAPbI_3$ thin layers through ionic exchange

As already explained, we focus here on $MAPbI_3$ thin layers fabricated in the presence of chlorine. Studies have revealed that no solid solution of $MAPb(I_{1-x}Cl_x)_3$ can be formed,[3] because of the large ionic difference between Cl^- and I^- (167 and 220 pm, respectively[14]). Observed in some reports, $MAPbCl_3$ was proposed as a crystallization intermediate for $MAPbI_3$ thin layers prepared in the presence of chlorine.[11,12] However, at the time of this study, little was understood about such crystallization path.

In this chapter we demonstrate the spontaneous formation of $MAPbCl_3$ in the precursor solution and follow, by means of *in-situ* XRD, the process of $MAPbI_3$ formation through ionic exchange. We then show that these results allow the rationalization of the observed performances obtained with solar cells based on similar $MAPbI_3$ thin films.

This work was performed in collaboration Dr. Pia Dally, a former PhD student at INES and was published in “Chemistry of Material” in 2020.[15]

Contents

2.1. IDENTIFICATION OF THE CRYSTALLIZATION INTERMEDIATE

As shown in Figure I.15, the XRD pattern of D.O. layers evidence the presence of diffraction peaks characteristic of cubic $MAPbCl_3$. One of the aims of this study was to determine at which stage of the synthesis process this phase forms.

These thin layers were obtained by spin coating a precursor solution on a substrate and subsequent annealing at 100 °C for 35 min (more in appendix A.1). The protocol for the deposition of the D.O. layers was optimized at INES to obtain best performing cells and the better long-term stability. The precursor solution is obtained by sequential solubilization of MAI and $PbCl_2$ in DMF, to obtain a solution of 0.8 M concentration and a ratio of 3 MAI : 1 $PbCl_2$. The solution obtained was turbid, and to fabricate the thin layers, filtration of the solution is needed. Interestingly, this observation is in stark contrast with what is obtained with L.C. precursor solution. This solution, which is limpid and does not require filtration before use, is obtained from the same precursor and precursors ratio, and the similar solution concentration is used (0.8 M). The difference between these solutions is the order of solubilization of the precursors.

Hence, we decided to investigate the nature of precipitate that forms spontaneously in D.O. precursor solutions and we centrifuged the turbid solution (before filtration). The

XRD pattern of this precipitate is displayed in Figure 2.1.a. **The major features of the pattern consisting of peaks with similar FWHM match the expected peak positions of cubic (Pm-3m) $MAPbCl_3$ with a lattice parameter of a = 5.684(5)** Å. As surprising as this spontaneous formation of $MAPbCl_3$ in D.O. precursor solution is, it is in agreement with the low standard Gibbs free energy of the formation of this structure from $PbCl_2$.[16]

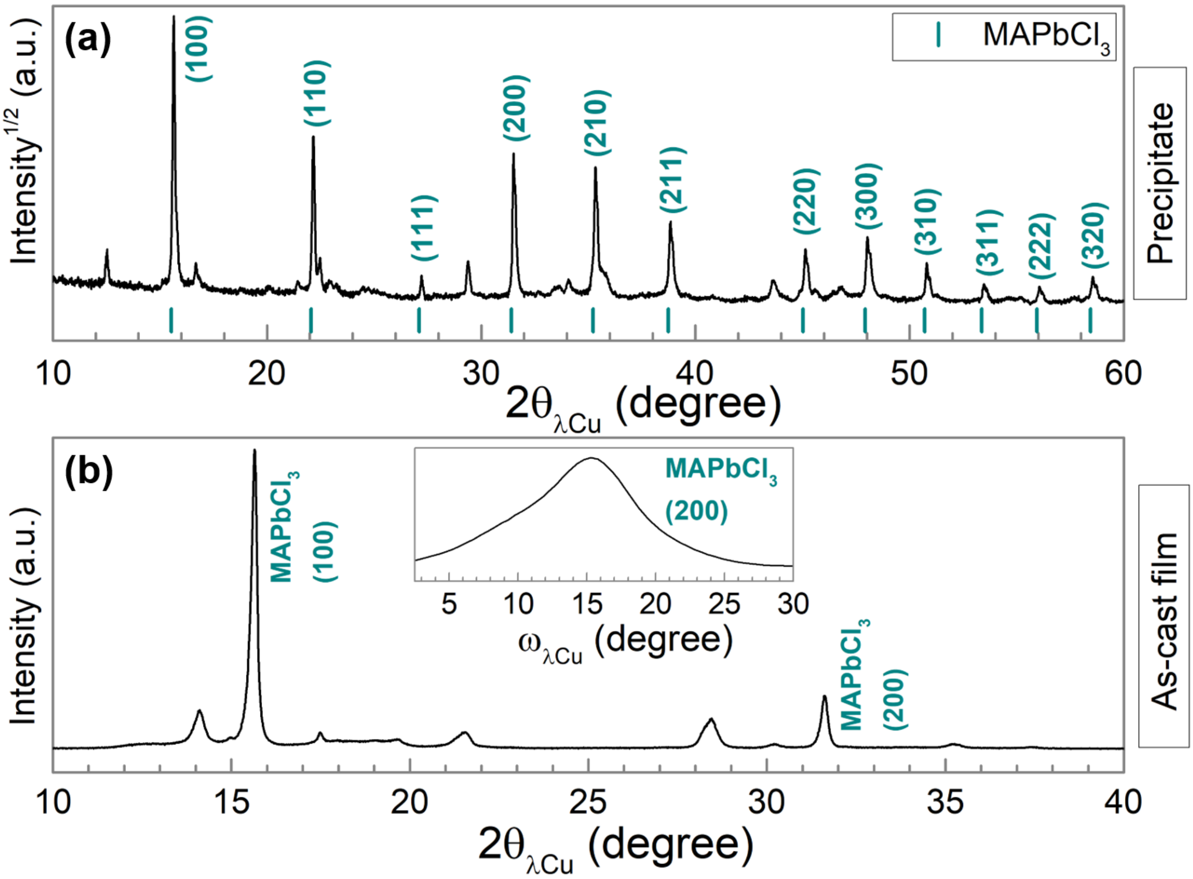

Figure 2.1: XRD pattern of the precipitate obtained after centrifugation of (a) D.O. precursor solution. The blue dashes point the presence of expected $MAPbCl_3$ diffraction peaks. (b) $\theta/2\theta$ pattern of the as-cast D.O. thin layers. The inset shows the rocking curve measurement performed on the peak at 31.41 °, proving a preferential orientation of $MAPbCl_3$ along [h00] direction.

As explained earlier, filtration of the solution is required before thin layers deposition. Hence, we investigated in a second step as-cast D.O. thin layers. That is to say, the precursors solution was spin-coated on the substrates in the glove box following normal procedure, and the XRD pattern of this layer was measured without annealing. The as-cast film was transferred from the glove box to the diffractometer by taking care of keeping the layer in an inert atmosphere (bag or box sealed in the glove box), and the measurements were performed in a diffractometer equipped with a graphite dome under which an N_2 atmosphere is maintained. The result is shown in Figure 2.1.b and revealed two intense peaks in the $2\theta = 10 - 40°$ range, which positions coincide with the (100) and (200) $MAPbCl_3$. Rocking curve measurement on the peak at 31.41° proved the texture of this phase along cubic [h00] $MAPbCl_3$ direction, with a mosaicity of ~ 10 °, similar to $MAPbI_3$ mosaicity on the final D.O. films.

Our measurements reveal the spontaneous formation of $MAPbCl_3$ in solution and the presence of this phase in as-cast films, before heat treatment.

The presence of $MAPbCl_3$ was observed in some previous reports about $MAPbI_3$ thin layers prepared in the presence of chlorine.[9,10,11,12] Interestingly, Pellet *et al.* demonstrated a rapid and spontaneous halogen exchange when exposing a MAPbX3 ($X = I^-$, Br^-, Cl^-) thin layers to a solution of MAX, X being a different halogen from the one contained in the initial layer.[17,18]

At the time of our study, no study was performed on the mechanism behind this supposed ion exchange. This question becomes even more important when considering the great lattice mismatch between the two perovskites: for $MAPbCl_3$, a = 5.684(5) Å, and for $MAPbI_3$ cubic phase at 100 °C: a = 6.312(2) Å (100 °C is the temperature at which the annealing is performed, thus the temperature of crystallization and supposed ionic exchange). Consequently, a large non-miscibility region between these two phases was observed.[3]

The mechanism behind the crystallization of $MAPbI_3$ from $MAPbCl_3$ seems particularly intriguing. Hence, we conducted an *in-situ* study of $MAPbI_3$ formation in D.O. thin layers at 100 °C, which we present in the following section.

2.2. MECHANISM OF THE $MAPbCl_3$ – $MAPbI_3$ ION EXCHANGE: AN *IN-SITU* STUDY

2.2.1. IDENTIFICATION OF THE CRYSTALLINE PHASES AND STAGES OF THE MECHANISM

The *in-situ* annealing study was performed on one Rigaku SmartLab diffractometer (see appendix B.6), which was equipped with an Anton-Paar temperature chamber and a graphite dome which allowed to maintain an inert atmosphere around the sample during the whole measurement. An as-cast D.O. thin layer is placed in the diffractometer, under the dome, and the temperature is increased to 100 °C. Once the sample reaches the desired temperature, 10 min long $\theta/2\theta$ measurements in the range $2\theta = 10 - 60$ ° are recorded continuously during the annealing process. We performed, during this experiment, $\theta/2\theta$ scans to probe the whole layer thickness.

Before going further into the description of our results, it is important to recall that while $MAPbI_3$ is tetragonal at RT (I4/mcm), it adopts a cubic Pm-3m structure at 100 °C, as it experiences a first order tetragonal – cubic phase transition around 57 °C. Hence, as the annealing is performed at 100 °C, $MAPbI_3$ crystallizes in its cubic Pm-3m phase.

Figure 2.2.a displays in an enlarged view (2θ range: 11 - 17 °) of the evolution of the first order diffraction peaks of the phases involved in the crystallization process. Qualitatively, it shows the decrease of the $(100)_C$ $MAPbCl_3$ peak area and a simultaneous increase of the area of $MAPbI_3$ $(100)_C$ diffraction peak (index C recalls the cubic symmetry of the corresponding phases), confirming the hypothesis of the crystallization of $MAPbI_3$ through halogen ion exchange from $MAPbCl_3$. The formation of I-Cl solid solution would lead to a gradual evolution of the peak position between the pure I and Cl phases as the ratio of two halogens in the perovskite structure evolves. Such phenomenon is not observed. Moreover, we observe the formation of hexagonal PbI_2 (P-3m1 space group), as its (001) Bragg line appears over time.

The raw data were refined using a pseudo-Voigt shape function. Figure 2.2.b displays the evolution of the peak areas of the three crystalline species of this mechanism, $MAPbCl_3$, $MAPbI_3$ and PbI_2 during annealing, allowing to distinguish three different stages in this ion exchange mechanism.

During the first stage, labelled (I) and colored in red in Figure 2.2.b, $MAPbCl_3$ peak area decreases while $MAPbI_3$ peak area increases, indicating a formation of the latter and a disappearance of the former.

The second stage (II), colored in light red, corresponds to the apparition of PbI_2 in the layer, coexisting with the two perovskite structures. PbI_2 is a known degradation product of $MAPbI_3$, explaining why, during this stage, as the peak area of PbI_2 increases, $MAPbI_3$ peak area starts to decrease. $MAPbCl_3$ peak area, on the other hand, continues to decrease.

Finally, during the last stage, labelled stage (III) and colored in green, $MAPbCl_3$ has completely disappeared from the layer, and both $MAPbI_3$ and PbI_2 peak areas do not evolve for the remaining 30 min of the experiment.

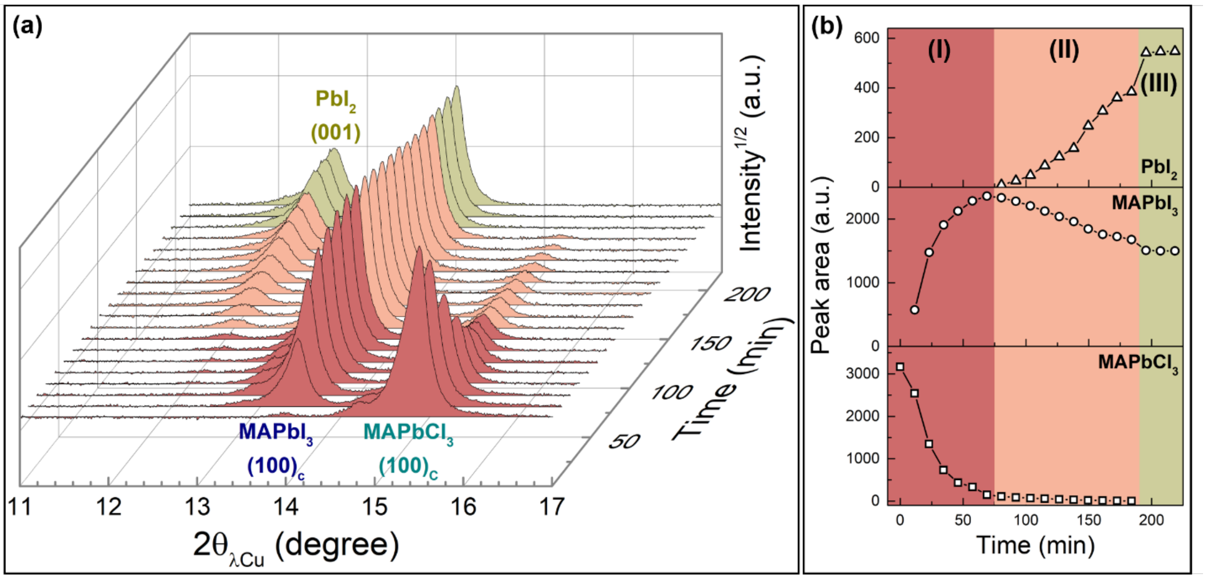

Figure 2.2: (a) Raw data of the *in-situ* crystallization experiment in the range $2\theta = 11 - 17°$, showing the three crystalline phases involved in the ion exchange mechanism: $MAPbCl_3$, $MAPbI_3$ and PbI_2. (b) Evolution of the peak areas of the three phases, which allow to distinguish a three-stages mechanism, each indicated by a different color.

The evolution of the FWHM corrected from the instrumental resolution for the three compounds during the *in-situ* experiment is displayed in Figure 2.3.a. The XRD peak broadening has two origins: size and/or strain (or distortion) effects, and to discriminate between both effects, multiple reflections are needed. Here, in the case of $MAPbCl_3$ and PbI_2, as the high angle reflection peaks display weak intensities, only first-order diffraction lines could be reliably fitted. However, the monotonous increase of the FWHM of $MAPbCl_3$ and decrease of PbI_2 FWHM is consistent with the disappearance of the former and the formation of the latter. In the case of $MAPbI_3$, the evolution is more complex, decreasing during the first stage before increasing in the second stage. A brutal decrease is observed as soon as the third and final stage starts.

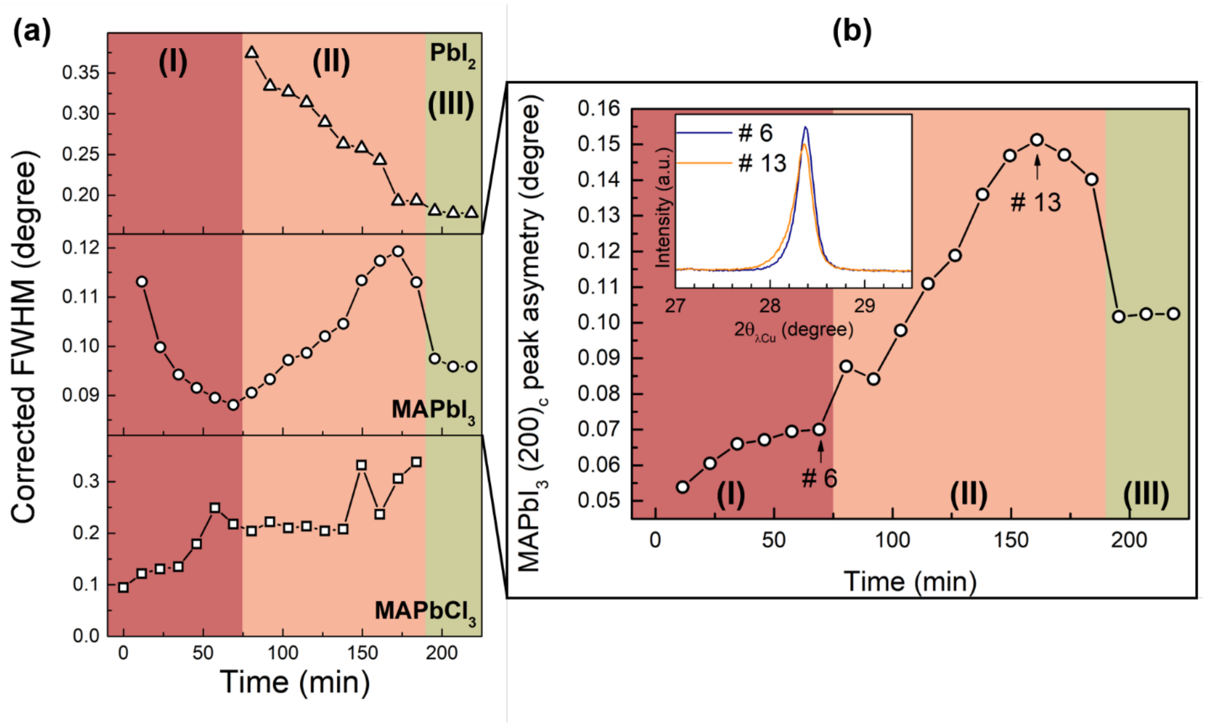

Figure 2.3: (a) Evolution of the peaks' corrected FWHM for the three crystalline species involved in the ion exchange mechanism. (b) Evolution of the asymmetry of the $MAPbI_3$ (200)C peak extracted from the asymmetric Pseudo-Voigt shape function, translating the levels of distortion Δd experienced by the material. The inset displays the (200)C $MAPbI_3$ peak shape from which the values pointed out in the main graph were extracted, showing the peak asymmetry.

To correctly reproduce the raw data, we had to introduce an asymmetric shape in the pseudo-Voigt function during the refinement, thus allowing to refine separately the left and the right HWHM (Half Width at Half Maximum) of the peak. The data displayed in Figure 2.3.a corresponds to the mean value. We followed, in Figure 2.3.b, the evolution of the difference between the left and right HWHM of $(200)_C$ $MAPbI_3$ peak (converted in FWHM), which we refer to in the following as the peak asymmetry. The insert in Figure 2.3.b shows how this asymmetry is reflected in the raw data. The same tendency is observed for all $MAPbI_3$ peaks and it is associated to the presence of distortions in the crystalline lattice. While the assymetry slowly increases during the crystallization first stage, a steep rise is observed during the second stage. An abrupt decrease precedes the stabilization of the asymmetry during the last stage. Following the evolution of the lattice parameter will allow to better understand the phenomenon described here.

Figure 2.4 displays the evolution of $MAPbI_3$ lattice parameter, and the color scale indicates the strain ϵ experienced by the compounds. This strain ϵ, which can be either positive or negative, is to be differentiated from the lattice distortion mentioned above and related to the peak width and asymmetry. Here, the strain, is calculated from the lattice parameters relatively to the lattice parameter of the bulk, considered as the reference, using the following equation:

$$\epsilon = \frac{a_{sample} - a_{bulk}}{a_{bulk}} \tag{2.1}$$

As it appears, $MAPbI_3$ displays compressive strain, which steadily increases during the first stage, until it reaches the maximum compressive strain value of ϵ = - 0.48 %. As the second stage begins and PbI_2 starts forming in the layer, $MAPbI_3$ strain is gradually relaxed, as lattice monotonously expands. Finally, as soon as $MAPbCl_3$ disappears from the layer in stage III, the lattice parameter abruptly increases and remains constant for the rest of the experiment.

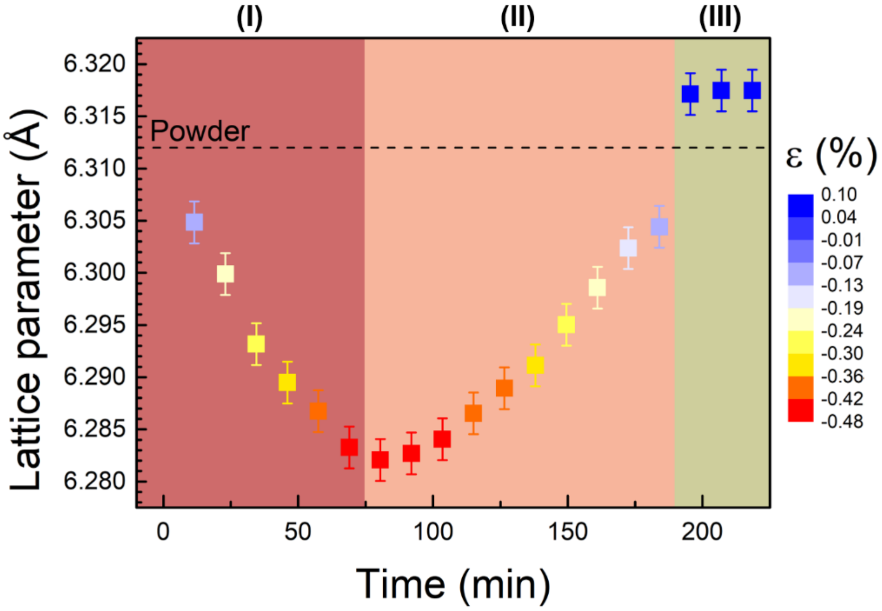

Figure 2.4: Evolution of cubic $MAPbI_3$ lattice parameter during the *in-situ* annealing experiment. The color denotes the strain level calculated from the bulk lattice parameter, which is represented by the dotted line in the graph.

This experiment confirms the formation of $MAPbI_3$ from $MAPbCl_3$ through ion exchange. We observed that, while both perovskite structures coexist in the layer, the iodine-based structure exhibits high compressive strain. The strain level increases until it eventually induces partial degradation of the $MAPbI_3$ as demonstrated by the formation of PbI_2. During this stage, the lattice parameters evolution indicates a gradual relaxation of the strain; however, the evolution of the peak shape indicates strongly increasing distortion in the crystalline lattice, indicating a gradient in lattice parameter in the layer depth. Both the distortion and the strain disappear as soon as $MAPbCl_3$ is fully converted.

Finally, we wanted to assess the efficiency of the ion exchange process. The question is to evaluate the proportion of cubic $MAPbCl_3$ which is converted in cubic $MAPbI_3$. The raw peak areas cannot be directly used to evaluate the relative amounts of the different phases as the peak intensity depends on the structure factor of the Bragg reflection and the unit cell volume (see appendix C for the full equation describing the origin of the diffraction peak area).

Here, considering that during all our θ-2θ measurements, we systematically observe peaks arising from the substrate, and as the peaks of interest are in a reduced 2θ range (between 12.5 and 15.5°) the absorption of the beam and the correction from the finite thickness of the thin layer can be neglected. Moreover, the Lorentz-polarization factor can be considered as constant over this reduced 2θ range. The peak integrated intensity I can thus be expressed as:

$$I \alpha \frac{V\,|F^2|}{v_a^2} \tag{2.2}$$

Where F the structure factor of the corresponding peak, v_a the volume of the unit cell, and V is the volume of the diffracting phase in the measured sample. V verifies:

$$V = N_{cells}\, v_a \tag{2.3}$$

Where N_{cells} is the number of diffracting unit cells. For $MAPbI_3$, $MAPbCl_3$ and PbI_2 the number of unit cells equals the number of lead atoms as for all three there is one formula per unit cell (Z = 1). We then end up with:

$$N_{Pb}\ \alpha\ \frac{I v_a}{|F^2|} \tag{2.4}$$

We calculated the structure factor of the corresponding reflection of the three phases (cubic (100) reflection for $MAPbCl_3$ and $MAPbI_3$ and hexagonal (001) PbI_2) using the equation B.15 which defines the structure factor (appendix B.3). The positions of the atoms in cubic Pm-3m $MAPbI_3$ and $MAPbCl_3$ were taken from the literature, with the lead atom and the halides in 1b and 3c Wyckoff positions, respectively. The carbon and the nitrogen atoms were both placed in 1a site, with an occupancy factor of 0.5 and large thermal displacement coefficients. Concerning PbI_2, we used the atomic positions reported in ICDD pattern 00-007-0235. The error bars where determined by varying the thermal displacement coefficient of the atoms between the different values reported in the literature.

Considering the first scan to determine $N_{Pb}^{MAPbCl_3}$ the initial number of lead atoms contained in $MAPbCl_3$, we then calculated $N_{Pb}^{MAPbI_3}$ and $N_{Pb}^{PbI_2}$ at the end of stage I and at the end of stage III. We found:

- End of stage I: $\frac{N_{Pb}^{MAPbI_3}}{N_{Pb}^{MAPbCl_3}} = 54 \pm 5\%$
- End of stage III: $\frac{N_{Pb}^{MAPbI_3}+N_{Pb}^{PbI_2}}{N_{Pb}^{MAPbCl_3}} = 55 \pm 5\%$

The fact that both values are equal proves that PbI_2 forms from the degradation of $MAPbI_3$, all the lead atoms from degraded $MAPbI_3$ participate in crystalline PbI_2 formation. On the other hand, it appears that only half of the $MAPbCl_3$ lead atoms form crystalline $MAPbI_3$. The missing lead atoms are very likely in an amorphous phase, as it seems highly unlikely to observe lead sublimation at 100 °C at atmospheric pressure. Such observation is not very surprising when considering the large lattice mismatch between the cubic phases of $MAPbCl_3$ and $MAPbI_3$ ($a = 5.684(5)$ Å and $6.312(2)$ Å, respectively) and the large strain values observed during this process. Moreover, in agreement with previous reports,[19] we already observed spontaneous amorphization of $MAPbI_3$ thin layers over time as a degradation mechanism. However, we want to highlight that the ion exchange efficiency might be better in the case of the classical annealing in the glove box during device fabrication.

2.2.2. Relative distribution of the different crystalline phases in the layer's depth

To further understand the ion exchange mechanism, we investigated eventual variations in the relative contributions of the different phases as a function of the probed depth. Grazing incidence measurements allow to probe different depths in the thin layers as the incident angle is varied. The probed depth can be estimated from the incident angle when knowing the penetration depth of the X-rays in the layer which depends on its density. More details can be found in appendix B.4.

We performed grazing incide measurements on a thin layer which was only partially annealed in our diffractometer, as can be seen from its $\theta/2\theta$ pattern, displayed in black in Figure 2.5.a. $\theta/2\theta$ measurements probe the whole perovskite thickness, as proved by the systematic observation of the substrate peaks which are indicated by the # symbol in all the patterns shown in this chapter. In such configuration, the partially annealed thin layer only exhibit $MAPbCl_3$ and $MAPbI_3$ peaks, suggesting that the second phase of the layer is not reached. However, the grazing incident measurement performed at incident angle $\omega = 0.35$ °, which allows to probe the upper part of the layers over a depth of $\sim 60\,\mathrm{nm}$, revealed a different pattern. Here, almost no contribution from $MAPbCl_3$ is observed and PbI_2 is detected. **This observation suggests that $MAPbCl_3$ phase is located in the lower part of the layer, close to the interface with the substrate, while PbI_2 is closer to the top part of the thin film**.

The localization of PbI_2 was confirmed by in-plane measurements with different incident angles performed on the fully annealed sample in which the quantity of PbI_2 is the highest. By increasing the incident angle, increasing layers depths are probed and by following the evolution of the $PbI_2/MAPbI_3$ ratio with the probed depth, we can qualitatively estimate the relative position of the degradation phase in the layer. Figure 2.5.c shows that as we probe deeper in the layer, the $PbI_2/MAPbI_3$ peak area ratio is smaller. This observation confirms that PbI_2 is not homogeneously distributed in the layer thickness but mainly located on the upper part of the film.

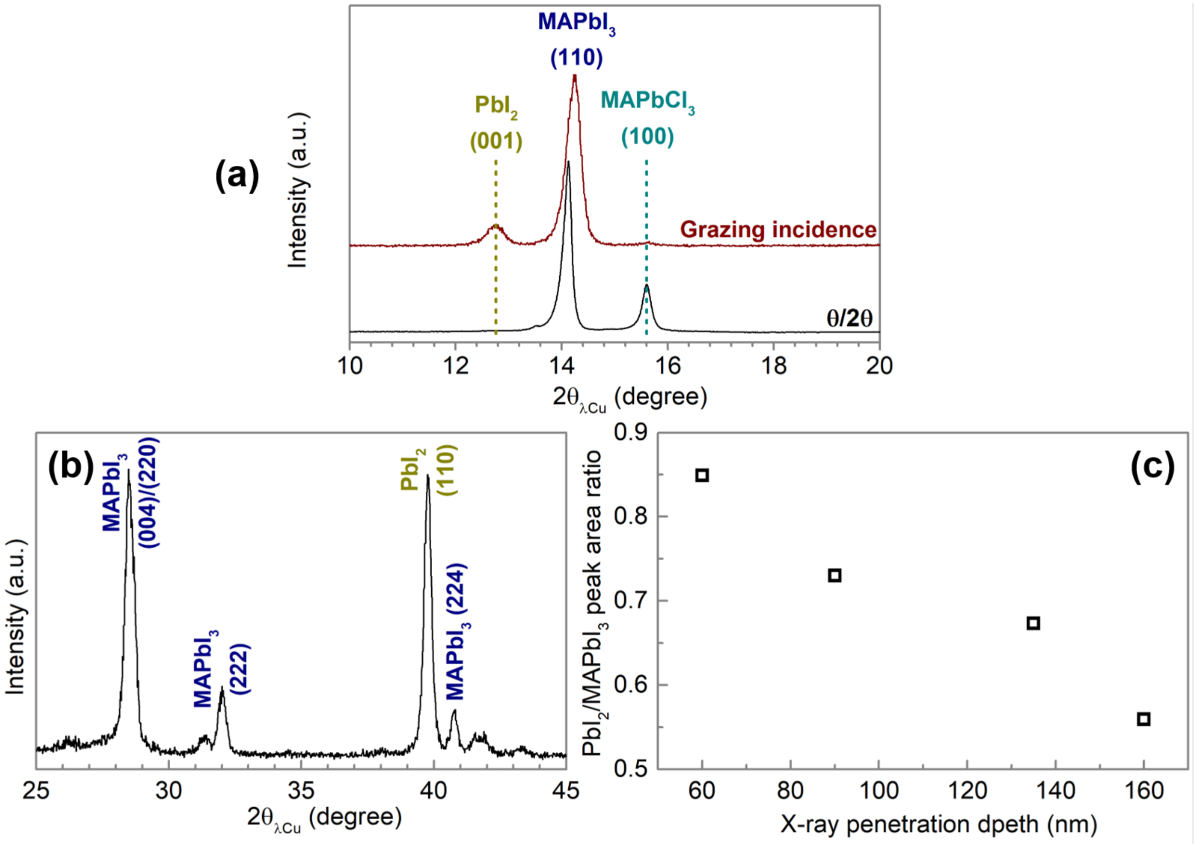

Figure 2.5: Probing the relative position of the three structure in the layer's depth. (a) $\theta/2\theta$ measurement (black) which probed the whole film thickness VS grazing incidence measurement (red) which probes only the upper part of the film (∼60 nm). (b) Example of an in-plane diffractogram, measured on a fully annealed sample, showing both $MAPbI_3$ and PbI_2 peaks. (c) Evolution of the peak area ratio of PbI_2 (110)/$MAPbI_3$ (004)/(220) as function of the penetration depth.

2.2.3. ION EXCHANGE MECHANISM

We have shown the spontaneous formation of $MAPbCl_3$ in solution when using the D.O. protocol, and observed that the layer obtained after spin-coating is a textured $MAPbCl_3$ thin layer. As MAI is known to quickly dissociate into its ionic components when put into DMF,[13] we believe that the layer also contains I^- and MA^+ in their ionic form, especially as MAI is introduced in excess in the precursor solution. Moreover, Unger *et al.* have demonstrated the evaporation of MACl from $MAPbI_3$ thin layers prepared in the presence of chlorine.[12]

Combining our results and the considerations listed above from the literature, we propose the following mechanism for the crystallization of $MAPbI_3$ from $MAPbCl_3$ through halogen ions exchange, which is illustrated in Figure 2.6.

Upon heating, the evaporation of MACl drives the conversion of $MAPbCl_3$ into $MAPbI_3$. **The conversion starts from the upper part of the layers and spreads through its thickness upon annealing**, justifying the presence of $MAPbCl_3$ in the lower part of the layers when the substrate is partially annealed. Nevertheless, **$MAPbI_3$ formed from this process is strained, and the increasing strain eventually induces partial decomposition and formation of PbI_2**. This decomposition starts before the ion exchange mechanism is completed, and is concomitant with a partial and gradual relaxation of the strain. This partial relaxation is however accompanied with an **increasing deformation of the lattice, indicating a gradient in the lattice parameter in the layer thickness**. This observation is in agreement with the fact that the conversion starts from the top part of the layer and propagates into its thickness, revealing that different parts of the layer are experiencing different strain levels, according to the conversion stage they experience. **The strain and the deformation abruptly disappear as soon as no more $MAPbCl_3$ is detected in the layer's thickness, and the formation of PbI_2 and degradation of $MAPbI_3$ stops**.

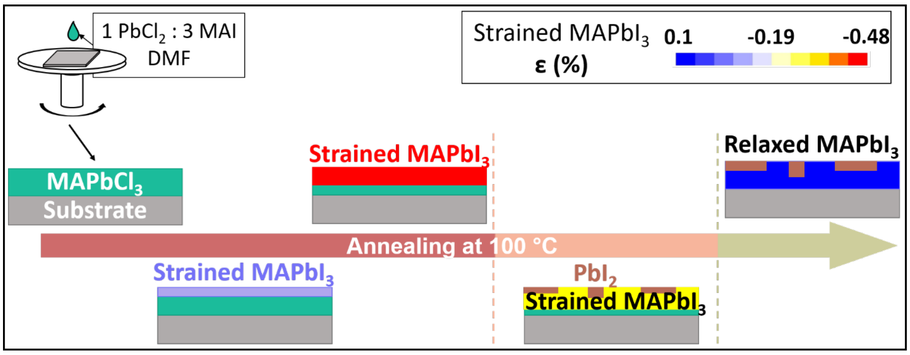

Figure 2.6: Schematic of the halide exchange mechanism identified.

2.3. DIRECT BRIDGE TO SOLAR CELLS APPLICATION

2.3.1. IMPACT OF ANNEALING TIME ON SOLAR CELLS PERFORMANCES

As explained in the beginning of this chapter, D.O. thin layers where developed at INES, where the annealing time was optimized to achieve the best devices in terms of efficiency and stability. Figure 2.7 reminds the typical RT microstructure of D.O. thin layers as used in solar cells. No PbI_2 diffraction peak and relatively low $MAPbCl_3$ peak intensity observed on these samples reveal that **the annealing is stopped at the end of the first stage of the ion exchange process, before the formation of PbI_2, indicating partial annealing of the sample when fabricating solar cell devices**.

The out-of-plane lattice parameters of this layer are calculated. As mentioned in the introduction of this part, these layers exhibit at RT double peak, which we attribute to a double texture [00l]/[hh0]. This phenomenon will be studied in details in the next chapter (chapter 3). For now, we take advantage of this double texture to calculate perpendicular lattice parameter of this layer, which are gathered in Table 2.1. As can be seen from comparison with the bulk material, these layers experience high perpendicular strain levels.

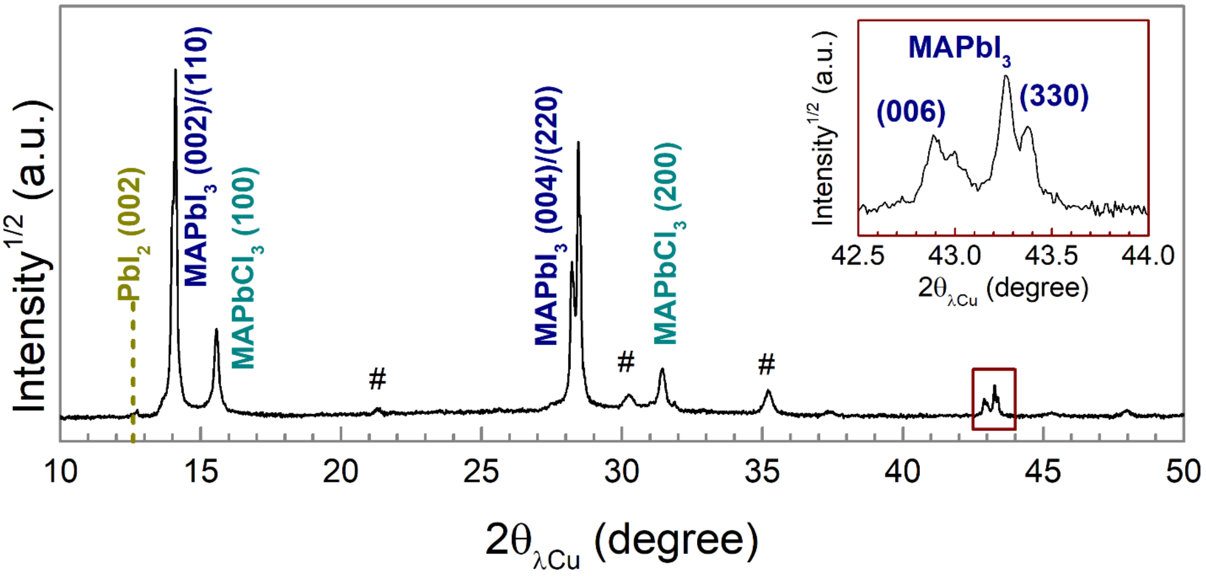

Figure 2.7: Typical $\theta/2\theta$ XRD pattern of a D.O. thin layer as used for solar cells making

	a_{perp} (Å)	c_{perp} (Å)
Bulk material	8.876(2)	12.667(1)
Partially annealed	8.859(5)	12.636(5)

Table 2.1: Lattice parameters of D.O. thin layers as used in solar cell compared to the bulk material lattice parameters

A question that naturally arises from this observation is whether any correlation can be found between the annealing time, and thus the ion exchange stage reached by the sample, the complex microstructure of the layers at RT after annealing and the device performances. Table 2.2 presents the evolution of the devices performances as a function of the annealing time of $MAPbI_3$ thin layers, obtained by the teams at INES on fresh cells and aged solar cells. After fabricating the glass/ITO/SnO_2/$MAPbI_3$ thin layers with different annealing times, a poly(triaryl amine) PTAA thin layer (hole-transport layer HTL) and a gold electrode were deposited to obtained the full perovskite solar cells. The aged devices were stored 500h in a glove box under inert atmosphere. More details about the solar cells fabrication and aging can be found in Pia Dally's thesis.[20]

Annealing time (T = 100°C)	25 min	35 min	45 min	60 min	90 min
PCE fresh cell (%)	8.4 ± 0.9	11.4 ± 0.5	11.3 ± 1.4	8.9 ± 1.2	6.5 ± 0.5
No. working cells/total no. of cells	4/5	8/8	7/8	8/15	4/8
PCE cells aged for 500h (%)	7.1 ± 1.5	10.7 ± 1	7.8 ± 1.7	N.E	N.E
*Δ*PCE (%)	- 15	- 6	- 31	N.E	N.E

Table 2.2: PCEs of solar cells obtained for various annealing times of the $MAPbI_3$ thin layers, for fresh cells and devices stored 500 h in a glove box under inert atmosphere. N.E. stands for Not Evaluated

It is quite interesting to observe that these results can be easily interpreted in the light of the mechanism highlighted earlier. We would like to point out that the absolute values of the annealing duration cannot be directly compared to the time scales observed during our *in-situ* experiment as the experimental set up was quite different. We can, however, perform a relevant qualitative comparison.

The maximal power conversion efficiencies of fresh cells were achieved for thin layers annealed 35 and 45 min. We have already highlighted that the optimal performances and stability are reached when the annealing is stopped before the beginning of the second stage, that is, before the formation of PbI_2, which correspond to 35 min annealing. Shorter or longer annealing times lead to lower efficiencies. In the former case, the annealing is stopped too early in the ion exchange process, and not enough $MAPbI_3$ is formed, whereas in the latter case (60 and 90 min annealing), the decomposition of $MAPbI_3$ into PbI_2 causes the poor efficiencies. The long term stability of the devices also seems impacted by the annealing times, as long annealing leads to a decrease of the PCE of 31 %, in opposition of the smaller loss of 6 % for 35 min annealed layer.

It is thus interesting to observe that the **presence of PbI_2 is more detrimental to the solar cells efficiencies than the high strain levels** experienced by $MAPbI_3$.

2.3.2. TEMPERATURE BEHAVIOR OF LAYERS OBTAINED THROUGH ION EXCHANGE

As mentioned earlier, $MAPbI_3$, which is tetragonal (I4/mcm) at RT, experiences a structural phase transition around 57 °C to a cubic Pm-3m structure. Working solar cells can be exposed to great temperature changes, between -40 and + 85 °C, and it is of high importance to know the impact of temperature cycling on the device, even more so if one of its components experiences a phase transition in temperature domain experienced by the device.

Hence, this paragraph is dedicated to the evolution of D.O. thin layers when exposed to increasing temperatures. This evolution is compared to the temperature of bulk $MAPbI_3$, used as a reference. For this study, $MAPbI_3$ powder was synthesized by solvent evaporation: stoichiometric amount of MAI: PbI_2 powder precursors were dissolved in GBL to obtain a 1 M solution. The solvent was evaporated at 100 °C and the obtained powder was ground. More details can be found in subsection 4.1.1.

Powder $MAPbI_3$ was refined at RT in a tetragonal I4/mcm symmetry, with lattice parameter of a = 8.876(2) Å and c = 12.667(1) Å, in good agreement with previous reports.[21] The relationship between the cubic and the tetragonal lattices is displayed in Figure 2.8.a, highlighting that the tetragonal a direction is defined as the cubic cell face diagonal. The tetragonal unit cell is doubled along the c direction with respect to the cubic cell. When describing the evolution of the lattice cell parameters across the cubic-tetragonal phase transition, it is usual to use the pseudo-cubic lattice parameters a^{T}_{pC} and c^{T}_{pC} for the tetragonal cell, which, based on the previous considerations, are calculated as follows:

$$a^T_{pC} = \frac{a^T}{\sqrt{2}} \quad and \quad c^T_{pC} = \frac{c^T}{2} \tag{2.5}$$

The temperature behavior of D.O. thin layers was investigated on one Panalytical X'pert diffractometer, which was equipped with a homemade heating plate, previously calibrated by our team. The experiment was performed under ambient atmosphere, and the sample were heated from RT to 100 °C. 12 min $\theta/2\theta$ measurements are performed for each temperature, after allowing 5 min to reach the thermal equilibrium. The result is displayed in Figure 2.8.b together with a comparison of the temperature-dependent evolution the bulk material.

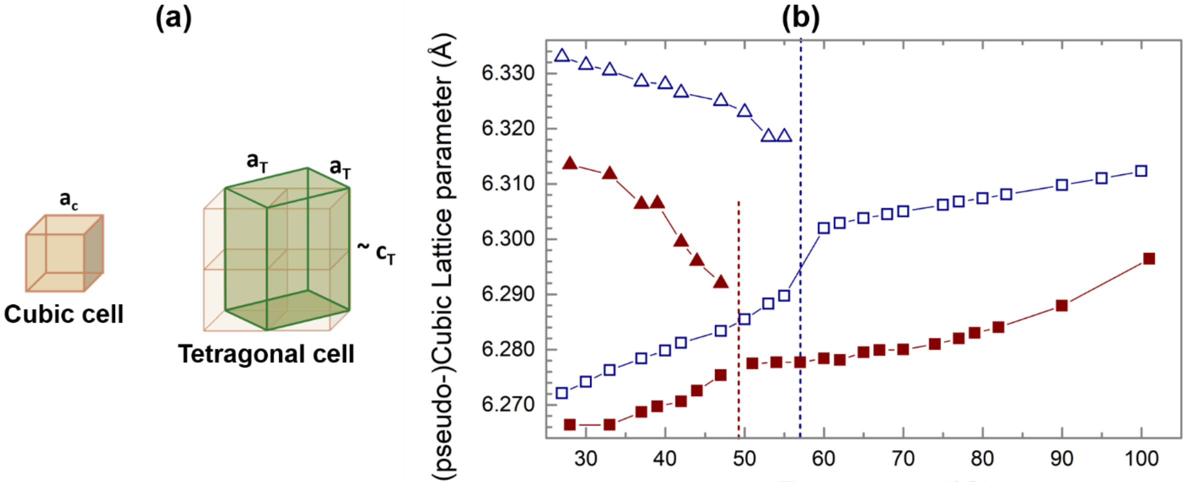

Figure 2.8: (a) $MAPbI_3$ cubic and tetragonal unit cells, highlighting the relationship between the two structures. (b) Evolution of $MAPbI_3$ lattice parameters upon heating in the tetragonal (below 57 °C) and cubic (above 57 °C) phases. (b) Temperature behavior of D.O. thin layers. The hollow symbols display the bulk material's lattice parameters while the plain colors symbols represent the thin layer's lattice parameter. Square and triangle symbols represent a and c lattice parameter, respectively. The blue and red dashed lines points the tetragonal-cubic transition temperature in the bulk and D.O. thin layers, respectively.

The experiment on D.O. thin layers revealed that the cubic-tetragonal phase transition happens around 49 °C, which is notably lower than the transition temperature of the bulk material (57 °C). This observation might be explained by the high compressive strain values observed on these layers earlier. Compressive strain is observed over the whole temperature range. As the sample's temperature was increased during this experiment, we observed the formation of PbI_2 indicating the degradation of the sample during the experiment. No evolution of the $MAPbCl_3$ peak area intensity was observed.

These results suggest that the high strain level experienced by these layers is responsible for a weaker long-term stability of the devices highlighted in the previous section.

2.4. About the impact of solution chemistry

As mentioned in the introduction of this part, different thin layers, prepared from the same precursors were studied. In opposition to D.O. thin layers, L.C. and H.C. thins layers were obtained from precursors solutions where $PbCl_2$ and MAI were dissolved simultaneously. D.O. precursors solution lead to instantaneous precipitation of a white powder which was identified as $MAPbCl_3$. However, interestingly, L.C. precursor solution, which has the same molar concentration as D.O. solution but different solubilization order, was clear at RT and not precipitation could be obtained through centrifugation.

In the case of H.C thin layers, the molar concentration of the precursors solution is doubled with respect to D.O and H.C. (1.6 and 0.8 M, respectively). Here, a turbid suspension was obtained at RT. In this case, the solution is not filtered prior to thin layer deposition but heated at 70 °C to achieve full dissolution.

In order to investigate the nature of the suspension formed in H.C. thin layers, we performed the same centrifugation as for D.O. solution. Two solutions were studied: one heated at 70 °C for 3h and left to cooled down to RT and one kept at RT, to observe if the heating process induces any changes. For both solutions, prolonged centrifugation did not allow to aggregate the suspension. Chlorobenzene, a perovskite anti-solvent used during the fabrication of H.C. and L.C. thin layers, is added to the precursors solution to favor precipitation. The XRD pattern of the two precipitates, shown in Figure 2.9, revealed the formation of the same weakly crystalline powder in both samples, with peak positions different from the ones expected for $MAPbCl_3$, $PbCl_2$, MAI or the crystallization intermediates identified in previous reports.[22,23,24] No other crystalline phase could be identified.

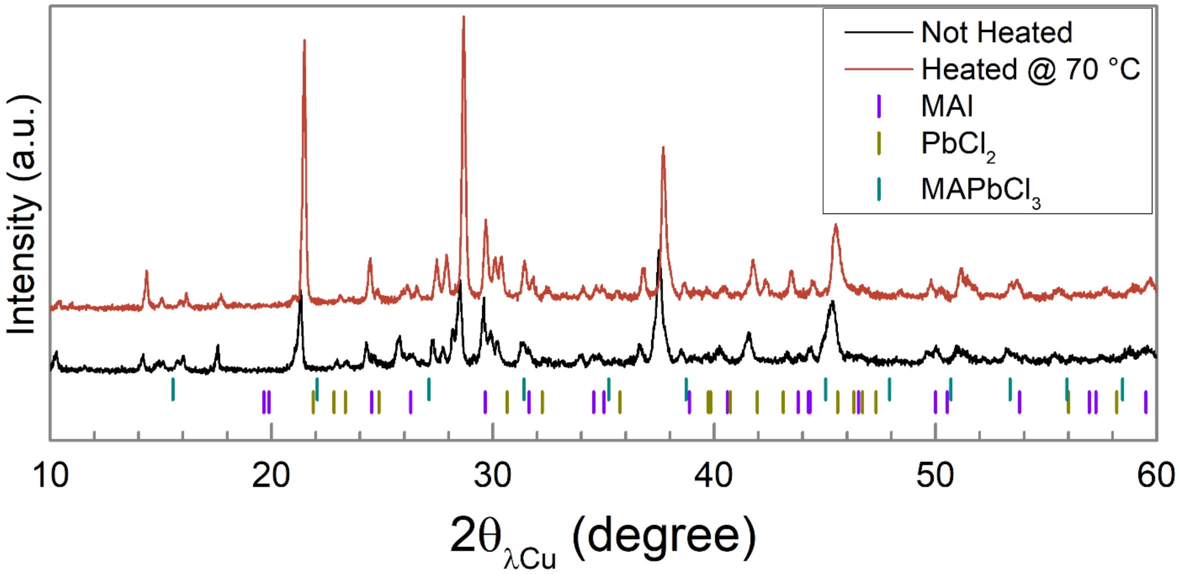

Figure 2.9: XRD pattern of the precipitate obtained after centrifugation of (a) H.C. precursor solutions.

This observation reveals that subtle changes in the synthesis such as the solubilization order can lead to very different solution chemistries. $PbCl_2$ is known to have a low solubility in DMF, but previous reports showed that this solubility can be strongly increased in the presence of MAI.[13] Our study, however, suggests an additional parameter to take into account: the solvation state of MAI. We demonstrated that pre-solubilization of MAI leads to the precipitation of $MAPbCl_3$ (D.O. precursors solution), while when dissolving MAI and $PbCl_2$ simultaneously in the solvant, no such precipitation is observed as full solubility is reached (L.C. solutions).

We showed here that the solution chemistry is highly impacted by what seems at first glance small parameters. Looking at the literature, where various precursors have been used (MACl as a chlorine source, or a PbI_2 – $PbCl_2$ mixture...), and where the solubilization conditions (order, stirring time and temperatures...) might differ from one report to another, one can easily understand that a large number of crystallization intermediates and paths can be identified, leading all to $MAPbI_3$ thin layers, with various microstructures.

2.5. CONCLUSION

This chapter was dedicated to the study of the mechanism of the crystallization of $MAPbI_3$ from $MAPbCl_3$ through ion exchange. At the time of this study, our results were the first proof of spontaneous formation of $MAPbCl_3$ suspension when mixing MAI and $PbCl_2$ precursors solution in DMF. Moreover, we demonstrated the important impact of the solublization order on the formation of this chlorine based-perovskite.

After demonstrating the presence of textured $MAPbCl_3$ phase in as-cast D.O. thin layers (before annealing), we performed an *in-situ* XRD study to investigate the mechanism of ion exchange. We demonstrated the formation of $MAPbI_3$ from $MAPbCl_3$ upon heating at 100 °C. However, the $MAPbI_3$ phase thus obtained is subjected to high strain levels, which eventually leads to its gradual degradation and the formation of PbI_2, a known degradation product of $MAPbI_3$. The formation of the latter is accompanied by a gradual relaxation of the strain and the complete disappearance of $MAPbCl_3$ leads to an abrupt strain relaxation of $MAPbI_3$ and stops its degradation into PbI_2. Moreover, we investigated the relative distribution of the different crystalline phases in the layer thickness, and we showed that the ionic exchange mechanism starts from the top part of the layer before propagating into its thickness.

Finally, this mechanism allowed us to correlate the perovskite layer annealing time and the devices performances and stability. We demonstrated that the presence of PbI_2 is more detrimental to the device efficiency than the high strain levels. However, studying the behavior of this samples upon temperature cycling revealed a decreased tetragonal-cubic phase transition temperature and weaker thermal stability.

References

[1] S. D. Stranks et al. “Electron-Hole Diffusion Lengths Exceeding 1 Micrometer in an Organometal Trihalide Perovskite Absorber”. en. In: *Science* 342.6156 (2013), pp. 341–344. DOI: `10.1126/science.1243982`.

[2] M. Bouchard et al. “Direct Evidence of Chlorine-Induced Preferential Crystalline Orientation in Methylammonium Lead Iodide Perovskites Grown on TiO_2”. en. In: *J. Phys. Chem. C* 121.14 (2017), pp. 7596–7602. DOI: `10.1021/acs.jpcc.6b11529`.

[3] A. Franz et al. “Determination of the miscibility gap in the solid solutions series of methylammonium lead iodide/chloride”. en. In: *Acta Crystallographica Section B* 74.5 (2018), pp. 445–449. DOI: `10.1107/S2052520618010764`.

[4] Y. Tidhar et al. “Crystallization of Methyl Ammonium Lead Halide Perovskites: Implications for Photovoltaic Applications”. en. In: *J. Am. Chem. Soc.* 136.38 (2014), pp. 13249–13256. DOI: `10.1021/ja505556s`.

[5] Q. Wang et al. “Transition from the Tetragonal to Cubic Phase of Organohalide Perovskite: The Role of Chlorine in Crystal Formation of $CH_3NH_3PbI_3$ on TiO_2 Substrates”. en. In: *J. Phys. Chem. Lett.* 6.21 (2015), pp. 4379–4384. DOI: `10.1021/acs.jpclett.5b01682`.

[6] D. Głowienka, T. Miruszewski, and J. Szmytkowski. “The domination of ionic conductivity in tetragonal phase of the organometal halide perovskite $CH_3NH_3PbI_{3-x}Cl_x$”. In: *Solid State Sciences* 82 (2018), pp. 19–23. DOI: `10.1016/j.solidstatesciences.2018.05.009`.

[7] X. Chen et al. “Characterization on crystal structure of $CH_3NH_3PbI_xCl_{3-x}$ perovskite by variable temperature powder X-ray diffraction”. In: *Materials Letters* 235 (2019), pp. 239–241. DOI: `10.1016/j.matlet.2018.09.151`.

[8] Q. Chen et al. “The optoelectronic role of chlorine in $CH_3NH_3PbI_3$(Cl)-based perovskite solar cells”. en. In: *Nature Communications* 6.1 (2015). DOI: `10.1038/ncomms8269`.

[9] K. Zhang et al. “Improve the crystallinity and morphology of perovskite films by suppressing the formation of intermediate phase of $CH_3NH_3PbCl_3$”. en. In: *Organic Electronics* 68 (2019), pp. 96–102. DOI: `10.1016/j.orgel.2019.01.044`.

[10] Hanadi Mehdi, Asya Mhamdi, and Abdelaziz Bouazizi. "Effect of perovskite precursor ratios and solvents volume on the efficiency of $MAPbI_{3-x}Cl_x$ mixed halide perovskite solar cells". en. In: *Materials Science in Semiconductor Processing* 109 (2020), p. 104915. DOI: `10.1016/j.mssp.2020.104915`.

[11] V. L. Pool et al. "Chlorine in $PbCl_2$ -Derived Hybrid-Perovskite Solar Absorbers". en. In: *Chem. Mater.* 27.21 (2015), pp. 7240–7243. DOI: `10.1021/acs.chemmater.5b03581`.

[12] E. L. Unger et al. "Chloride in Lead Chloride-Derived Organo-Metal Halides for Perovskite-Absorber Solar Cells". In: *Chem. Mater.* 26.24 (2014), pp. 7158–7165. DOI: `10.1021/cm503828b`.

[13] S. T. Williams et al. "Role of Chloride in the Morphological Evolution of Organo-Lead Halide Perovskite Thin Films". en. In: *ACS Nano* 8.10 (2014), pp. 10640–10654. DOI: `10.1021/nn5041922`.

[14] R. D. Shannon. "Revised effective ionic radii and systematic studies of interatomic distances in halides and chalcogenides". en. In: *Acta Cryst A* 32.5 (1976), pp. 751–767. DOI: `10.1107/S0567739476001551`.

[15] A. A. Medjahed et al. "Unraveling the Formation Mechanism and Ferroelastic Behavior of $MAPbI_3$ Perovskite Thin Films Prepared in the Presence of Chloride". en. In: *Chem. Mater.* 32.8 (2020), pp. 3346–3357. DOI: `10.1021/acs.chemmater.9b04239`.

[16] I.L. Ivanov et al. "Thermodynamics of formation of hybrid perovskite-type methylammonium lead halides". en. In: *The Journal of Chemical Thermodynamics* 116 (2018), pp. 253–258. DOI: `10.1016/j.jct.2017.09.026`.

[17] N. Pellet et al. "Transforming Hybrid Organic Inorganic Perovskites by Rapid Halide Exchange". en. In: *Chem. Mater.* 27.6 (2015), pp. 2181–2188. DOI: `10.1021/acs.chemmater.5b00281`.

[18] K. Chen et al. "Pseudomorphic Transformation of Organometal Halide Perovskite Using the Gaseous Hydrogen Halide Reaction". en. In: *Chem. Mater.* 28.15 (2016), pp. 5530–5537. DOI: `10.1021/acs.chemmater.6b02233`.

[19] Hee Joon Jung et al. "Stability of Halide Perovskite Solar Cell Devices: In Situ Observation of Oxygen Diffusion under Biasing". en. In: *Advanced Materials* 30.39 (2018), p. 1802769. DOI: `https://doi.org/10.1002/adma.201802769`.

[20] P. Dally. "Cellules Solaires à base de Pérovskites : De la caractérisation des matériaux à l'amélioration des rendements et de la stabilité". PhD thesis. 2019.

[21] P.S. Whitfield et al. "Structures, Phase Transitions and Tricritical Behavior of the Hybrid Perovskite Methyl Ammonium Lead Iodide". In: *Sci Rep* 6 (2016), p. 35685. DOI: `10.1038/srep35685`.

[22] K. H. Stone et al. "Transformation from crystalline precursor to perovskite in $PbCl_2$-derived $MAPbI_3$". en. In: *Nature Communications* 9.1 (2018), p. 3458. DOI: `10.1038/s41467-018-05937-4`.

[23] A. A. Petrov et al. “Crystal Structure of DMF-Intermediate Phases Uncovers the Link Between CH_3 NH_3PbI_3 Morphology and Precursor Stoichiometry”. en. In: *J. Phys. Chem. C* 121.38 (2017), pp. 20739–20743. DOI: `10.1021/acs.jpcc.7b08468`.

[24] D. P. Nenon et al. “Structural and chemical evolution of methylammonium lead halide perovskites during thermal processing from solution”. en. In: *Energy Environ. Sci.* 9.6 (2016), pp. 2072–2082. DOI: `10.1039/C6EE01047D`.

Chapter 3

Microstructure of $MAPbI_3$ thin layers: the role of ferroelasticity

The crystallization of $MAPbI_3$ thin films in presence of chlorine is now largely accepted to induce a preferential orientation of the grains along the [hh0] direction. However, the study of the microstructure of $MAPbI_3$ thin layers obtained through different protocols in the previous chapter revealed that some layers present a two-fold [00l]/[hh0] texture. Observed as well on some previous reports but not commented, this double texture is yet to be understood. Questions arise around the nature of this double texture and the conditions leading to its spontaneous formation in some layers while not in others.

This chapter presents our findings as we investigated and attempted to answer the above questions. We start by reviewing the different observations made concerning the apparition of the double texture on the different thin layers presented in the introduction of this part. After providing the definition of ferroelasticity, we demonstrate, using X-ray imaging at ESRF, that the [00l]/[hh0] texture is a manifestation of the ferroelastic twins in $MAPbI_3$ thin layers.

As they are cooled down from 100 °C to RT after synthesis, $MAPbI_3$ thin layers experience a ferroelastic cubic-tetragonal phase transition. Knowing that strain can drive the orientation of ferroelastic materials, we investigated the effect of the strain experienced by the cubic $MAPbI_3$ on the microstructure, to rationalize the dominant [hh0] texture. The notable mismtch between the large coefficients of thermal expansion of the halide perovskites and the substrate on which the films are deposited is considered as a possible origin of the stress. This is discussed for the different types of layers presented earlier.

Contents

3.1. OBSERVATION OF [00L] ORIENTED GRAINS

POLYCRYSTALLINE $MAPbI_3$ THIN LAYERS

So far, our work mainly focused on layers obtained from solutions in which chlorine-containing precursor was used ($PbCl_2$). We thus start this paragraph by inspecting the microstructure of thin layers where no chlorine was added. In the following, and for the sake of clarity, the thin layers obtained from precursor solutions free of $PbCl_2$ or containing the latter will be labelled $MAPbI_3$ and $MAPbI_3$(Cl), respectively, even though no Cl is incorporated into the structure.

As explained in the first chapter of this manuscript, when no chlorine is introduced in the precursors solution, polycrystalline thin layers with random orientation of the grains are obtained.[1] Typical θ-2θ diffractogram of such a thin layer is presented in Figure 3.1.a, displaying all the expected tetragonal I4/mcm $MAPbI_3$ Bragg peaks. Flat rocking curves are measured around (hh0) peaks, indicating no preferential orientation, unlike the diffractograms presented in the previous chapter. However, a close inspection of the θ-2θ pattern reveals an intriguing feature, highlighted in the inset of Figure 3.1.a: the (00l) diffraction lines are not observed. We performed LeBail refinement on this pattern which converged, leading to a good agreement between position of the calculated lines and the observed ones. The perpendicular lattice parameters were refined as a_{perp} = 8.872(2) Å and c_{perp} = 12.658(4) Å, slightly smaller than the values of the bulk material (a =

8.876(2) Å and c = 12.667(1) Å), indicating out-of-plane compressive strain, similarly to what Zhao *et al.* observed on their samples.[2]

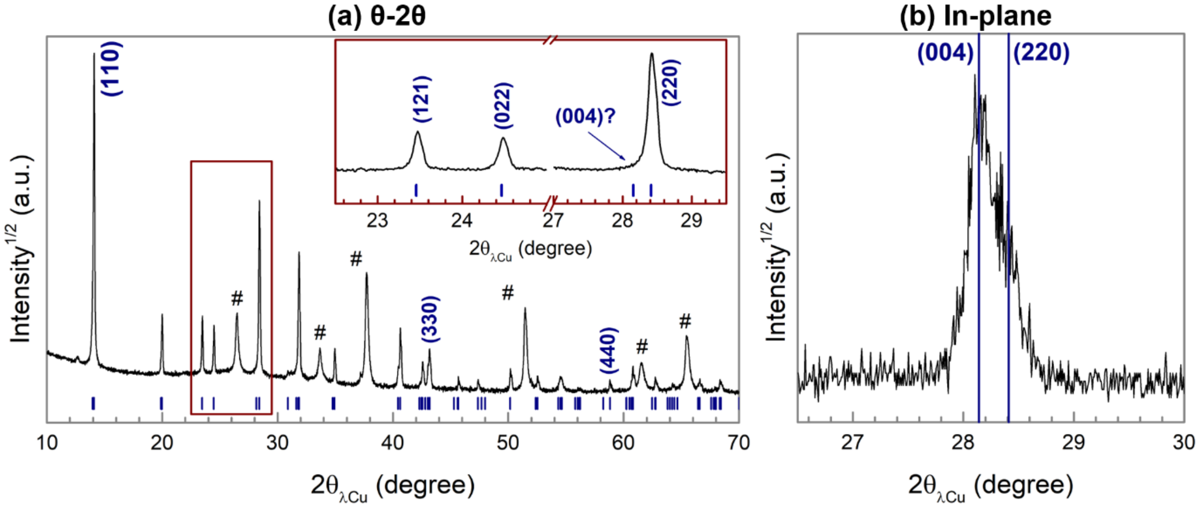

Figure 3.1: XRD pattern of $MAPbI_3$ thin layer obtained without chlorine. (a) θ-2θ pattern of the layer. The blue dashes point the expected peak positions for tetragonal I4/mcm $MAPbI_3$ thin layer; obtained from LeBail refinement of the pattern with a = 8.872(1) *Å* and c = 12.658(3) *Å*. An enlarged view of the pattern in the range $2\theta = 22 - 29$ ° is shown in the inset, highlighting the good agreement between the calculated and observed diffractions lines, as well as the absence of the (004) Bragg peak at its expected position. # symbol denotes the position of the Bragg peaks of the FTO/TiO_2 substrate. (b) In-plane diffraction pattern measured on the sample, with incident beam angle of $\omega = 0.35$ °, showing the presence of both (00l) and (hh0) lines. The continuous blue line marks the peak position expected for un-strain $MAPbI_3$ sample.

The refinement confirms the absence of (00l) peaks, as can be seen in the enlarged view of the diffraction pattern in Figure 3.1.a which points to the expected position for the (004) peaks. As a θ-2θ measurement only probes the direction perpendicular to the sample's plane, we performed in-plane measurements on $MAPbI_3$ thin layer to probe the direction parallel to the sample's surface. The (00l) peaks are observed in this diffractogram, shown in Figure 3.1.b. We reported the positions of the (004) and (220) peaks expected from an un-strained material (calculated from the bulk sample lattice parameters), however, the lesser resolution of in-plane measurements does not allow to make any meaningful conclusion about the in-plane strain state.

The surprising absence of the (00l) peaks from the out-of-plane measurements is systematic: we varied the substrate (FTO/TiO_2, ITO/SnO_2, Si/SiO_2) and the synthetic protocol (fast crystallization[3] or solvent engineering[4] methods), always resulting in thin layers where (00l) are not observed. **It indicates that when $MAPbI_3$, synthesized without chlorine, is deposited as a thin layer, the tetragonal c-axis oriented**

perpendicularly to the sample's plane is disfavored.

TEXTURED MAPbI$_3$(Cl) THIN LAYERS

As previously mentioned, when introducing chlorine in the precursors solution, a preferential orientation along [hh0] tetragonal MAPbI$_3$ direction is observed. A second texture direction along [00l] has also been observed on the different layers studied here. In the case of D.O. MAPbI$_3$(Cl) thin layers, as mentioned in chapter 2, the double texture [00l]/[hh0] is systematically observed at RT. However, concerning L.C. and H.C. thin layers, the apparition of the double peak is not systematic. Majority of the layers exhibit unique [hh0] texture, while some others randomly display the presence of the texture along [00l].

Table 3.1 summarizes typical perpendicular lattice parameters of the thin layers studied here. The high compressive strain level observed on D.O. layers was explained in the previous chapter as a consequence of its crystallization through ion exchange. Concerning the L.C and H.C thin layers, their lattice parameters are very close to the thin layers prepared without chlorine, indicating, here again, strain levels in good agreement with previous reported values in MAPbI$_3$ thin layers.[2] H.C and L.C thin layers exhibit very similar microstructures: close lattice parameters, same preferential orientation along [hh0] with possible, however rare, formation of [00l]-oriented grains. Hence, in the following, these two types of layers will be considered as equivalent while being differentiated from D.O thin layers.

	a_{perp} (Å)	c_{perp} (Å)
Bulk material	8.876(2)	12.667(1)
$MAPbI_3$ layer No Cl	8.872(2)	12.658(4)
$MAPbI_3$(Cl) L.C. [00l] and [hh0]	8.870(2)	12.640(2)
$MAPbI_3$(Cl) H.C. [hh0] only*	8.867(2)	-
$MAPbI_3$(Cl) H.C. [00l] and [hh0]*	8.876(4)	12.658(5)
$MAPbI_3$(Cl) D.O. [00l] and [hh0]	8.861(4)	12.628(4)

Table 3.1: Bulk material lattice parameters and perpendicular lattice parameters of the different thin layers studied: $MAPbI_3$ (no Cl in fabrication process) and $MAPbI_3$(Cl) obtained with the different protocols. The stars indicate that the lattice parameters displayed is the average lattice parameters obtained for all samples prepared (HC [hh0]-oriented only: 15 samples, HC [hh0] and [00l]-oriented: 6 samples), the error bar is the standard deviation from this average value.

An interesting feature was observed when studying the impact of temperature cycling on H.C. thin layers, as shown in Figure 3.2.

Starting from a sample with only [hh0]-oriented grains (inset of Figure 3.2.a), the evolution of the lattice parameters upon heating the sample is followed. As a comparison, the reference bulk sample lattice parameters are shown in open black symbols. The evolution displayed in Figure 3.2.a is rather different from what observed on the powder. After this heating ramp, the sample is left to cool down, without controlling the cooling ramp. RT XRD pattern of the same thin layer after this first heat treatment, shown in inset Figure 3.2.b, surprisingly revealed the formation of [00l]-oriented grains. A second heating ramp is performed on the sample, as shown in Figure 3.2.b., showing a behavior closer to the reference.

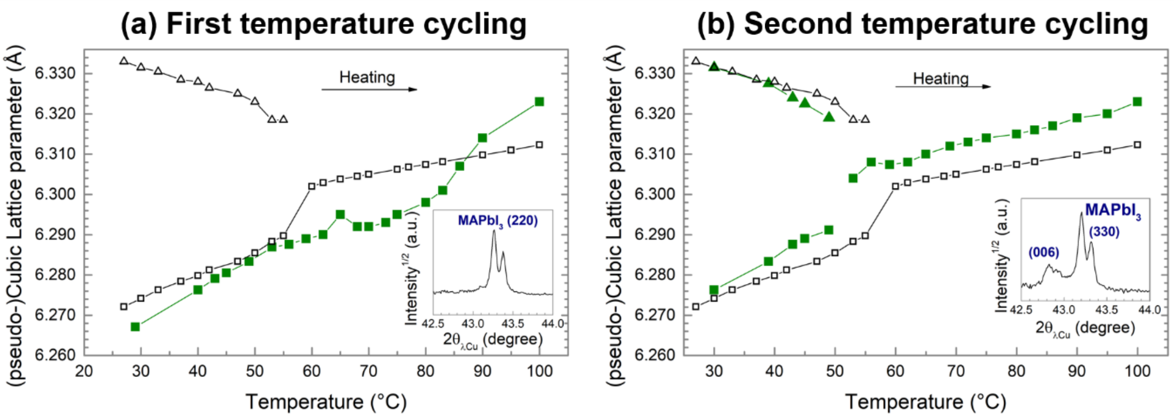

Figure 3.2: Temperature behavior of H.C. thin layers and its impact on their microstructure. (a) A first heating ramp is performed, starting from a sample exhibiting only [hh0]-oriented grains. (b) The inset shows the microstructure of the same layer, following a not-controlled cooling down from 100 °C after the previous temperature cycling (in panel (a)), highlighting the formation of a double texture [00l]/[hh0]. The main graph shows the temperature behavior of this sample after apparition of the [00l]-texture. In both panels, open black symbols indicate the lattice parameters of the bulk reference ($MAPbI_3$ powder) and full green symbols indicate the lattice parameters of the thin layers. The square and triangle symbols respectively indicate the a and c lattice parameter.

Such intriguing behavior was not systematically observed, however, it illustrates the dependance of the texture of H.C. $MAPbI_3(Cl)$ thin layers on their thermal history. Observing such modification of the grains orientation upon temperature cycling can be related to the ferroelastic character of the tetragonal-cubic phase transition of $MAPbI_3$ compound. In the following, we provide a general definition of ferroelasticity before relating this property to our problematic.

3.2. Ferroelastic twin domains in $MAPbI_3$

3.2.1. Ferroelasticity : definition

In 1969, Aizu introduced the concept of ferroelasticity and detailed the crystallographic symmetries that could lead to this property. Ferroelastic materials, very much like ferroelectrics or ferromagnets, present two or more equally stable states which can be switched through external stimuli. In the case of ferroelasticity, these states are twin domains, differing in terms of crystallographic orientation and the external stimuli is mechanical stress. The domains are not oriented randomly but are joined through domain walls, also called twin boundaries, which follow specific symmetry operations, known as twin law.

Figure 3.3 shows the formation of ferroelastic twin domains in an initially cubic structure. For clarity, only two directions are displayed in the figure. As the temperature is lowered, the sample experiences a phase transition to a tetragonal phase, and three (two in the scheme) elongation directions are possible, thus generating three (two in the scheme) thermodynamically and statistically equivalent domains. The observation of needle-like domains has been identified as a typical fingerprint of ferroelastic twins.[5]

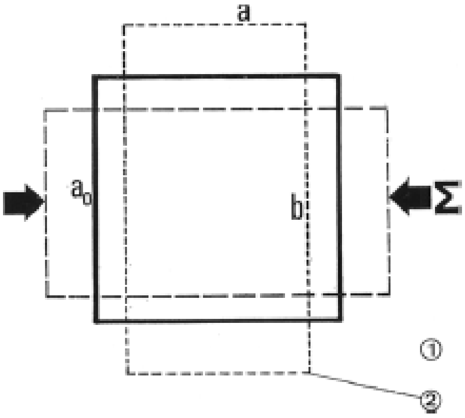

Figure 3.3: Schematic of two ferroelastic domains and ferroelasticity. When lowering the temperature, the high temperature cubic phase a0 experiences a phase transition to a tetragonal phase and three directions for the elongation are possible. Here, for clarity, only two are shown. If the elongation happens horizontally (vertically), orientation a (b) is obtained. Both states are energetically equivalent and ferroelasticity states that one orientation can be converted into the other through external mechanical strain. Adapted from.[6]

Contrary to usually static twins, ferroelastic twin walls are dynamic, evolving upon applying external mechanical stress to lower the system elastic energy. Hence, in the same fashion as for other ferroic properties, ferroelastic hysteresis stress - strain loops can be obtained.[5,6,7] A material can be purely ferroelastic ($SrTiO_3$), or combine both ferroelasticity and ferroelectricity ($BaTiO_3$ and $PbTiO_3$).[5] In the case of $MAPbI_3$, most of the samples are synthesized in the cubic phase (at around 100 °C) and subsequently cooled down to RT, thus experiencing a phase transition from cubic Pm-3m to tetragonal I4/mcm around 57 °C. In his classification, Aizu identified this phase transition as ferroelastic, making the observation of ferroelastic twin domains in $MAPbI_3$ possible.

3.2.2. FERROELASTICITY IN $MAPbI_3$

Polarized light microscopy images at RT of $MAPbI_3$ single crystal and thin layers revealed the existence of domains with different crystalline orientations, as shown in Figure 3.4.a.[8,9] Similarly, multiple TEM, SEM, AFM and PFM studies showed the existence of intragrains striped, needle-like structure of thin layers, as shown in Figure 3.4.b. Using Transmission Electron Microscopy (TEM) and Selected Area Electron Diffraction (SAED), Rothmann *et al.* demonstrated that these stripped structures arise from the existence, in the layer, of two twin domains,[10] which they attributed to the ferroelastic character of $MAPbI_3$.

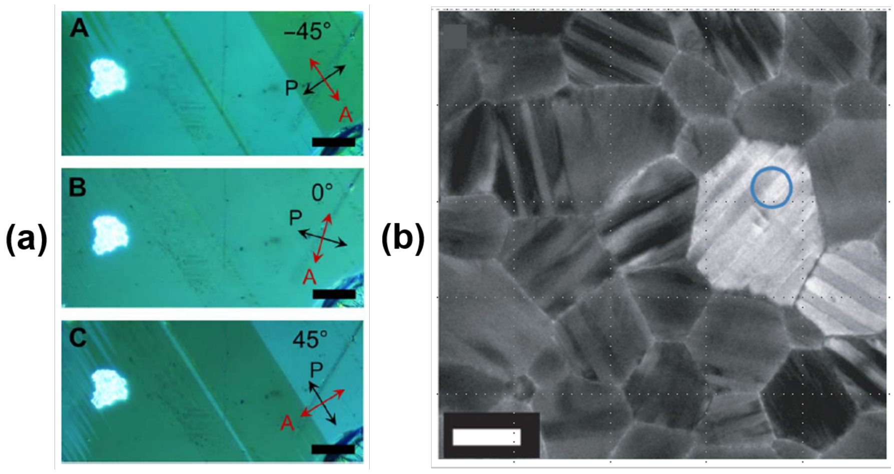

Figure 3.4: (a) Polarized light microscopy images of a $MAPbI_3$ single crystal, showing different orientation domains with the same crystal. Adapted from.[8] (b) TEM image of $MAPbI_3$ thin layers exhibiting striped structure inside grain boundaries. Adapted from.[10]

Strelcov *et al.* established the first ferroelastic hysteresis loop on $MAPbI_3$ thin layers by bending the sample with increasing bending radii, generating increasing stress. Compressive and tensile in-plane stress was achieved by concave or convex bending, respectively. The team followed, through polarized light microscopy, the evolution of the fraction of the area of the domains with different contrast and obtained an "indirect" ferroelastic hysteresis loop, thus confirming the ferroelastic nature of $MAPbI_3$. However, no information concerning the respective orientations of the domains were obtained.[8]

The twin formation is a consequence of the cubic-tetragonal phase transition experienced by the sample during its fabrication process. During such phase transition, the loss of the cubic three-fold axis generates three possibilities for the orientation of the tetragonal c-axis, thus leading to three possible domains (Figure 3.5.a). Rothmann *et al.* however observed only two twin domains, illustrated in Figure 3.5.b, for which the tetragonal c axis lies in the sample's plane.[10] This observation could be explained by the result shown in the previous section: polycrystalline $MAPbI_3$ thin layers do not exhibit grains with the tetragonal c axis perpendicular to the sample's plane. Rothmann *et al.*'s study was performed on mainly polycrystalline $MAPbI_3$ thin layers deposited without chlorine.[10] A classical θ-2θ XRD measurement probes only the direction perpendicular to the layer. Thus, the two twins identified by Rothmann *et al.* will both contribute to the (hh0) peaks (see the directions indicated by the axis in Figure 3.5.b) and cannot be distinguished by this technique. It is highly possible that they are present in our layers, and hence, both domains will be considered as equivalent in the following. The third variant, on the other hand, generates the (00l) peaks (Figure 3.5.c). Previous reports assumed the observation of the (00l) diffraction lines in XRD to be explained by the formation of the third variant in their thin layers.[11] However, it should be kept in mind that standard XRD measurements average the signal over a large sample area and can hardly evidence the presence of twins in such layer samples. To solve this question, we turned to X-ray imaging and used Full Field Diffraction X-ray Microscopy technique available at ESRF, which we present in the next paragraph.

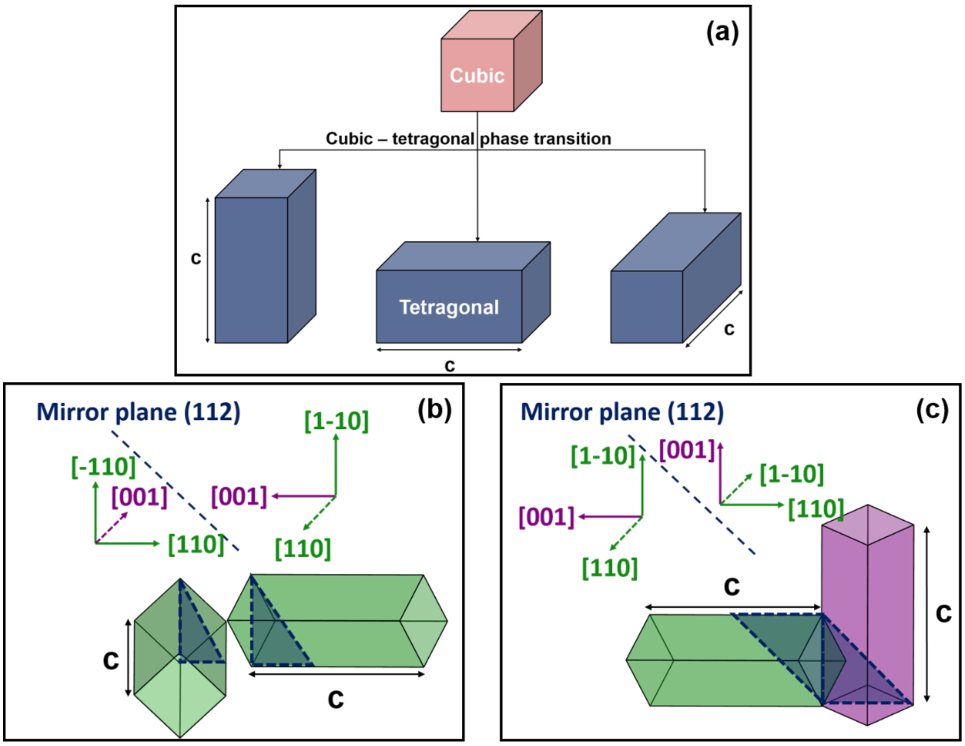

Figure 3.5: (a) Illustration of a cubic – tetragonal phase transition and the three possible directions for the elongation that generates the tetragonal c direction. (b). Schematic of the two twins identified by Rothmann *et al.* through TEM[10] and which would have the same signature in classical θ-2θ XRD measurements. (c) illustration of the third twin variant, following the same twin law, which was not reported by Rothmann *et al.* but which would lead to different XRD signatures. In (b) and (c), the twin plane is represented in blue.

3.2.3. FFDXM AT ESRF: IMAGING CRYSTALLOGRAPHIC DOMAINS USING X-RAYS

While classical X-ray scattering experiments offer high precision in the determination of the lattice parameters, the strain and the tilt of various crystalline samples, the information extracted are an average over the large probed area, and sample inhomogeneities are often hard to track using XRD. The ID01 beamline at ESRF combines high reciprocal space resolution offered by X-ray scattering, with the direct space resolution allowed by X-ray imaging. No specific sample preparation is needed and a large X-rays energy range is available. Moreover, different techniques are available on the beamline: in addition to classical grazing-incidence and small angle X-ray scattering, nano-diffraction mapping and coherent diffraction imaging are possible. We will focus, in the following, on the Full-Field Diffraction X-ray Microscopy technique (FFDXM) which can be viewed as the X-ray counterpart of dark field TEM..[12,13,14]

Figure 3.6.a shows the experimental set up of an FFDXM experiment. X-ray imaging lenses (Beryllium Compound Refractive Lenses – Be CRLs) are placed downstream of the sample, allowing to detect a magnified image of the scattered beam. Each pixel of the 2D detector measures the beam scattered at the same angle from different regions of the sample. A large field of view of 230 x 230 μm^2 is reached at 8 keV using the Be CRLs. The detection is insured by a camera (Andor sCMOS, 6.5 µm pixel size) mounted behind 15 µm of Gadox scintillator, placed inside a vacuum pipe where it can be freely translated, allowing to tune the lens - detector distance from 3.0 to 6.5 m. With a focal distance of 10 cm, a magnification ratio of 65x is reached when the detector is the furthest away from the sample, which in turn, corresponds to an effective pixel size of 100 nm.

In other words, **with only one acquisition, with the detector positioned at a given scattering angle value, a direct space image of 230 x 230 μm^2 of the sample is obtained, with signal arising only from the parts of the sample diffracting at the selected scattering angle, with a spatial resolution of 100 nm**. Practically, if one considers the example of a single crystalline sample, one can observe the defects on the sample in the direct space in one shot.

A 2D direct space micrograph is obtained for each image acquisition. The sample is vertically mounted on a motorized stage, which allows sample rotation in the horizontal plane. Combining the latter rotation with the circular motion of the vacuum pipe and thus the detector around the sample, all classical XRD thin layers measurements are possible: grazing-incident, θ-2θ and rocking scans (cf. Appendix B.4 for more details about the different measurement configurations). Here, a rocking θ or radial θ-2θ scan yields respectively spatially resolved lattice tilt or strain information within the illuminated area and Figure 3.6.b shows an example of a θ-2θ scan. A classical XRD diffractogram around the (004) and (220) $MAPbI_3$ reflections is reconstructed by integrating the per pixel intensities of each image. Figure 3.6.b shows the FFDXM image of one [00l] oriented and one [hh0] oriented grain, taken respectively at the peak of the (004) and the (220) $MAPbI_3$ reflections. These micrographs were measured in the same region of the sample, illustrating the direct space identification of grains presenting different crystallographic orientations.

The large field of view, the high resolution in direct space (100 nm) and in reciprocal space, combined with the quick acquisition time make this technique highly interesting for identifying the different crystallographic domains present in $MAPbI_3$ thin films and their distribution in the layer.

The experiments and the data treatment were performed in close collaboration with Dr. Tao Zhou, post-doctoral fellow at ESRF at the time of the experiment (May 2017 and April 2018), now working at Argonne, USA. During the experiments, we adapted the acquisition time to minimize sample degradation under X-ray beam. Cross correlation was used to match the images taken at different angles before the calculation of lattice strain and tilt.

In the following, we expose the results we obtained by combining laboratory XRD with different configurations and FFDXM to answer the questions around the double texture of $MAPbI_3$ thin layers.

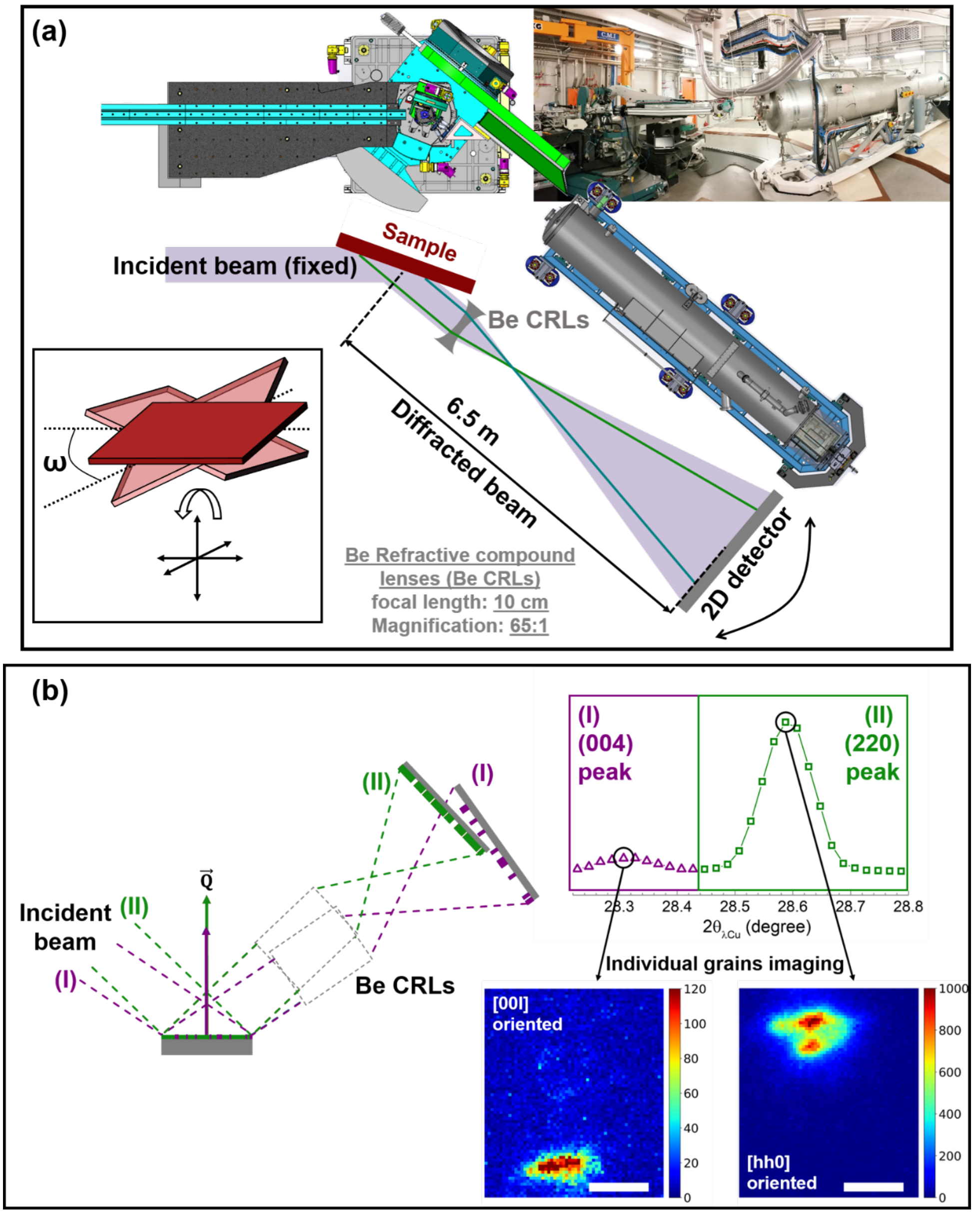

Figure 3.6: (a) Picture and schematic representation of the diffractometer at ID01 with the characteristic values of the FFXDM experiments we performed at 8 keV. The inset illustrates the translations and rotations directions possible on the motorized sample stage. (b) Illustration of the scattering geometry for a θ-2θ experiment using the FFXDM, and the resulting diffraction pattern. The two images are selected regions from the micrograph obtained at the designated angles on the figure, both taken on the same region of the sample and showing the diffraction contrast of this technique which allows to spatially differenciate grains with different orientations in the same sample. Scale bar : 2 µm.

3.2.4. PROVING THE TWIN NATURE OF THE DOUBLE ORIENTATION IN $MAPbI_3$

In the following, [hh0]-oriented crystals will be labeled A domains (or grains) and [00l]-oriented crystals C domains (or grains), as can be seen in Figure 3.7.

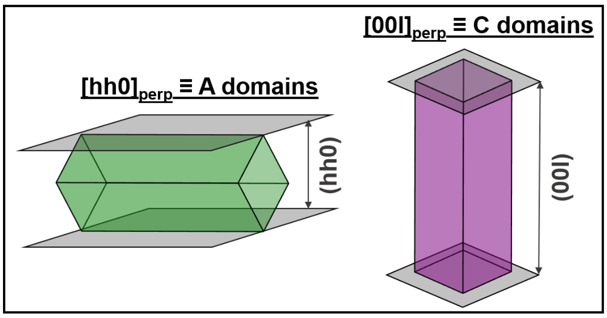

Figure 3.7: Schematic representation of A and C domains. Black surfaces help visualize the direction probed when performing θ-2θ measurements.

Based on diffraction contrast, samples presenting a high degree of preferential orientation allow to obtain more favorable signal/noise ratio on FFDXM micrographs. Previously, our team has shown that deposition of $MAPbI_3(Cl)$ thin layers on a single crystalline TiO_2 substrate enhances the preferential orientation.[1] Hence, for this study, $MAPbI_3(Cl)$ thin layers have been deposited on rutile TiO_2 (100) using the L.C. protocol. The laboratory θ-2θ pattern of the sample used for this experiment is shown in Figure 3.8.a, showing both A and C domains. Out-of-plane lattice parameters are summarized in Table 3.2.

	a_{perp}(Å)	c_{perp}(Å)
Layer of interest	8.870(2)	12.640(2)
Bulk material	8.876(2)	12.667(1)

Table 3.2: Perpendicular lattice parameters of the layer studied at ID01, compared with bulk sample lattice parameters.

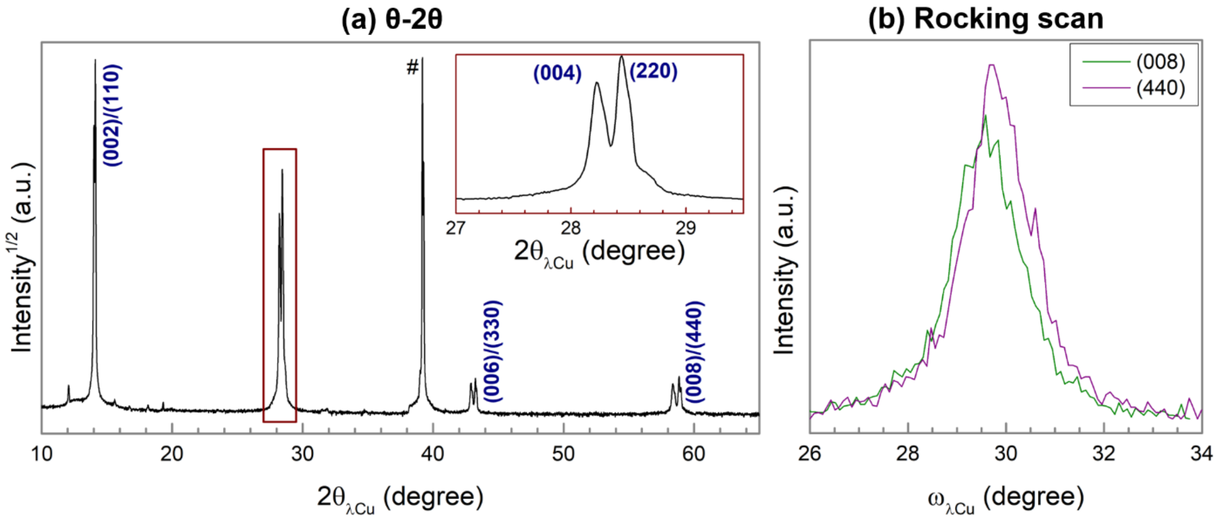

Figure 3.8: Laboratory characterization of the sample studied at ID01 : (a) θ-2θ pattern, (b) rocking curves measured at the (008) and (440) diffraction lines of $MAPbI_3$. # symbol points rutile TiO_2 (100) peak position.

Both A and C domains display a mosaicity of $\sim 2°$, as shown in Figure 3.8.b. Despite being smaller than the typical values obtained on classical substrates ($\sim$ 5 - 10 °), the tilt of the domains cannot be ignored. Hence, to obtain a complete description of both domains, we acquired FFDXM micrographs while performing 5 data points rocking scans around (004) and (220) peaks, to take into account grain tilt. Figure 3.9.a shows the measurement configuration, where the direction of the $\mathbf{Q}$ vector is varied and its amplitude fixed when measuring the mosaicity along each texture direction. The obtained rocking curves are displayed on the middle part of this figure. The right part shows two micrographs obtained when stacking the 5 micrographs measured on each domain, thus displaying all the C (top micrograph) and A (bottom micrograph) domains. It is hard to conclude anything from these micrographs, and thus, to extract the information desired, we drew a correlation map. The principle behind the correlation map is explained in Figure 3.9.b, with a simple case. In this example, the initial set of images is constituted of two groups, A and B, each containing 3 images, labelled from 1 to 3. All images are composed of four pixels. To obtain a cross-correlation map, all images of one group are compared to the images of the other group in pairs: 1A is compared to 1B, then to 2B . . . etc generating a 3x3 correlation map. The percentage of pixels at the same position displaying the same color is then reported on the correlation map for all the pairs, where a 0 value indicates completely different images (1A and 1B for example), and 0.5 value shows that half of the pixels of the two images of interest are similar (1A and 2B for example).

We applied this method to our rocking curve micrographs. The two images groups, corresponding to A and C domains contain each five micrographs measured during the rocking scans, generating a 5x5 correlation map. Each micrograph is constituted of 2560 x 2160 pixels; each pixel contains the diffracted intensity measured at the corresponding position. The obtained correlation map is displayed in Figure 3.9.c, showing the highest percentages along the diagonal, and decreasing values when moving away from it. It indicates that comparing grains with different tilting angles leads to poor spatial correlation, but the latter is maximal for grains with the same tilting angles. Independent grains would have resulted in low correlation coefficients for all the pairs, with different values randomly distributed on the correlation map. **These spatial and tilt correlations strongly indicate that the two A and C domains are twins inside a same grain**, within the resolution of the FFDXM ($\sim 100\,\mathrm{nm}$).

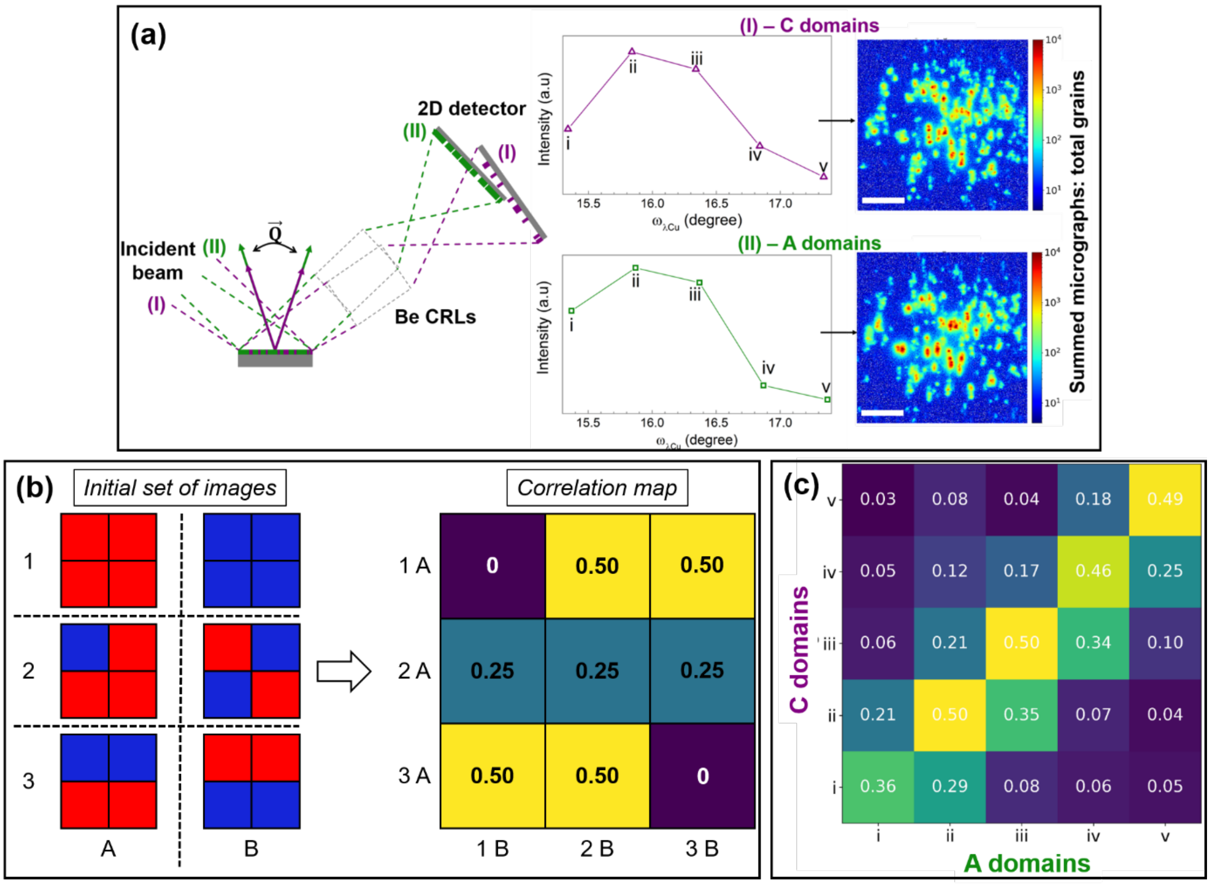

Figure 3.9: Rocking curve measurements with FFDXM at ID01. (a) Measurement configuration (left part), obtained rocking curves for both A and C domains (middle part) and resulting summed micrographs showing all A and C grains. White scale bar: 30 µm (b) Schematic explaining the procedure to obtain a correlation map. (c) Correlation map of A and C domains obtained from rocking curve measurements.

During this experiment, we had the opportunity to observe an expected but always surprising manifestation of ferroelasticity: domain switching. We preformed repetitive

θ-2θ scans in a same region of the sample, presenting both A and C domains. It is important to highlight that we optimized our measurement strategy to minimize the synchrotron beam-induced degradation of $MAPbI_3$ grains which starts for doses around 6E6 ph/μm^2. The spatial resolution allowed to follow the evolution of the inter-reticular distance under the beam for both domains individually. An adapted region of interest that ensures at least 90 % beam homogeneity was selected for data treatment. As scans are repeated, and thus the X-ray dose received by the sample increased, we note a sudden and abrupt change in C domains inter-reticular distance, as shown in Figure 3.10, and d becomes closer to the value characteristic values of A domains. Statistical analysis lead to observing this behavior in a number of individual domains, however, we never observed A domains transforming into C ones.

This result suggests ferroelastic switching of the domains under the 8 keV X-ray beam. We did not identify the detailed mechanism relating the photon absorption to the mechanical stress responsible for domain switching. Ion diffusion, which is well known in these systems, is most likely involved.

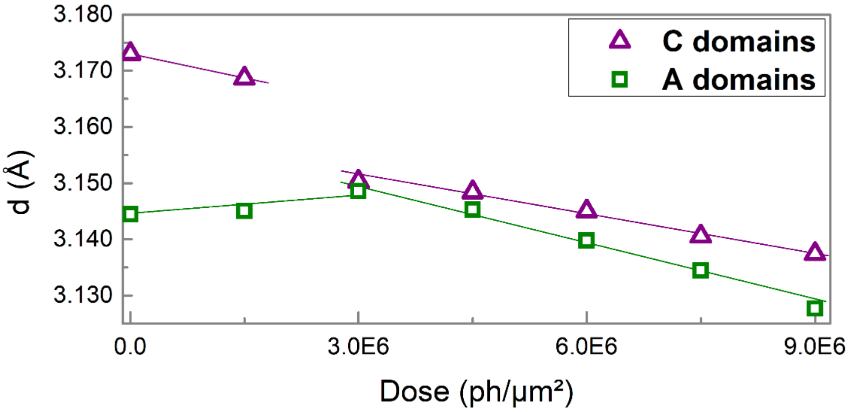

Figure 3.10: Evolution of the inter-reticular distance of initially A and C domains when exposed to increasing X-ray beam dose.

3.3. STRAIN IN THE CUBIC PHASE AND THE TWIN DOMAIN FORMATION AT RT

At this stage, we are left with one question: why are A domains favored to the detriment of C domains in $MAPbI_3$ thin layers? For this section, our study will focus only of H.C., L.C. $MAPbI_3(Cl)$ and $MAPbI_3$ thin layers. The case of D.O. thin layers will be discussed in the next section. As highlighted in section 3.1, the thin layers of interest exhibit lower strain values compared to D.O. thin layers. Similar values were reported in the literature[2] and the origin of this strain was explained by a large mismatch between the thermal expansion coefficient (CTE) of the perovskite and the substrate it was deposited on.

Hybrid halide perovskites are known to exhibit very large CTE's, and for example, $FAPbI_3$ and $FASnI_3$ (FA = formamidinium organic cation) exhibit the largest CTE values reported on any 3D crystalline solid near RT.[15] In the case of $MAPbI_3$, we evaluated the CTE from the temperature behavior of the powder sample used as a reference in Figure 3.2 and in the previous chapter. The volumetric α_V and linear thermal expansion coefficient α_a were obtained as follows:

$$\alpha_V = \frac{1}{V}\frac{\delta V}{\delta T} \quad and \quad \alpha_a = \frac{1}{a}\frac{\delta a}{\delta T} \tag{3.1}$$

The values, presented in Table 3.3, are close from the previously reported ones.[16] When put in perspective and compared with the reported volumetric CTE values for crystalline Si (0.08 x 10-4 K-1) or for $BaTiO_3$ (0.06 x 10-4 K-1), the values reported in Table 3.3 for the hybrid halide perovskite appear to be very large indeed.

	Tetragonal **a** direction Linear CTE $\alpha_\mathrm{a}^\mathrm{T}$ (@ 30 °C)	Tetragonal c direction Linear CTE $\alpha_\mathrm{c}^\mathrm{T}$ (@ 30 °C)	Cubic linear CTE $\alpha_\mathrm{L}^\mathrm{C}$ (@ 65 °C)	Cubic Volumetric CTE $\alpha_\mathrm{V}^\mathrm{C}$ (@ 65 °C)
CTE (K^{-1})	1.32×10^{-4}	-1.06×10^{-4}	0.40×10^{-4}	1.17×10^{-4}

Table 3.3: Volumetric and linear CTEs of $MAPbI_3$

All the thin layers were deposited on glass/FTO/TiO_2 or glass/ITO/SnO_2, and as shown in Figure 3.11, the substrate shows negligible peak shifting in comparison with $MAPbI_3$, in agreement with their respective CTE values ($\alpha_\mathrm{V} = 0.37 \times 10^{-5}\,K^{-1}$ and $\alpha_\mathrm{V} = 0.85 \times 10^{-5}\,K^{-1}$, for glass and ITO respectively). Considering the fact that $MAPbI_3$ thin layers are prepared at 100 °C before cooling down to RT, the large CTE mismatch between the perovskite and the substrate might induce strain in the layer during the cooling ramp, as reported by Zhao *et al.*.[2]

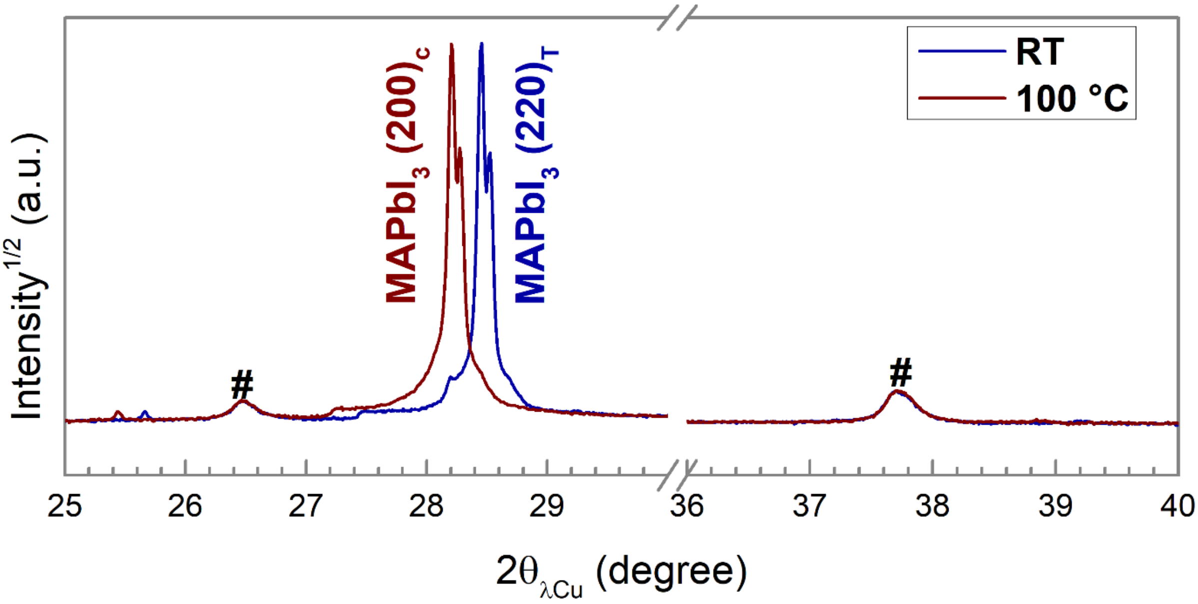

Figure 3.11: Illustration of the negligible expansion of the substrate (glass/FTO/TiO_2) between RT at 100 °C compared to $MAPbI_3$. The substrate peak positions are marked by the # symbol. Peak splitting is here due to $K_{\alpha1}$ and $K_{\alpha2}$ X-ray source wavelength.

To get a deper insight, we decided to follow the evolution of the layer lattice parameter upon cooling from 100 °C down to the tetragonal phase.

To do so, we heated, in our diffractometer, a H.C $MAPbI_3$(Cl) sample to 100 °C, and monitored through $\theta/2\theta$ measurements its perpendicular lattice parameter evolution as we controlled its cooling ramp. When RT was reached, the sample exhibited only A domains, with the tetragonal c axis lying in the sample's plane. The decrease of the perpendicular lattice parameter with the temperature is shown in Figure 3.12

The most relevant parameters to be considered in the case of strained layer on a substrate are the in-plane lattice parameters. To access these parameters, one could perform reciprocal space mapping of an asymmetric reflection or in-plane measurements (see appendix B.2). However, for our systems, because of the high mosaicity of the layers and the weak intensity resulting, these measurements do not allow the determination of the in-plane lattice parameters with the precision needed for these considerations. However, the in-plane lattice parameters can be calculated from the elastic constants of $MAPbI_3$ in the hypothesis of a bi-axial stress.

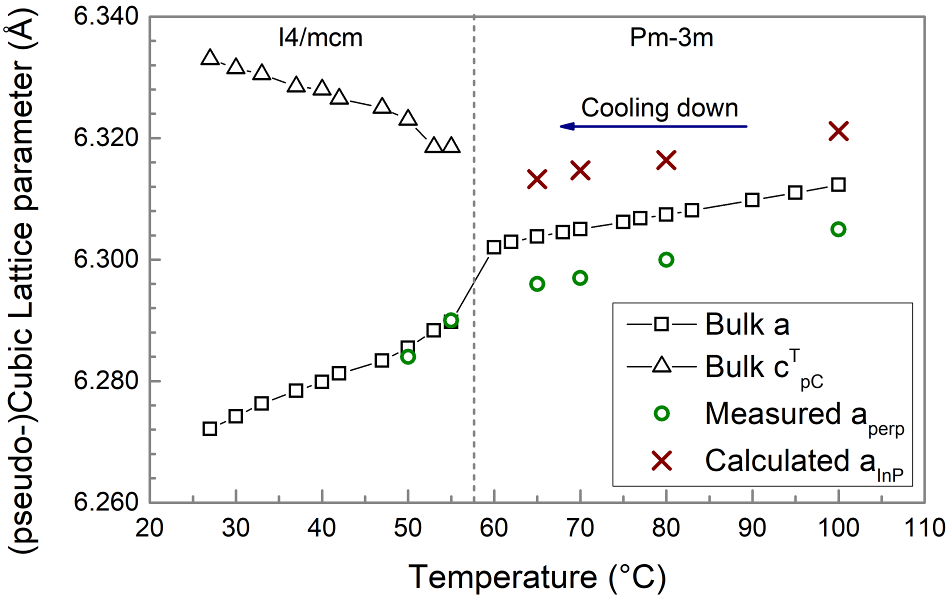

Figure 3.12: Evolution of the measured perpendicular and calculated in-plane lattice parameter during controlled cooling down from 100 °C. The open symbol points the lattice parameters of the un-strained, bulk reference sample.

The relationship between the strain and stress is defined by Hooke's law as :

$$\epsilon = \mathbf{S}\sigma \quad or \quad \sigma = \mathbf{C}\epsilon \tag{3.2}$$

Where ϵ and σ are the strain and stress tensors, respectively, which are mediated by the elastic stiffness tensor C or its inverse, the compliance **S**.

Assuming that the layer strain mainly arises from the interaction with the substrate, the stress applied by the substrate can be assimilated to a biaxial stress. For the cubic phase and for domains oriented along [100] direction, the relationship between the perpendicular and the in-plane strain can be expressed as follows:

$$\epsilon_{inP} = \frac{\epsilon_{perp}}{2s_{12}}(s_{11} + s_{12}) \tag{3.3}$$

Where s_{11} and s_{12} are the entries of the elastic compliance tensor. In 2014, Feng determined the elastic stiffness constants, using first principle calculations, for cubic, tetragonal and orthorhombic $MAPbI_3$ (and other MA-based halide perovskites).[17] For cubic $MAPbI_3$, these constants were later experimentally confirmed.[18]

ϵ_{perp} in equation Equation 3.3 is calculated from the perpendicular lattice parameter measured during the $\theta/2\theta$ measurements as follows:

$$\epsilon = \frac{a_{sample} - a_{bulk}}{a_{bulk}} \tag{3.4}$$

The calculated in-plane lattice parameters for different temperatures between 100 °C and the cubic-tetragonal phase transition are reported on Figure 3.12. The results revealed that the sample exhibits out-of-plane compressive strain at 100 °C, which translates into in-plane tensile strain. The strain level in this sample was found to be representative of the one observed in $MAPbI_3$ and $MAPbI_3$(Cl) H.C. and L.C. layers, and very likely associated to the high film/substrate CTE mismatch..[2] It is however worth underlining that the evolution of the layer lattice parameter between 100 °C and 60 °C is close to the one observed with bulk $MAPbI_3$.

As the sample is cooled down and approaches the cubic-tetragonal phase transition, the in-plane cubic lattice parameter is close to the value of un-strained tetragonal cT lattice parameter. This clearly favors the formation of A tetragonal domains, minimizing the strain experienced by the layer at RT, and consequently its elastic energy.

3.4. About thin layers obtained through ion exchange

Concerning now D.O. thin layers, we exhibited insection 3.1, the texture of these layers at RT reveals the following features:

1. Systematic observation of A and C domains.
2. **Out-of-plane θ-2θ measurements systematically revealed (00l) peaks to be broader than (hh0)**. Analysis of the FWHM of both domains reveals that while A domains exhibit perpendicular coherence length close to 300 nm, similar to the typical thin film thickness, C-domains have smaller coherence lengths of approximately 150 nm. This phenomenon was not observed on H.C. and L.C. thin layers, as for most of our samples, the FWHM of both (hh0) and (00l) were equivalent, indicating similar crystalline coherent lengths.

We thus decided to probe, in the laboratory, whether the A and C domains are homogeneously distributed in the layer. To do so, we performed several in-plane measurements on one sample with varying the incident beam angle to probe different depths: a higher penetration angle leads to a greater probed layer depth. When performing in-plane measurement, planes perpendicular the texture direction are observed. [hh0] oriented grains in the perpendicular direction will generate, amongst others, (hh0) and (00l) peaks in the in-plane direction, while [00l]-oriented grains generate only (hh0) peaks, as illustrated in Figure 3.13 and Table 3.4.

	θ-2θ contribution	In-plane contribution
A domain	(hh0)	(hh0) + (00l)
C domain	(00l)	2 (hh0)

Table 3.4: Contribution of each of A and C domains to (hh0) and (00l) peaks in both θ-2θ and in-plane measurements.

According to Table 3.4, a sample presenting only A domains should have equivalent in-plane (hh0) and (00l) peak areas; (004)/(220) peak area ratio would be ∼1. For samples with both A and C domains, (hh0) peak is expected to be more intense, as both domains contribute to this reflection while the (00l) peak intensity originates from A domains only, hence, (004)/(220) < 1 .

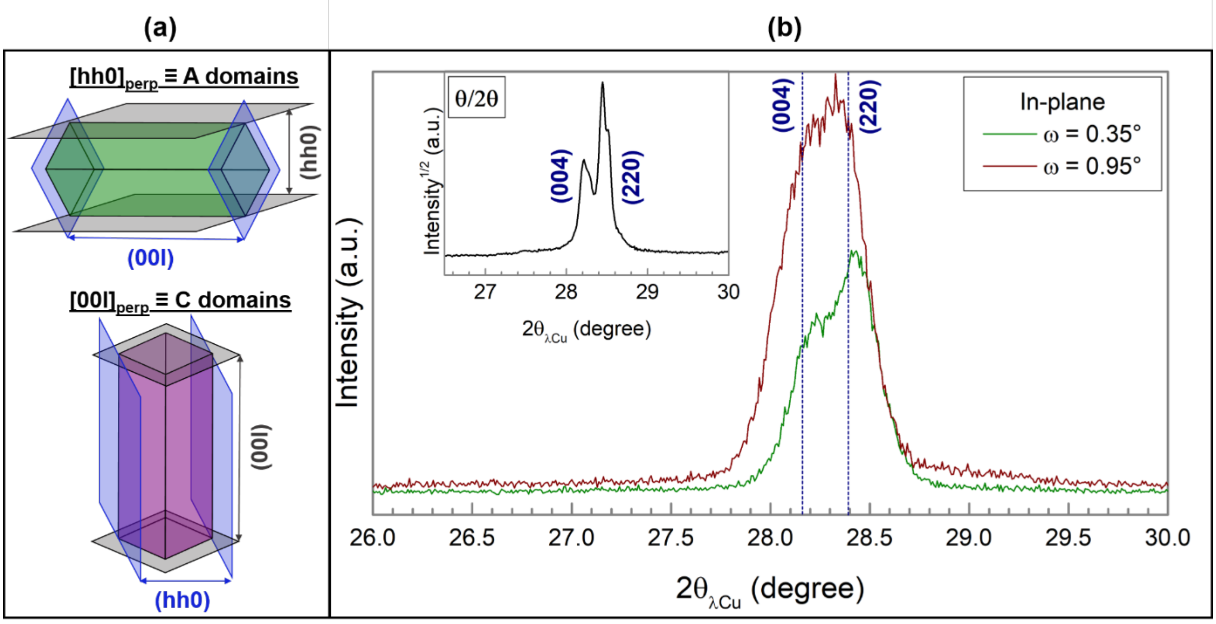

Figure 3.13: (a) Schematic representation of the orientation of the A and C domains. The black and blue surfaces help visualizing the direction probed during θ-2θ and in-plane measurements, respectively. For clarity, only one in-plane direction is displayed. (b) In plane pattern obtained on a layer exhibting both A and C domains, with varying the incident angle ω, thus varying the probed layer depth.

Probed depth (nm)	60 nm ($\omega = 0.35$ °)	160 nm ($\omega = 0.95$ °)
A domains only	1.1	1
A and C domains	0.6	1

Table 3.5: Evolution of the (004)/(220) peak areas ratio with the probed depth during in-plane measurements on sample exhibiting only A domains or both A and C domains.

Figure 3.13.b shows the result of these measurements for the lowest and highest incident angles measured and Table 3.5 gathers the probed depths corresponding to both incident angles as well as the (004)/(220) peak areas ratio calculated from both measurements. For comparison, the evolution of this ratio was evaluated on a sample exhibiting only A domains (H.C. thin layer). The choice of these angles and the procedure to calculate the corresponding penetration depths are explained in Appendix B.2.

When only A domains are present in the layer, the peak area ratio is around 1 and does not evolve between the two probed depths. However, for the sample where A and C domains coexist, the ratio varies when varying the incident angle. Probing the first 60 nm of the layers leads to a peak area ratio of 0.6, which clearly indicates the presence of C domains on this part of the layer. When probing deeper parts of the layer, the ratio increases and becomes closer to 1. **These observations clearly indicate that, for D.O. thin layers, the C domains occupy the top part of the layer, away from the $MAPbI_3$(Cl)/substrate interface, in good agreement with their smaller coherence lengths**.

In the case of the highly strained D.O. layers, film/substrate CTE mismatch does not drive the texture. The strain has been shown in chapter 1 to result from the $MAPbI_3$ formation mechanism in which the perovskite crystalline lattice is strongly distorted by the Cl-I ion exchange process. The presence of C domains in the upper part of the layer, thus on top of A domains, very likely allows to reduce the elastic energy accumulated in the distorted lattice.

3.5. Conclusions

The second chapter of this manuscript was dedicated to the study of the microstructure of $MAPbI_3$ thin layers and the dominant [hh0] texture.

Using FFDXM, an X-ray imaging technique available at ESRF, we demonstrated that [hh0]-oriented and [00l]-oriented grains are twin domains obeying the twin law defined in the literature. In the former, the tetragonal c axis lies in the sample's plane while this axis is perpendicular to the sample's plane in the latter. So far, it had not been proven that the $MAPbI_3$ / $MAPbI_3(Cl)$ thin layer texture observed in the XRD patterns was related to the presence of twins. Our experiments proved that A and C domains are twin domains by demonstrating their spatial and tilt correlation and we observed the switching of C-domains into A-ones.

$MAPbI_3$ thin layers are prepared at 100 °C, before being cooled down to RT. A large CTE mismatch is observed between the perovskite and its substrate. At high temperature, $MAPbI_3$ is cubic, and as its temperature is lowered, it experiences a ferroelastic phase transition to a tetragonal symmetry around 60 °C. By following the evolution of the measured out-of-plane lattice parameter as the sample is cooled down and assuming a biaxial stress resulting from the interaction with the substrate, we could explain the appearance of the [hh0] texture in the tetragonal phase, tensile in-plane strain of the cubic phase before phase transition favoring A domains.

Concerning the highly strained layers studied in chapter 2, we demonstrated that these latter domains form on the upper part of the film, away from the interface with the substrate, in opposition to the low strained layers where, when present, C domains are coherent over the whole layer thickness, as A ones. The formation of C domains allows to relax the high stress induced in the crystalline lattice by Cl-I ion exchange

References

[1] M. Bouchard et al. "Direct Evidence of Chlorine-Induced Preferential Crystalline Orientation in Methylammonium Lead Iodide Perovskites Grown on TiO_2". en. In: *J. Phys. Chem. C* 121.14 (2017), pp. 7596–7602. DOI: `10.1021/acs.jpcc.6b11529`.

[2] J. Zhao et al. "Strained hybrid perovskite thin films and their impact on the intrinsic stability of perovskite solar cells". en. In: *Sci. Adv.* 3.11 (2017), eaao5616. DOI: `10.1126/sciadv.aao5616`.

[3] M. Xiao et al. "A Fast Deposition-Crystallization Procedure for Highly Efficient Lead Iodide Perovskite Thin-Film Solar Cells". en. In: *Angew. Chem.* 126.37 (2014), pp. 10056–10061. DOI: `10.1002/ange.201405334`.

[4] N. J. Jeon et al. "Solvent engineering for high-performance inorganic–organic hybrid perovskite solar cells". en. In: *Nature Materials* 13.9 (2014), pp. 897–903. DOI: `10.1038/nmat4014`.

[5] E. K.H. Salje. "Ferroelastic Materials". en. In: *Annu. Rev. Mater. Res.* 42.1 (2012), pp. 265–283. DOI: `10.1146/annurev-matsci-070511-155022`.

[6] J.-C. Toledano. "La ferroélastictié". In: *Ann. Télécommun* 29.7-8 (1974). DOI: `doi.org/10.1007/BF02996935`.

[7] K. Aizu. "Possible Species of "Ferroelastic" Crystals and of Simultaneously Ferroelectric and Ferroelastic Crystals". In: *Journal of the Physical Society of Japan* 27.2 (1969), p. 1374. DOI: `10.1143/JPSJ.27.387`.

[8] E. Strelcov et al. "$CH_3NH_3PbI_3$ perovskites: Ferroelasticity revealed". en. In: *Sci. Adv.* 3.4 (2017), e1602165. DOI: `10.1126/sciadv.1602165`.

[9] B. Huang. "Ferroic domains regulate photocurrent in single-crystalline CH3NH3PbI3 films self-grown on FTO/TiO_2 substrate". en. In: *npj Quantum Materials* 3 (2018), p. 30. DOI: `10.1038/s41535-018-0104-5`.

[10] Mathias Uller Rothmann et al. "Direct observation of intrinsic twin domains in tetragonal CH3NH3PbI3". en. In: *Nature Communications* 8 (2017), p. 14547. DOI: `10.1038/ncomms14547`.

[11] R. M Kennard et al. “Ferroelastic Hysteresis in Thin Films of Methylammonium Lead Iodide”. en. In: *Chem. Mater.* 33.1 (2021), pp. 298–309. DOI: `10.1021/acs.chemmater.0c03776`.

[12] J. Hilhorst et al. “Full-field X-ray diffraction microscopy using polymeric compound refractive lenses”. In: *J. App. Cryst.* 47.6 (2014), pp. 1882–1888. DOI: `10.1107/S1600576714021256`.

[13] S. J. Leake et al. “The Nanodiffraction beamline ID01/ESRF: a microscope for imaging strain and structure”. en. In: *J. Synchrotron Rad.* 26.2 (2019), pp. 571–584. DOI: `https://doi.org/10.1107/S160057751900078X`.

[14] T. Zhou et al. “Lattice Tilt Mapping using Full Field Diffraction X-Ray Microscopy at ID01 ESRF”. en. In: *Microsc Microanal* 24.S2 (2018), pp. 128–129. DOI: `10.1017/S1431927618013028`.

[15] D. H. Fabini, R. Seshadri, and M. G. Kanatzidis. “The underappreciated lone pair in halide perovskites underpins their unusual properties”. en. In: *MRS bulletin* 45 (2020), pp. 467–477. DOI: `10.1557/mrs.2020.142`.

[16] T. J. Jacobsson et al. “Determination of Thermal Expansion Coefficients and Locating the Temperature-Induced Phase Transition in Methylammonium Lead Perovskites Using X-ray Diffraction”. In: *Inorg. Chem.* 54.22 (2015), pp. 10678–10685. DOI: `10.1021/acs.inorgchem.5b01481`.

[17] J Feng. “Mechanical properties of hybrid organic-inorganic $CH_3NH_3BX_3$ (B = Sn, Pb; X = Br, I) perovskites for solar cell absorbers”. en. In: *APL Materials* 2.8 (2014), p. 081801. DOI: `10.1063/1.4885256`.

[18] A. C. Ferreira et al. “Elastic Softness of Hybrid Lead Halide Perovskites”. en. In: *Phys. Rev. Lett.* 121.8 (2018), p. 085502. DOI: `10.1103/PhysRevLett.121.085502`.

Conclusion on the detailed study of $MAPbI_3$ thin layers

The first part of this thesis was dedicated to the study of $MAPbI_3$ thin layers.

The first chapter evidenced the role of the solubilization order on the crystallization intermediate of $MAPbI_3$ thin layers prepared in the presence of chlorine. We identified one crystallization path where $MAPbCl_3$ is the crystallization intermediate and $MAPbI_3$ is formed through ionic exchange upon annealing at 100 °C. We reported the detailed mechanism of this ion exchange, highlighting the high strain levels induced by this mechanism, due to the large lattice parameter difference of $MAPbI_3$ and $MAPbCl_3$ and the absence of formation of $MAPb(I_{1-x}Cl_x)_3$ solid solutions. Moreover, we demonstrated the impact of the annealing time, and thus the ion exchange stage reached by the sample, on the efficiency and the stability of the solar cells devices.

The second chapter was dedicated to the study of the microstructure of these thin layers. We demonstrated that the double texture [hh0]/[00l] observed on some $MAPbI_3(Cl)$ thin layers is due to the presence of ferroelastic twins in the layer. This chapter focuses on samples obtained through a different crystallization path that the one presented in the first chapter. These layers experience lower strain levels, likely induced by the high CTE mismatch between the perovskite layer and its substrate.

Part II

Impact of ion mixing on the hybrid halide perovskite structure

General context of the study and motivations

First hybrid halide material to be used as an active layer in solar cells, $MAPbI_3$ quickly revealed its weaknesses (thermodynamic unstability, structural phase transition near the temperature reached by devices in function…). The promises held by the hybrid halide perovskite compounds led the research teams to develop new systems that would preserve the impressive optoelectronic properties of $MAPbI_3$ while showing enhanced stability. Different approaches where developed, such as mixing 3D with 2D materials inside the devices, or through compositional engineering.

We focused our efforts in this last direction. Earlier reports showed a spectacular enhancement of the solar cells stability when using complex material such as $Cs_{z'}Rb_zFA_{1-y}MA_yPb(I_{1-x}Br_x)_3$ (see chapter 1 for more details). However, phase segregation and inhomogeneities in the distribution of the different components lead the community to favor the use of simpler systems. At the time of this PhD, the most popular systems are $FA_{1-x}MA_xPb(I_{1-y}Br_y)_3$ and $Cs_zFA_{1-z}Pb(I_{1-x}Br_x)_3$. In both cases, both A and X perovskite sites are occupied by two different ions, making the materials still rather complex. A number of fundamental studies are being conducted on these systems, but most of them performed on thin layers, investigating the film composition inhomogeneities and its impacts on the local structural properties. Moreover, most of these studies are performed on the 5-components systems, making hard to disentangle the impact of the different sites on the material properties. While the inorganic cage is known to have a predominant role in the intrinsic properties of the compounds (electronic and main crystallographic features), the role of the organic cation cannot be ignored.

In our team, solar cell devices with high efficiencies (maximum PCE of 21.75 %) and satisfying long-term stability (un-capsulated devices retained $\sim$ 90 % of their stability after 90 days under argon atmosphere) where fabricated, incorporating a mixed-ions perovskite layer: $FA_{0.85}MA_{0.15}Pb(I_{0.85}Br_{0.15})_3$. With the goal of understanding the role of each substitution on the intrinsic properties of this final compounds, we decided to substitute one ion at a time (either the organic cation or the halogen) in pure compounds. Thus, we studied three families of solid solutions: we gradually substituted the iodide in $MAPbI_3$ and $FAPbI_3$ by bromide, leading to the two families $MAPb(I_{1-x}Br_x)_3$ and $FAPb(I_{1-x}Br_x)_3$ and we replaced FA^+ by increasing amounts of MA^+ in the $FA_{1-x}MA_xPbI_3$ family. We present this study in two chapters: the first one (chapter 4) exposes the synthetic strategy we used to obtain our samples as well as the study of their structural properties at room temperature. In the second chapter (chapter 5), we conducted temperature-dependent XRD measurements on the obtained solid solutions and established their temperature-composition phase diagrams. Finally, and in each chapter, the structural properties of $FA_{0.85}MA_{0.15}Pb(I_{0.85}Br_{0.15})_3$ were investigated in light of our findings on the quaternary compounds.

Chapter 4

Intrinsic properties of mixed ions perovskites at room temperature

In this chapter, we present a detailed study of different hybrid halide perovskite solid solutions at RT. After considering the formability of the different families from the geometrical point of view, we briefly present the synthesis method we developed to fabricate our samples. We then take some time to inspect the four end compounds: $\mathrm{MAPbI_3}$, $\mathrm{FAPbI_3}$, $\mathrm{MAPbBr_3}$ and $\mathrm{FAPbBr_3}$ revealing some intrinsic structural features of each compound and comparing them. Thereafter, and keeping in mind what we learned from the end compounds, we start the study of the 3 families of solid solutions $\mathrm{MAPb(I_{1-x}Br_x)_3}$, $\mathrm{FAPb(I_{1-x}Br_x)_3}$ and $\mathrm{FA_{1-x}MA_xPbI_3}$.

As $\mathrm{FAPbI_3}$ is known to form a stable hexagonal phase at RT, we performed a systematic study on the FA-based compounds on the stabilization of the α-cubic phase against polymorphism and we compared the effect of each site on this phenomenon. Furthermore, we inspected the lattice parameter, intrinsic strain and the band gap evolution upon ion substitution for each family.

Finally, based on our results and the literature, we conduct a critical comparison of all three solid solutions, discussing the advantages and drawbacks of each substitution. The room temperature intrinsic structural and optical properties of a 5-components compounds, used for photovoltaic applications, will be inspected and discussed in light of the results obtained from the quaternary materials..

Contents

4.1. COMPOUNDS FORMABILITY AND GENERAL SYNTHETIC PATH

Explained in the first chapter of this thesis, two geometrical factors, based on the radii of the ions composing the material of interest, are widely used to predict the stability of a 3D perovskite network. Equations 1 and 2 define tolerance factor t and the octahedral factor μ, respectively.

$$t = \frac{r_A + r_X}{\sqrt{2}(r_B + r_X)} \tag{4.1}$$

$$\mu = \frac{r_B}{r_X} \tag{4.2}$$

Where r_A, r_B and r_X are the ionic radii of the species occupying, respectively, the A, B and X sites of the ABX_3 perovskite structure. Despite being necessary, these two factors are not solely sufficient to explain the non-perovskite structure of some compounds (such as $AgBiO_3$[1]). The stability domain of inorganic oxide perovskite was empirically defined as $0.75 < t < 1$ and $0.41 < \mu < 0.73$, allowing to predict the stability of a large number of compounds.[2] In these systems, cubic lattices are obtained when t = 1. Smaller t value leads to octahedral tilting and thus tetragonal or orthorhombic cells whereas tolerance factors higher than 1 induce the formation of hexagonal crystals with various polymorphs. In 2008, by extending the systematic stability study to halide perovskites, Li et al redefined the formability region for these promising compounds to be slightly different: $0.81 < t < 1.11$ and $0.44 < \mu < 0.90$, enabling to include 96% of the studied systems in this domain.[3]

For our study, where ions are gradually replaced by others with different sizes in the structure, we evaluated the evolution of the two factors upon ion substitution for the three families we planned to study. Effective radii of the organic molecular cation were taken from Kieslich *et al.*[4] and inorganic ionic radii from Shannon *et al.*.[5] The values are gathered in Table 4.1 and the evolution of the calculated tolerance factor is shown in Figure 4.1. Concerning the octahedral factor, as it only depends on the radii of the ions in B and X sites, it remains unchanged in the $FA_{1-x}MA_xPbI_3$ family. For the same Br^- contents, µ evolves identically in both $FAPb(I_{1-x}Br_x)_3$ and $MAPb(I_{1-x}Br_x)_3$ families, monotonously increasing from 0.541 (0% Br^-) to 0.607 (100 % Br^-), remaining in the formability region cited earlier.

	Pb^{2+}[5]	I^-[5]	Br^-[5]	MA^+[4]	FA^+[4]
Ionic radii (pm)	119	220	196	216	253

Table 4.1: Ionic radii of the ions constituting the perovskites compounds of interest.

For x values of 0 and 1, the tolerance factor of end compounds can be red in Figure 4.1. One observes that all four end compounds fall in the stability range defined earlier by Li *et al.* for halide compounds.[3] In the case of $FAPbI_3$, as mentioned in the first chapter, the perovskite phase is not stable at RT, a hexagonal structure being thermodynamically favored over the cubic structure. All published reports about this polymorphism attribute this behavior the large ion radii of FA^+ which leads to a high tolerance factor. The black dotted line in Figure 4.1 represent the limit of $t = 1$ defined as the stability condition of the cubic structure in the case of inorganic oxide perovskites. $FAPbI_3$ falls under this limit when using Shannon ionic radii reported in Table 4.1. Moreover, the calculated tolerance factor for $FAPbBr_3$ is higher than 1 and one would expect the formation of hexagonal polymorph for this compound. No reports of such structure have been published, and $FAPbBr_3$ is stable in a cubic structure at RT. Moreover, studies have been performed on $FAPbCl_3$ compounds, where smaller Cl^- ion leads to even larger t factor, but here again, no hexagonal polymorph was reported.[6]

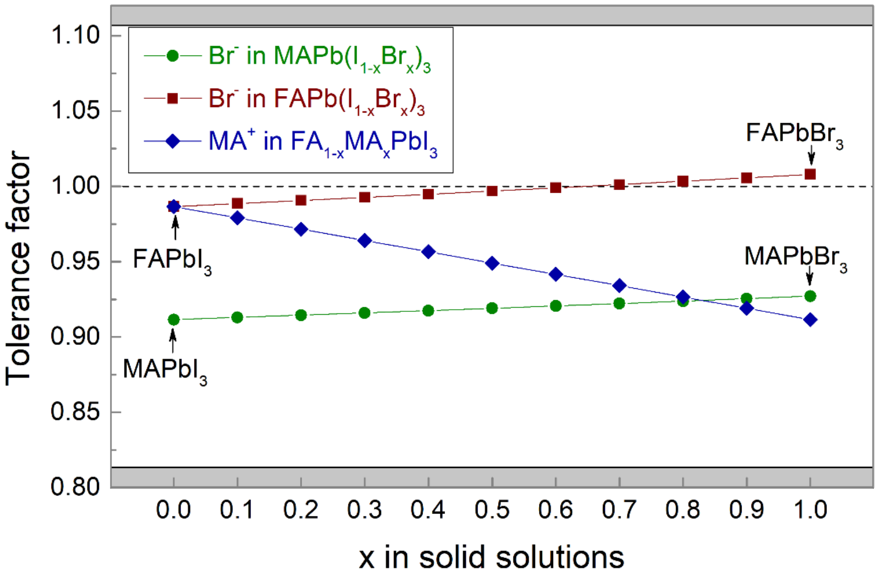

Figure 4.1: Tolerance factor as a function of inserted ions in the perovskite structure: % of Bromine in $MAPb(I_{1-x}Br_x)_3$ and $FAPb(I_{1-x}Br_x)_3$ families and % MA in $FA_{1-x}MA_xPbI_3$ family. The grey regions correspond to the non-formability region defined by Li *et al.*[3] and the dotted black line is positioned at $t = 1$ to help visualize the stability limit defined for inorganic oxide compounds.

The tolerance factor concept seems to fail to predict the stability of FA-based compounds. Travis *et al.* highlighted that the approximation of hard, unpolarizable spheres is less valid in the case of halide perovskites because of the lower electronegativity and greater chemical softness of halides. To address this problem, the group reevaluated the ionic radii of the B ions depending on the halide it is bonded to in the perovskite structure. Three different ionic radii where thus defined for Pb^{2+}, according to the halide of the perovskite structure (Pb^{2+} in Pb-I: 103 pm and in Pb-Br: 98 pm).[7] Using these values, the tolerance factor calculated for $FAPbI_3$ and $FAPbBr_3$ are, respectively, 1.03 and 1.07, both still above the limit set for oxide compounds and below the one defined of halides. Moreover, $FAPbBr_3$ exhibits, here again, a higher t value than $FAPbI_3$, contradicting once more with the structural arrangements expected from the geometrical point of view. The molecular organic cation being non-spherical, the definition of the effective radii of the organic cation can be challenging.[7] Gholipour *et al.* recently introduced the molecular globularity, defined as the ratio of the real molecular surface to the surface of a sphere of an equivalent volume.[8] However, this formalism did not allow to rationalize the behavior of $FAPbI_3$ and $FAPbBr_3$ as the factor they defined cannot be assimilated to an ionic radii in the calculation of the tolerance factor and they arbitrarily set the value for the tolerance factor of $FAPbI_3$ to 1. Still in the quest to obtain better predictions on the formability of perovskite materials, Bartel *et al.* revisited the definition of the tolerance factor using a systematic approach to screen and correlate a gigantic number of data and extract a predictive model (in the vein of the data science discipline).[9] Despite the enhanced match found between the predicted halide perovskite structural stability and the experimental data, the new tolerance factor calculated for both $FAPbI_3$ and $FAPbBr_3$ still falls in the stability region predicted by their model.

Hence, the geometrical considerations (tolerance factor) classically used for predicting the stability of cubic inorganic perovskite fails to explain the stable hexagonal and cubic structures of $FAPbI_3$ and $FAPbBr_3$ respectively, at RT. Additional consideration might be needed and will be addressed in subsection 4.2.1.

Concerning the mixed compounds, as shown in Figure 4.1, the tolerance factor are intermediate values between the pure compounds. We observe, that Br^- introduction have less impact on the tolerance factor value than MA^+ introduction.

4.1.1. Developed synthetic protocol

As the following study is focused on the intrinsic properties of the materials, we chose to synthesize and work on powder samples for all materials. Even though ion migration is particularly easy in these compounds,[10] which would make possible a solid state synthesis, we chose to use the liquid-phase approach to minimize the reaction time and temperature.

Figure 4.2 shows the difference steps for the synthesis of our samples. Precursor powders (nature and quantities are detailed in appendix A.2) are dissolved in a solvent and left to stir. The choice of the solvent is of particular importance. A few good solvents are known and used for making hybrid halide perovskites: DMF (dimethylformamide), DMSO (dimethyl sulfoxide), GBL (γ-butyrolactone), NMP (N-Methyl-2-pyrrolidone). Surprisingly, when studying pure compounds with MA^+ or FA^+ cations in the perovskite A site, Saidaminov *et al.* have shown unexpected behaviors of the perovskites in some solvents: a retrograde solubility in GBL for iodine-based materials and in DMF for bromine-based compounds.[11] In other words, when increasing the temperature of a solution containing for example $MAPbI_3$ dissolved in GBL, instead of increasing (as generally observed), the solubility decreases, leading to precipitation of $MAPbI_3$ at high temperature. No effect of the organic cation has been noted. This property has allowed researchers to obtain large single crystals in record times. When synthesizing powders of compounds with mixed halogens ($MAPb(I_{1-x}Br_x)_3$ and $MAPb(I_{1-x}Br_x)_3$), depending on the solvent used, different solubility tendencies can be observed, which could lead to phase segregation. The choice of the solvent will thus be different from one family of compounds to another, depending on the nature of halogens of the desired sample. The reasons motivating our choices will be explained for each family of compounds.

After dissolution of the precursors, the solvent is evaporated in a drybox (relative humidity 25-40%) by pouring the solution in a petri dish heated on a hot plate. The temperature of the hot plate is adapted beforehand to counteract the poor thermal conductivity of the glass and achieve the temperature chosen for the synthesis (depending on each family of compounds). As soon as the solvent is completely evaporated, the obtained material is ground to obtain a fine and uniform powder. In some cases, an additional annealing step is required, as will be explained in the following.

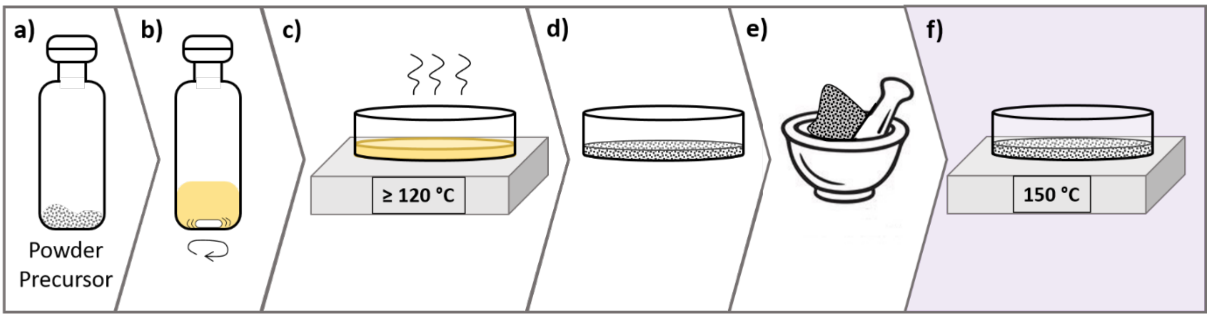

Figure 4.2: Powders synthesis protocol. (a) Precursor powder mixing (see appendix A.2) (b) Addition of solvent (DMF and GBL for purely bromide and iodide compounds respectively, NMP for mixed halides) to form a 1M solution and stirring at room temperature. (c) and (d) Solvent evaporation between 100 °C and 120 °C for compounds containing one type of halogen and 140 °C for mixed halogen compounds. Step performed in a drybox (relative humidity: 25-40%). (e) Grinding of the obtained powder. (f) Annealing step required for some compounds.

4.2. END COMPOUNDS : A COMPARATIVE OVERVIEW

Four end compounds were synthesized and studied as starting points to our work on mixed ion materials. GBL and DMF were used, respectively, as solvents for iodine-based compounds ($MAPbI_3$ and $FAPbI_3$) and bromide-based compounds ($MAPbBr_3$ and $FAPbBr_3$). Powder samples were obtained by evaporating the solvent at 100 °C. No further annealing step is required for the end compounds.

	$MAPbI_3$[12]	$MAPbBr_3$[13]	$FAPbI_3$ *[14]	$FAPbBr_3$[15]
Space group @ RT	I4/mcm	Pm-3m	Pm-3m	Pm-3m
Lattice parameter (Å)	a = 8.874 c = 12.671	5.929	6.358	5.986

Table 4.2: Space group and lattice parameter of the end compounds at RT as reported in the litterature. The star in $FAPbI_3$ reminds that the cubic structure is only metastable at RT.

Table 4.2 summarizes the space group and lattice parameters of the end compounds as reported in the literature. Before further describing the end compounds, it seemed important to us to adress the polymorphism of $FAPbI_3$ which was mentioned in the previous section, as it is this hexagonal phase which is thermodynamically stable at RT.

4.2.1. POLYMORPHISM IN HYBRID LEAD HALIDE PEROVSKITES

As explained in the first chapter of this manuscript, the main reason behind the lack of use of $FAPbI_3$ in solar cells despite its greater theoretical efficiency compared to $MAPbI_3$ is the instability of the perovskite phase. Cubic black perovskite $FAPbI_3$ evolves after synthesis, spontaneously, more or less rapidly, depending on the exterior conditions, but inevitably to a yellow, photo-inactive phase, as shown in Figure 4.3. Interestingly, such polymorphic behavior is not observed on the other 3 end-compounds, and we pointed out in subsection 4.1.1 by considering $FAPbBr_3$ that this phenomenon cannot be explained by geometrical considerations only. This section is mainly dedicated to the study of the hexagonal polymorphs in $FAPbI_3$. The last paragraph will focus on $FAPbBr_3$, trying to provide elements to understand why such polymorphism is not observed in the other compounds.

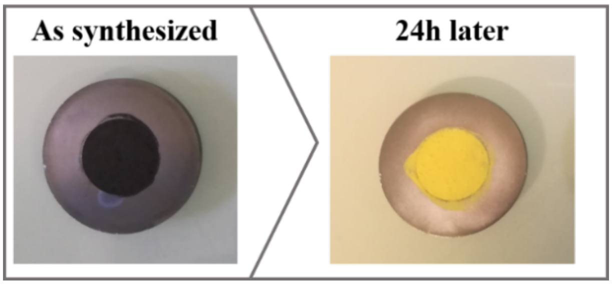

Figure 4.3: Spontaneous evolution of $FAPbI_3$ from a black cubic perovskite phase after synthesis to a yellow non-perovskite phase after sometime.

Well documented in the literature, the yellow phase crystallizes in a hexagonal lattice ($P6_3/mmc$ space group),[16] and is commonly qualified as the δ-phase. Multiple studies have shown that the black perovskite cubic phase (α-phase) can be recovered by heating the yellow sample to 150 °C (423 K) or more,[16,17] stabilizing the α-phase at room temperature for few hours up to few days.

To gain more insight into the polymorphism of $FAPbI_3$ and this phase transformation, we performed temperature dependent XRD measurements while heating in-situ our sample. The results are shown in Figure 4.4. Starting from the yellow polymorph which we refined, in agreement with the literature, in the hexagonal space group $P6_3/mmc$, with lattice parameters (a = 8.676 (3) Å, c = 7.929 (3) Å) close to the documented values (Figure 4.4.a)).[16] XRD patterns were recorded while heating, as shown in Figure 4.4.b). The sample was heated at a speed of 120 °C/min, a 10 min delay time was left before each measurement to reach thermal equilibrium, and each acquisition lasted 50 min. We observe three domains in temperatures: below 398 ± 5 K, where only the hexagonal phase is observed. Between 398 ± 5 and 427 ± 1 K, both the hexagonal and the cubic phase coexist. The former completely disappears at 428 ± 1 K and above. The temperature of disappearance of the yellow phase is close to the one reported in the literature. Moreover, we observed a domain of phase coexistence, indicating a first-order phase transition. After completing the transformation, the sample was cooled down to room temperature (speed: 120 °C/min). The recorded data were refined with good agreement in the cubic Pm-3m space group, with a lattice parameter of a = 6.357(2) Å (Figure 4.4.c)), here again, close to the values reported in the literature.[16]

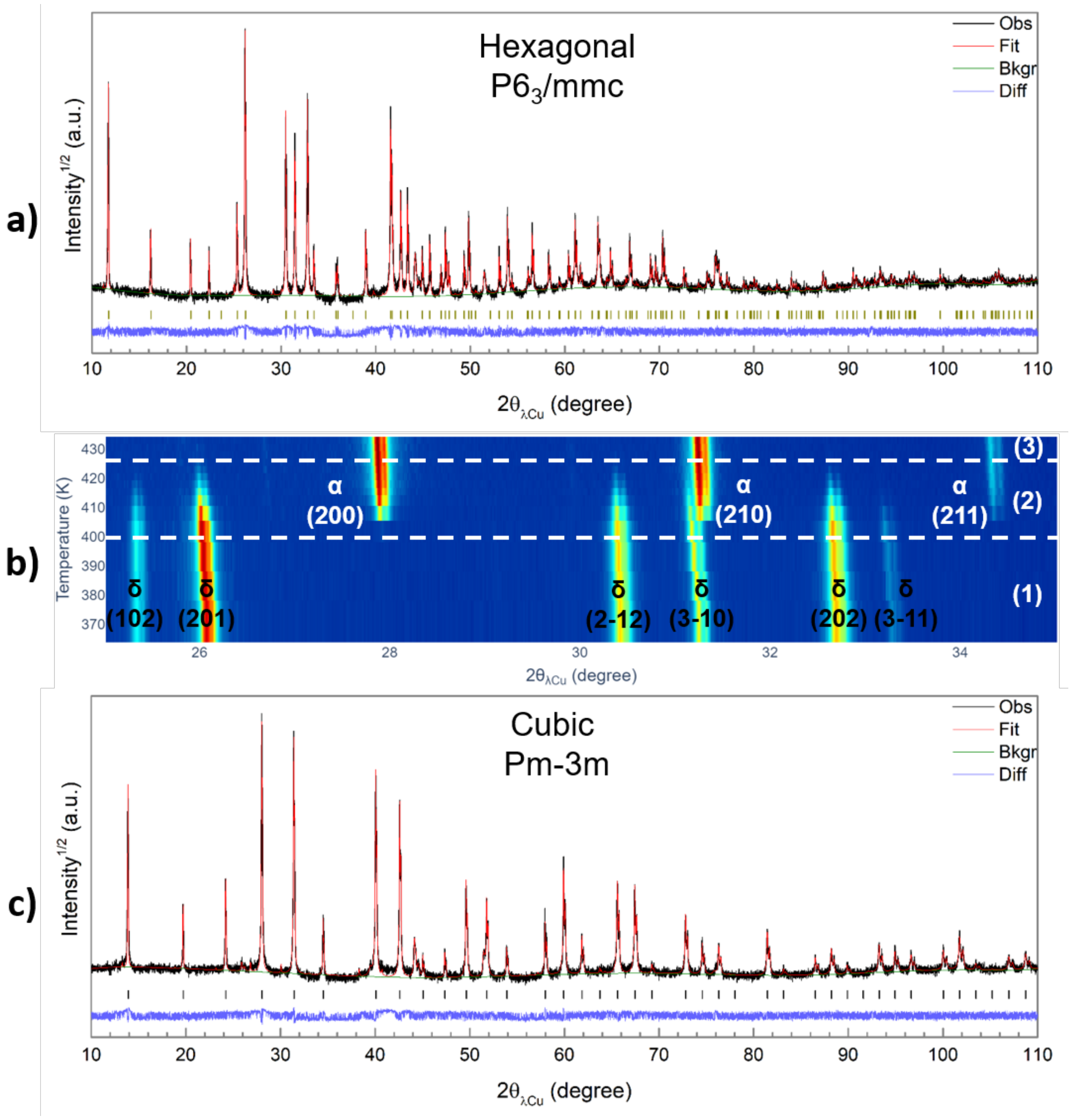

Figure 4.4: (a) Le-Bail refinement of FAPbI$_3$ hexagonal δ-phase (P63/mmc, a = 8.676 Å, c = 7.929 Å) at RT. (b) Contour plot in the 25-35° 2θ range during in-situ heating of the δ-phase and its transformation in α-phase. The (hkl) indices of all observed peaks are indicated. Three distinct steps are observed: (1) temperatures where only δ-phase is present. (2) coexistence of both δ-phase and α-phase. (3) pure α-phase. (c) Le-Bail refinement of the black cubic perovskite phase (Pm-3m, a = 6.357 Å) obtained after in-situ heating in our diffractometer.

Figure 4.4 shows the structure of both the δ and the α FAPbI$_3$-phases. In the former, the $[PbI_6]^{4-}$ octahedra are connected from their faces, creating a 1D-network along the c direction, with the organic cation in the middle, linking the two inorganic chains. The α-phase exhibits octahedra connected through their corners. Such hexagonal and cubic arrangement are both labeled as perovskite structures in the large perovskite structural family (in inorganic oxide compounds), and we will keep this formalism here.

As highlighted in Figure 4.4, the closest distance between two lead atoms in the hexagonal phase is along the c direction where $\mathrm{d(Pb-Pb)_{hex}} = c/2 \sim 3.97\text{Å}$. In the cubic phase, the distance is equal to the lattice parameter: $\mathrm{d(Pb_Pb)_{cub}} = a \sim 6.36\text{Å}$, indicating closer lead atoms in the hexagonal structure than in the cubic symmetry.

To achieve the transition from the hexagonal to the cubic phase, a number of atomic motions is needed between the different ions, with unavoidable breaking/forming of Pb-I bonds.[17] While a lot of studies are carried out to suppress the formation of the δ-phase, few have been devoted to understanding its mechanism. Combining experimental data and DFT, Marronier *et al.* have explained this phenomenon by the increase in the dynamic motion of the octahedra with increasing temperature, allowing to form the perovskite phase.[18] Also using DFT calculations, Chen *et al.* proposed a complex pathway for the transition, displaying over 40 steps of ion motions.[17]

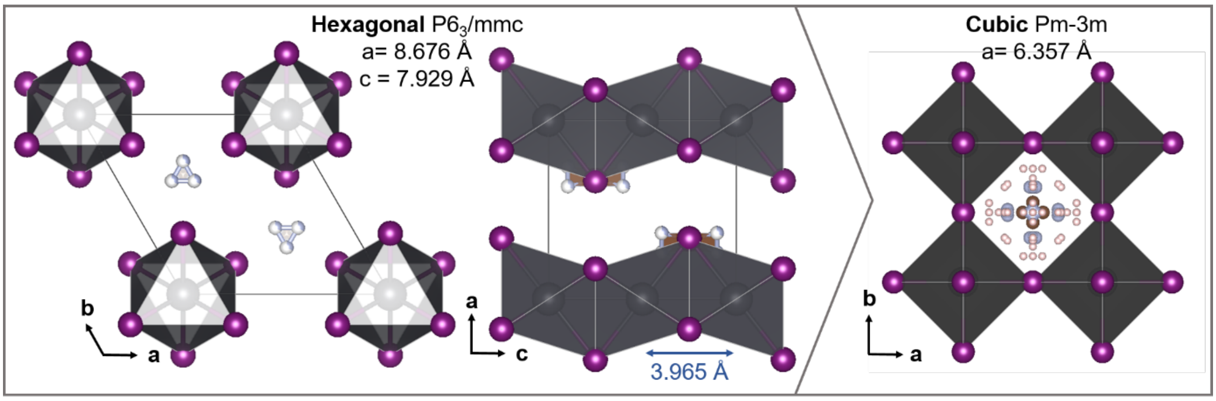

Figure 4.5: Structure of the two $\mathrm{FAPbI_3}$ know polymorphs: hexagonal δ-phase (left panel) and cubic α-phase (right panel).

A "simpler" mechanism can be found when considering different hexagonal polymorphs. The polymorphism of $\mathrm{FAPbI_3}$ is not an isolated phenomenon in the large perovskite structural family. Transition metal oxide perovskite such as $\mathrm{BaMnO_3}$, SrMnO3[19] and $\mathrm{BaRuO3_3}$[20][21] exhibit such polymorphism. By applying high temperature and/or high pressure, different hexagonal structures can be obtained for the same compound and the cubic phase can be stabilized at high temperature/pressure. In the case of hybrid lead halide perovskite, considering the weak interaction between the organic cation and the inorganic cage, the high ion dynamics and the high diffusivity of the $\mathrm{I^-}$ in the structure, one can expect to encounter the different hexagonal polymorphs in conditions close to the ambient ones.

HEXAGONAL POLYTYPES

In the following, we will discuss different hexagonal structures, which vary only along the c direction and remain identical along the two others. Such structural variations are classified as a subset of polymorphism, called polytypism.[22] As explained earlier, the cubic structure exhibits a 3D network of corner-sharing octahedra, adopting a cubic stacking of the octahedra (c), while in the δ-phase, the face-sharing octahedra adopt an infinite 1D hexagonal packing (h). The hexagonal polytypes are a combination of both types of stacking: c and h and a large number of polytypes can be imagined. Figure 4.6 shows examples of some polytypes and their designation according to Ramsdell's notation.

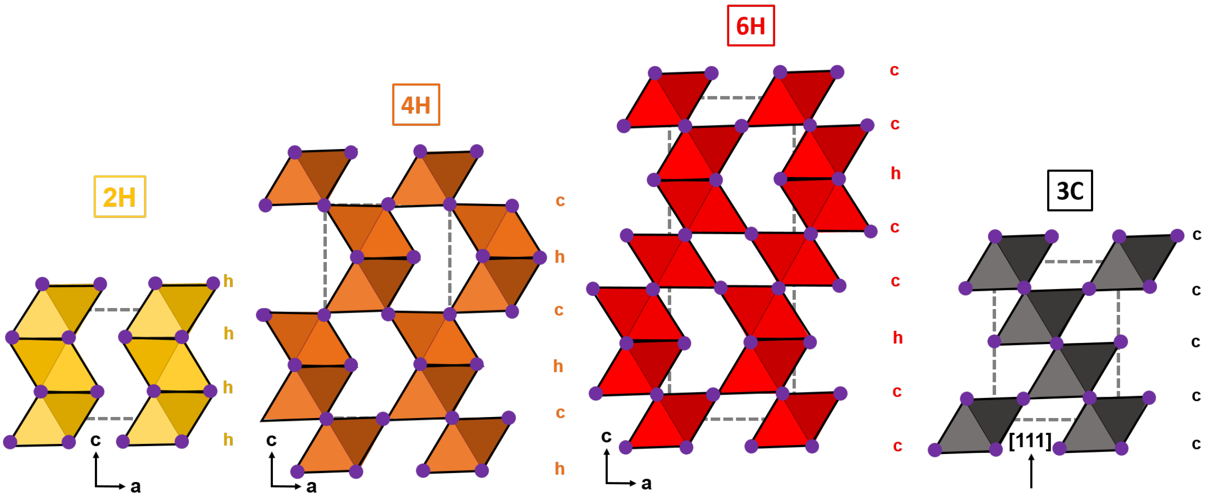

Figure 4.6: Schematic of the various packings leading to the different hexagonal polytypes and hexagonal-cubic polymorphism. Purely face sharing octahedra lead to a 1D hexagonal stacking (h), describing the δ-FAPbI$_3$ phase (in yellow). This polytype is noted 2H according to Ramsdell's notation. The cubic α-phase is described by purely corner-sharing octaheras, describing a cubic stacking c (3C, in grey). The 4H and 6H stackings can be seen as intermediary structures, with both h and c stackings.

Concerning the so-called 2H phase, in yellow in Figure 4.6, considering one octahedra layer, the same packing configuration is encountered on the second layer after the one of interest, justifying a 2H label, which described the well-known δ-FAPbI$_3$ phase. The black structure in Figure 4.6, which corresponds to the cubic structure viewed from the larger diagonal of the cube, shows a cubic packing (corner-sharing), repeating itself every 3 layers, thus called 3C. The 4H and 6H structures display both h and c packings. In the case of 4H, h and c alternates while for the 6H polytype, h packings are separated by two layers of corner sharing octahedra. In all the polytypes, the A cation occupies the cavities lefts between the octahedra stacking.

Upon increasing temperature and/or pressure, oxide hexagonal structures such as $BaRuO_3$ were demonstrated to undergo polytypic transformation following the 2H → 9R → 4H → 6H → 3C sequence.[21] Such sequence changes the octahedra connectivity which is known to play an important role in the material properties (band gap, multiferroics...[19,21,23]). One of the driving forces in such polytypism was found to be electrostatic repulsion between the B atoms along the c chains which would exceed, with increasing pressure, the strength of the A-X bond and allows octahedral displacement.[21]

Hybrid halide perovskites hexagonal polytypes

The first report of hexagonal polytypes in hybrid lead halide perovskite is found in the work of Gratia *et al.*.[22] Through adapted synthetic routes, they managed to obtain and analyze single crystals of mixed cation and mixed halide perovskites $FA_{1-x}MA_xPb(I_{1-x}Br_x)_3$ crystallizing in the 2H, 4H and 6H structures. They exhibited a variation in their optical properties (color and thus band gap) according to the different octahedral connectivity: a high connectivity (2H) leads to a large band gap, hence the yellow color. When inserting c stacking in the structure (4H and 6H), the band gap decreases, leading to orange and red colors, respectively, until the total c stacking of the black compound.[22]

Following their work, Cordero *et al.* looked for these polytypes in $FAPbI_3$. By applying a pressure as low as 0.2 GPa on the yellow phase, they observed a color change to orange, indicating the decreased octahedral connectivity. They highlighted the shorter Pb-Pb distance in the 2H yellow packing (indicated in blue in Figure 4.4), leading to increased electrostatic repulsion in comparison to structures with c stacking where longer Pb-Pb bonds induce a smaller repulsion. Thus, when applying pressure, 4H and 6H polytypes become more competitive. By evaluating the cell volume per unit formula in these polytypes, they observed a decrease of the volume when decreasing the connectivity, until reaching the cubic cell volume. This smaller volume is due to a contraction along the c direction, accompanied by a small expansion in the ab plane, corner-sharing octahedra being more closely packed than face-sharing octaheras. They could not, however, confirm the presence of the different polytypes proved by optical observation (change in color and band gap) with XRD measurements.[23]

In the following, when the polytypes are mentioned, the δ-phase designates the 2H stacking, while 4H and 6H will be labelled as such, using Ramsdell's notation.

In light of these information, we come back to our experiment of δ to α transition upon heating. Analyzing closely our data, we did not observe peaks corresponding the 6H and 4H phases. However, they revealed another interesting feature. As shown in Figure 4.7.a upon heating, an anisotropic line broadening is observed: some peaks ((2-12), (h0h)) become wider than others ((2-10), (3-10), (00l)). The single peak fitting results shown in Figure 4.7.b) translate this non-negligible anisotropic line broadening. By performing a LeBail refinement over the whole 2θ range, we found that this broadening arises from anisotropic strain and not anisotropic size (we will detail the procedure for anisotropic strain fitting in TOPAS in the next paragraph).

Figure 4.7.c and d show, respectively, the evolution of the lattice parameters and the volume of the hexagonal phase while heating. While the volume expands as expected when the temperature is increased, the c lattice parameter contracts (the quicker expansion along the ab plane compensate and allows the volume expansion). The same observation is reported in other works.[16]

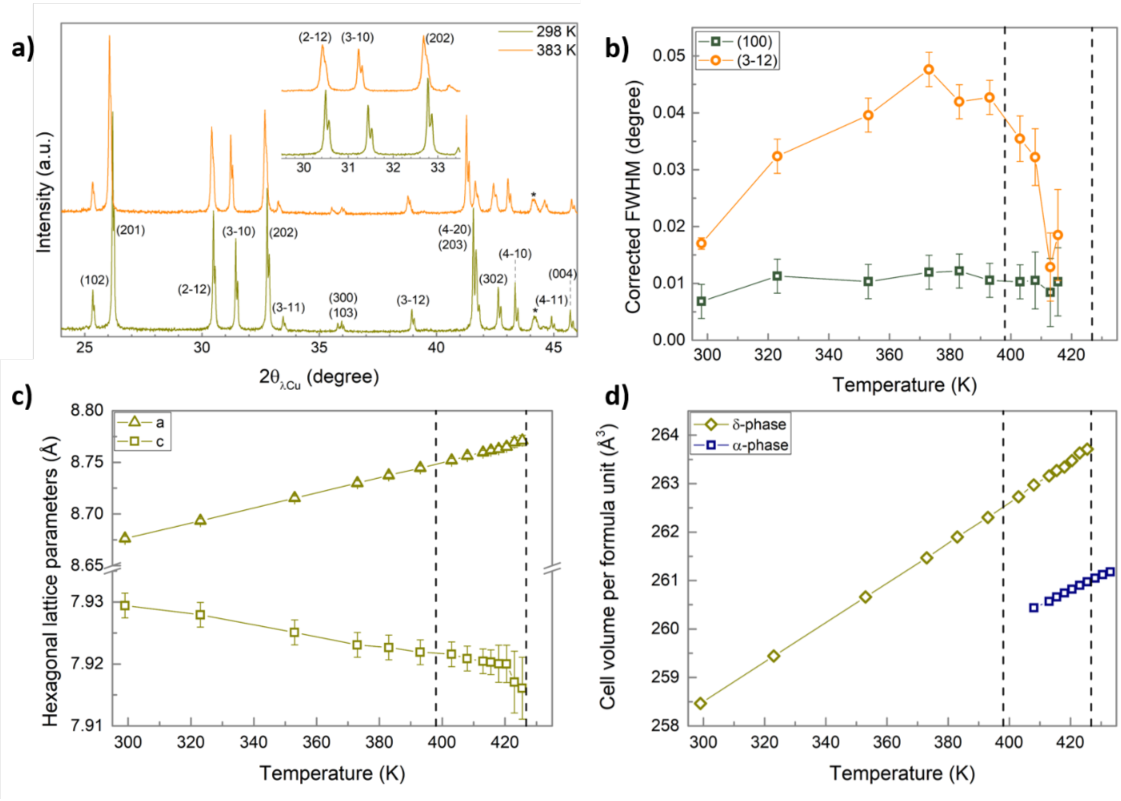

Figure 4.7: Polymorphism of $FAPbI_3$ upon heating. (a) XRD pattern of δ-phase at RT (298 K) and 383 K showing an anisotropic line broadening of the XRD peaks. (b) Evolution of the corrected FWHM of different peaks: the (100) which shows the smallest broadening upon heating and (3-12) which is one of the peaks that shows the strongest peak broadening upon heating. (c) Evolution of the a and c hexagonal lattice parameters upon heating. (d) Evolution of the δ and α-phase cell volumes per formula unit upon heating. The vertical black dashed lines in figures (b), (c) and (d) indicates the different step in the conversion process: δ-phase only (1), both δ and α-phase (2) and α-phase only (3).

Figure 4.8 illustrates the interreticular distances which shows the strongest broadening (a) and the ones which merely broadens upon heating (b). Again, during this experiment, the broadening was found to be induced by strain effects, noted $\epsilon = \Delta d/d$, indicating a higher dispersion in the distance between the planes of interest. In a more general description, peak broadening affects only (hkl) peaks with h and/or k different from 0 and l indices different from 0. This indicates that great dispersion in the distance between face-sharing octahedra rises upon heating, as shown in Figure 4.8.a, hinting to a weakening of the interaction between those units.

Furthermore, we observed that heating induces a contraction in the hexagonal c direction (Figure 4.7.c), which would lead to closer Pb-Pb atoms as, in this structure, we highlighted earlier that d(Pb-Pb) = c/2. Hence, **upon heating, as c contracts, the electrostatic repulsion between Pb^{2+} atoms increases, probably leading to the weakening of the interaction between the adjacent octahedra hinted by the anisotropic peak broadening observed above**.

This is in good agreement with the observation made on inorganic oxide perovskite where electrostatic repulsion has been observed as the driving force of the polytypism.[21] Interestingly, in opposition to these compounds, no 2H-4H-6H-3C polytypic sequence was observed in $FAPbI_3$, and the hexagonal 2H structure directly converts into 3C, but we noted the coexistence of both arrangements at high temperature.

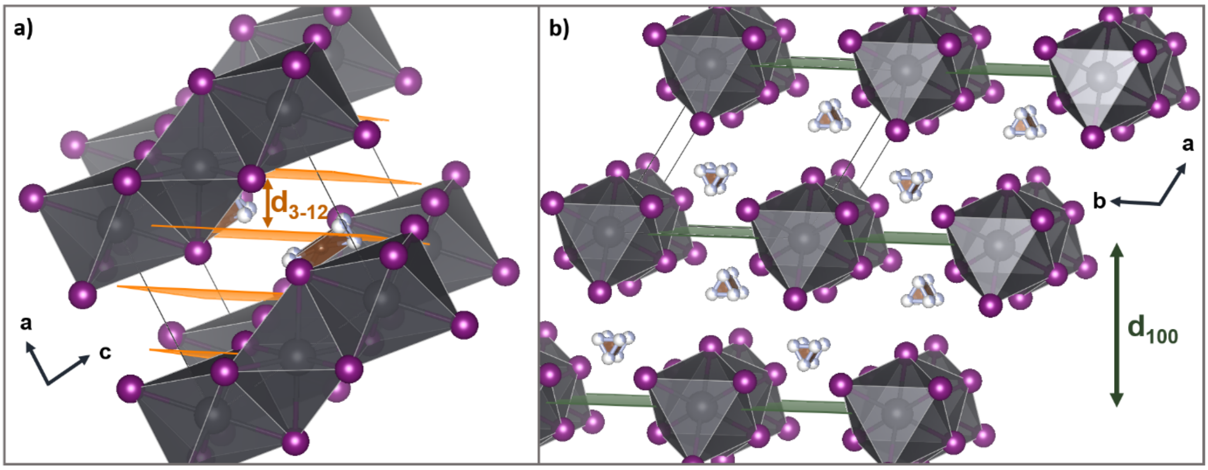

Figure 4.8: Directions of δ-phase showing the hexagonal planes and illustration of the corresponding interreticular distance probes by XRD : (a) in orange, the [3-21] planes. (b) in green, the [100] planes.

Cubic $FAPbI_3$ is stable at high temperature, and this phase can be kinetically trapped at RT for some time after heat treatment, as Chen *et al.* evidenced the hysteretic nature of the transition from δ to α-phase.[17] In the following, studies on α-$FAPbI_3$ were performed on sample heated at 150 °C for 1h to ensure the formation of the perovskite cubic phase.

In the case of $FAPbBr_3$, tolerance factor calculations shown in section 4.1 showed a slightly higher value than for $FAPbI_3$. We could thus expect to have the same polymorphism as in the latter. Surprisingly, no hexagonal polymorphs have ever been reported for $FAPbBr_3$. Through single crystal XRD, Gratia *et al.* showed, in their mixed halide compounds, that Br preferentially occupies corner sharing octahedra.[22] Here again, one can explain this observation in terms of electrostatic repulsion. In a hexagonal packing, the Pb atoms are rather close to one another, as explained earlier. In the case of a $[PbBr_6]^{4-}$ octahedron, the Pb-X bonds are shorter than in a $[PbI_6]^{4-}$ octahedron, leading to even closer Pb-Pb atoms if stacked hexagonally. Our temperature dependent experiment showed that the short Pb-Pb in δ- $FAPbI_3$ are highly disturbed if slightly shrunk (when increasing temperature). We can thus imagine that a high electrostatic repulsion would arise in a hexagonal arrangement of $[PbBr_6]^{4-}$, where the screening by the Pb-Br bond will not be enough despite the high electronegativity of Br^-, to counter act this phenomenon, making the hexagonal packing not possible for $FAPbBr_3$.

As $MAPbI_3$ (different organic cation than $FAPbI_3$) and $FAPbBr_3$ (different halide than $FAPbI_3$) do not experience polymorphism, the impact of ion substitution in $FAPb(I_{1-x}Br_x)_3$ and $FA_{1-x}MA_xPbI_3$ solid solutions on the polymorphism is inspected in this chapter (see section 4.1 and subsection 4.5.1).

4.2.2. Intrinsic and anisotropic strain, lattice parameters and band gap

Before the detailed study of the mixed ions compounds, let us take a look at the starting compounds $MAPbI_3$, $MAPbBr_3$, $FAPbI_3$, $FAPbBr_3$. Except $MAPbI_3$ which is tetragonal, all the other compounds adopt a cubic Pm-3m symmetry at RT, as reported in Table 4.2. Sun *et al.* evidenced the existence of intrinsic strain in $MAPbBr_3$ and $FAPbBr_3$ as well as non-negligible strain anisotropy in these compounds.[24] We observed, on our samples, a particularly clear anisotropic line broadening in $FAPbBr_3$, as demonstrated in Figure 4.9.

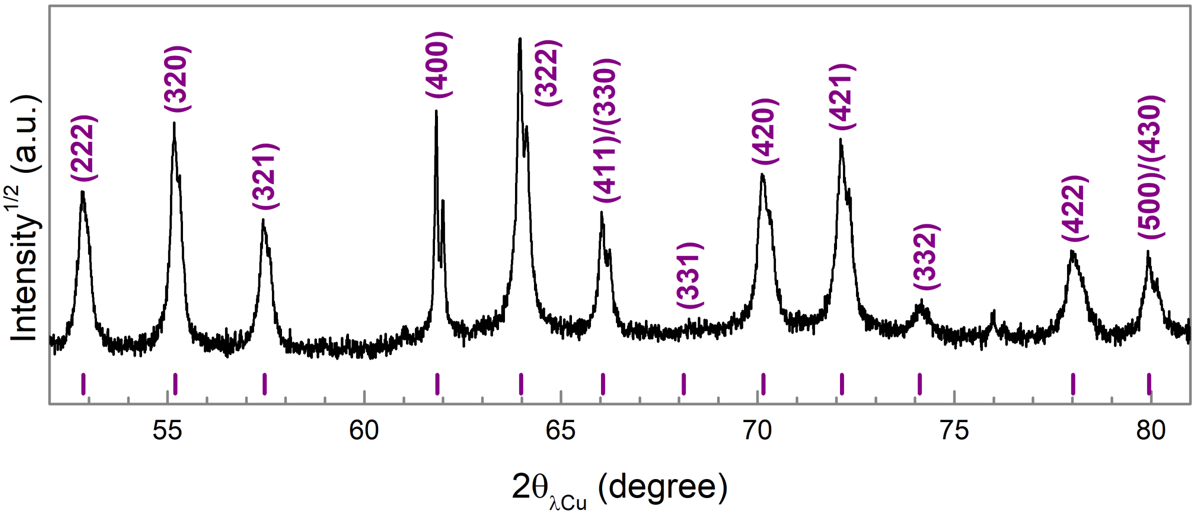

Figure 4.9: Raw DRX pattern of $FAPbBr_3$ powder. The purple sticks indicate the expected cubic Pm-3m perovskite peaks for a lattice parameter of a = 5.995(2) $\AA$, matching the observed lines.

To obtain a clear overview on the presence of intrinsic strain and its anisotropy on the end compounds, we drew the Williamson-Hall plots for the 3 main directions in a cubic crystal: [100], [110] and [111]. More details about Williamson-Hall plots can be found in appendix B.4. This model assumes that the peak broadening arises from size or strain effects, and Williamson-Hall plots are the linear evolution of the product of the corrected FWHM by $\cos(\theta)$ as function of $\sin(\theta)$. The obtained lines allow to identify the origin of the peak broadening: the intercept of line is inversely proportional to the crystallite size and the slope is proportional to the intrinsic strain $\epsilon = \Delta d/d$ which characterizes the percentage of deviation from nominal d value.

The obtained Williamson-Hall plots are shown in Figure 4.10. $MAPbI_3$ being tetragonal at room temperature, we used data measured at 100 °C in its cubic phase for the sake of a qualitative comparison of strain values. No comparison can be made concerning anisotropic line broadening. The lines presented in Figure 4.10 are the linear fitting obtained from the raw data. We need, however, to specify that to obtain these lines, we neglected the (300), (500) and (330) cubic reflections. The reason behind this is that at least two different reticular directions contribute to the intensity and FWHM of these peaks, directions which may not be subject to the same amplitude of anisotropic strain thus disturbing the final result. [100] and [110] linear fits where performed with 3 points and [111] is drawn from the only two available peaks.

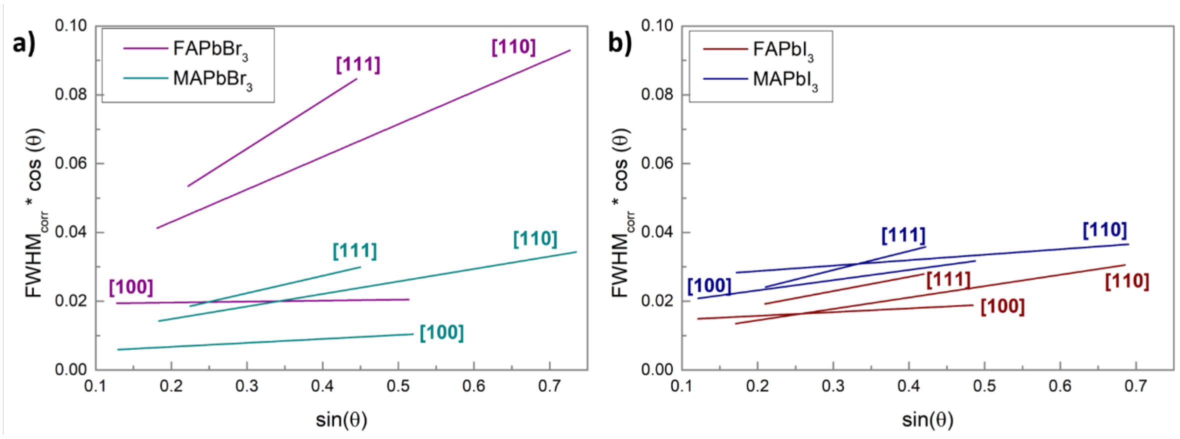

Figure 4.10: Williamson-Hall plot for the 4 end-compounds $FAPbBr_3$ and $FAPbBr_3$ (a), $FAPbI_3$ and $MAPbI_3$ (b) for cubic directions [100], [110] and [111]. $MAPbI_3$ being tetragonal at RT, we used data from measurements performed at 100 °C (see Part 1 of this manuscript). Same x and y scales were used in both graphs to highlight the differences between iodine-based and bromine-based compounds.

The first striking observation from Figure 4.10 is the **highest strain value arising from $FAPbBr_3$ in comparison with all three other compounds**. More lattice defects (dislocations, vacancies…) are observed in $FAPbBr_3$. This observation could be linked to the high tolerance factor value of $FAPbBr_3$, which adopts, nonetheless, a cubic structure, probably because of the electrostatic repulsion.

Another striking feature is the presence of **anisotropic strain within the three studied directions**. In the case of $FAPbBr_3$ almost no strain is observed along [100] (flat line in the limit of our resolution) whereas the **highest strain is obtained along the [111] direction**. The same trend is observed on $MAPbBr_3$ and $FAPbI_3$. In the case of $MAPbI_3$, the highest slope can still be found for [111] direction, but the lowest one is along [110] and not [100]. It is hard to conclude anything from this last observation as the data are taken from measurements performed at a different temperature. The tendency of having the highest strain along [111] and the lowest along [100] agrees with the mechanical properties measured by Sun *et al.* which found the highest hardness values along [100] and the lowest along [111].[25]

From our measurements, $FAPbBr_3$ shows the highest strain anisotropy. It is however harder to conclude comparing the Williamson-Hall plots of $MAPbBr_3$ and $FAPbI_3$. One way to get an easier and more reliable comparison is to look closely at the quality of the fits when considering an isotropic line broadening during LeBail refinement. The left panels of Figure 4.11 show the measured data in black and the calculated patterns from the LeBail refinement considering isotropic line broadening in red. An enlarged view on the (222) and (400) diffraction lines is shown, these two peaks corresponding to the direction showing the highest and the lowest strain, respectively. As expected, $FAPbBr_3$ shows the worst refinement of all three samples. The substitution of the organic FA^+ cation by MA^+ results in an improved fit, however the FWHM of the (222) and (400) peaks are still, under and over-estimated, respectively, leading to higher and lower calculated peak intensities with respect to the observed data. Finally, substitution of Br^- by I^- anions in the FA-based compounds decreases significantly the anisotropic line broadening. These observations allow us to say that the nature of the halogen ion has more impact on the strain anisotropy than the organic cation. Moreover, I-based compounds exhibit smaller strain anisotropy than Br-based ones and strain anisotropy is enhanced in FA-based in comparison to MA-based samples. Adopting a different symmetry at RT, $MAPbI_3$ is kept out of this comparison.

It might be interesting to consider these results in the light of the trend observed by the work of Laurita *et al.* who, through X-ray PDF studies, evidenced the presence of dynamical Pb off-centering along the [111] direction. The electronic configuration of the Pb^{2+} cation shows a lone pair s^2p^0 which can hybridize and lead to different stereochemical expression depending on the mixing of orbitals with the surrounding ions. This stereochemical activity can be tuned through composition. The team found that FA^+ based compounds will show higher Pb^{2+} displacement than MA^+ based ones, and Br^- induces higher Pb^{2+} off-centering than I^-, furthermore noting that the organic cations have smaller influence on the off-centering than the halogens.[26] This off-centering of Pb^{2+} cations could explain the strain anisotropy evidenced earlier and they observed the same impact magnitudes of the ions as what we extracted from our data.

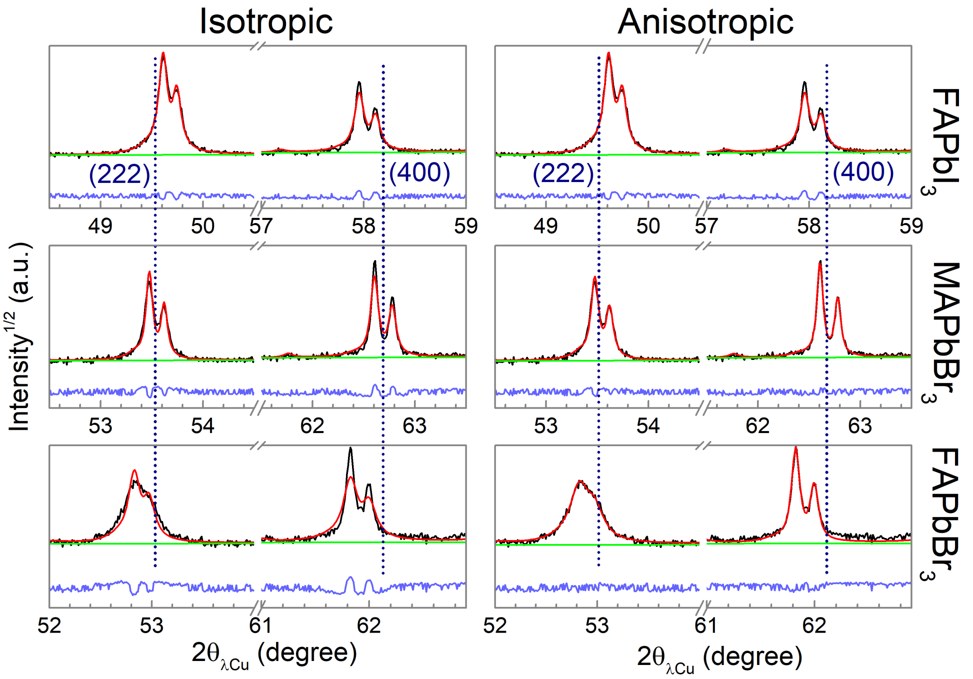

Figure 4.11: XRD measured (black) and calculated (red) pattern for, from top to bottom, $FAPbI_3$, $MAPbBr_3$ and $FAPbBr_3$ when considering an isotropic strain model (left panels) or an anisotropic model (right panels) during the LeBail refinement.

To model the strain anisotropy, TOPAS software proposes the Stephens model.[27] To refine anisotropic line broadening caused by strain effects, Stephens developed a phenomenological model based on the assumption that each crystallite has its own lattice parameters. Considering the expression of the d spacing from Miller indices M_{hkl}, a Gaussian distribution of the lattice metrics in the powder and the covariance matrix of these lattice metrics, the variance of M_{hkl} (defined as $1/d^2$) can be expressed as:

$$\sigma^2(M_{hkl}) = \sum_{HKL} S_{HKL} h^H k^K l^L \tag{4.3}$$

Where S_{HKL} is the anisotropic strain parameter defined for H+K+L = 4. By considering the specific symmetries of each crystal system, Stephens identified the anisotropic strain parameters relevant for each one (S_{400} and S_{220} for the cubic system… etc). Moreover, he introduced a parameter η which allows mixing Gaussian and Lorentzian contributions to the description of the peak shape. On the other hand, Stephens model does not describe stacking faults.

We observed that refining the parameter η as well as the strain parameters can lead to quite a discrepancy in the values of the refined S_{HKL} while maintaining the same goodness of fit. To obtain comparable results, η was fixed to 1 which means the peaks where refined with a Lorentzian shape. Moreover, the anisotropic parameters where introduced in the fitting one by one, to avoid refinement with non-relevant parameters. In the case of our cubic systems, only the S_{220} parameter was introduced.

We used this model to fit the anisotropic strain induced line broadening we observe on our samples. The results are shown in the right panel of Figure 4.11, revealing a clear improvement of the refinement quality for both $MAPbBr_3$ and $FAPbBr_3$, however not for $FAPbI_3$, indicating that while visible, the phenomenon is too weak to be fairly reproduced by the model. Concerning $MAPbI_3$, in both cubic and tetragonal phases, visual inspection of the refinement revealed a good agreement between the isotropic model and the data, thus not justifying the use of the anisotropic model. In the case of hexagonal δ-$FAPbI_3$ studied in section 4.2, only the S_{202} parameter of the hexagonal anisotropic model was used to reach satisfying refinements ensuring a high precision in the determination of the lattice parameters shown in Figure 4.7.

Table 4.3 summarizes the parameters characterizing our samples. Besides XRD measurements, we performed UV-visible absorption spectroscopy to extract the band gap. The method used for this calculation is detailed in appendix C.1.

The lattice parameters and band gap values are close to those reported in the literature.[13,28,29] As predicted, the substitution of MA^+ by the larger cation FA^+ leads to larger cell parameters and smaller band gaps, in both I^- and Br^--based compounds. We also observe that it induces higher strain values, which can be understood as a consequence of the larger distance between the lead and the halogen ions, resulting in a weaker interaction in the inorganic cage and thus larger density of lattice defects. It should be noted that the absolute strain values extracted from fits using anisotropic strain cannot be directly compared with values of isotropic strain. Hence, the comparison of halogen substitution is not direct. We can nevertheless remind our observation concerning the enhanced anisotropic strain in bromide-base compounds.

Compounds	$FAPbBr_3$	$MAPbBr_3$	$MAPbI_3$	$FAPbI_3$
Lattice parameter (Å)	5.995(2)	5.929(2)	a = 8.876 (3) c = 12.669(4)	6.358(2)
Intrinsic strain (%) $*10^4$	1.3	0.8	2.2	2.6
S_{220} anisotropy	388	15	-	-
Band gap (eV)	2.24	2.27	1.50	1.43

Table 4.3: Lattice parameter, intrinsic strain and its anisotropy amplitude and band gap at RT for the four studied end-compounds.

4.2.3. Going further : Rietveld refinement and hybrid halide perovskite structure

In addition to lattice parameters and microstructural information, XRD patterns also give access to atomic positions or site occupancy in a crystal. While LeBail refinement does not apply any constrains on the relative peak intensities to access to the lattice parameters and the microstructure, Rietveld refinement allows refining the positions of the different atoms of the compound of interest in the lattice and its site occupancy by refining the peak intensities. More details are given in appendix B.4.

We performed Rietveld refinement on our end compounds using atomic positions that are available in the literature. As the X-rays are more sensitive to heavy elements, the organic cations will have a much smaller contribution to the diffraction pattern in comparison with electron rich Pb^{2+} and X^{-}. Thus, we decided to replace the organic cation with an atom exhibiting equivalent scattering power (FA^{+} was replaced by manganese and MA^{+} by potassium) as the center of the inorganic cage, to limit the number of refined parameters. Figure 4.12 shows, for example, the best refinement obtained for $FAPbI_3$ and $FAPbBr_3$. Visual observation shows the poor quality of the refinements which failed to reproduce all the observed peak intensities. Similar observations can also be found in some works in the literature.[30] We should precise that the LeBail refinement performed on all the samples yielded satisfactory results, especially when encountering strain anisotropy as was detailed in the previous section. Rietveld refinement was performed by keeping fixed all the parameters refined during LeBail refinement, thus focusing only on the relative peak intensities.

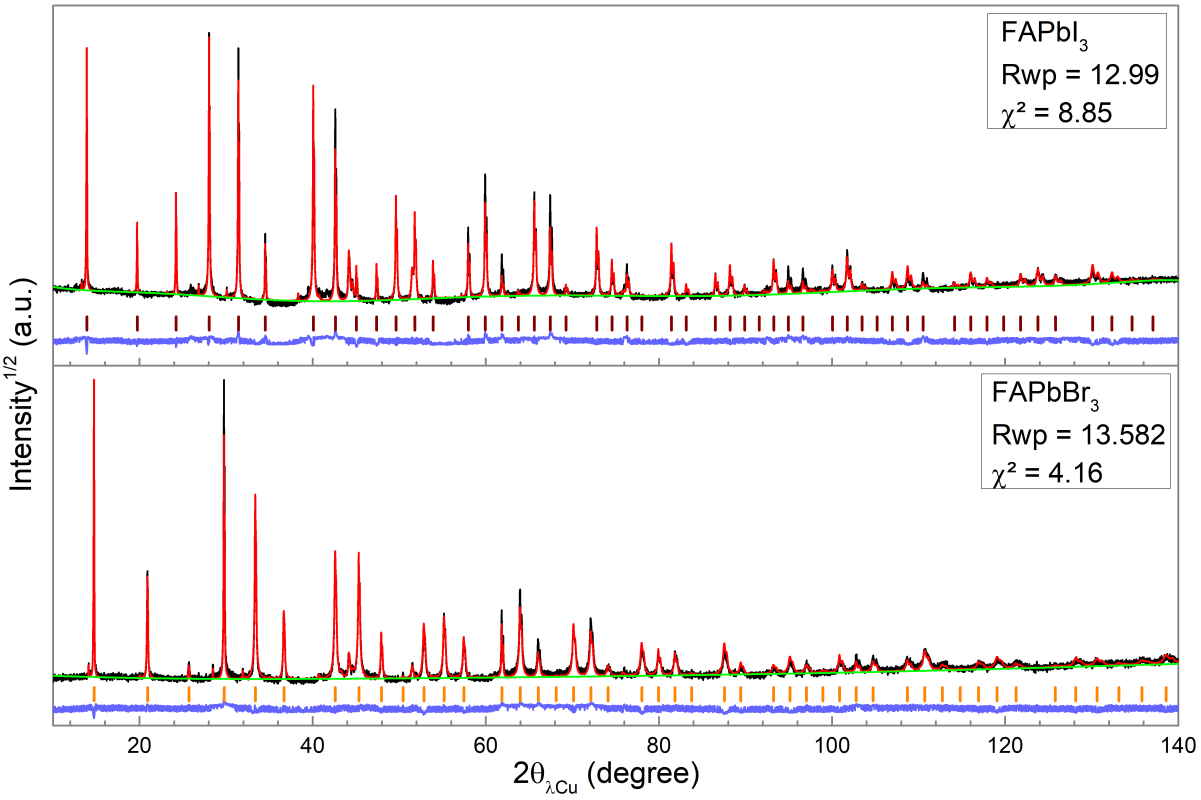

Figure 4.12: Example of Rietveld refinements for $FAPbI_3$ (top panel) and $FAPbBr_3$ (bottom panel), showing the poor quality of the refinement for both samples. In both panels, the black line is the measured pattern Yobs, the red line is the refined pattern Ycalc, the green line is the refined background and the blue one is the difference Yobs- Ycalc. The colored dashes represent the expected diffraction lines of the cubic Pm-3m phase.

Moreover, we observed intriguing discrepancies of the relative intensities of XRD peaks measured on different samples, all of which were obtained following the same synthetic path. Figure 4.13 displays these differences observed on 3 different samples of $MAPbBr_3$, synthesized and measured in the same conditions (same diffractometer, same measurement configuration, same optic elements). While the intensity of the (210) peak is similar for all samples, a huge difference is observed for the (200) peak. Here again, we would like to point out the fact that the LeBail refinement reached satisfying results. Lattice parameters and intrinsic strain were rather close, the main difference between the three samples is the value of the anisotropic strain parameter. The results are displayed in Table 4.4.

Sample	**1**	**2**	**3**
Lattice parameter (Å)	**5.930 (2)**	**5.930 (2)**	**5.929 (2)**
Anisotropic strain parameter S_{220}	**30.9**	**14.2**	**15.7**
10^4 ϵ (%)	**0.5**	**0.7**	**0.8**

Table 4.4: Lattice and strain parameters extracted from LeBail refinement of the three different samples presented in Figure 4.13.

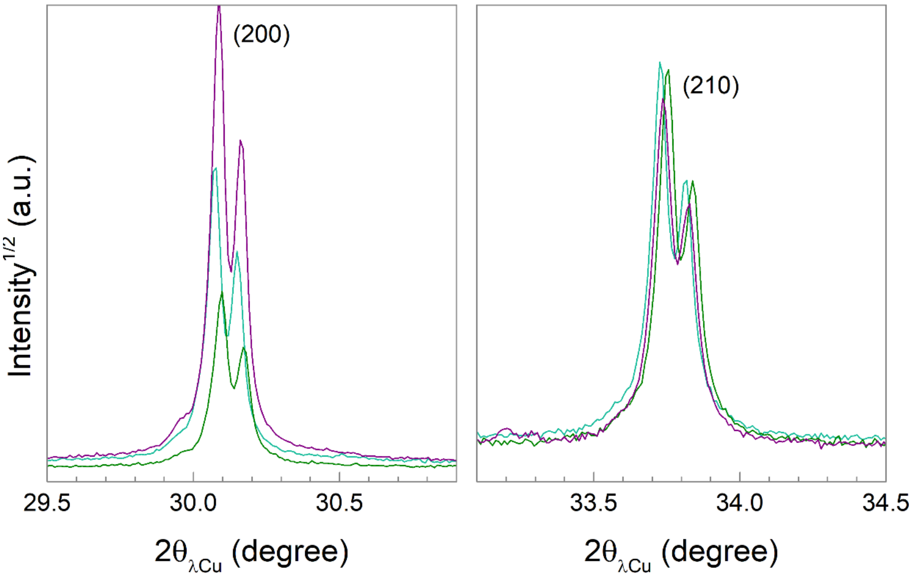

Figure 4.13: Comparison of 3 different samples of $MAPbBr_3$, all synthesized in the same conditions, showing noticeable differences in the peaks relative intensities from one sample to another. All measurements were performed in the same conditions (same diffractometer, same configuration, same optic elements).

Recent works have shown interesting features concerning the local structure of hybrid halide perovskites. Pair Distribution Function (PDF) experiments allow accessing information on the long range (10 to 20 Å) but also on the short range (1 to 10 Å) interactions, thus revealing the local ordering in the crystals. Bernasconi *et al.*[31,32] showed, for both $MAPbCl_3$ and $MAPbBr_3$ that while the long range ordering is well described by the cubic model, this model fails to reproduce the short range pattern. Satisfactory agreement is reached when using an orthorhombic model, showing local distortions of the octahedra. Zhao *et al.* used the same experimental method on cubic $MAPbI_3$ and $FAPbI_3$ showing the same local disorder. Using DFT calculations, the theoretical predictions of intrinsic properties (electronic structure, local structure) matched best the experimental results when considering a large polymorphic cell instead of the usual small cell with only one unit formula. This large cell allows accounting for the anharmonic tilts and B-atom displacement in the octahedra in the cubic phase, which plays an important role in the intrinsic properties of perovskite structure.[33] To go even further, recent work using Raman spectroscopy highlighted a liquid-like relaxational behavior of cubic and tetragonal $MAPbI_3$, far from what is expected in solid state physics.[34]

While all these literature examples cannot directly explain why our Rietveld refinements fail to reproduce the experimental data, they allow emphasizing another problematic with these intriguing materials. Intensively used, classical solid-state tools to characterize crystals (mainly crystallography) allow reproducing the average behavior and properties of hybrid halide perovskites, but fails to reproduce the local arrangement of atoms which show a high dynamical degree of freedom and distortion. However, these local properties are not to be neglected as they play an important role in the intrinsic properties of the material (band structure, ferroic behavior. . .). It seems to us that it would be of great interest for this field to dedicate more efforts to the use of tools that are able probe the local order (PDF, Raman spectroscopy) and the dynamics of organic cations but also the octahedra (solid-state NMR, Raman spectroscopy, inelastic neutron and X-ray scattering . . .).

Understanding the reasons behind the variable relative intensities from one sample to another can be the subject of an independent study, combining precise control of the synthesis parameters and Rietveld refinement. As fascinating as it is, it was not the objective of my PhD, as we intended to focus our efforts on the study of the hybrid halide perovskite solid solutions. LeBail refinement already allows extracting interesting results in terms of lattice parameters and microstructural information which, in addition to band gap estimation, is highly informative of the solid solution behavior as we will show in the following sections.

4.3. $MAPb(I_{1-x}Br_x)_3$ SOLID SOLUTION

As explained in the introduction of this part, we decided to study mixed ions hybrid halide perovskites, by substituting one element at a time. The first family of compounds we present here are $MAPb(I_{1-x}Br_x)_3$ solid solutions. Band gap tuning from 1.5 to 2.3 eV is expected when increasing the amount of bromide introduced, making these compounds highly interesting for multi-junction solar cells[35] or as color-selective photodiodes for color imaging.[13] Studies have shown a complete miscibility on the full range of bromide-iodide ratio on thin layers[36][37] while others performed on powders have exhibited a large miscibility gap for Br contents between 0.29 and 0.92.[13] However, these solid solutions were predicted to be thermodynamically unstable against phase segregation at RT.[38] Marchenko *et al.* showed, using a semi-empirical approach the existence of a large non-miscibility zone in the $MAPb(I_{1-x}Br_x)_3$ solid solutions which leads to a deviation from

Vegard's law, confirming the results of Lehmann *et al.*.[39]

To obtain their samples, Lehmann *et al.* used different solvents, depending on the bromide composition (GBL for low Br-content, DMF for high Br-content, and a mixture of GBL and DMF for intermediate compositions) The material preparation was performed at 100 °C. As mentioned earlier in this chapter, the retrograde solubility of perovskites in different solvents, depending on the halide nature, makes the solvent choice more difficult and of great importance when synthesizing mixed halide compounds. In our approach, we tried, unsuccessfully, to avoid this different solubility trends upon increasing temperature. Few attempts with DMSO as a solvent were not successful: no perovskite samples could be obtained. We chose, for $\mathrm{MAPb(I_{1-x}Br_x)_3}$ solid solution to use NMP as a solvent. While $\mathrm{MAPbI_3}$ and $\mathrm{MAPbBr_3}$ showed, respectively, a direct and a retrograde solubility in this solvent (see appendix A.2), NMP possesses a higher boiling point than DMF (202 °C and 153 °C respectively), thus allowing us to perform our synthesis at higher temperatures. This approach is inspired by solid state synthesis protocols for alloys, where phase segregation is suppressed by increasing the reaction temperature. We optimized the synthesis temperature in order to avoid sample degradation but also to limit the reaction time and found the optimal temperature to be around 140 °C.

4.3.1. The beneficial impact of annealing

An additional annealing step was required for some compounds of this family. Figure 4.14.a) shows the XRD pattern of an alloy containing 60% Br after the solvent evaporation and grinding (designated as "as synthesized"). One can observe a non-negligible peak asymmetry, similar on all peaks. The black pattern on the figure was measured on the same sample, after a post-synthetic heat treatment at 150 °C for 3 hours (labelled "annealed"). The initially asymmetric peaks have become more symmetric and the relative intensity of the peaks at high angles ($2\theta \geq 50$)) increased, suggesting an improved long range ordering and a decrease in the crystalline defects.

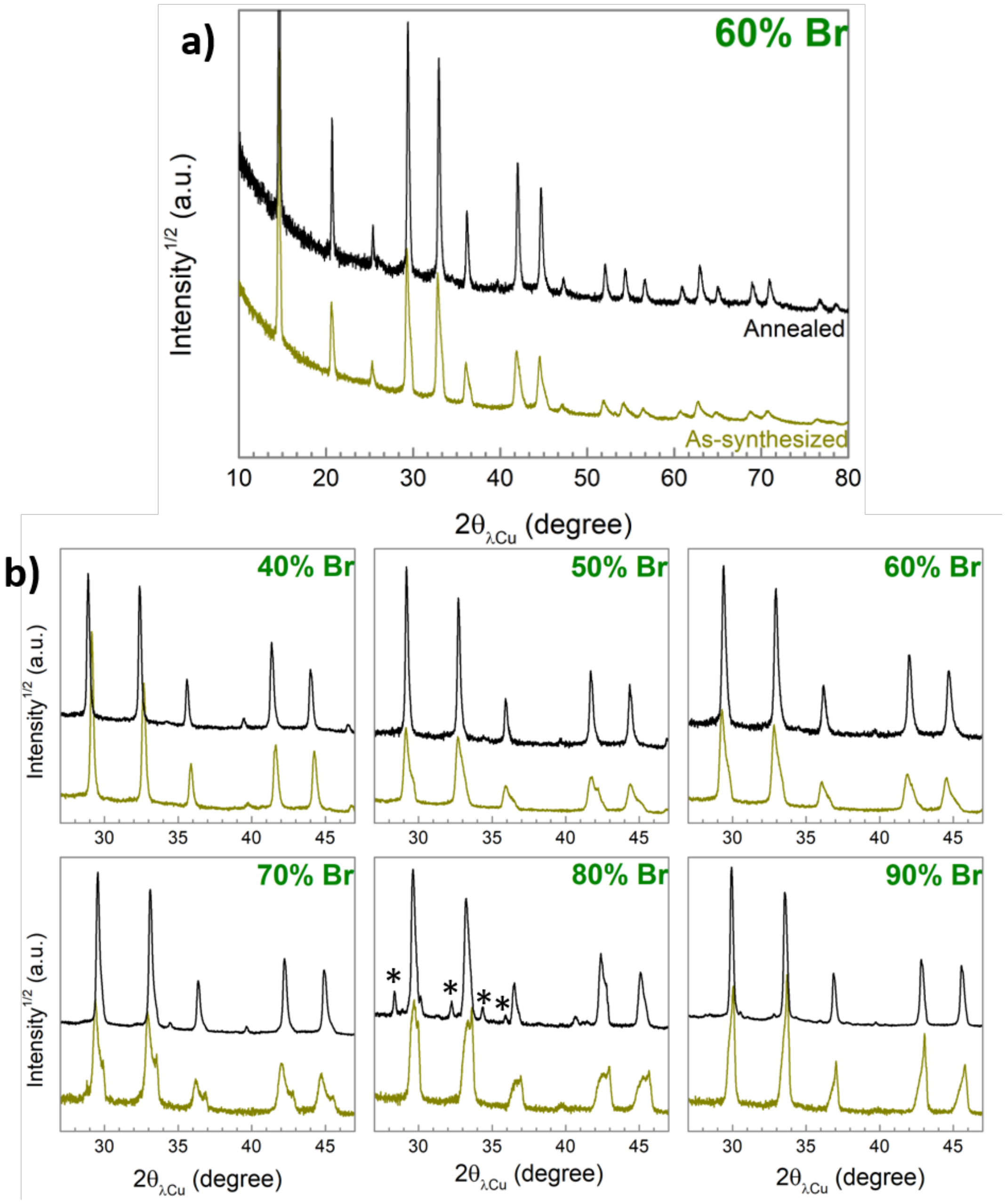

Figure 4.14: XRD patterns highlighting the beneficial impact of annealing on MAPb($I_{1-x}Br_x$)$_3$ solid solution. (a) Wide view of the diffraction pattern before and after annealing of a sample containing 60 % Br and taken as an example. Increased intensites at high angles as well as more symmetric peak shapes indicate of the enhanced crystalline quality of the sample after annealing. (b) Enlarged view illustrating the evolution of the sample after annealing (black). While sample containing 40 % Br is not impacted by annealing, all the other compositions benefits from this supplementary step. In the 80 % Br panel, the stars indicate peaks of PbIBr phase (ICDD 04-007-5333), a degradation product appearing as a result of too long annealing.

For low bromide contents ($x \leq 40$ %) no annealing step is needed. To illustrate that, the first panel of Figure 4.14.b shows that annealing a sample containing 40 % Br has little effect. The other panels on the figure show the peak asymmetry observed for higher bromide concentrations (50 to 90 % Br) before post-synthetic annealing and the positive effect of the latter on these materials. The annealing temperature was 150 °C, chosen to be higher than the synthesis temperature but not high enough to degrade the sample. The annealing time was optimized to balance the improvement of the peak shape (and thus the crystallinity) while avoiding material's degradation (as can be seen in Figure 4.14.b for the sample containing 80 % Br). Table 4.2 in appendix A.2. gathers the optimized annealing times for the different compositions.

The photograph of all the samples of the $MAPb(I_{1-x}Br_x)_3$ family in Figure 4.15.b shows a gradual evolution of the color of the compounds, from black to orange, upon increasing the bromide content in the material. EDX measurements were performed to quantify the chemical composition of the samples. A minimum of 30 measurements on each sample allowed to obtain good statistics on the bromide content. The results are shown in Figure 4.15.b, where we can see a good correspondence between the theoretical values which correspond to the percentages introduced in the precursor solutions and the values extracted from EDX measurements. XRD patterns were measured on all the samples and showed that samples containing 0 ($MAPbI_3$) and 10 % Br were tetragonal at RT. A cubic symmetry was observed for higher Br-contents. Figure 4.15.c depicts the evolution of the peaks in the 27.5 – 30.5 ° 2θ range, showing the (004) and (220) peaks for the tetragonal I4/mcm phases and the (200) for the cubic Pm-3m ones. A monotonous evolution of the peak position is observed indicating smaller lattice parameters when increasing the bromide content, as well as a noticeable peak broadening. The latter, caused by increasing intrinsic strain, will be discussed now.

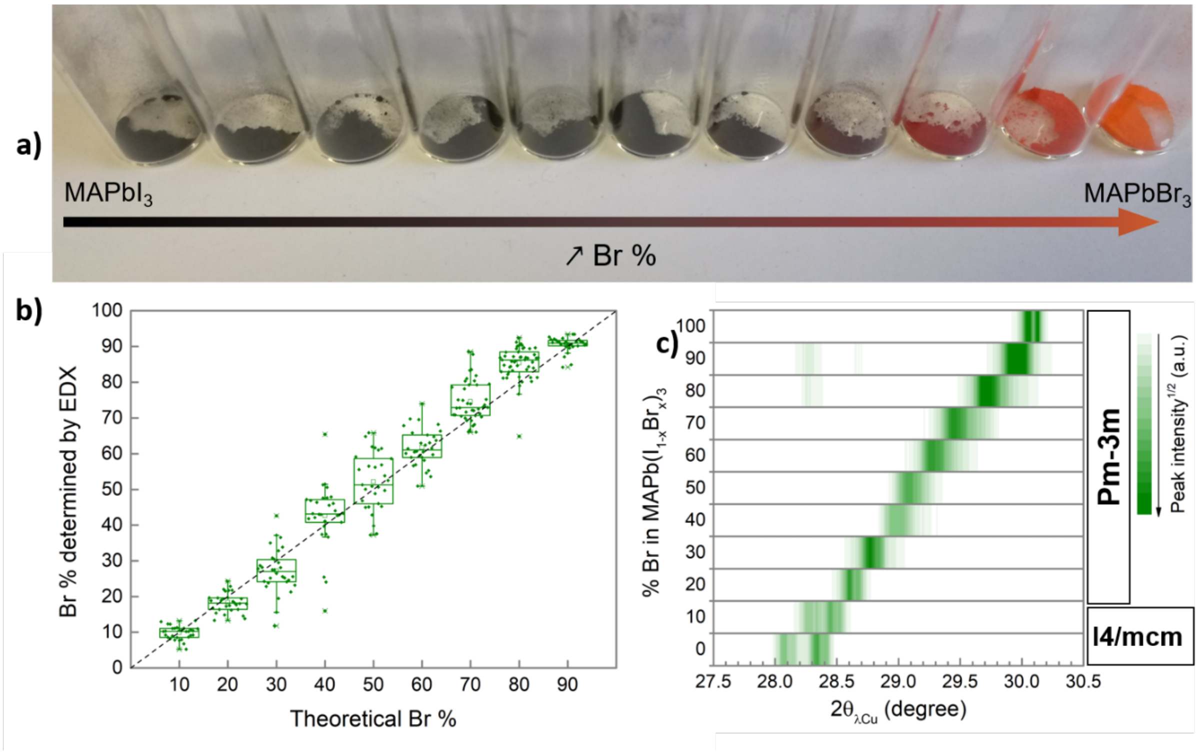

Figure 4.15: (a) Photograph of the samples obtained for the full compositional range in the MAPb($I_{1-x}Br_x$)$_3$ solid solutions, showing a gradual change in the color from black to orange when increasing the bromide content. (b) Statistical representation of the bromide percentage in the material calculated from EDX measurements, showing a good agreement with expected and final composition. The black dotted line (y = x) is a guide for the eye to evidence this good agreement. (c) Evolution of the (004)T and (220)T Bragg reflection for 0 and 10 % Br (tetragonal I4/mcm lattice at RT) and (200)C for higher bromide content (cubic Pm-3m lattice at RT), showing a gradual shift of the peak position to higher angles, indicating a shirking in the lattice parameters.

4.3.2. STACKING FAULTS AND INTRINSIC STRAIN

Peak broadening is observed when introducing increasing amounts of bromide in the material. We examined closely the shapes of the obtained peaks. As shown in Figure 4.16, the peak shapes vary a lot on a reduced 2θ range, as it is most visible for the sample containing 90 % Br^- on the graph. In presence of phase segregation, which means multiple phases with different lattice parameters in the same sample, broad and asymmetric peaks are obtained. Most importantly, when the different phases adopt the same symmetry as it is expected here, the peaks over the whole 2θ range display the same asymmetric shape. Over a reduced 2θ range of 20 ° for example, the resolution can be considered as constant and diffraction peak should have the same shape and FWHM. It is the case on our samples before the annealing as can be observed in Figure 4.14, but the same cannot be said for some of the samples after annealing, as is displayed in Figure 4.16.

An anisotropic line broadening can be considered as it has been done earlier for end compounds. By performing a single peak refinement and extracting the FWHM with the corresponding (hkl) indices, no logic in the peak broadening could be found. Thus, we attribute the difference in peak shapes to the existence of random stacking faults in the crystals, which can be caused by an inhomogeneous distribution of the different halides in the material. Because of the size difference between bromide and iodide (196 pm and 220 pm respectively, cf. Table 4.1), an inhomogeneous distribution of the halides in the material would generates the stacking faults, leading to different peaks shapes where hardly any systematic behavior can be found.

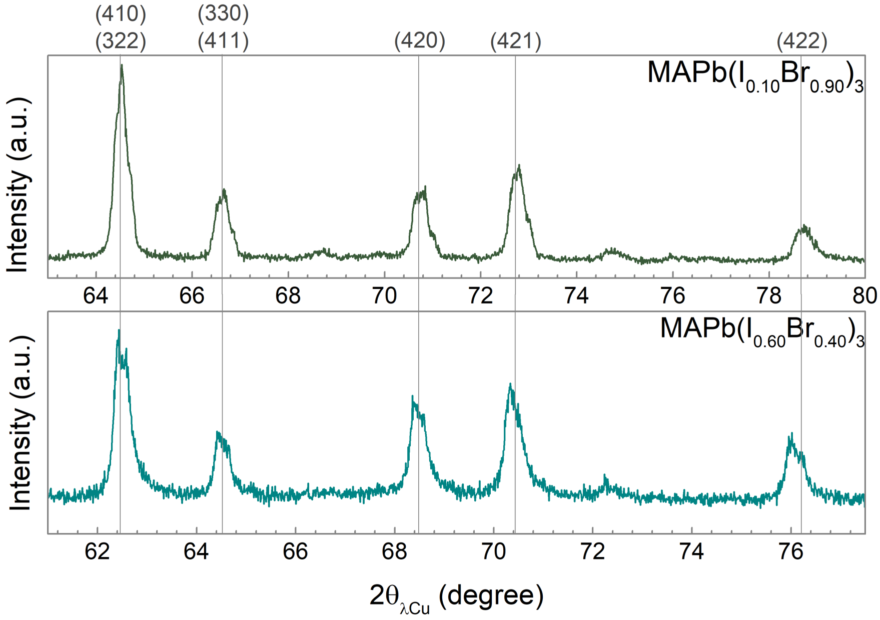

Figure 4.16: XRD patterns of two samples (40 and 90 % Br) showing different peak shapes over a reduced 2θ range of 17 °.

In order to obtain more insight into these stacking faults, we decided to run LeBail refinements on our XRD patterns, considering an isotropic strain. The evolution of the peaks FWHM over the measurement range could not be described when considering isotropic size effects causing the peak broadening, which is coherent with the fact that manual grinding generates micrometric grains. The stacking faults lead to peaks with various shapes that are not described by the isotropic model, even more when the defects are inhomogeneously distributed in the crystal, making them hard to be encountered for in a refinement. Hence, using an isotropic model leads to poorer fits when in presence of these defects. A qualitative idea of the worsening of the fits can be obtained by considering the refinement discrepancy indices. We chose to follow the evolution of the χ^2 factor extracted from the refinement conducted on TOPAS. The χ^2 factor allows evaluating the goodness of the fit relatively to the best fit that could be obtained (more in appendix B.4). An increase in this factor indicates a worsening of the fit. This comparison is very qualitative, and to make it meaningful, we made sure to refine all the patterns in the same conditions: same measurement statistics (counting times), same number of background definition parameters, all parameters fitted in the same order.

Figure 4.17 shows the evolution of χ^2 upon increasing Br-content in the material, as well as two enlarged views of the refinement of two samples: 20 % Br which gives the lowest χ^2 and 80 % Br for which χ^2 is one of the highest. The refinement of the sample containing 20 % Br shows a good agreement between the observed and the calculated peak position, FWHM and intensity whereas the calculated pattern for the 80 % Br sample matches correctly the peak positions and FWHM but fails to reproduce the peak shape. The χ^2 increases noticeably when introducing 40 % Br or more in the sample, translating an increase in the stacking faults. A small decrease is noted for 80 an 90 % Br. Despite the good quality of the refinement for pure $MAPbBr_3$ in terms of peak position, shape, FWHM and area, χ^2 could not be decreased for reasons that I cannot explain.

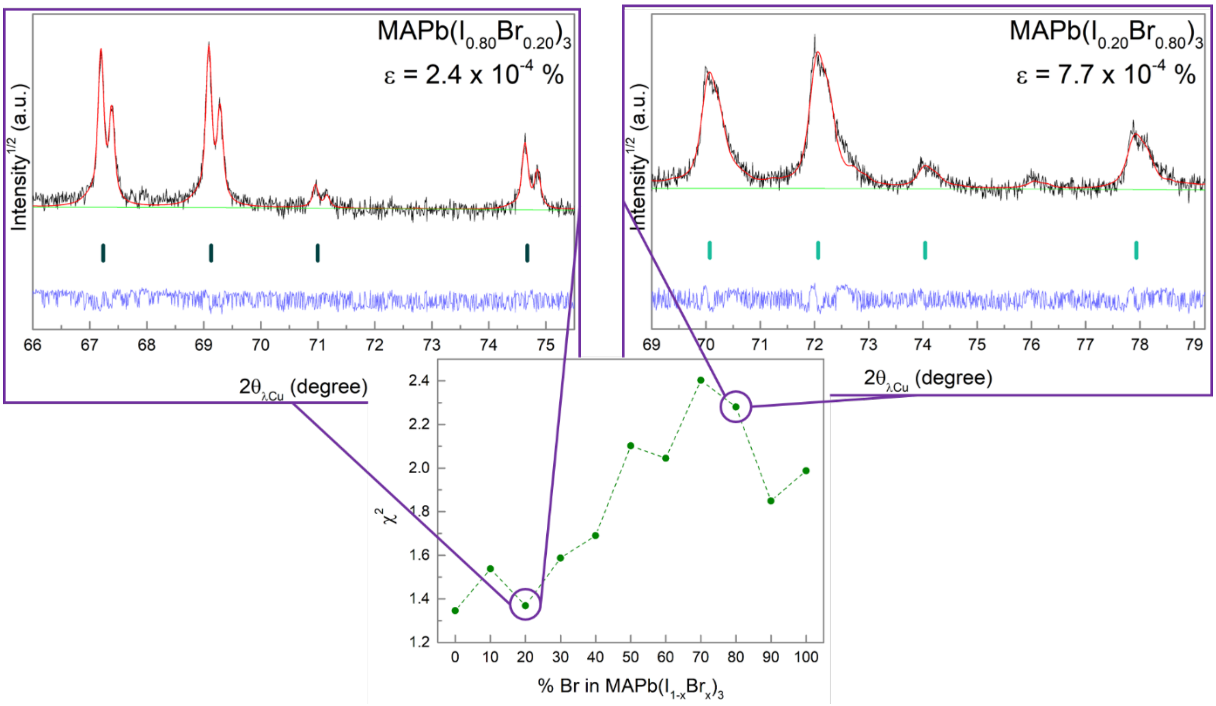

Figure 4.17: Evolution of the LeBail refinement parameter χ^2 over the whole composition range of our solid solution, showing a worsening of the fits with increasing bromide content. The two inset figures illustrate one of the best refinement obtained (for 20 % Br) and one of the worst (80 % Br).

It is interesting to observe the non-symmetric effect of halide mixing on both end compounds: iodine contents as low as 10 % or 20 % in the $MAPbBr_3$ lattice induces more defects (worse refinement) in the lattice whereas relatively fewer defects are observed when introducing up to 40 % Br in $MAPbI_3$ crystals. The same asymmetry is observed from the synthetic point of view: a unique phase is spontaneously obtained when introducing up to 40 % of Br in a $MAPbI_3$ lattice whereas introducing as little as 10 % iodine in $MAPbBr_3$ leads to a phase segregation, and additional thermal energy is required to achieve a single phase. This observation can be rationalized when considering the halides ionic sizes: Br^- ions being smaller than I^-, they lead to a smaller lattice ([pseudo-]cubic lattice parameters of a = 5.9286 Å and 6.267 Å for $MAPbBr_3$ and $MAPbI_3$, respectively) where it requires more energy to introduce a larger ion. On the contrary, the larger $MAPbI_3$ lattice cell accommodates more easily the addition of a smaller ion.

Following the evolution of the sample overtime can bring quite precious information, and indeed a very interesting behavior was observed. As it is shown in Figure 4.18, which displays the example of $MAPb(I_{0.10}Br_{0.90})_3$, when left at ambient conditions, the measurement of the same sample two months after its synthesis shows a striking peak shape evolution, becoming more uniform. Performing a LeBail refinement on the sample after aging, using the isotropic strain broadening model reaches enhanced agreements in comparison with the fresh sample. A direct comparison of χ^2 is not possible as the two samples have not been measured in the same conditions: the fresh sample was measured in the temperature chamber of our diffractometer before our temperature-dependent studies that will be shown in the following chapter, while the aged sample was measured on a classical sample holder, equipped with a blade to reduce diffusion from the sample environment and thus reduce the background. Nevertheless, visual inspection of the refinements suffices to conclude to a better refinement on the aged sample.

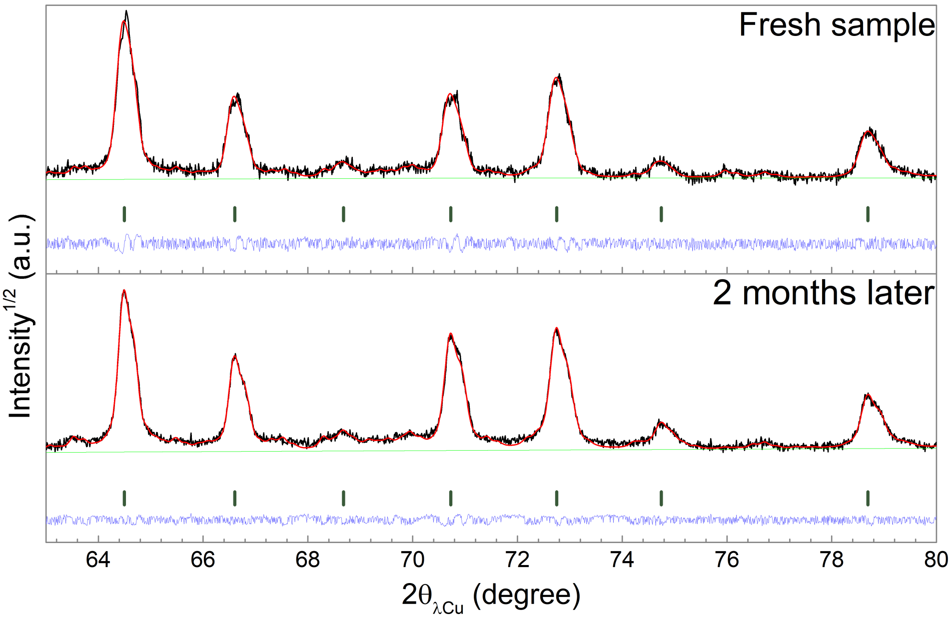

Figure 4.18: XRD pattern of MAPb($I_{0.10}Br_{0.90}$)$_3$ after synthesis and annealing (top panel), and the same sample 2 months later (bottom panel) and corresponding LeBail refinements, showing that the initially inhomogeneous peak shapes that could not be reproduced with an isotropic model evolve to become more symmetric and homogeneous, resulting in a better match with the refinement.

	Fresh sample	Aged 2 months
a (Å)	5.952(2)	5.952 (2)

Table 4.5: Lattice parameters and intrinsic strain values for fresh and 2 months old MAPb($I_{0.10}Br_{0.90}$)$_3$ sample.

Table 4.5 compares the results of the refinement shown in Figure 4.18. Despite one refinement being worse than the other, they both lead to similar lattice parameters, the differences being in the error range. It can be explained by the fact that the refinement of the fresh sample fails to reproduce correctly the average peak shape but manages to fit correctly the peak position, as can be observed in Figure 4.18. However, since the refinement does not model the peak shape correctly, estimation of the intrinsic strain in these compounds is not reliable.

Here, the sample was left under ambient condition (light and atmosphere) and we demonstrated the improvement of the peak shapes which could indicate a homogenization of the halides distribution in the crystal. The same observation was made on other samples, particularly $MAPb(I_{0.30}Br_{0.70})_3$ which initially lead to the worst agreement indices (Figure 4.17). We did not observe phase segregation up to 3 months' storage.

Studies on thin films have shown ion segregation over exposure to light. Numerous studies have been conducted to explain such phenomena, and the current accepted interpretation is that local electric fields generated under light exposure drives the ion migration.[35] Here, our measurements seem to indicate that such phenomenon does not happen over time and light exposure on our powder samples.

As mentioned earlier, **for Br^- compositions of x = 40 − 90 %, an additional annealing step is needed as it first appears that the samples show severe phase segregation. After the annealing step, XRD measurements reveal that these samples can be described as a single phase, displaying however a number of lattice defects which could be due to an inhomogeneous distribution of the halides in the crystals. Nevertheless, it is important to emphasize that, at this stage, no large iodide and bromide-rich region is observed. Moreover, over time and/or upon light exposure, the lattice defects seem to become more homogenous, as we observe improved peak shapes**.

Theoretical reports have shown that these solid solutions are thermodynamically stable above 343 K.[38] Our results seem to indicate that the annealing step helps to stabilize the single-phased structure at RT by introducing additional thermal energy, which could promote halide migration and reduce the presence of iodine-rich and bromine-rich regions. Additional experimental work is needed to investigate the stability over longer periods of time of samples obtained by this high temperature method, and to probe the effect of thermal annealing on thin layers and their stability over light exposure.

In the following, all of our studies have been performed on the fresh sample, despite the observed defects in the structure. We showed, however, that the structural information extracted from the measurements at that time are similar to what is obtained when the sample reaches a better crystal quality. We thus still consider our results to be reliable.

4.3.3. LATTICE PARAMETER, INTRINSIC STRAIN AND BAND GAP EVOLUTIONS

In addition to XRD measurements, UV-visible absorption spectra have been acquired to extract the optical band gap of our materials. Experimental procedure for the measurement on our powder samples is given in appendix C.1. We measured the absorption spectra between 300 and 1100 nm for the whole composition range, and the result is shown in Figure 4.19. A gradual shift of the absorption edge is observed upon increasing the bromide content, indicating, as expected, a band gap tuning through composition. To extract the band gap, we used the Tauc plot method (procedure detailed in appendix C.1) and the resulting curves are displayed in Figure 4.20.a). The evolution of the extracted band gaps is plotted in the insert, showing a linear evolution with increasing Br-content. In their work, Lehmann *et al.* observed a miscibility gap for bromide concentration between 29 and 92 %, and showed that within this range, the same band gap value was extracted for all the compositions.[13] The evolution of the band gap evidenced on our samples constitutes one more strong argument that we formed a solid solution over the whole composition range.

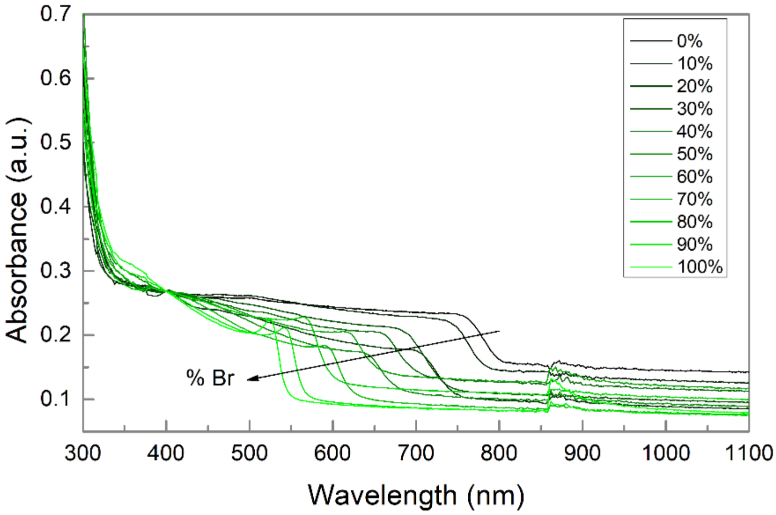

Figure 4.19: Absorption specta of MAPb($I_{1-x}Br_x$)$_3$ solid solution samples over a 300 – 1100 nm wavelength range.

Figure 4.20.b gathers the lattice parameters and the intrinsic strain over the whole family of compounds. The plotted lattice parameter for $MAPbI_3$ and MAPb($I_{0.90}Br_{0.10}$)$_3$ which are tetragonal at RT, is the pseudocubic lattice parameter a_{pC} calculated from the tetragonal lattice parameters a^T and c^T using the following equation:

$$a_{pC} = \sqrt[3]{\frac{a_T^2 \times c_T}{4}} \tag{4.4}$$

The lattice parameters show an evolution close to Vegard's law, despite the predictions made in the literature.[39]

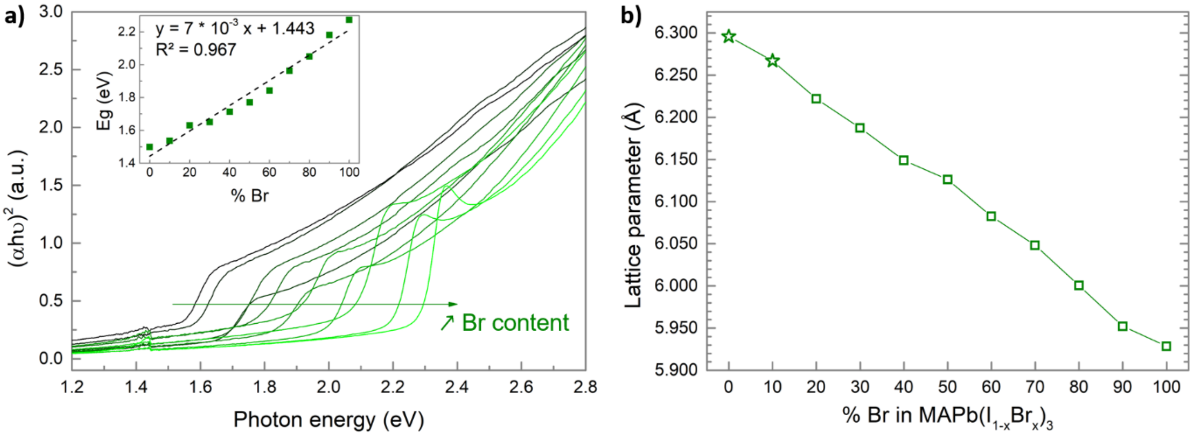

Figure 4.20: (a) Tauc plot showing the evolution of the absorption edge from low to high energies as the bromide content increases. The inset graph shows the extracted band gap and its linear evolution over the whole composition range. (b) Evolution of the lattice parameter. The stars indicate that the plotted lattice parameter is a pseudo-cubic lattice parameter calculated from the tetragonal parameters of the 0 and 10 % Br samples. The error bars being smaller than the markers, they have been omitted for clarity.

By combining detailed data inspection of XRD measurements with UV-visible absorption spectroscopy, **we showed a full solubility of bromide and iodide ions in the $\mathbf{MAPb(I_{1-x}Br_x)_3}$ solid solutions. Interestingly, despite the presence of important lattice defects in our materials, as shown by the XRD peak shapes, the properties of the samples in terms of lattice parameters and band gap evolution in function of the composition follow the prediction of Vegard's law**. We believe that our approach where the samples are synthesized at higher temperature and annealed afterwards leads to full solubility and stability over time.

4.4. $FAPb(I_{1-x}Br_x)_3$ SOLID SOLUTIONS

The second family solid solutions we studied is $FAPb(I_{1-x}Br_x)_3$. A recent theoretical study predicted a full solubility of the halides,[40] while experimental reports showed different results. To the best of our knowledge, all the investigations have been performed on thin layers. While some studies reported the presence of a miscibility gap between 30 and 50 % of inserted bromide,[41,42] others have not commented the poor crystallinity of their samples in this same range of composition.[37,43] Finally, some teams have suggested a symmetry lowering to a tetragonal phase but with conflicting ranges of composition.[40,41,44]

To obtain our powder samples, we had to use different solvents: for low Br contents ($x_{Br-} \leq 20$ %), GBL was the only solvent to lead to highly crystalline powder. The samples were synthesized at 120 °C. For high Br contents ($x_{Br-} \geq 60$ %), NMP was used, in the same way as for $MAPb(I_{1-x}Br_x)_3$ and the solvent was evaporated at 140 °C. Moreover, no post-synthetic annealing step was needed here. Finally, and in good agreement with the literature, for middle range compositions ($30 \% \leq x_{Br-} \leq 50 \%$), no cubic structure could be obtained (the obtained powder was inspected through XRD after each synthesis), despite varying the solvent (GBL, NMP, DMF, DMSO). We bring, in the following, rationalization elements to this observation. As the starting material is the $FAPbI_3$ which shows spontaneous polymorphism at RT, we start this section by investigating the effect of halide substitution on this behavior. We move afterwards to the characterization of the obtained perovskite $FAPb(I_{1-x}Br_x)_3$ phases.

4.4.1. Effect of halide substitution on $FAPbI_3$ polymorphism

In the same way as $FAPbI_3$, low-Br containing samples are obtained in the black perovskite phase after synthesis. Visual inspection of these samples over time revealed changes in their color, as illustrated in Figure 4.21. Multiple syntheses were performed to ensure the reproducibility of our observations.

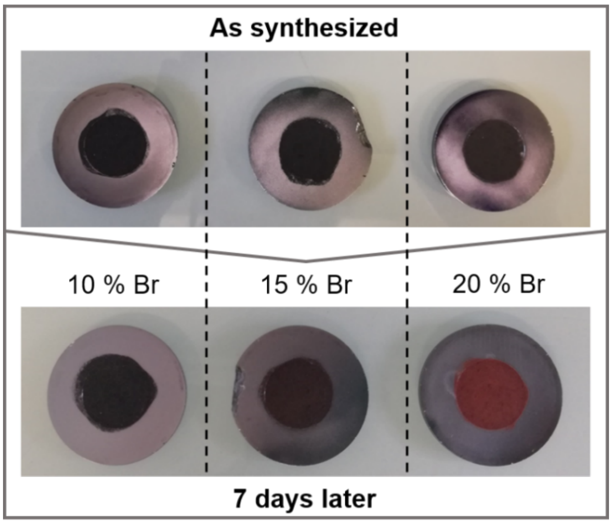

Figure 4.21: Photographs showing the spontaneous evolution of $FAPb(I_{1-x}Br_x)_3$ samples with low bromine content (10, 15 and 20 %) after one week under ambient conditions.

Evaluation of the exact transition kinetics was not our main focus in this study, as it depends a lot on the sample's environment (temperature, humidity, etc). Despite being performed under identical conditions, replicates of the synthesis of the sample containing 10 % Br led to different behaviors. While some samples retained the cubic perovskite phase for up to 1 month after synthesis, other samples exhibited XRD peaks characteristic of the δ-FAPbI$_3$ phase in addition to cubic perovskite ones, one week after the synthesis (Figure 4.22). The conclusion to be drawn from this observation is that while introduction of 10 % Bromide in the FAPbI$_3$ lattice seems to slow its transition to the δ-phase, the α-phase remains metastable.

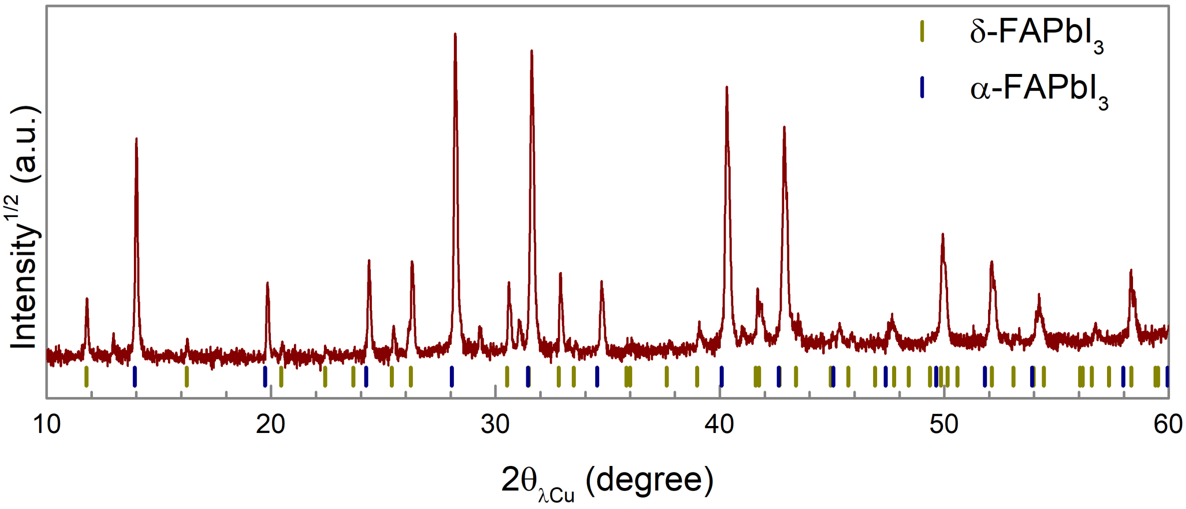

Figure 4.22: XRD pattern of FAPb(I$_{1-x}$Br$_x$)$_3$ containing 10 % Bromide measured one week after its synthesis and showing peaks characteristic for both δ and α-FAPbI3 phases.

For higher Br-contents (15 and 20 %), the sample color evolves to become reddish (Figure 4.21), different from the bright yellow observed for δ-FAPbI$_3$ (Figure 4.3). Replicate syntheses showed that this evolution is reproducible and cannot be avoided. XRD measurements revealed the formation of the same crystallographic phase in both samples. A full-range XRD pattern was measured on the sample containing 20 % Br when the phase conversion was complete (partial measurements over an optimized 2θ range were performed at regular intervals until no more peaks of the cubic α phase were observed). All the peaks of this phase were attributed to the hexagonal 4H polymorph identified by Gratia *et al.*.[22] The structure of this polymorph is shown in Figure 4.6, showing alternating hexagonal and cubic stackings. LeBail refinement was performed leading to lattice parameters of a = 8.7658(2) Åand c = 15.1834(2) Å, similar to the reported values.

Moreover, we registered and compared the UV-visible signature of this sample with the one obtained for δ-FAPbI$_3$. The latter exhibits a single and very well defined absorption peak around 450 nm, which might be attributed to quantum confinement effects in the 1D octahedral structure, as photogenerated electron-hole pairs are confined in two directions in space. 4H-20 %Br, on the contrary, shows multiple absorption features, similar to what Gratia *et al.* measured on thin layers of (FAPbI$_3$)$_{0.80}$(MAPbBr$_3$)$_{0.20}$. Importantly, all of these absorption edges happen at higher wavelengths, in coherence with the red color, evidencing a smaller band gap. This latter phenomenon is explained by the elements discussed in section 4.2: 4H hexagonal structure exhibits lower octahedra connectivity than the 2H (δ-phase) hexagonal polytype, directly impacting the band gap. In the 4H polytype, the confinement effects are smaller than in the 2H structure due to the corner-sharing of the 2-octahedra subunits and mixed hexagonal/cubic stacking, which leads to a smaller band gap.

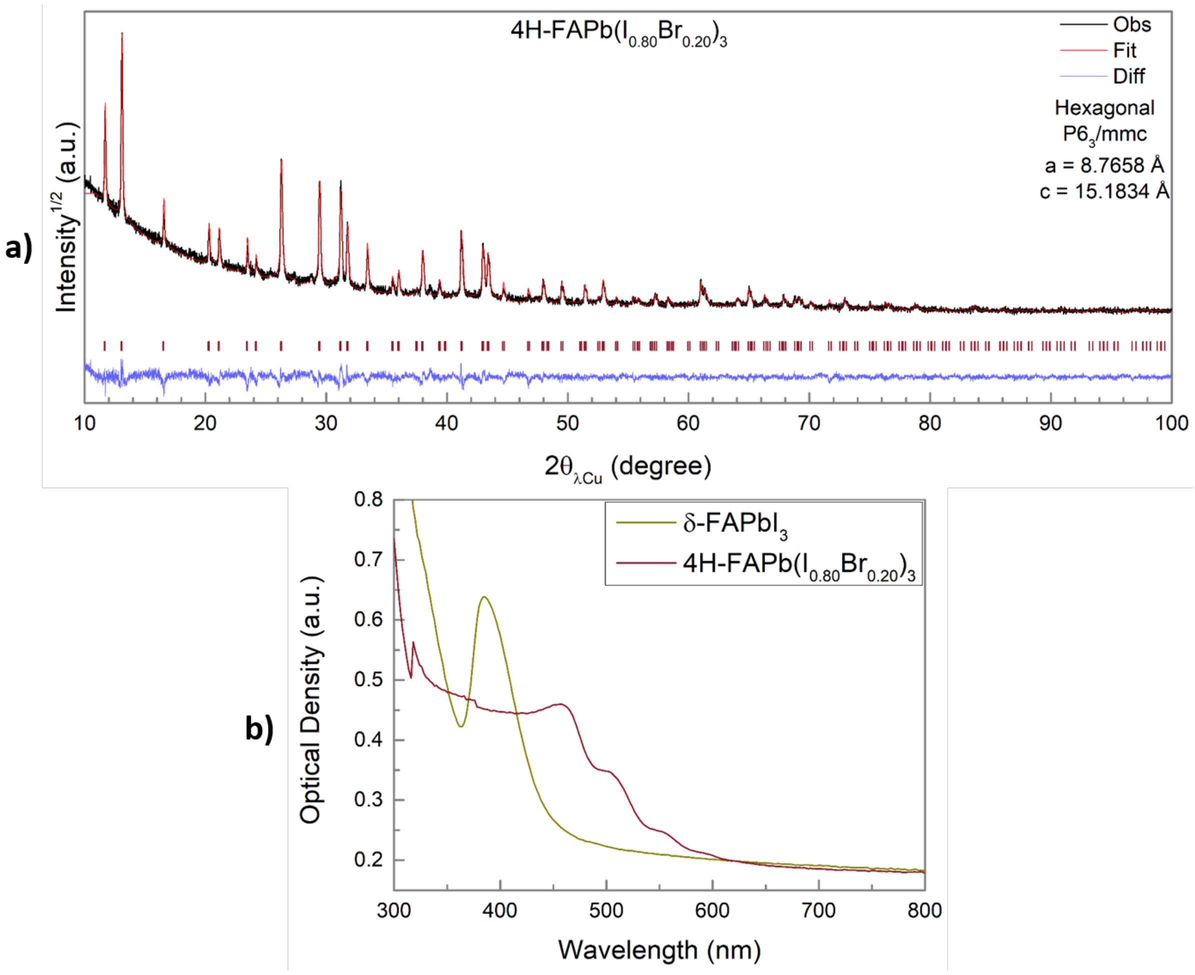

Figure 4.23: (a) LeBail refinement of the red phase of $FAPb(I_{0.80}Br_{0.20})_3$ confirming the presence of the hexagonal 4H polytype. (b) comparison of the 2H-FAPbI3 (δ-phase) and red $FAPb(I_{0.80}Br_{0.20})_3$ UV-vis absorption spectra, showing different signatures arising from the two samples.

To summarize the results on the samples with low Br content, introducing up to 20 % Bromide does not suppress $FAPbI_3$ polymorphism. **The initially cubic crystals eventually evolve into the 2H hexagonal polytype even when introducing up to 10 %-Br in the lattice. When increasing the bromide content up to 20 %, the initially 3C sample evolves into the 4H polytype**, alternating hexagonal and cubic stacking of the $[PbX_6]^{4-}$ octahedra. Through single crystal XRD measurements, Gratia *et al.* observed that in 4H and 6H polytypes, Br^- anions preferentially occupied the corner sharing octahedra (cubic packing), leaving the iodine anions at the center of the face-sharing ones.[22] As mentionned in subsection 4.2.1, **this observation can be explained by the high electrostatic repulsion that would be generated if** $[PbBr_6]^{4-}$ **octahedra were hexagonally packed**. This preferential site occupancy of bromine allows explaining the apparition of the 4H-hexagonal polytype when introducing 15 and 20 % Br^- in $FAPbI_3$.

When heated to 150 °C, the three samples (10, 15 and 20 % Br) recovered the cubic Pm-3m phase. Similarly to pure $FAPbI_3$, this latter arrangement can be stabilized for few hours at RT after heat treatment, before eventual polymorphic transformation.

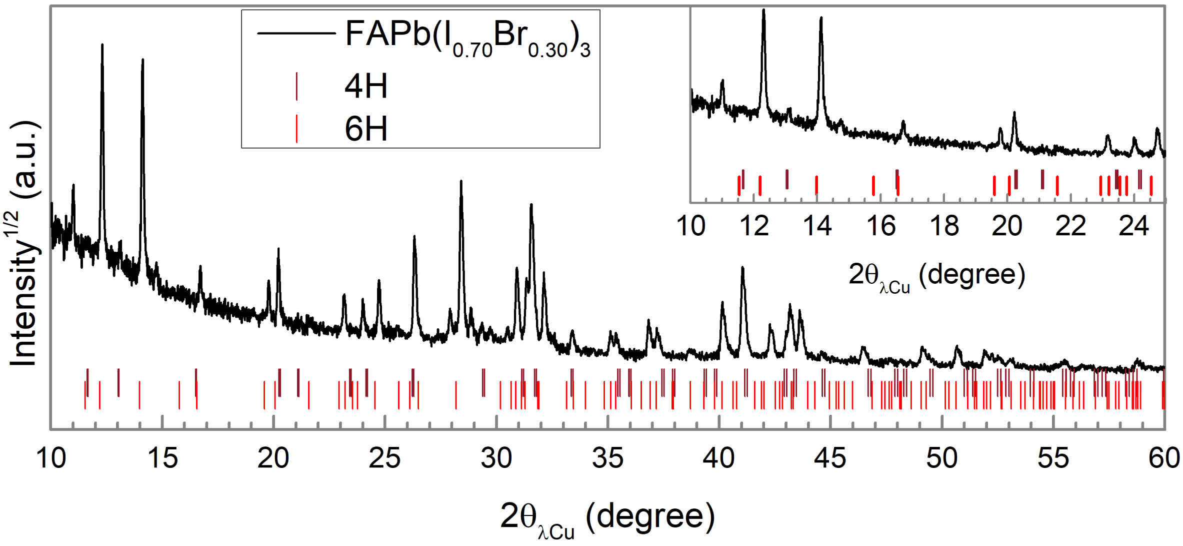

Figure 4.24: XRD pattern of a $FAPb(I_{1-x}Br_x)_3$ sample containing 30 % Br showing that the observed peak match those expected for the 4H and 6H hexagonal polytypes identified by Gratia *et al.*.[22] An enlarged view is presented in the inset of the figure.

Concerning the sample containing 30 to 50 %Br, as explained earlier and in agreement with the literature, no perovskite phase could be obtained. The synthesis lead to red-orange samples, and XRD measurement revealed poorly crystalline samples, with the same low intensity peaks present for all the samples. Figure 4.24 shows the similarities of the XRD pattern of a sample containing 30 % Bromide and the expected peaks for both 6H and 4H. We can say that the obtained material contained at least two hexagonal polytypes. We already know that when in presence of FA^+ anions, while the $[PbI_6]^{4-}$ preferentially adopt a hexagonal packing, a corner-sharing packing is more favorable for $[PbBr_6]^{4-}$. **In presence of equivalent contents of** I^- **and** Br^- **($30\ \% \leq x_{Br} \leq 50\ \%$), $FAPb(I_{1-x}Br_x)_3$ compounds seem to form different hexagonal polytypes**

over the whole temperature domain probed here (up to 200 °C), with different alternating sequences of hexagonal and cubic packed octahedra layers. Annealing up to 200 °C did not allow to form a cubic 3C perovskite packing. Finally, **for higher bromide composition (x $\geq$ 60 %), the cubic Pm-3m structure was obtained and no polymorphic behavior was observed**.

4.4.2. CUBIC PEROVSKITE PHASE CHARACTERIZATION AT RT

After investigating the polymorphism in this family of compounds, we now focus on the characterization of the cubic phases obtained. In most of the figures of the section, the 30 to 50 % Br compositional range will be covered by a grey area, as these samples adopt a hexagonal structure.

Figure 4.25.a shows a photograph of the obtained sample, exhibiting in the same way as in the MAPb($I_{1-x}Br_x$)$_3$ family, a gradual change in color from black (FAPbI$_3$) to orange (FAPbBr$_3$). Here again, the amount of bromide in the sample was tested by EDX (Figure 4.25.b), showing a good agreement between the introduced and the observed values. Finally, Figure 4.25.c illustrates the shift to higher angles of the (200) Pm-3m peak measured by XRD, indicating a smaller lattice when increasing the amount of Br^- in the crystal.

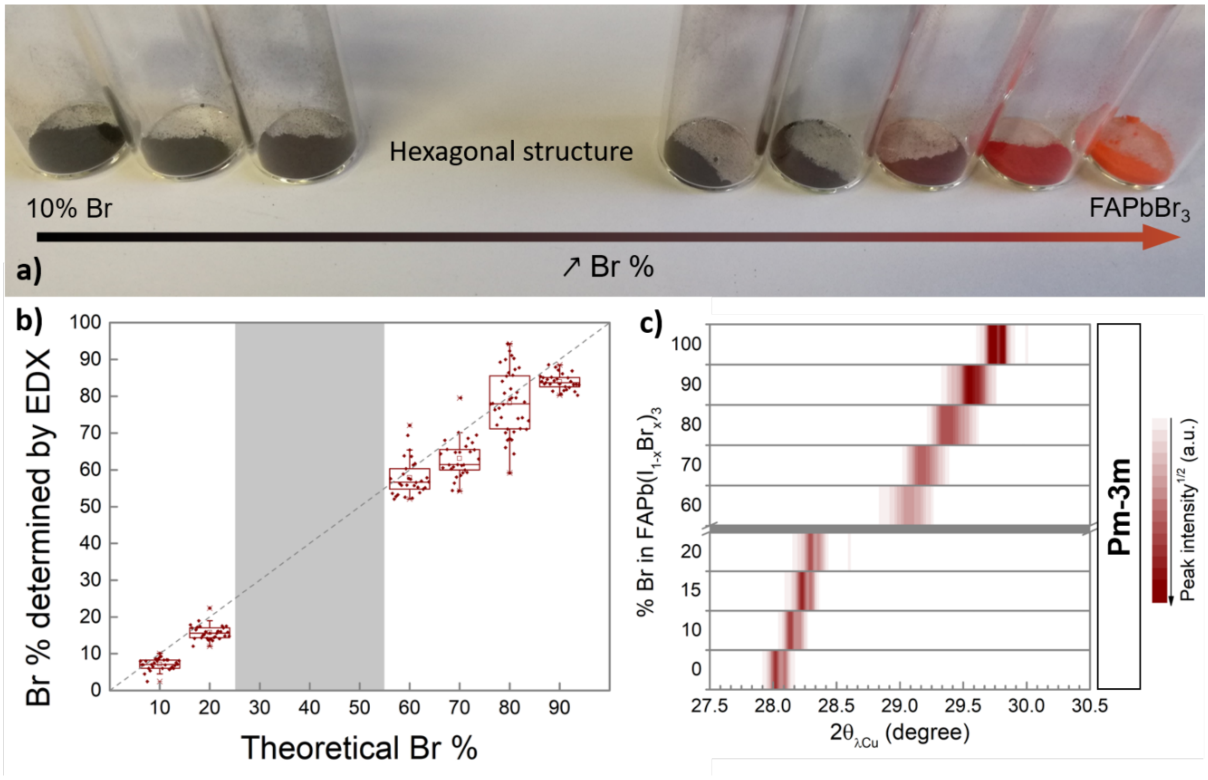

Figure 4.25: (a) Photograph of the perovskite $FAPb(I_{1-x}Br_x)_3$ samples, showing a gradual change in the color from black to orange when increasing the bromide content. (b) Statistical representation of the bromide percentage in the material calculated from EDX measurements, showing a good agreement with expected and final composition. (c) Evolution of the (200) cubic Pm-3m Bragg peak, showing a gradual shift of the peak position to higher angles, indicated a shrinking of the crystal unit cells.

Here, no additional annealing step was needed. As the Br contents introduced in the sample increased, peak broadening is observed, as can be seen in Figure 4.25. However, in opposition to $MAPb(I_{1-x}Br_x)_3$ samples, the peak shape was uniform and symmetric over the whole XRD pattern for all the compositions studied here, indicating that the cubic $FAPb(I_{1-x}Br_x)_3$ did not exhibit the stacking faults which we attributed to inhomogeneous halides distribution in the MA-based mixed halide compounds. LeBail refinement was performed (Figure 4.26), allowing us to attribute this broadening, to intrinsic strain effects.

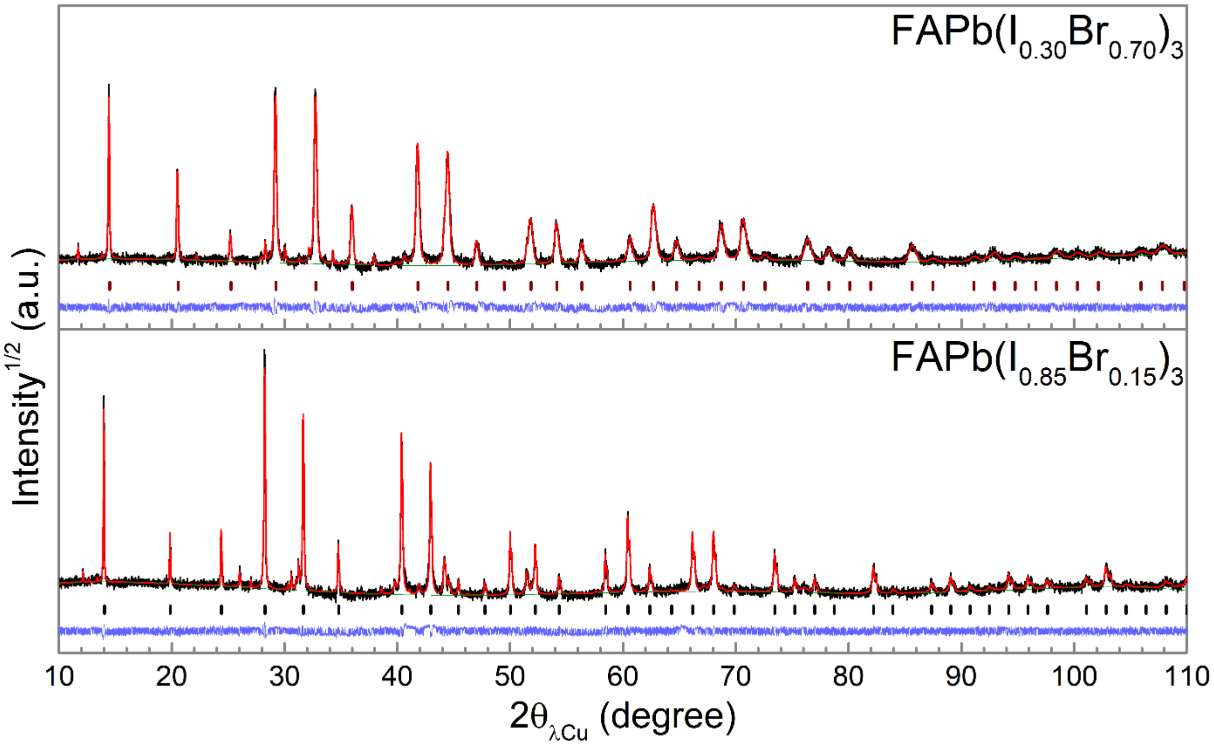

Figure 4.26: Example of LeBail refinement on two $FAPb(I_{1-x}Br_x)_3$ samples with different Br-composition: 15 % Br (bottom panel) and 70 % (top panel).

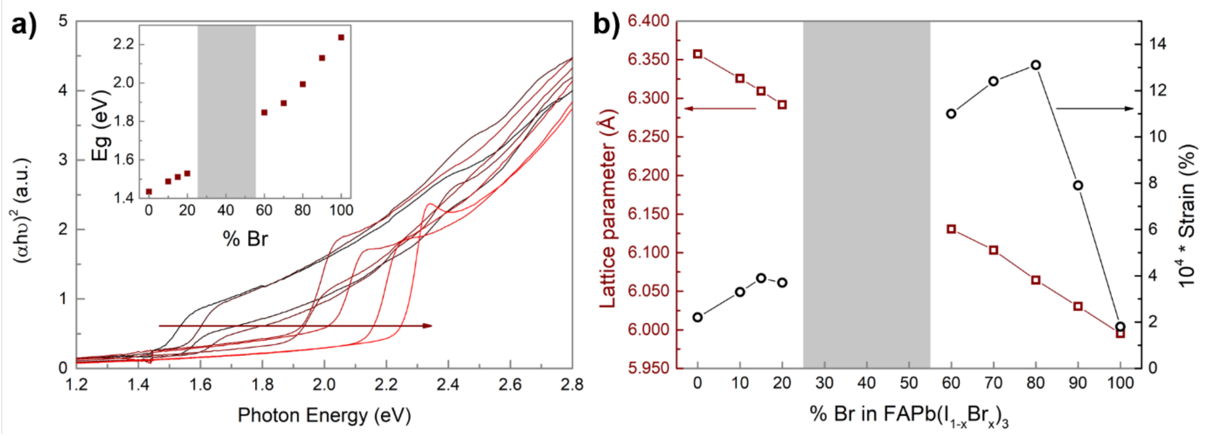

Figure 4.27: (a) Tauc plot showing the evolution of the absorption edge from low to high energies as the bromide content increases. The inset graph shows the extracted band gap and its evolution with increasing Br-content. (b) Evolution of the lattice parameter (in red) and the intrinsic strain from XRD measurements. The error bars being smaller than the markers, they have been omitted for clarity

Here again, samples' band gap was extracted from UV-visible spectroscopy, through the Tauc-plot method. Displayed in Figure 4.27, the absorption edge and thus the band gap (in inset), gradually and linearly evolve, indicating a band gap tuning from 1.43 ($FAPbI_3$) to 2.24 eV ($FAPbBr_3$) through composition. The lattice parameters extracted from LeBail refinements show a linear evolution (Figure 4.27.b in red), following Vegard's law. Concerning the intrinsic strain displayed in Figure 4.27.b) in black, it slowly increases before the hexagonal structure region, and quite high values are observed after the gap, with a maximum reached around 80 % Br. The asymmetry of the Br-content dependency of the strain observed here resembles the one reported on $MAPb(I_{1-x}Br_x)_3$ solid solution and it can be explained by the same ion radii and lattice metrics arguments.

Let us summarize our findings concerning the halide substitution in $FAPb(I_{1-x}Br_x)_3$ solid solution family. **We demonstrated that the introduction of Br^- in $FAPbI_3$ lattice does not suppress its polymorphism as increasing amounts of Br^- lead to the stabilization of different hexagonal polytypes** : 2H for 0 % $\leq x_{Br} \leq$ 10 %, 4H for 15 % $\leq x_{Br} \leq$ 20 % and at least two different hexagonal structures (4H and 6H) for 30 % $\leq x_{Br} \leq$ 50 %. Stable cubic Pm-3m structure is adopted at RT for $x_{Br} \geq$ 60 %. Low Br-containing samples ($x_{Br} \leq$ 20 %) can be stabilized at RT in a cubic Pm-3m structure after heat treatment for some time, while this cubic arrangement could not be stabilized for intermediary compositions 30 % $\leq x_{Br} \leq$ 50 % where the hexagonal structures remains favored for the whole temperature domain probed. **These observations where explained by the electrostatic repulsion of Pb^{2+} which makes the hexagonal arrangement of $[PbBr_6]^{4-}$ octahedra unstable.**

The compositions for which the cubic structure could be obtained were found to exhibit linear evolution of the band gap and the lattice parameters, following Vegard's law. However, important intrinsic strain was observed, with higher values for Br-rich samples.

4.5. $FA_{1-x}MA_xPbI_3$ family : effect of cation substitution at RT

Thanks to their easy fabrication, $FA_{1-x}MA_xPbI_3$ compounds have been synthesized under various forms (single crystals,[45,46,47] powders[48] and thin layers[49,50]) over the whole composition spectra (from 0 to 100 % FA^+ ions in the structure). The complete solubility of FA^+ in MA^+ is well established. Figure 4.28 recalls the structure of the two molecular cations, illustrating the larger permanent electric dipole of MA^+ in comparison to FA^+ (2.2 D in the former and 0.2 D in the latter[51]).

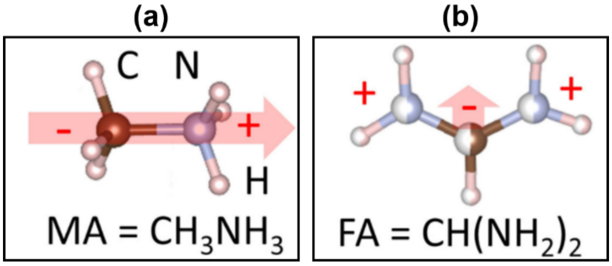

Figure 4.28: Structure of the organic cations methylammonium MA^+ (a) and formamidinium FA^+ (b). The red arrow indicates the direction and the magnetude of the dipolar moment of these molecular cations. Adapted from[52]

To obtain their powder samples, Pisanu *et al.* precipitated the compounds by controlling the cooling of the solution temperature, filtrating the obtained precipitate and then vacuum drying for 24h.[48] We used an easier and quicker synthetic path, presented above. $FAPbI_3$ and $MAPbI_3$ exhibiting the same retrograde solubility behavior in GBL, we used this solvent to make our samples. The solvent was dried at 120 °C and pure powder was obtained, with no need for further annealing. Inspired by Weber *et al.*,[46] we quantified the relative proportions of the organic compounds in the final sample through 1H liquid state NMR. The results are presented in Table 4.6, showing values estimated from NMR fairly close to the expected ones.

Expected MA %	10	20	30	40	50	60	70	80	90
Calculated MA % from NMR	7	18	29	35	47	61	74	85	96

Table 4.6: Expected VS estimated from NMR amounts of FA^+ ions inserted in the perovskite structure.

Following the same logic as in the previous section, we start by investigating the effect of organic cation substitution on $FAPbI_3$ polymorphism before focusing on the resulting perovskite phase.

4.5.1. Effect of cation substitution on $FAPbI_3$ polymorphism

In this section, we consider $FAPbI_3$ to be the starting material in which we introduce increasing amounts of MA^+ cations. When only 10 % of FA^+ is substituted by MA^+, the δ-phase (2H stacking) appears rather quickly. Figure 4.29 top panel displays the XRD pattern measured on the sample 45 days after its synthesis; the sample being kept for the whole time at ambient conditions. All peaks were identified as corresponding either to the δ-phase or the cubic 3C stacking, as shown by the LeBail refinement over the whole measurement range displayed in Figure 4.29 top panel.

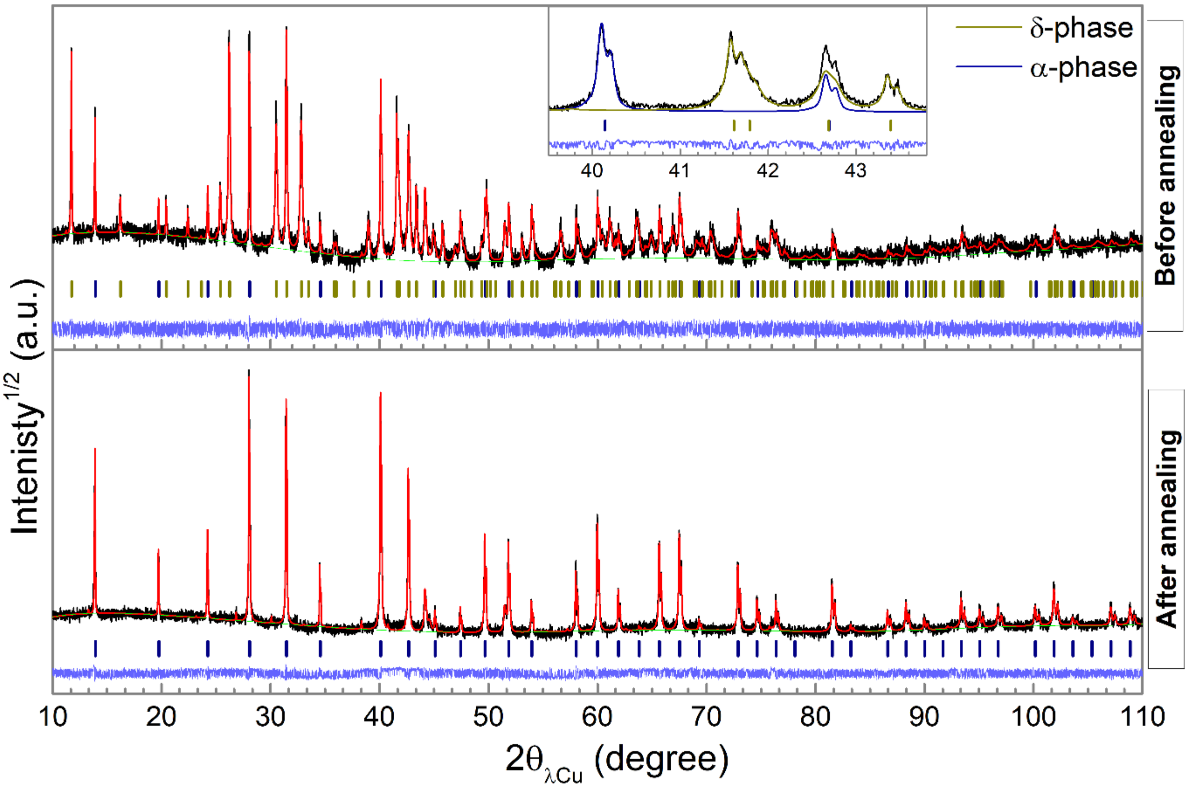

Figure 4.29: LeBail refinement of $FA_{0.90}MA_{0.10}PbI_3$. Top panel shows the powder profile of the sample aged for 45 days at ambient condition, displaying both δ and α-phases. Bottom panel shows the same sample after annealing at 150 °c for 1h, leading to the disappearance of the δ-phase.

Interestingly, anisotropic line broadening was observed on the peaks corresponding to the hexagonal structure, similarly to what was observed during the conversion of δ to α-$FAPbI_3$ upon heating (subsection 4.2.1). Earlier, we observed that (hkl) peaks with h and/or k non-zero and l no zero exhibit larger FWHM than other peaks and we explained this phenomenon by the weakening of the interaction between face-sharing octahedra. Here, the measurement was performed during the conversion of the sample from the cubic phase to the hexagonal polymorph, as both phases coexist. We can thus say that the anisotropic line broadening can, here again, be attributed to the weak interaction between adjacent $[PbI_6]^{4-}$ as the conversion process for corner-sharing to face-sharing is in progress.

The sample was annealed at 150 °C for 1h and, as shown in the bottom panel of Figure 4.29, a unique cubic Pm-3m phase was recovered and stabilized for few days before apparition of δ-phase once again, following the same behavior as $FAPbI_3$.

Moreover, we followed the evolution over time of samples containing higher MA^+ cations, tracking if any polymorphism can be detected. Samples were followed for 2 months. As shown in Figure 4.30, introducing 20 % MA^+ allows to suppress the cubic-hexagonal polymorphism, at least at the time scale of our study. No α to δ-phase transformation is observed for higher MA^+ contents. In agreement with previous reports,[53] **the introduction of 20 % MA^+ allows to suppress the polymorphism in $FAPbI_3$**.

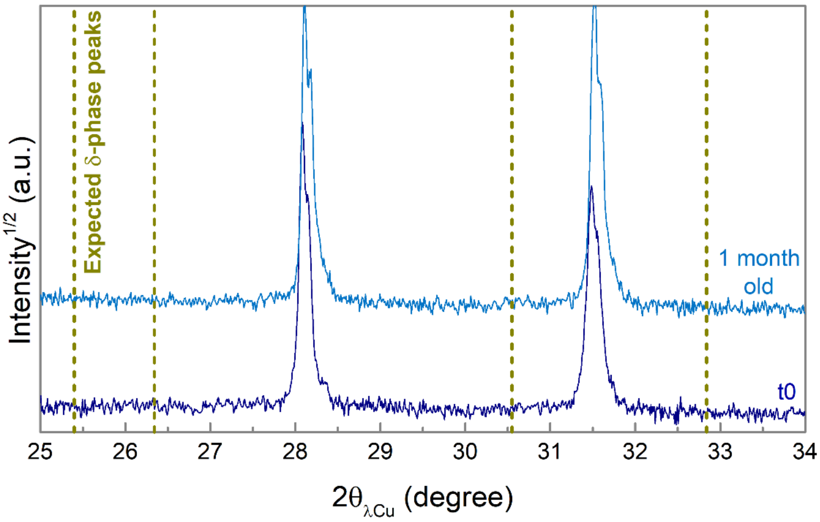

Figure 4.30: Tracking the evolution of $FA_{0.80}MA_{0.20}PbI_3$ over time, evidencing the stability of the α-cubic phase.

It is interesting to point that, in opposition to $FAPb(I_{1-x}Br_x)_3$, no other hexagonal polymorphs than 2H structure were observed. **The substitution of FA^+ by MA^+ is found to be highly effective to suppress the polymorphism of $FAPbI_3$. This observation might be linked to the strong impact of the cation substitution on the tolerance factor**, as pointed out in Figure 4.1, in subsection 4.1.1. Even though we demonstrated that the tolerance factor cannot be considered as the only requirement for the cubic structure stability, it remains a good indicative factor. In the case of $FA_{1-x}MA_xPbI_3$ compounds, cation substitution quickly leads to a decrease of the tolerance factor value. Despite the higher polarity of MA^+ cation, the hydrogen bonds were found to be rather weak at RT in both $FAPbI_3$ and $MAPbI_3$,[51] hence the stabilization cannot be explained by the creation of H-bonds when introducing MA^+ in the compound. Tolerance factor, and thus size arguments, seem to be the more valid justification for the cubic structure stabilization.

In the following, besides $FA_{0.90}MA_{0.10}PbI_3$ which needed thermal annealing to retain a little longer the cubic perovskite phase, all the sample were studied as synthesized, without further annealing.

4.5.2. Cubic perovskite phase characterization at RT

A photograph of the samples over the whole composition range is shown in Figure 4.31.a. α-FAPbI3 and $MAPbI_3$ having close band gap values (Table 4.3) being both black, it is no surprise to see that samples in the $FA_{1-x}MA_xPbI_3$ retain the black color for all compositions. An enlarged color-map of the RT XRD measurement of all the samples around the cubic (200) peak is displayed in Figure 4.31.b. It shows a small but gradual shit of the peak to the higher angles when increasing the amount of MA^+ inserted in the lattice, in agreement with the smaller lattice parameter of $MAPbI_3$ in comparison with α-FAPbI3. As thoroughly discussed in the first part of the manuscript, $MAPbI_3$ adopts a tetragonal symmetry at RT. $FAPbI_3$ is cubic at RT,[28] and we observe that the cubic symmetry is retained up to 80 % of MA^+ cation insertion. For samples containing 90 % MA^+, the sample adopts $MAPbI_3$ tetragonal symmetry at RT.

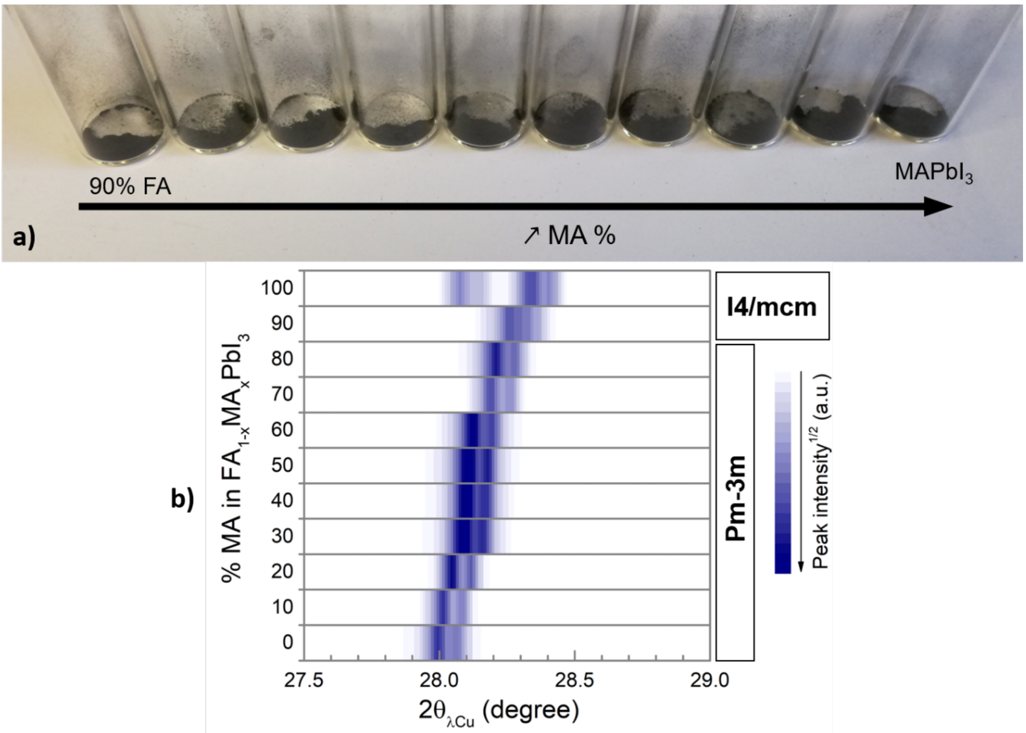

Figure 4.31: (a) Picture of the $FA_{1-x}MA_xPbI_3$ solid solutions family. The sample remain black over the whole compositional range. (b) Evolution of the (200) cubic Pm-3m Bragg peak, showing a gradual shift of the peak position to higher angles, indicated a shirking in the lattice parameters. Note the small range of variation of the peak position (1.5 °) in comparison with the two previous families (3°). Furthermore, note that both 90 and 100 % MA^+ containing samples exhibit a tetragonal symmetry at RT

In opposition to what we highlighted for the mixed halides solid solutions, increasing the amount of inserted ions in the $FA_{1-x}MA_xPbI_3$ lattice did not result in a noticeable increase of the peaks FWHMs as can be seen from Figure 4.31.a. However, we observed the appearance of non-negligible strain anisotropy. To our knowledge not reported in the literature, this anisotropy was not easily detected, and it is while performing LeBail refinement with an isotropic strain model that we noticed that the refinements did not reproduce correctly the peaks intensities and FWHMs for all samples (an example can be seen in Figure 4.32.b) top panel). The same method as in subsection 4.2.2. was used to identify the direction of the anisotropic strain induced peak broadening. Single peak fitting was performed on TOPAS to obtain corrected FWHM and we drew Williamson-Hall plots. Figure 4.32.a illustrates the sample which exhibited the highest anisotropy: $FA_{0.50}MA_{0.50}PbI_3$. It clearly appears that, similarly to end-compounds, smaller strain is observed along [100] direction, while [110] and [111] directions exhibit higher strain, both in the same range. Here again, Stephens cubic lattice model was used to refine the strain anisotropy: Lorentzian peak shape was used and only S_{220} parameter was refined, allowing to reach satisfying results (Figure 4.32.b bottom panel).

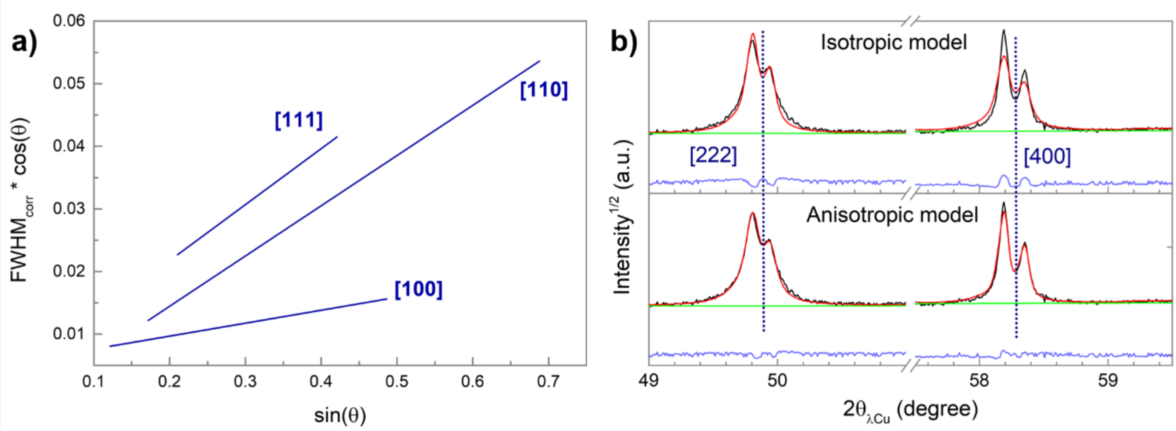

Figure 4.32: Anisotropic line broadening in $FA_{0.50}MA_{0.50}PbI_3$. (a) Williamson-Hall plot obtained from single-peak fitting, showing enhanced strain along [110] and [111]. (b) Comparison of the LeBail refinement using isotropic strain (top panel) and anisotropic strain (bottom panel).

As explained earlier, samples with 90 and 100 % MA^+ adopt a tetragonal lattice at RT and no direct comparison with the other samples can be done. However, while no anisotropy is needed for $MAPbI_3$, tetragonal $FA_{0.10}MA_{0.90}PbI_3$ exhibits noticeable anisotropic line broadening. While finding the direction showing anisotropy was easily done through single peak fitting and Williamson-Hall plot in the case of cubic cells, it is not as easy for this sample. In addition to being tetragonal and thus having multiple reflections contributing to the same peak, a and c lattice parameters are quite close, making the determination of each plane real contribution to the peaks' FWHMs hard to be extracted in a persuasive way. Thus, drawing an informative Williamson-Hall plot in this case can be delusive. Furthermore, Stephen Tetragonal model did not lead to conclusive results, probably for the same reasons we just developed.

Table 4.7 summarizes the anisotropic strain parameter S_{220} extracted from our refinements for the samples adopting a cubic symmetry at RT. All the refinements where performed in the same conditions to be comparable. As stated earlier, the sample containing both cations in equal proportions is the one exhibiting the highest value of the anisotropic strain parameter S_{220}. The value of this parameter decreases gradually when going closer in composition to the end compounds $FAPbI_3$ and $MAPbI_3$.

% MA^+	0	10	20	30	40	50	60	70	80
S_{220}	0	0	3.1 ± 0.5	25.3 ± 1	33.4 ± 1	57.5 ± 2	18.2 ± 1	9.4 ± 1	13.9 ± 1
10^4 ϵ (%)	2.6	2.3	1.6	2.1	2.1	1.2	2.5	2.3	2.5

Table 4.7: Anisotropic strain parameter extracted for LeBail refinement using cubic Stephens model on TOPAS Software

The anisotropic strain observed on the end compounds observed in subsection 4.2.2. might be explained as the manifestation of local off-centering the Pb atoms along the [111] direction. However, the organic cation was found to play little impact of this off-centering,[26] hence, this phenomenon is not the origin of the strain anisotropy observed in $FA_{1-x}MA_xPbI_3$ compounds. Additional experimental work is needed to investigate this behavior. Figure 4.33 shows the different cubic directions investigated here, the spacing they refer to and the concerned atoms.

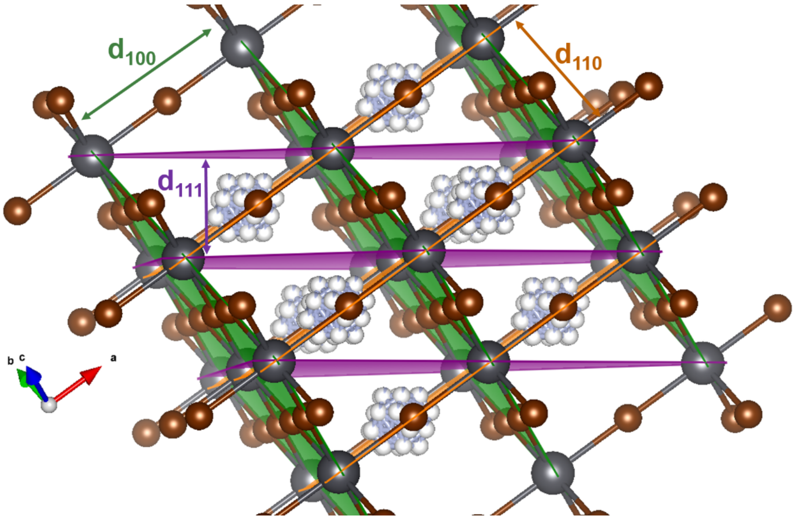

Figure 4.33: Structure of cubic Pm-3m crystal, showing the different spacing we focused on in our study of the anisotropic line broadening: d100 in green, d110 in orange and d111 in purple.

Finally, similarly to what we did for the other family of compounds, we evaluated the band gap of our materials, plotting the found values in Figure 4.34.a. The insert shows a noisier evolution than what was displayed in the previous sections, but it must be due to the reduced evolution range observed for these materials which remain black on the whole compositional range. Moreover, the evolution of the lattice parameter when increasing the percentage of introduced MA^+ show an evolution very close to being linear, thus following Vegard's Law. These last observations are in agreement with previous reports.[46]

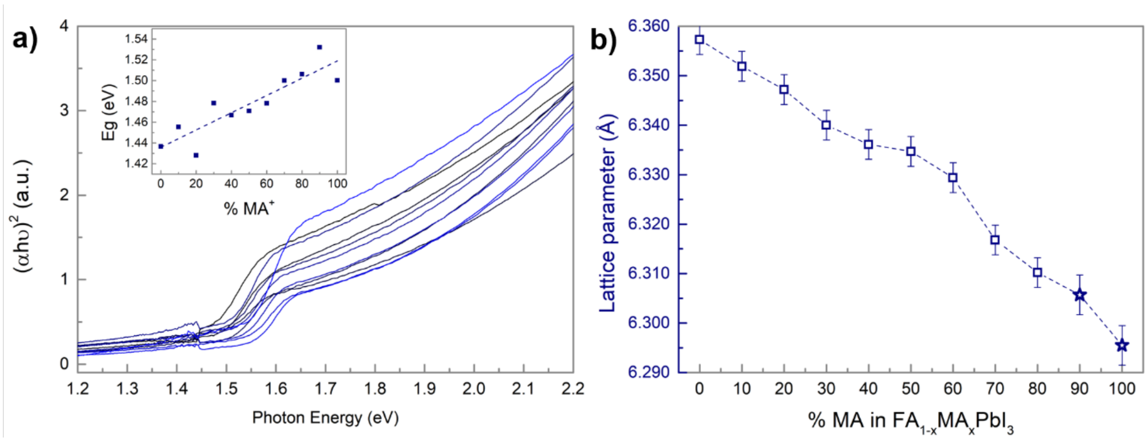

Figure 4.34: (a) Tauc plot showing the evolution of the absorption edge upon increasing the content of MA^+ cations in the crystal. The inset graph shows the extracted band gap, showing a greater dispersion then for the other families, most probably due to reduced evolution range (b) Evolution of the lattice parameter over the compositional range. The stars indicate that the plotted lattice parameter is a pseudo-cubic lattice parameter.

To summarize our results on the intrinsic properties of $FA_{1-x}MA_xPbI_3$ solid solution family at RT, we found that the introduction of 20 % of MA^+ allows to suppress the polymorphic behavior of $FAPbI_3$ **and stabilize the cubic Pm-3m structure at RT, in agreement with previous reports.[53] The cubic compounds exhibit, here again, band gap and lattice parameter evolution in function of composition close to Vegard's law. Finally, lower strain levels than with mixed halide compounds are observed, but non-negligible strain anisotropy is reported when the sample contains close amounts of both FA^+ and MA^+ cations**.

4.6. LEARNING FROM QUATERNARY SOLID SOLUTIONS: INVESTIGATION OF A PHOTOVOLTAIC INSPIRED MIXED CATION MIXED HALIDE COMPOUND

4.6.1. CROSS-COMPARISON OF THE QUATERNARY SOLID SOLUTIONS: INFLUENCE OF THE ORGANIC CATION AND THE HALOGEN

After a detailed study on each solid solution family, we will know try to cross-compare them to get more insight on the role of the halides and the organic cations of the RT properties of hybrid lead halide perovskites.

First of all, let us discuss the influence of organic cation and halogen site on the polymorphism of $FAPbI_3$. Stabilization of the α-perovskite phase when replacing the halogens in $FAPb(I_{1-x}Br_x)_3$ compounds was not observed until 60 % of the halogen site was occupied by bromide. The structure stable at RT for samples containing 10 % Br or less is the 2H hexagonal polymorph of $FAPbI_3$. When the Br content is increased to 20 %, it is the 4H polymorph which is stable at RT. For theses compositions ($x_{Br} \leq 20$ %), thermal annealing above 150 °C leads to a transition to the cubic Pm-3m structure, which can be trapped kinetically and stabilizes at RT for few hours after such thermal treatment. For intermediary compositions ($30 \leq x_{Br} \leq 50$ %), we revealed that the cubic Pm-3m structure cannot be stabilized up to 200 °C, as the sample preferentially crystallizes in different hexagonal structures (4H and 6H).

The electrostatic repulsion appears to play a more predominant role in the formation of the hexagonal phase than the tolerance factor. The tolerance factor predicts a hexagonal structure for $FAPbBr_3$ whereas it is the cubic structure which is observed. We explained that this observation might be due to the Pb-Pb electrostatic repulsion that would arise in an hexagonal $FAPbBr_3$ arrangement because of the small size of Br^-. The same electrostatic repulsion considerations might explain the formation of the 4H and

6H hexagonal polymorphs when introducing Br^- ions in $FAPbI_3$ lattice, as these polymorphs exhibits different sequences of alternating hexagonal ($[PbI_6]^{4-}$ octahedra) and cubic ($[PbI_6]^{4-}$ octahedra) octahedra stacking.

On the other hand, introducing as little as 20 % of MA^+ in $FAPbI_3$ lattice allows to stabilize the cubic structure for more than one month. Furthermore, no other hexagonal polymorphs were observed in the $FA_{1-x}MA_xPbI_3$ solid solution family. We attribute this stabilization to the great impact of the cation size on the tolerance factor, where increasing amounts of MA^+ notably decrease its value.

The substitution of the organic cation seems to be more efficient in stabilizing the cubic structure at RT, as relatively low substitution percentage is needed and no additional polymorphs are observed in this case.

We now consider the influence of the different sites substitution on the perovskite phase. We observed, in agreement with what was predicted in the literature, band gap tuning through compositional engineering. Halide substitution allows a larger range of accessible band gaps (from 1.50 to 2.3 eV) in comparison to cation substitution (around 1.5 - 1.48 eV eV). However, **such halide mixing induced large intrinsic strain and crystalline defects in both families**. For $MAPb(I_{1-x}Br_x)_3$ solid solution, our measurements revealed that despite a number of lattice defects, the compounds exhibit an average behavior following Vegard's law in term of lattice parameter and band gap. Concerning $FAPb(I_{1-x}Br_x)_3$, besides the intermediary compositions where no cubic structure could be stabilized, the compounds similarly obeyed Vegard's law. For both these families, we observed an asymmetry of the Br-content dependency of the strain/lattice defects, which we attributed to size effects and the ability of the small crystals (Br-rich) to accommodate larger ions (I^-).

The lattice parameters and band gap in $FA_{1-x}MA_xPbI_3$ solid solutions evolved here again following Vegard's law. Lower intrinsic strain levels were observed when alloying the two organic cations, but strain anisotropy, reaching its maximum when both cations are introduced in equal amounts, was revealed.

The results presented above indicate that halide mixing is less favorable than organic cation alloying, the former inducing higher strain levels. Moreover, in the case of $FAPb(I_{1-x}Br_x)_3$ compounds, halide substitution does not suppress the polymorphism of the perovskite. On the other hand, lower strain levels and efficient polymorphism suppression makes $FA_{1-x}MA_xPbI_3$ solid solutions more favorable, as they exhibit less crystalline defects. These results points at $FA_{1-x}MA_xPbI_3$ compounds as best suited materials for photovoltaic applications.

However, as mentioned in the first chapter, FA^+ being more hygroscopic than MA^+, these systems suffer from poor stability again moisture. One of the solution employed in the literature is the introduction of Cs^+ cations in $FAPbI_3$ lattice. The large radii difference between the two cations have been shown to induce non negligible octahedral tilting[54][55][56] leading to an enhanced the perovskite phase stability. However, the same studies revealed that Cs-containing solid solutions show higher mixing energies then FA-MA alloys, making the former less stable over time, easily prone to phase segregation and thus apparition of δ-phase.[56] Recent studies showed that samples containing the three FA^+, MA^+ and Cs^+ ions are more stable against phase segregation,[57] and in regards of our results presented here, we believe that such compounds might be highly interesting for future technological advances.

4.6.2. INTRINSIC PROPERTIES OF A MIXED CATION MIXED HALIDE COMPOUND

In the precedent sections we discussed in details the structural properties of the mixed halide ($MAPb(I_{1-x}Br_x)_3$ and $FAPb(I_{1-x}Br_x)_3$ solid solutions) and mixed cation ($FA_{1-x}MA_xPbI_3$ family) quaternary compounds as well as of their ternary end-compounds. We could establish a complete picture of the structural evolution of the solid solutions over the whole compositional range and explain the observed behavior. In the following, we will investigate an even more complex system: the quinary mixed organic cation/mixed halide compound $FA_{1-x}MA_xPb(I_{1-y}Br_y)_3$. However, in this case we do not aim to explore the full parameter space by gradually varying x and y, we will only focus on a single composition ($FA_{0.85}MA_{0.15}Pb(I_{0.85}Br_{0.15})_3$), which has been optimized for achieving the best performance in perovskite solar cells. These optimizations have been initially performed by several teams, motivated by different aspects. In particular, Jeon et al. demonstrated that adding 15% of $MAPbBr_3$ to $FAPbI_3$ resulted in a synergistic effect induced by MA^+ and Br^- in the obtained structure, which led to the stabilization of the black perovskite phase.[58] Furthermore, the best quality of dense and pinhole-free thin films was obtained with this composition as compared to others, e.g., $(FAPbI3)_{0.85}(FAPbBr3)_{0.15}$ and $(FAPbI3)_{0.85}(MAPbI3)_{0.15}$. Finally, by varying the halide composition in $(FA_{1-x}MA_xPb(I_{1-x}Br_x)_3$, the band gap of the resulting perovskites can be tuned from around 1.6 to 2.3 eV. This feature is of predominant importance for the use of perovskites in combination with established silicon technology in tandem solar cells. The latter can push the efficiency beyond the Shockley-Queisser limit of single-junction cells, which show a theoretical maximum efficiency of 33.7 % for an absorber having a band gap of 1.34 eV. In such tandem cells, the role of the perovskite is to convert efficiently solar light in the UV and visible spectral range where silicon is less well performing than in the near infrared. Simulations have shown that a band gap of 1.7 – 1.8 eV is required for the perovskite solar cell to ideally complement the silicon subcell (band gap 1.1 eV),[59] and such values of band gap are achievable through halide composition engineering.

One roadblock for the use of mixed halide perovskites in solar cells is their operational instability, i.e. under irradiation phase segregation into iodine-rich and bromine-rich domains occurs. This process is reversible, and after storing in the dark the initial properties can be recovered. A detrimental effect of this behavior is that it reduces significantly the open circuit voltage VOC, due to the appearance of intra-band gap defect states.[60] Several factors have been identified driving light- (or current-) induced halide segregation, such as inhomogeneous lattice strain induced by a gradient of charge carriers generated across the absorber layer[61] and the presence of a large concentration of halide vacancies favoring bromine and iodine diffusion[62] and the local electric fields generated under light exposure are now proposed to enhance such halide migration.[35] In this context, in-depth structural investigations contribute significantly to the improved understanding of the properties and aging behavior of such complex multi-cation/multi-anion perovskites currently used in solar cells.

The mentioned composition of $FA_{0.85}MA_{0.15}Pb(I_{0.85}Br_{0.15})_3$ has been used in perovskite solar cells prepared by Dr. Jiajiu Ye who was a post-doctoral fellow in our team at the same time as my PhD. Device efficiencies of up to 21.75% with a high VOC of 1.21 V have been obtained in a cell structure comprising a doped SnO_2 bilayer as the electron transport layer (Figure 4.35)..[63]

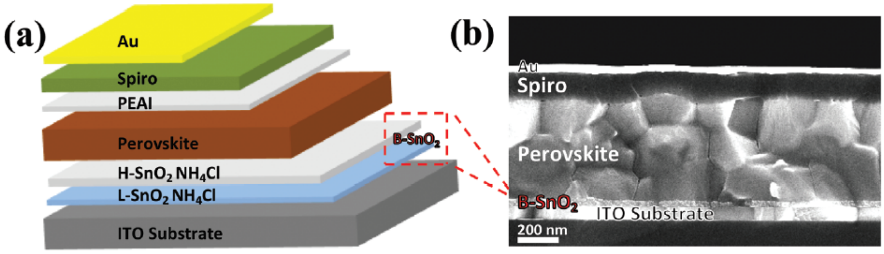

Figure 4.35: (a) Schematic device structure, b) cross-sectional SEM image of the solar cell using $FA_{0.85}MA_{0.15}Pb(I_{0.85}Br_{0.15})_3$ as absorber layer achieving a power conversion efficiency of 21.75% (VOC: 1.21 V, JSC: 23.6 mA/cm2, FF: 0.762). Adapted from.[63]

For the structural investigations, we synthesized a powder sample of this compound using the same protocol as for the rest of our samples. The solvent used was GBL and the synthesis temperature was 120 °C. No post-synthetic annealing was needed. The real amount of Br^- introduced in the material was evaluated by EDX at 13.6 ± 3 % and the FA^+/MA^+ was extracted from 1H NMR measurements which indicated 10/90, both values been close to what we expected. For simplicity, in the following, the sample will be referred to as FAMAPbIBr. As shown in Figure 4.36, the sample adopted a cubic Pm-3m symmetry, with a lattice parameter of a = 6.295(2) Å.

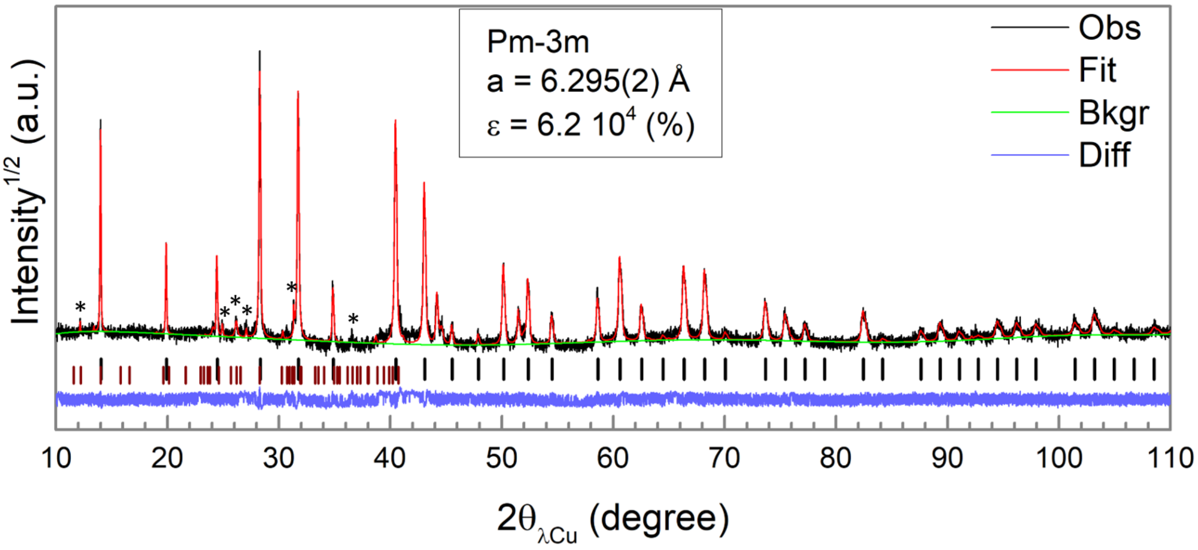

Figure 4.36: XRD pattern and LeBail refinement of the FAMAPbIBr sample, showing a cubic Pm-3m symmetry at RT (black dashes). The dark red dashes correspond to the first peaks expected for the 6H hexagonal polytypes, matching the position of the peaks indicated by the stars and which appeared one month after the synthesis.

Figure 4.37 places the intrinsic properties of the mixed cation mixed halide compounds in regard to the results obtained in the previous sections on the quaternary solid solution. The composition of the sample shows that we have principally $FAPbI_3$ in which 15 % of MA^+ and Br^- are introduced. **Both the lattice parameter and the band gap values are close to the ones of $\mathbf{FAPb(I_{0.85}Br_{0.15})_3}$.** This is in good agreement with the small amount of MA^+ introduced which has little influence on these properties compared to halide substitution.

However, XRD measurement revealed high intrinsic strain value for the FAMAPbIBr compound ($\epsilon = 6.2 \text{ x } 10^4$ %), which is found to be larger than in its quaternary counterparts ($FAPb(I_{0.85}Br_{0.15})_3$: $\epsilon = 3.3 \text{ x } 10^4$ % and $FA_{0.8}MA_{0.20}PbI_3$: $\epsilon = 1.6 \text{ x } 10^4$ %). This indicated that, **the soft character of the hybrid lead halide perovskite allows to accommodate a large number of anions with different sizes, but the quality of the crystalline stacking decreases when doing so**.

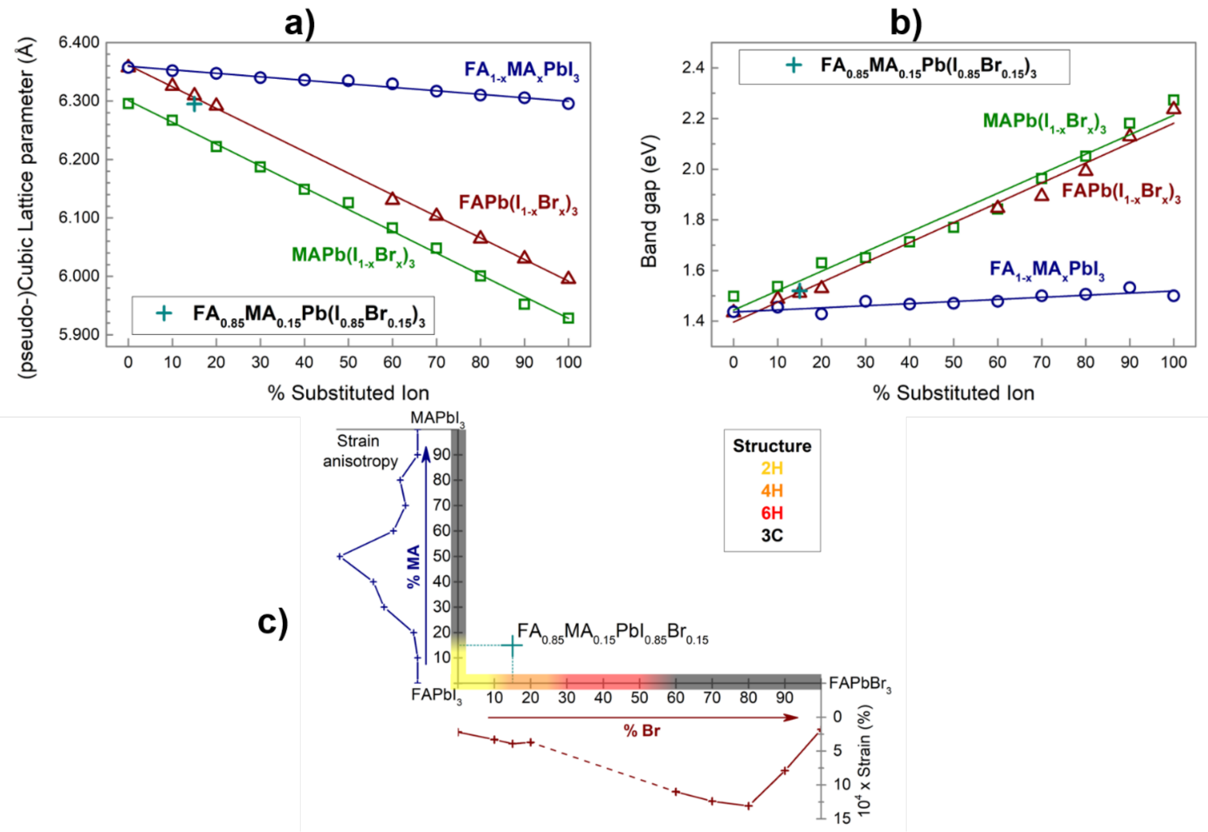

Figure 4.37: Evolution of (a) (pseudo-)cubic lattice parameter and (b) band gap upon ion substitution in the three solid solution families investigated here: $MAPb(I_{1-x}Br_x)_3$, $FAPb(I_{1-x}Br_x)_3$ and $FA_{1-x}MA_xPbI_3$. The blue cross in both panels represent the parameters evaluated for the quinary mixed organic cation/mixed halide compound studied. (c) schematic representation of the polymorphic behavior of FA-based compounds, as extracted from the previous sections, and the mixed cation mixed halide compound is positioned on this map.

Next, as $FAPbI_3$ is the major component of the material, we examined whether any polymorphism could be detected. The pattern shown in Figure 4.36 was measured 45 days after the synthesis. We observed the apparition of small peaks, indicated by the stars in the figure (the intensity being plotted in square root scale, the small peaks appear more intense than they really are). The peaks position could be attributed to the 6H hexagonal polytype. We saw that introducing 15 % of Br^- in $FAPbI_3$ leads to the formation of the 4H polytype, which exhibits more c-stacking then the 2H (δ) polytype. Here, in addition to Br^-, we introduced 15 % of MA^+ which we demonstrated earlier to favor c-packing of the octahedra. The apparition of a small amount of the 6H polytype over time can be explained by the fact that MA^+ helps to retains a fraction of the c-stacking, but not enough was introduced to completely suppress the apparition of h-packing, leading to the slow evolution of the perovskite sample to the 6H intermediary phase. It is however important to note that while we report here this evolution on powder sample, the behavior of the sample with a same composition but in a thin film configuration can be different.

4.7. CONCLUSION

This chapter presents the synthesis and the detailed study of room temperature intrinsic structural properties of hybrid halide perovskites, in particular the four end compounds ($MAPbI_3$, $MAPbBr_3$, $FAPbI_3$ and $FAPbBr_3$) and their solid solutions $MAPb(I_{1-x}Br_x)_3$, $FAPb(I_{1-x}Br_x)_3$ and $FA_{1-x}MA_xPbI_3$.

By investigating the end compounds, we evidenced the existence of anisotropic line broadening, which we found to be strain-related. Using both Willamson-Hall plots and visual inspection of the refinements, we formulated a hypothesis on the influence of the organic cation and the halogen of this anisotropic strain, which might be related to the Pb-off centering reported in the literature. More experimental work has to be done in this direction.

We closely examined the spontaneous evolution of $FAPbI_3$ from the black cubic perovskite to hexagonal yellow phase. Based on temperature dependent XRD study and literature, we proposed a mechanism for this complex behavior, showing the weakening of the interaction of adjacent $[PbI_6]^{4-}$ along the 1D face-sharing chains in the hexagonal packing. This weakening allows the rotation of some octahedra and thus the formation of corner-sharing octahedra layers, eventually converting the 1D octahedra chains into a long-range 3D cubic structure. Electrostatic repulsion appears to be the driving force of this conversion mechanism. Moreover, we highlighted the stability of the cubic structure of $FAPbBr_3$ despite the high tolerance factor calculated for this compounds, further proving the impact of the electrostatic repulsion on the hybrid halide perovskites cubic arrangement.

We then substituted either the organic cation or the halogen in the $FAPbI_3$ structure and studied its impact on the hexagonal phase apparition. We showed that while electrostatic repulsion can suppress polymorphism in $FAPbBr_3$, replacing I^- by Br^- ions is not enough in mixed halide compounds. When up to 50 % of Br^- are inserted in the $FAPbI_3$ structure, other hexagonal polytypes appears. Moreover, no cubic structure could be stabilized for intermediary compositions in bromide (30 to 50 %) where different hexagonal polymorphs were observed. The substitution of FA^+ by MA^+ appeared to have a stronger impact on the stabilization of the cubic phase, as, introducing as little as 20 % MA^+ in $FAPbI_3$ allows to suppress the polymorphism of this compound.

We proved solid solution formation over the whole composition range in $MAPb(I_{1-x}Br_x)_3$ despite previous reports in the literature, thanks to an additionnal annealing step in the synthesis process. Our samples initially showed stacking faults in the final material after the synthesis. Despite such lattice defects, the behavior of the compounds evolved gradually with the increase of inserted Br in the lattice. Such observation is in good agreement with the well-known defector tolerant character of the hybrid halide perovskites. These crystal defects disappeared overtime, thanks to halide migration but also our high temperature process which suppressed single halogen rich regions, allowing to avoid phase segregation.

We showed the expected band gap tuning through halide mixing on both $MAPb(I_{1-x}Br_x)_3$ and $FAPb(I_{1-x}Br_x)_3$, but we also evidenced the presence of high intrinsic strain in both solid-solutions, indicating degraded crystalline quality. All of the studied samples showed an evolution of the lattice parameters following Vegard's law, despite the crystalline defects mentioned.

Finally, we studied one mixed organic cation mixed halide sample: $FA_{0.85}MA_{0.15}Pb(I_{0.85}Br_{0.15})_3$ which shows the expected band gap and lattice parameter values, but exhibits a higher strain level then its 4-components counterparts, showing increasing crystalline defects when adding more cations / anions in the lattice. This compound exhibits excellent photovoltaic properties with a power conversion efficiency exceeding 21 %, however, the structural defects may be at the origin of a decrease of long-term stability and degradation.

References

[1] C. Li, K. C. K. Soh, and P. Wu. “Formability of ABO_3 perovskites”. en. In: *Journal of Alloys and Compounds* 372.1-2 (2004), pp. 40–48. DOI: `10.1016/j.jallcom.2003.10.017`.

[2] L. M. Feng et al. “Formability of ABO_3 cubic perovskites”. en. In: *Journal of Physics and Chemistry of Solids* 69.4 (2008), pp. 967–974. DOI: `10.1016/j.jpcs.2007.11.007`.

[3] C. Li et al. “Formability of ABX_3 ($X = F$, Cl, Br, I) halide perovskites”. en. In: *Acta Crystallographica Section B* 64.6 (2008), pp. 702–707. DOI: `10.1107/S0108768108032734`.

[4] G. Kieslich, S. Sun, and A. K. Cheetham. “Solid-state principles applied to organic–inorganic perovskites: new tricks for an old dog”. en. In: *Chem. Sci.* 5.12 (2014), pp. 4712–4715. DOI: `10.1039/C4SC02211D`.

[5] R. D. Shannon. “Revised effective ionic radii and systematic studies of interatomic distances in halides and chalcogenides”. en. In: *Acta Cryst A* 32.5 (1976), pp. 751–767. DOI: `10.1107/S0567739476001551`.

[6] S. Govinda et al. “Critical Comparison of $FAPbX_3$ and $MAPbX_3$ ($X =$ Br and Cl): How Do They Differ?” en. In: *J. Phys. Chem. C* 122.25 (2018), pp. 13758–13766. DOI: `10.1021/acs.jpcc.8b00602`.

[7] W. Travis et al. “On the application of the tolerance factor to inorganic and hybrid halide perovskites: a revised system”. en. In: *Chem. Sci.* 7.7 (2016), pp. 4548–4556. DOI: `10.1039/C5SC04845A`.

[8] S. Gholipour et al. “Globularity-Selected Large Molecules for a New Generation of Multication Perovskites”. en. In: *Adv. Mater.* 29.38 (2017), p. 1702005. DOI: `10.1002/adma.201702005`.

[9] C. J. Bartel et al. “New tolerance factor to predict the stability of perovskite oxides and halides”. en. In: *Sci. Adv.* 5.2 (2019), eaav0693. DOI: `10.1126/sciadv.aav0693`.

[10] N. Pellet et al. “Transforming Hybrid Organic Inorganic Perovskites by Rapid Halide Exchange”. en. In: *Chem. Mater.* 27.6 (2015), pp. 2181–2188. DOI: `10.1021/acs.chemmater.5b00281`.

[11] M. I. Saidaminov et al. “Retrograde solubility of formamidinium and methylammonium lead halide perovskites enabling rapid single crystal growth”. en. In: *Chem. Commun.* 51.100 (2015), pp. 17658–17661. DOI: `10.1039/C5CC06916E`.

[12] T. Baikie et al. “Synthesis and crystal chemistry of the hybrid perovskite $(CH_3NH_3)PbI_3$ for solid-state sensitised solar cell applications”. en. In: *Journal of Materials Chemistry A* 1.18 (2013), p. 5628. DOI: `10.1039/c3ta10518k`.

[13] F. Lehmann et al. “The phase diagram of a mixed halide (Br, I) hybrid perovskite obtained by synchrotron X-ray diffraction”. en. In: *RSC Adv.* 9.20 (2019), pp. 11151–11159. DOI: `10.1039/C8RA09398A`.

[14] D. H. Fabini et al. “Reentrant Structural and Optical Properties and Large Positive Thermal Expansion in Perovskite Formamidinium Lead Iodide”. en. In: *Angew. Chem.* 128.49 (2016), pp. 15618–15622. DOI: `10.1002/ange.201609538`.

[15] E. C. Schueller et al. “Crystal Structure Evolution and Notable Thermal Expansion in Hybrid Perovskites Formamidinium Tin Iodide and Formamidinium Lead Bromide”. In: *Inorg. Chem.* 57.2 (2018), pp. 695–701. DOI: `10.1021/acs.inorgchem.7b02576`.

[16] O. J. Weber et al. “Phase Behavior and Polymorphism of Formamidinium Lead Iodide”. en. In: *Chem. Mater.* 30.11 (2018), pp. 3768–3778. DOI: `10.1021/acs.chemmater.8b00862`.

[17] T. Chen et al. “Entropy-driven structural transition and kinetic trapping in formamidinium lead iodide perovskite”. en. In: *Sci. Adv.* 2.10 (2016), e1601650. DOI: `10.1126/sciadv.1601650`.

[18] Arthur Marronier. “Anharmonicity and Instabilities in Halide Perovskites for Last Generation Solar Cells”. PhD thesis. Université Paris Saclay, 2018.

[19] B. L. Chamberland, A. W. Sleight, and J. F. Weiher. “Preparation and characterization of $BaMnO_3$ and $SrMnO_3$ polytypes”. In: *Journal of Solid State Chemistry* 1.3-4 (1970), pp. 506–511. DOI: `10.1016/0022-4596(70)90133-7`.

[20] Seung-Tae Hong and Arthur W. Sleight. “Crystal Structure of 4H $BaRuO_3$: High Pressure Phase Prepared at Ambient Pressure”. en. In: *Journal of Solid State Chemistry* 128.2 (1997), pp. 251–255. DOI: `10.1006/jssc.1996.7200`.

[21] J.-G. Cheng et al. “A New Perovskite Polytype in the High-Pressure Sequence of $BaIrO_3$”. en. In: *J. Am. Chem. Soc.* 131.21 (2009), pp. 7461–7469. DOI: `10.1021/ja901829e`.

[22] P. Gratia et al. “The Many Faces of Mixed Ion Perovskites: Unraveling and Understanding the Crystallization Process”. en. In: *ACS Energy Lett.* 2 (2017), pp. 2686–2693.

[23] F. Cordero et al. “Influence of Temperature, Pressure, and Humidity on the Stabilities and Transition Kinetics of the Various Polymorphs of $FAPbI_3$”. en. In: *J. Phys. Chem. C* 124.42 (2020), pp. 22972–22980. DOI: `10.1021/acs.jpcc.0c06342`.

[24] S. Sun. “Synthesis, characterization and properties of hybrid organic-inorganic perovskites for photovoltaic applications”. en. PhD thesis. University of Cambridge, 2017.

[25] S. Sun et al. “Factors Influencing the Mechanical Properties of Formamidinium Lead Halides and Related Hybrid Perovskites”. en. In: *ChemSusChem* 10.19 (2017), pp. 3740–3745. DOI: `10.1002/cssc.201700991`.

[26] G. Laurita et al. “Chemical tuning of dynamic cation off-centering in the cubic phases of hybrid tin and lead halide perovskites”. en. In: *Chem. Sci.* 8.8 (2017), pp. 5628–5635. DOI: `10.1039/C7SC01429E`.

[27] P. W. Stephens. “Phenomenological model of anisotropic peak broadening in powder diffraction”. en. In: *J Appl Crystallogr* 32.2 (1999), pp. 281–289. DOI: `https://doi.org/10.1107/S0021889898006001`.

[28] M. T. Weller et al. “Cubic Perovskite Structure of Black Formamidinium Lead Iodide, α-[HC(NH$_2$)$_2$]PbI$_3$, at 298 K”. en. In: *J. Phys. Chem. Lett.* 6.16 (2015), pp. 3209–3212. DOI: `10.1021/acs.jpclett.5b01432`.

[29] A. A. Zhumekenov et al. “Formamidinium Lead Halide Perovskite Crystals with Unprecedented Long Carrier Dynamics and Diffusion Length”. en. In: *ACS Energy Lett.* 1.1 (2016), pp. 32–37. DOI: `10.1021/acsenergylett.6b00002`.

[30] A. Franz et al. “The influence of deuteration on the crystal structure of hybrid halide perovskites: a temperature-dependent neutron diffraction study of FAPbBr$_3$”. en. In: *Acta Crystallogr B Struct Sci Cryst Eng Mater* 76.2 (2020), pp. 267–274. DOI: `10.1107/S2052520620002620`.

[31] A. Bernasconi and L. Malavasi. “Direct Evidence of Permanent Octahedra Distortion in MAPbBr$_3$ Hybrid Perovskite”. In: *ACS Energy Lett.* 2.4 (2017), pp. 863–868. DOI: `10.1021/acsenergylett.7b00139`.

[32] A. Bernasconi et al. “Ubiquitous Short-Range Distortion of Hybrid Perovskites and Hydrogen-Bonding Role: the MAPbCl$_3$ Case”. In: *J. Phys. Chem. C* 122.49 (2018), pp. 28265–28272. DOI: `10.1021/acs.jpcc.8b10086`.

[33] X.-.G Zhao et al. “Polymorphous nature of cubic halide perovskites”. en. In: *Phys. Rev. B* 101.15 (2020), p. 155137. DOI: `10.1103/PhysRevB.101.155137`.

[34] R. Sharma et al. “Elucidating the atomistic origin of anharmonicity in tetragonal CH$_3$NH$_3$PbI$_3$ with Raman scattering”. en. In: *Phys. Rev. Materials* 4.9 (2020), p. 092401. DOI: `10.1103/PhysRevMaterials.4.092401`.

[35] C. Rehermann et al. “Origin of Ionic Inhomogeneity in MAPb(I$_x$Br$_{1-x}$)$_3$ Perovskite Thin Films Revealed by In-Situ Spectroscopy during Spin Coating and Annealing”. en. In: *ACS Appl. Mater. Interfaces* 12.27 (2020), pp. 30343–30352. DOI: `10.1021/acsami.0c05894`.

[36] J. H. Noh et al. “Chemical Management for Colorful, Efficient, and Stable Inorganic–Organic Hybrid Nanostructured Solar Cells”. en. In: *Nano Lett.* 13.4 (2013), pp. 1764–1769. DOI: `10.1021/nl400349b`.

[37] T. J. Jacobsson et al. “An exploration of the compositional space for mixed lead halogen perovskites for high efficiency solar cells”. en. In: *Energy Environ. Sci.* 9 (2016), pp. 1706–1724. DOI: `10.1039/C6EE00030D`.

[38] F. Brivio, C. Caetano, and A. Walsh. “Thermodynamic Origin of Photoinstability in the $CH_3NH_3Pb(I_{1\text{-}x}Br_x)_3$ Hybrid Halide Perovskite Alloy”. en. In: *J. Phys. Chem. Lett.* 7.6 (2016), pp. 1083–1087. DOI: `10.1021/acs.jpclett.6b00226`.

[39] E. I. Marchenko et al. “Transferable Approach of Semi-Empirical Modeling of Disordered Mixed-Halide Hybrid Perovskites $CH_3NH_3Pb(I_{1\text{-}x}Br_x)_3$: Prediction of Thermodynamic Properties, Phase Stability, and Deviations from Vegard’s Law”. en. In: *J. Phys. Chem. C* 123.42 (2019), pp. 26036–26040. DOI: `10.1021/acs.jpcc.9b08995`.

[40] Z. Muhammad et al. “Tunable relativistic quasiparticle electronic and excitonic behavior of the $FAPb(I_{1-x}Br_x)_3$ alloy”. en. In: *Phys. Chem. Chem. Phys.* 22.21 (2020), pp. 11943–11955. DOI: `10.1039/D0CP00496K`.

[41] G. E. Eperon et al. “Formamidinium lead trihalide: a broadly tunable perovskite for efficient planar heterojunction solar cells”. en. In: *Energy Environ. Sci.* 7.3 (2014), p. 982. DOI: `10.1039/c3ee43822h`.

[42] W. Rehman et al. “Charge-Carrier Dynamics and Mobilities in Formamidinium Lead Mixed-Halide Perovskites”. In: *Adv. Mater.* 27.48 (2015), pp. 7938–7944. DOI: `10.1002/adma.201502969`.

[43] B. Slimi et al. “Synthesis and characterization of perovskite $FAPbBr_{3-x}I_x$ thin films for solar cells”. en. In: *Monatsh Chem* 148.5 (2017), pp. 835–844. DOI: `10.1007/s00706-017-1958-0`.

[44] X. Ni. “Effect of Br content on phase stability and performance of $H_2N{=}CHNH_2Pb(I_{1-x}Br_x)_3$ perovskite thin films”. en. In: *Nanotechnology* 30 (2019), p. 165402. DOI: `10.1088/1361-6528/aafeb6`.

[45] W.-G. Li et al. “A formamidinium–methylammonium lead iodide perovskite single crystal exhibiting exceptional optoelectronic properties and long-term stability”. en. In: *J. Mater. Chem. A* 5.36 (2017), pp. 19431–19438. DOI: `10.1039/C7TA04608A`.

[46] O. J. Weber, B. Charles, and M. T. Weller. “Phase behaviour and composition in the formamidinium–methylammonium hybrid lead iodide perovskite solid solution”. en. In: *J. Mater. Chem. A* 4.40 (2016), pp. 15375–15382. DOI: `10.1039/C6TA06607K`.

[47] A. Fransisco-Lopez et al. “Phase Diagram of Methylammonium/Formamidinium Lead Iodide Perovskite Solid Solutions from Temperature-Dependent Photoluminescence and Raman Spectroscopies”. en. In: *J. Phys. Chem. C* 124.6 (2020), pp. 3448–3458. DOI: `10.1021/acs.jpcc.9b10185`.

[48] A. Pisanu et al. “The $FA_{1-x}MA_xPbI_3$ System: Correlations among Stoichiometry Control, Crystal Structure, Optical Properties, and Phase Stability”. en. In: *J. Phys. Chem. C* 121.16 (2017), pp. 8746–8751. DOI: `10.1021/acs.jpcc.7b01250`.

[49] N. Pellet et al. “Mixed-Organic-Cation Perovskite Photovoltaics for Enhanced Solar-Light Harvesting”. en. In: *Angew. Chem.* 53.12 (2014), pp. 3151–3157. DOI: `https://doi.org/10.1002/anie.201309361`.

[50] D. J. Kubicki et al. “Cation Dynamics in Mixed-Cation $(MA)_x(FA)_{1-x}PbI_3$ Hybrid Perovskites from Solid-State NMR”. In: *J. Am. Chem. Soc.* 139.29 (2017), pp. 10055–10061. DOI: `10.1021/jacs.7b04930`.

[51] K. L. Svane et al. “How Strong Is the Hydrogen Bond in Hybrid Perovskites?” en. In: *J. Phys. Chem. Lett.* 8.24 (2017), pp. 6154–6159. DOI: `10.1021/acs.jpclett.7b03106`.

[52] F. Cordero et al. “Cation reorientation and octahedral tilting in the metal-organic perovskites MAPI and FAPI”. en. In: *Journal of Alloys and Compounds* 867 (2021), p. 158210. DOI: `10.1016/j.jallcom.2020.158210`.

[53] A. K. Jena, A. Kulkarni, and T. Miyasaka. “Halide Perovskite Photovoltaics: Background, Status, and Future Prospects”. en. In: *Chem. Rev.* 119.5 (2019), pp. 3036–3103. DOI: `10.1021/acs.chemrev.8b00539`.

[54] Dibyajyoti Ghosh et al. “Good Vibrations: Locking of Octahedral Tilting in Mixed-Cation Iodide Perovskites for Solar Cells”. en. In: *ACS Energy Letters* 2.10 (2017), pp. 2424–2429. DOI: `10.1021/acsenergylett.7b00729`.

[55] R. Prasanna et al. “Band Gap Tuning via Lattice Contraction and Octahedral Tilting in Perovskite Materials for Photovoltaics”. en. In: *J. Am. Chem. Soc.* 139.32 (2017), pp. 11117–11124. DOI: `10.1021/jacs.7b04981`.

[56] Jiajia Zhang et al. “Effect of cation replacement on the phase stability of formamidinium lead iodide perovskite”. en. In: *The Journal* (2019), p. 8.

[57] L. T. Schelhas et al. “Insights into operational stability and processing of halide perovskite active layers”. en. In: *Energy Environ. Sci.* 12.4 (2019), pp. 1341–1348. DOI: `10.1039/C8EE03051K`.

[58] Nam Joong Jeon et al. “Compositional engineering of perovskite materials for high-performance solar cells”. en. In: *Nature* 517.7535 (2015), pp. 476–480. DOI: `10.1038/nature14133`.

[59] M. T. Hörantner et al. “The Potential of Multijunction Perovskite Solar Cells”. en. In: *ACS Energy Lett.* 2.10 (2017), pp. 2506–2513. DOI: `10.1021/acsenergylett.7b00647`.

[60] E. L. Unger et al. “Roadmap and roadblocks for the band gap tunability of metal halide perovskites”. en. In: *J. Mater. Chem. A* 5.23 (2017), pp. 11401–11409. DOI: `10.1039/C7TA00404D`.

[61] A. J. Barker et al. “Defect-Assisted Photoinduced Halide Segregation in Mixed-Halide Perovskite Thin Films”. en. In: *ACS Energy Lett.* 2.6 (2017), pp. 1416–1424. DOI: `10.1021/acsenergylett.7b00282`.

[62] M. C. Brennan et al. “Light-Induced Anion Phase Segregation in Mixed Halide Perovskites”. en. In: *ACS Energy Lett.* 3.1 (2018), pp. 204–213. DOI: `10.1021/acsenergylett.7b01151`.

[63] J. Ye et al. “Doped Bilayer Tin(IV) Oxide Electron Transport Layer for High Open-Circuit Voltage Planar Perovskite Solar Cells with Reduced Hysteresis”. en. In: *Small* 17.5 (2021), p. 2005671. DOI: `https://doi.org/10.1002/smll.202005671`.

Chapter 5

Temperature dependent phase diagram of mixed ions hybrid halide perovskites

Detectors and optoelectronic devices, where hybrid halide perovskites are foreseen to be used, can be exposed to quite large temperature ranges when installed. Knowing how the different components of the devices behave upon temperature helps improving them in terms of stability, robustness... Moreover, studying the influence of temperature on the structure is an inevitable and crucial step when studying new compounds as it allows reaching a better understanding of the materials, their structure and the different interactions taking place at the atomic scale.

In this chapter, we conduct temperature dependent XRD measurements on the hybrid mixed halide compounds $\mathrm{MAPb(I_{1-x}Br_x)_3}$ and $\mathrm{FAPb(I_{1-x}Br_x)_3}$ which were introduced in the previous chapter. The first section presents the experimental setup we used in our laboratory and the measurement strategy we developed, according to the experimental constraints we faced. Next, the temperature behavior of MA-based samples is presented. The next section sets out the results obtained on the FA-based compounds. In both sections, a first part is dedicated to presenting the behavior of end compounds, by comparing our data to the existing reports. This allows to better understand the behavior of the mixed halide compounds presented afterwards and thus to explore the temperature-composition phase diagram of both $\mathrm{MAPb(I_{1-x}Br_x)_3}$ and $\mathrm{FAPb(I_{1-x}Br_x)_3}$ solid solutions. Finally, in the last section of this chapter, the temperature behavior of the compound used in photovoltaic devices $\mathrm{FA_{0.85}MA_{0.15}Pb(I_{0.85}Br_{0.15})_3}$ is fully investigated and put in regard with previous results.

Contents

5.1. EXPERIMENTAL SET-UP AND MEASUREMENT STRATEGY

At the beginning of my second year of PhD, the laboratory received a Bruker D8 Advanced diffractometer (Cu wavelength), equipped with an Anton-Paar temperature chamber that allows to reach temperature ranging from 83 to 873 K together with the control of the chamber atmosphere (primary vacuum, inert atmosphere or air). Photograph of the temperature chamber and the control devices is presented in appendix B.6. We used this setup to establish the phase diagram of our mixed halides solid solutions $MAPb(I_{1-x}Br_x)_3$ and $FAPb(I_{1-x}Br_x)_3$. We decided not to investigate the phase diagram of $FA_{1-x}MA_xPbI_3$ as it has already been reported.[1,2]

Before starting our experiments, we needed to establish our goals, the measurement conditions and strategy in order to optimize the measurement time considering the experimental constrains and the large number of samples we wanted to measure. First of all, the heating system was calibrated using $RbNO_3$ compound which displays well established characteristic phase transition from trigonal to cubic symmetry at 437 K.[3] We found that working under vacuum causes a large temperature shift of at least 50 °C and we obtained the best results when performing our experiment under atmospheric pressure. To calibrate the cooling system, we used $MAPbBr_3$. Performing an extensive bibliographic review, we found that the transition temperatures of $MAPbBr_3$ were well documented and similar values were reported in a large number of articles, leading us to use it as a calibration compound for the cooling system. When working at low temperatures, maintaining a reduced inert gas pressure in the sample environment ensures reaching the thermal equilibrium. We tested different inert gas pressure values in the temperature chamber (P = 100, 200 and 500 hPa) to observe that it had little effect on the transition temperatures. Thus, we started all of our experiments by purging the chamber's atmosphere using a primary pump and performing 3 cycles of inert N_2 gas filling – vacuum to insure inert conditions, then we set the pressure to at P = 100 hPa and cooled the system.

Secondly, we looked at the autonomy of the cooling system. To reach 83 K, the temperature chamber is cooled with liquid nitrogen, which is stored in a 100 L Dewar vessel and then injected in the chamber through Venturi effect. The Dewar was used to its fullest capacity when programming a 1h long plateau every 20 K between 90 and 270 K. During this plateau, 10 min were dedicated to stabilizing the programmed temperature and ensuring thermal equilibrium in the sample. A 50 minutes measurement in the 10 - 110 ° 2θ range was then performed before changing the temperature again at a 120 °C/min speed. Following this procedure, 10 measurements could be performed at temperatures inferior to 280 K. Between 280 and 380 K, the same sequence was repeated every 10 K. The aim of this study was not to perform a detailed characterization of the phase transition, but to determine the transition temperatures and the different crystalline structures adopted by the different compounds. Figure 5.1 shows a contour plot of calibration data the data obtained on $MAPbBr_3$ in the 90 – 380 K range, exhibiting phase transitions at 140 ± 10 K and 230 ± 10 K, close from the reported values of 148 K and 230 K.[4] These phase transitions will be discussed in more details in subsection 5.2.3. The temperature chamber is made of Nickel, and we found Ni diffraction lines in our diffractograms, indicated by the black diamonds in Figure 5.1.

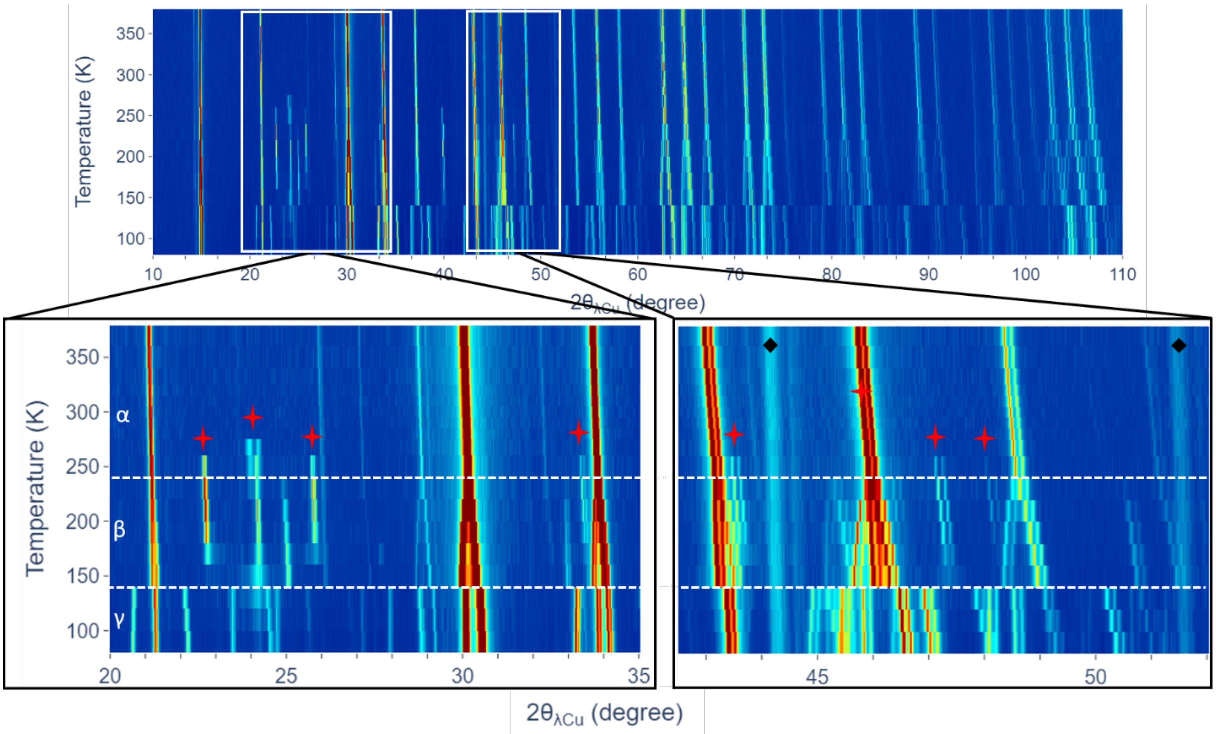

Figure 5.1: Example of the data obtained during temperature dependent XRD experiment performed on $MAPbBr_3$ in the 90 − 380 K range. The red stars indicate ice peak positions (P3m1, ICDD: 04-012-5069) and the black diamonds the Ni peak positions arising from the temperature chamber.

An intriguing feature was observed during the low temperature measurements. We observed, over time, the growth of additional diffraction peaks that we identified as crystallized ice (P3m1, a = 4.511 Å and c = 7.346 Å; ICDD: 04-012-5069), evidenced with the red stars in Figure 5.1. Monitoring the pressure in the sample chamber, we observed that it was slowly rising from the initially set P = 100 hPa to eventually reach atmospheric pressure after 11h of measurement (time spent at low temperatures). We found that the gas flow injector of the set up was not airtight, leading to infiltration of air over time because of the initially reduced pressure. This explains why the ice peaks appear in the diffractograms over time (not present at 90 K, but grows with time spend at low temperatures). Performing LeBail refinement, we were able to refine $MAPbBr_3$ and the ice using the same sample displacement parameter, thus indicating that the ice crystallizes close to the sample, which is coherent with the fact that the liquid nitrogen flow and thus the "cold point" is directed through the sample's mounting location.

That said, we performed, for all of our samples, measurements at RT before and after cooling, in other words, before and after exposure to ice, and we compared these two measurements. We found, for all our samples, that the two measurements are identical (peak positions, intensities, FWHMs and baseline levels), indicating that ice formation did not degrade our samples, validating our results which are not caused by degradation and irreversible processes.

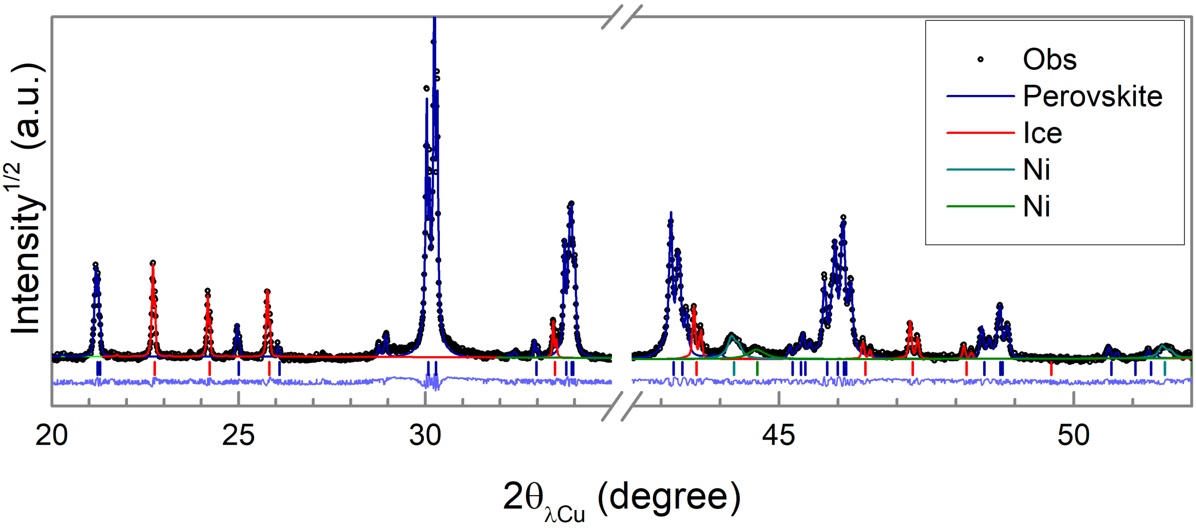

Figure 5.2: Example of refined diffraction pattern of $MAPbBr_3$ at 210 K , showing a tetragonal I4/mcm perovskite pattern, a trigonal P3m1 ice pattern and cubic Fm-3m Ni diffraction lines, showing that satisfying refinements are achieved even with the two additional and unwanted phases.

Amusing enough, we could take advantage of this lack of airtightness. After a first measurement at RT, we purge the atmosphere around the sample and set the desired pressure, then we cool the system to 90 K and launch measurements each 20 K as explained earlier in this section. Considering the whole measurement time to bring the sample back to RT, the sample environment is back to atmospheric pressure, which allows to directly launch the high temperature part of the experiment (we showed that reduced pressure at high temperature lead to important temperature shift). We could thus program measurements from 90 to 380 K and launch it without intervening on the sample's atmosphere. Such program lasted for 22h, with measurements recorded every 20 K from 90 to 270 K and every 10 K from 280 to 380 K, and adding a final measurement at 298 K to check that the sample did not evolve during the temperature cycling.

Figure 5.2 shows that all the observed phases (perovskite, ice and nickel) are well accounted for in LeBail refinements.

5.2. TEMPERATURE BEHAVIOR OF MA-BASED COMPOUNDS

5.2.1. STRUCTURAL PHASE TRANSITIONS IN $MAPbI_3$

$MAPbI_3$, which was extensively studied in the literature, has been the sole focus of the first part of this thesis. It is well established now that it crystallizes at RT in a tetragonal I4/mcm. In terms of Glazer notation (cf. subsection 1.2.2), this tetragonal arrangement is noted as $a^0a^0c^-$, meaning that there is only one tilt, along the c axis and the two adjacent octahedra layers along the tilting direction do not rotate in the same direction. This explains why the tetragonal cell is doubled in comparison to the cubic cell along c. As a considerable amount of information have already been published, we did not conduct a low temperature study of $MAPbI_3$ and we present instead, in the following, a summary of the major results reported for this compound.

Heating $MAPbI_3$ induces a phase transition to the high symmetry Pm-3m cubic phase, where the octahedra are not tilted, thus described as $a^0a^0a^0$ in Glazer's notation. One should keep in mind that we are describing here the average structure, the hybrid halide perovskites exhibits local, anharmonic tilting even in the cubic symmetry as explained in the previous chapter (4.2.3), which are not treated in this work. Phase transition occurs at 330 K and the nature of this transition is not clear yet: some experimental data exhibited a first order transition while others observed a second order transition. Still unclear, Whitfield *et al.* closely studied the phase transition, observing a domain of coexistence of both cubic and tetragonal phases. However, the critical exponent they extracted indicated a tricritical phase transition, which predicts a vanishing region of phase coexistence at the tricritical point.[5]

Cooling the RT tetragonal $MAPbI_3$ leads to a phase transition to a lower symmetry orthorhombic phase around 160 K, described by the Pnma space group ($a^-b^+a^-$ in Glazer's notation). Howard and Stokes demonstrated that Pnma is not a subgroup of I4/mcm,[6] thus a continuous second order transition cannot be expected. It is confirmed by the experimental data obtained, for instance, by Whitfield *et al.* and which, as shown in Figure 5.3, exhibit the coexistence of both tetragonal and orthorhombic phases.

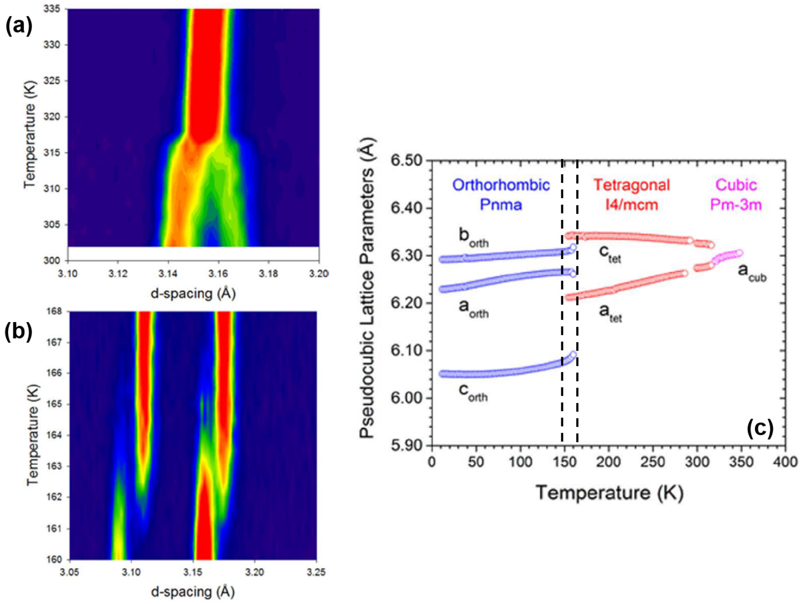

Figure 5.3: Temperature induced structural changes in $MAPbI_3$. (a) showing the merging of the (004) and (220) tetragonal peaks into (200) cubic peaks at high temperature, indicating the cubic-tetragonal phase transition. (b) looking from the top part of the figure to the bottom, the tetragonal (004) and (220) reflection disappearing while the orthorhombic (040) and (202) reflection appear. A region where both phases coexist is observed, confirming the first order phase transition. (c) Evolution of the (pseudo-) cubic lattice parameters. All three panel adapted from.[5]

Concerning the cations dynamics, in agreement with most reports, Whitfield found the organic cation to be fully disordered over 24 equivalent orientations in the cubic phase. Transition to the tetragonal phase induced a locking of a number of degrees of freedom, leading to partially ordered cations, with eight equivalent positions and dynamic disorder in the ab plane. Finally, the orthorhombic phase exhibits fully ordered MA cations and the strongest hydrogen bonds values observed in all three structural phases.[5]

5.2.2. STRUCTURAL PHASE TRANSITIONS IN $MAPbBr_3$

The temperature behavior of pure $MAPbBr_3$ is similar to $MAPbI_3$ in many regards. Upon temperature lowering, three crystallographic phases are adopted by the compound: the high temperature cubic Pm-3m ($a^0a^0a^0$ in Glazer's notation) transits into a tetragonal I4/mcm ($a^0a^0c^-$ in Glazer's notation) upon cooling, and further temperature lowering leads to an orthorhombic Pnma structure ($a^-b^+a^-$ in Glazer's notation). The transition temperatures are however different: the cubic-tetragonal phase transition is observed at 240 ± 10 K, in agreement with the literature, hence, $MAPbBr_3$ adopts a cubic symmetry at

RT and the orthorhombic phase appears at 138 ± 1 K. Figure 5.4 summarizes our data on the cubic, tetragonal and orthorhombic phase, showing the evolution of the peaks positions (a) and the (pseudo-)cubic lattice parameters (b). Pseudo-cubic lattice parameters are calculated in the orthorhombic and the tetragonal phase from the orthorhombic a^O, b^O and c^O and tetragonal a^T and c^T lattice parameters using the following equations:

For the orthorhombic phase:

$$a^O_{pC} = \frac{a^O}{\sqrt{2}}\ ,\ b^O_{pC} = \frac{b^O}{2}\ and\ c^O_{pC} = \frac{c^O}{\sqrt{2}} \tag{5.1}$$

For the tetragonal phase

$$a^T_{pC} = \frac{a^T}{\sqrt{2}}\ and\ c^T_{pC} = \frac{c^T}{2} \tag{5.2}$$

Concerning the dynamics of the MA^+ cations, in the $PbBr^{3-}$ cage, similar behavior to $MAPbI_3$ was reported: the fully disordered cations in the cubic cell become partially ordered when lowering the symmetry to the tetragonal cell with disorder in the ab plane. Fully ordered cations were observed in the orthorhombic structure.[7,8]

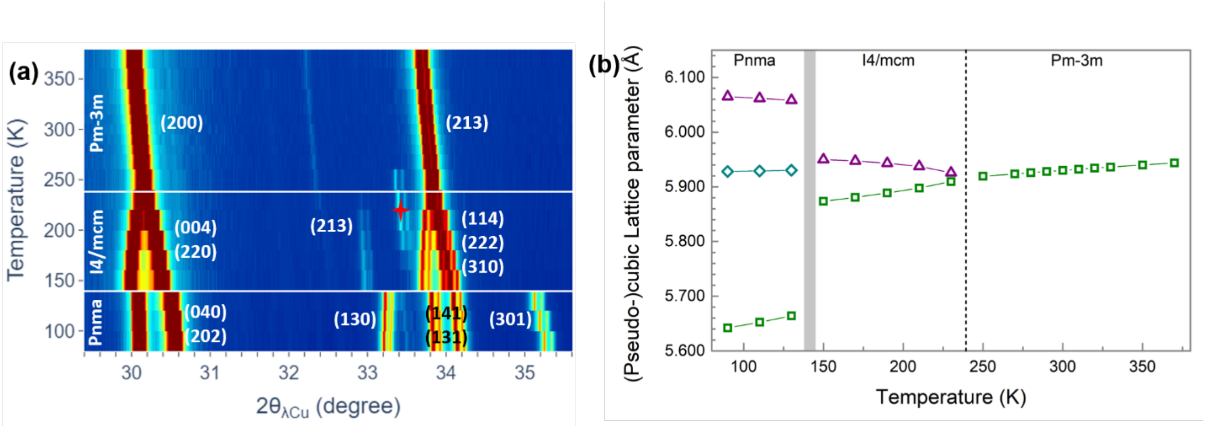

Figure 5.4: Temperature behavior of $MAPbBr_3$. (a) contour plot showing three phases distinguishable from the evolution of the Bragg peaks: cubic Pm-3m at high temperature, tetragonal I4/mcm is marked by the apparition of the (213) reflection and the splitting of the cubic (200) peak into tetragonal (004) and (220). Finally, the orthorhombic Pnma is characterized by a sharp evolution of the peak positions and the apparition of (301) reflection. (b) Evolution of the (pseudo-)cubic lattice parameters over the studied temperature range. The error bars being smaller than the markers, they have been neglected.

The grey area in Figure 5.4.b represents a temperature domain between 145 ± 4 K and

138 ± 1 K where structural changes between tetragonal I4/mcm and orthorhombic Pnma phases are observed. As mentioned earlier, these two space groups are not related by a group-subgroup relationship, making a smooth second order transition not possible. Since $MAPbBr_3$ adopts the same space groups as $MAPbI_3$, one could expect this domain to be a coexistence domain of the tetragonal and the orthorhombic phases.

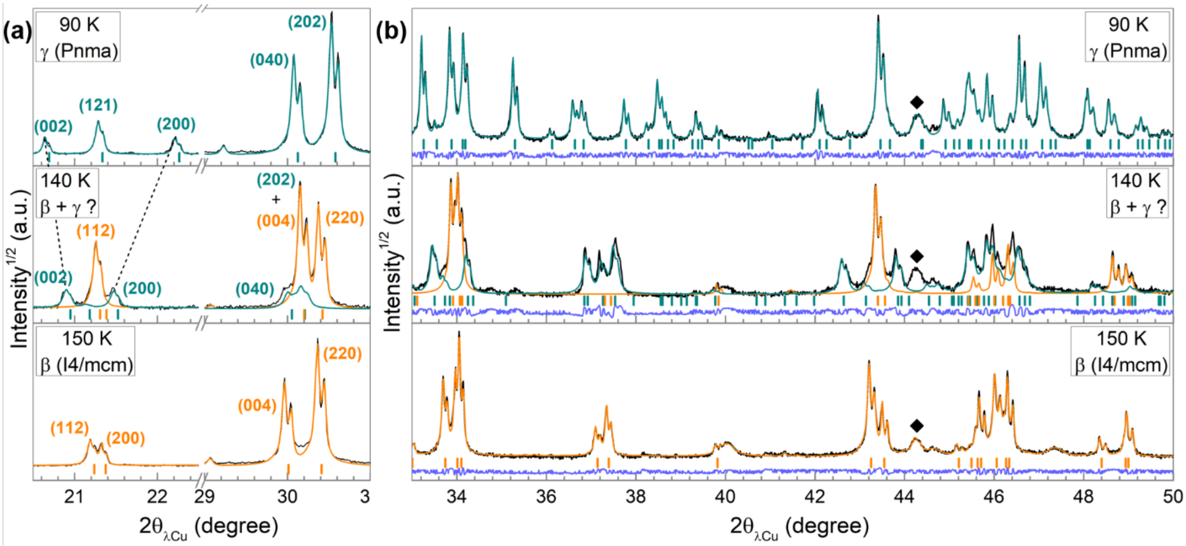

Figure 5.5: XRD pattern of $MAPbBr_3$ at 90 K (orthorhombic Pnma), 140 K (unknown phase, probably coexistence of tetragonal and orthorhombic) and 150 K (tetragonal I4/mcm) at two different 2θ ranges: (a) between 20.5 and 31° and (b) between 33.5 and 50 °. The black line represents the observed data, the green and orange lines represents the calculated pattern for, respectively, the orthorhombic phase and the tetragonal phases. The black diamond indicates the diffraction lines arising from the samples chamber and attributed to Ni.

Observing the behavior of the lattice parameters of $MAPbI_3$ in Figure 5.3, we can highlight the smooth evolution of the orthorhombic and tetragonal lattice parameters during the coexistence of the two phases: no abrupt change is observed. However, in the case of $MAPbBr_3$, our data reveals a sudden change in the peak positions when entering the temperature domain of interest. The dashed lines in Figure 5.5.a highlight the great difference in the peak positions of the pure orthorhombic phase and the pattern measured at 140 K, in the temperature range of interest. This sudden change hints that, here, in contrast to $MAPbI_3$, it might not be an orthorhombic-tetragonal phases coexistence that is observed.

We attempted to refine the pattern at 140 K by assuming such phase coexistence. However, the refinement was no straightforward as the lattice parameters values cannot be deduced from the values refined for pure tetragonal and orthorhombic phases close to the phase transition because of the sudden change mentioned earlier. We determined the starting values for our refinement by observing the diffraction pattern of this phase and comparing it to the orthorhombic and tetragonal patterns. The data are displayed in Figure 5.5. First, we observed that in the 2θ range 20.5 – 22.5°, three peaks are present, resembling the orthorhombic pattern (Figure 5.5.a.). The middle peak shows a greater relative intensity than in the Pnma pattern, which could be explained by the presence of the tetragonal phase, which displays also a diffraction line at this position. We hypothesized that in this range, the peak at lowest and highest angles could be, respectively, the $(002)_{\mathrm{ortho}}$ and the $(200)_{\mathrm{ortho}}$ peaks, allowing us to estimate the orthorhombic a and c lattice parameters. In the 29 – 31° 2θ range, a first low intensity bump is observed, followed by two intense peaks. Both the orthorhombic and the tetragonal phases exhibit two intense peaks near these positions, but we observed that the first intense peak is higher in intensity than the second, in opposition to what is observed in the two reference patterns. We thus assumed that the intense peak at 30 ° is the superposition of two contributions. Comparison of the patterns at higher angles indicated that characteristic peaks of the orthorhombic phase have weak intensities, suggesting that the predominant phase is the tetragonal one. Hence, we assumed that the bump observed at low angle in the 29 – 31° 2θ range corresponds to the $(040)_{\mathrm{ortho}}$, the $(202)_{\mathrm{ortho}}$ and $(004)_{\mathrm{tetra}}$ reflections would coincide in the peak around 30.0° and the second intense line would correspond to the tetragonal (220) peak. Using these starting lattice parameters values, we refined the pattern and the result is shown in Figure 5.5.b. The calculated pattern did not match perfectly all the observed lines, especially in the 2θ range 36-38°, as proved by the value of χ^2 discrepancy index which was higher for the refinement of the pattern at 140 K ($\chi^2 = 4.5$) than the ones performed at 90 and 150 K ($\chi^2 = 3.13$ and 2.59, respectively).

This observation indicates that between 145 ± 4 K and 138 ± 1 K, $MAPbBr_3$ does not display an orthorhombic – tetragonal phase coexistence, but an additional structure is formed.

Through high-resolution capacitive dilatometry performed on $MAPbBr_3$ single crystals, Keshavarz *et al.* extracted the length change $\Delta L/L$ as a function of temperature. Phase transitions would appear as peaks in a $\Delta L/L = f(T)$ plot, and they observed three distinct peaks when studying $MAPbBr_3$. In addition to the two peaks corresponding to the cubic-tetragonal and tetragonal-orthorhombic phase transitions, they observed another peak, at the temperature where the unknown structure appears. This observation agrees with our conclusion that the unknown phase may not be a coexistence of tetragonal and orthorhombic phase, but another structure. Temperature dependent photoluminescence (PL) studies did not show any specific PL features displayed at the corresponding temperatures.[9] While some papers identified this phase as a tetragonal P4/mmm[10],[9] others failed to identify the structure, describing it as "transient lines which could not be indexed either as tetragonal or as orthorhombic"[11] or as an incommensurate phase.[4]

Our pattern could not be refined using the proposed tetragonal P4/mmm symmetry Poglitsch, 1987][9] and we could not find any structure to describe correctly the measured data. While the question around nature of this phase is not definitively answered, it is worth noting the difference in behavior between $MAPbBr_3$ and $MAPbI_3$, the latter showing a low temperature behavior which was rather easily explained.

Before starting the next paragraph which reports our findings on the temperature-dependent behavior of the $MAPb(I_{1-x}Br_x)_3$ solid solutions, Figure 5.6 presents a short summary of the temperature-dependent behavior of the two end compounds $MAPbBr_3$ and $MAPbI_3$. Both show the same main features: upon cooling, the highest symmetry Pm-3m cubic cell transforms into a tetragonal I4/mcm structure. Further cooling induced additional octahedra tilting as the structure transits into an orthorhombic Pnma structure. Besides the difference in the temperature at which the transition happens, the main distinction between $MAPbI_3$ and $MAPbBr_3$ comes from the transition state between tetragonal and orthorhombic symmetries. While $MAPbI_3$ shows a domain of coexistence of both structures, the study of $MAPbBr_3$ reveals the formation of a structure which nature is still under debate.

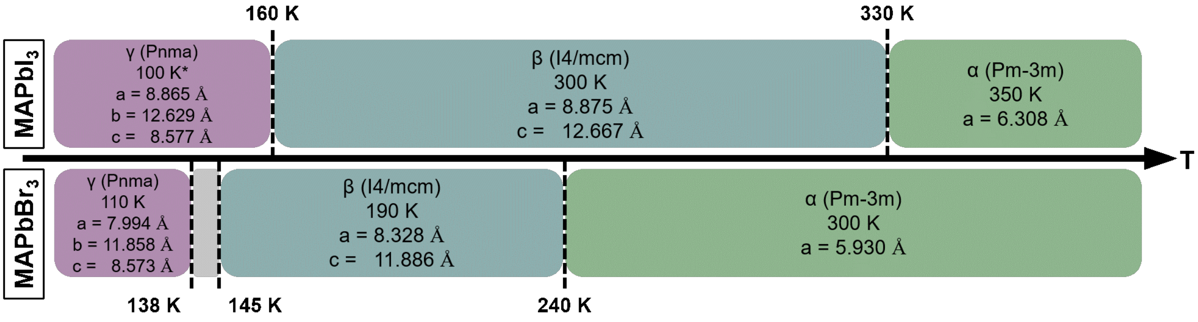

Figure 5.6: Summary of the temperature-induced phase transitions in both $MAPbI_3$ and $MAPbBr_3$ between 100 and 400 K. All reported lattice parameters values were taken from our experiments, expect for the orthorhombic $MAPbI_3$ for which we used the values refined by Weller *et al.*.[12] The temperatures indicated inside the different boxes correspond to the temperatures at which the indicated lattice parameters where extracted. The temperatures indicated between the boxes are the phase-transition temperatures we found.

5.2.3. PHASE DIAGRAM OF $MAPb(I_{1-x}Br_x)_3$ SOLID SOLUTIONS

After studying the behavior of the two end compounds $MAPbI_3$ and $MAPbBr_3$, we now present the results on the temperature induced phase transitions in $MAPb(I_{1-x}Br_x)_3$ solid solutions which one can expect to behave similarly to the end compounds. Figure 5.7 shows contour plots on selected 2θ ranges for all measured samples. The compound containing 40 % Br is not displayed here as we did not have enough time to measure the same range of temperatures as for all the other samples. Fortunately, as we are investigating multiple compositions, the one missing did not compromise our understanding of the general behavior of the family of compounds.

For sake of clarity, and to avoid an overcrowded figure, the Miller indices of the peaks of interest are only displayed on the first panel of Figure 5.7 which corresponds to the sample containing 10 % Br. The 2θ ranges on all panels were selected to have the same width (6° range) and to display the same peaks, thus taking into account the differences in lattice parameters between the different compositions. Symbols α, β and γ present on all the panels indicate the structure adopted by the compounds, respectively cubic Pm-3m, tetragonal I4/mcm and orthorhombic Pnma in the temperature domains limited by the white lines which identifies the phase transition. To determine the temperature of the cubic-tetragonal phase transition, two indicators can be used. Firstly, the broadening and splitting of cubic (220) and (210) reflections and secondly, the apparition of the (213) tetragonal reflection which is extinct in the cubic phase. We indicate the latter reflection with an orange diamond on Figure 5.7. Similarly to the previous contour plots presented in this chapter, the red star indicates the peaks arising from ice and the black squares marks peaks of a parasitic phase, here PbIBr (ICDD 04-007-5333) observed on the samples containing 80 and 90 % Br (peaks already existing before cycling and which intensities and FWHMs do not evolve during and after the measurement).

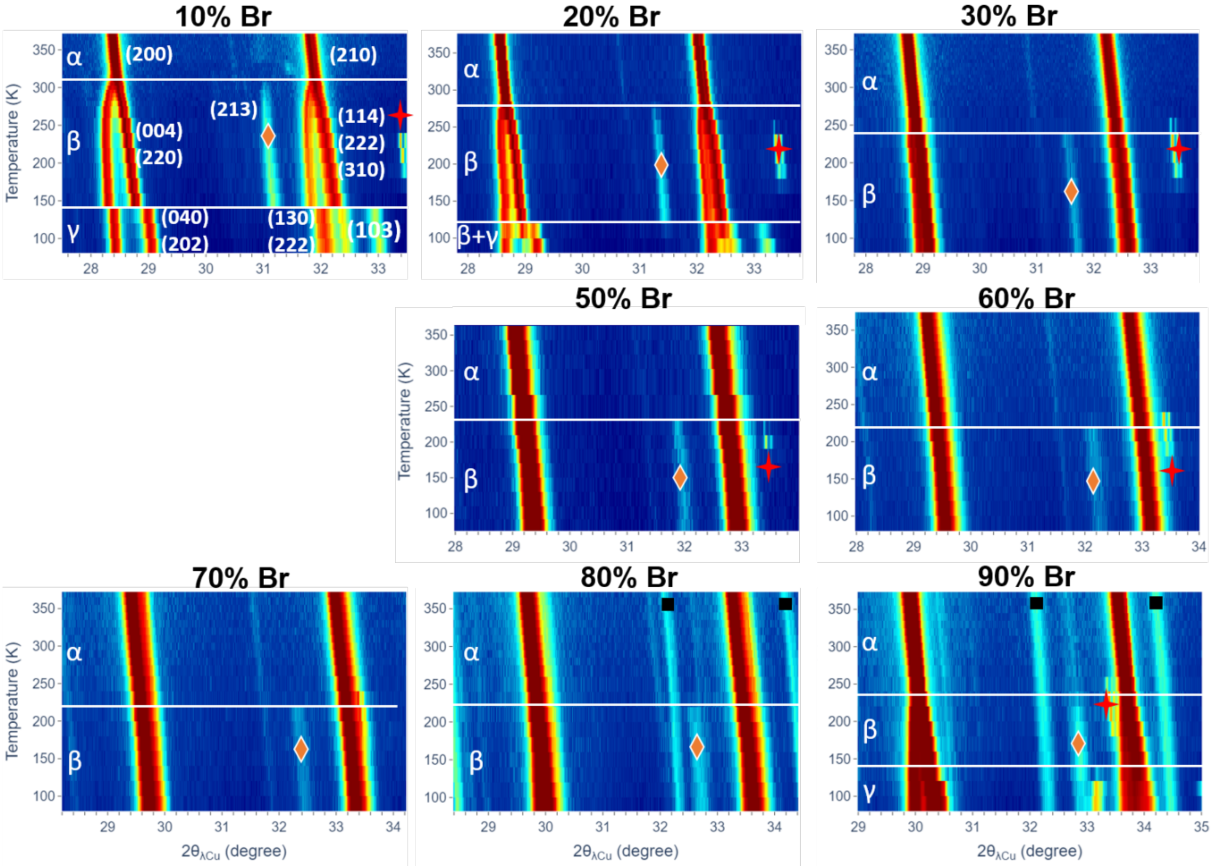

Figure 5.7: Contour plot showing the temperature induced structural changes between 90 and 380 K in $MAPb(I_{1-x}Br_x)_3$ solid solutions. The sample containing 40 % Br is not represented here as the full temperature range could not explored on this sample. The first panel, which shows the evolution of the sample containing 10 %, details the indices of the perovskite phases peaks that are displayed in all the panels. The symbols α, β and γ correspond, respectively, to the cubic, tetragonal and orthorhombic phases. The orange diamond marks the position of the (213) reflection which is the indication of cubic-tetragonal phase transition. The red stars indicate the position of the ice peaks and the black square represent position of degradation PbIBr (ICDD 04-007-5333), which are present in 80 and 90 % Br from the beginning of the experiment and does not evolve in intensity, FWHM and peak positions. Intensities, displayed as the color scale, are presented in logarithmic scale.

Inspection of the contour plots leads to the following observations:

For 10 and 20 % Br (low bromide content) : visual inspection reveals two phase transitions: first, a cubic - tetragonal phase transition at high temperatures (317.5 ± 2.5 and 295 ± 5 K for 10 and 20 % Br respectively). Secondly, the tetragonal – orthorhombic phase transition is observed at 140 ± 10 and 120 ± 10 K for 10 and 20 % Br respectively. The cubic, tetragonal and orthorhombic phases were refined using Pm-3m, I4/mcm and

Pnma space groups, respectively, for both samples, showing a behavior similar to end-compounds $MAPbI_3$. Acquiring pattern every 20 K, we did not observe coexistence between the tetragonal and the orthorhombic phases for 10 % Br. However, for 20 % Br, a close inspection in the low temperature scans revealed the coexistence of these low temperature phases over a range of 40 K and we did not observe purely orthorhombic structure on this sample over the temperature range we measured.

For 30 to 80 % Br (intermediary to high bromide content) : The first feature observed for these compositions is the absence of the tetragonal-orthorhombic phase transition in the probed temperature range. While identifying the cubic-tetragonal phase transition in 30 % Br is still possible by following the broadening of the cubic (200) reflection upon cooling, it becomes harder for higher Br-content. The (213) tetragonal reflection, which is extinct in the cubic phase, is the most reliable mean to determine the cubic-tetragonal phase transition for these compounds. The orange diamond in Figure 5.7 marks its position and its apparition upon cooling indicates the transition of the sample to the tetragonal phase. The white horizontal lines in all panels are added as a guide for the eye to identify the temperature of the phase transition. Interestingly, the transition cubic-tetragonal transition happens at close values for all these compositions, between 220 ± 10 and 250 ± 10 K.

For 90 % Br (high bromide content) : This final concentration, the closest to the end compound $MAPbBr_3$ displays the re-apparition of the orthorhombic phase at 130 K after the transition of the cubic phase to tetragonal around 240 K. We would like to point out that anisotropic peak broadening was observed on the tetragonal phase at this composition. This feature was correctly taken into account using Stephen's Model in Topas (cf subsection 4.2.2), by using the Low Tetragonal anisotropy model and refining the S_{400} anisotropic parameter. The same anisotropic line broadening was observed in the orthorhombic phase, but it was harder to refine, due to the high intrinsic strain in this compound (cf subsection 4.3.3) which resulted in broad peaks, even more so in the orthorhombic phase, making the refinement tricky and less reliable. Cubic and tetragonal phases were refined using Pm-3m and I4/mcm space groups and the low temperature orthorhombic patterns agreed with a Pnma symmetry.

All the determined phase transition temperatures are reported in Figure 5.8 which present the full phase diagram of $MAPb(I_{1-x}Br_x)_3$ solid solutions family of compounds. Concerning the sample containing 40 % Br on which we measured only a few temperatures, we estimated the transition temperature to be at the center of the temperature domain delimited by the highest temperature at which we observed the tetragonal phase and the lowest temperature which displayed the cubic symmetry, hence the larger error bars for this composition on the phase diagram.

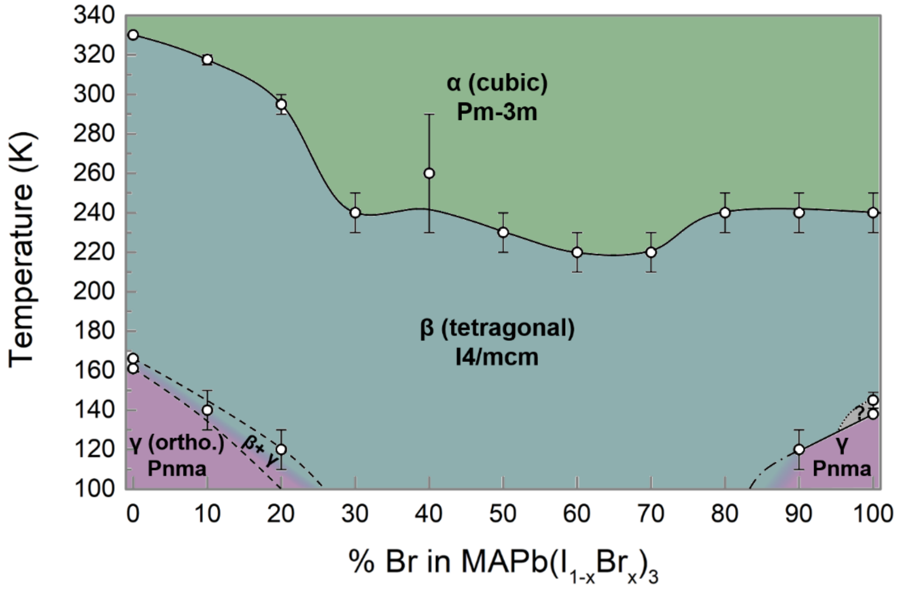

Figure 5.8: Phase diagram of $\mathrm{MAPb(I_{1-x}Br_x)_3}$ solid solutions showing the phase transitions observed between 90 and 400 K.

The temperature behavior of $\mathrm{MAPb(I_{1-x}Br_x)_3}$ reveals two main features. First, while the introduction of increasing amounts of Br induces a lowering of the cubic-tetragonal phase transition temperature, this transition is never lowered below 210 K. For intermediate Br concentration (30 to 70 %), this transition temperature in mainly constant, at a temperature slightly lower than in the pure compound $\mathrm{MAPbBr_3}$. Secondly, the tetragonal – orthorhombic phase transition is greatly impacted by halide mixing. Coexistence of tetragonal and orthorhombic phases is observed in $\mathrm{MAPbI_3}$ over a narrow temperature domain of approximately 5 K.[5] When introducing 10 % Br, no phase coexistence is noted in our measurements, and as we acquired a pattern every 20 K, we can say that the phase coexistence takes place over a temperature range smaller than 20 K. However, the sample containing 20 % Br, showed a large temperature domain of 40 K where both orthorhombic and tetragonal structures coexist. When increasing the amount of bromide in the samples, even at the lowest temperature we reached (90 K), no orthorhombic phase was observed. We previously showed that increasing Br content in the lattice induced increasing crystal defects in the lattice at RT. Our observation would suggest that as the defects in the packing increases, highest symmetries are favored to the detriment of low symmetry orthorhombic phase. We can understand that as disorder grows, an average high symmetry is reached on the long range in the sample.

Next, we extracted the lattice parameters of all the samples for all the measured temperatures and reported them in Figure 5.9. To avoid complicating the graph, we only focused on the cubic and tetragonal lattice parameters and did not add the evolution of the orthorhombic lattice parameters.

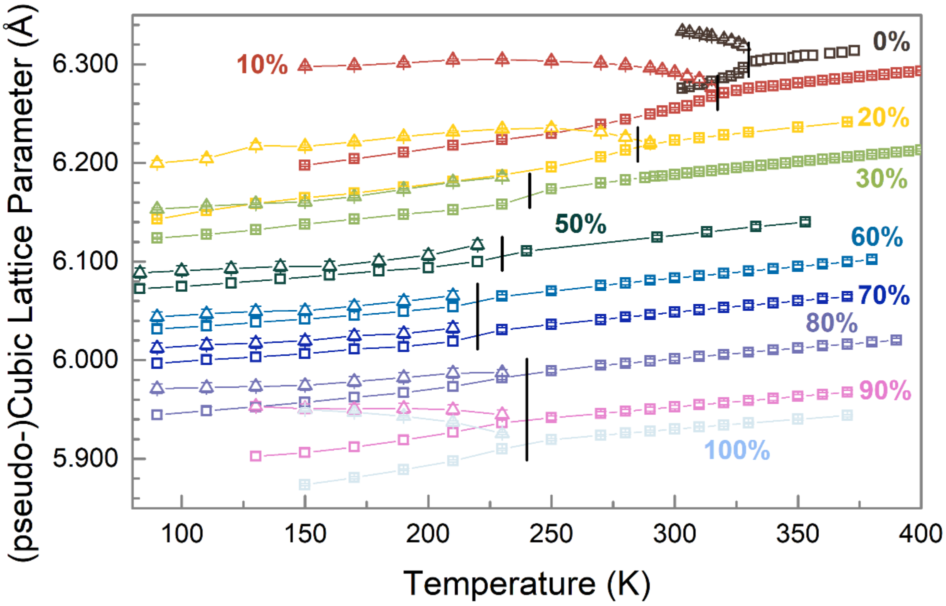

Figure 5.9: Tetragonal lattice parameters reduced as pseudo-cubic lattice parameters and cubic lattice parameter for $MAPb(I_{1-x}Br_x)_3$ solid solutions over the whole measured temperature range. a and c lattice parameters are marked, respectively, by the triangle and square symbols. Black vertical lines indicate the cubic – tetragonal phase transition temperature for each sample. The errors bars are smaller than the markers.

The first observation concerns the difference between a and c tetragonal lattice parameters for all compounds. The reported values of a^T_{pC} and c^T_{pC} for intermediary compositions (x = 50 to 80 % Br) are quite close over the whole probed temperature range, in opposition to the behavior observed in pure compounds and compounds with x = 10, 20, 30 and 90 % Br. This behavior is highlighted in Figure 5.10.a where the evolution of the tetragonal factor against the Br content is reported. The tetragonal factor is the ratio a^T_{pC}/c^T_{pC} and it characterizes the deviation of the tetragonal cell from the cubic structure: this factor is equal to 1 for a cubic lattice, and the lower the value, the more important the tetragonal distortion (more elongation along c here). Since the samples exhibit different cubic – tetragonal phase transitions, to obtain comparable data, the tetragonal factor was calculated at a reduced temperature of – 0.08 for all compounds. The reduced temperature T_{red}, which allows to compare the temperature behavior of sample with different transition temperatures, is calculated as:

$$T_{red} = \frac{T - T_t}{T_t} \tag{5.3}$$

Where T_t is the transition temperature. Figure 5.10.a shows **the increase of the tetragonal factor for intermediate Br compositions, as it becomes quite close**

to 1 when 50 to 80 % of Br are introduced in the lattice.

The second observation concerns the temperature evolution of the tetragonal c lattice parameters. As can be seen in Figure 5.9, in both pure compounds, c parameter shrinks as the temperature is increased over the whole temperature stability domain of the tetragonal structure, indicating a directional negative thermal expansion (NTE) coefficient along c. As more Br in introduced in the lattice, the temperature domain of the NTE of c gets smaller (10 and 20 % Br), until it eventually becomes smaller than 20 K (the temperature interval between two measurements) for composition of 30 to 70 % Br. The NTE is observed again on samples containing more than 80 % Br .

These two observations are related to the precision of determination of the tetragonal lattice parameters, which we now address. First of all, the cubic-tetragonal phase transition cannot be questioned. Figure 5.7 distinctively shows the apparition of the (213) tetragonal peak on all panels, which, despite a rather weak intensity, is clearly marked when using a logarithmic scale. Second consideration would be on the resolution between the two peaks. Figure 5.7 shows that is it hard to distinguish any peak broadening when entering the tetragonal phase for compositions between 50 and 70 % Br. The precision in the determination of the c parameter will only rely on the weak additional peaks (such as (213)), leading to a lower precision. That said, it is worth noting that in the case of 30 % Br, where peak broadening is clearly observed when cooling and thus a higher precision in the lattice parameters is obtained, we do not observe the NTE along c. Moreover, refinement of the data obtained from the sample containing 80 % Br, for which peak broadening upon cooling remains hard to see, showed a convergence of the lattice parameters when the sample's temperature was close to the transition temperature. Hence the validity of our observation on the evolution of the tetragonal factor and the directional NTE along c.

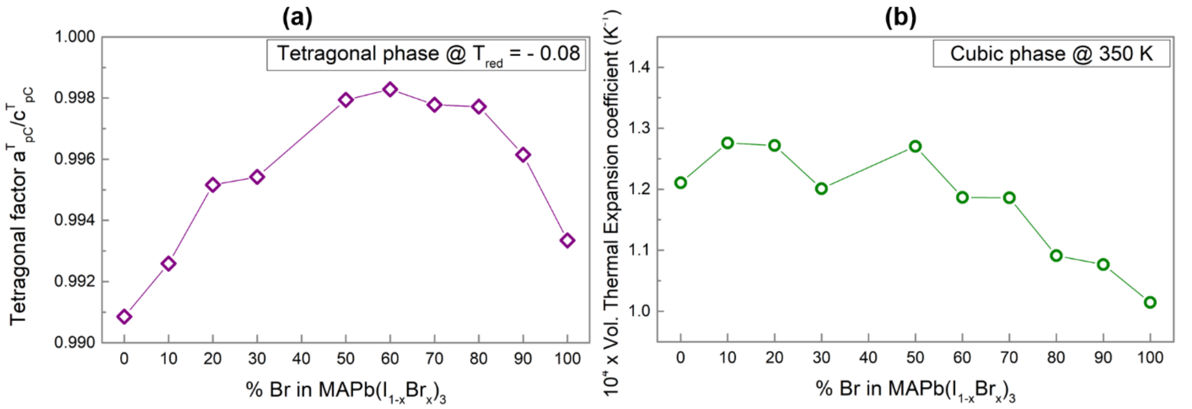

Figure 5.10: (a) Tetragonal factor of $MAPb(I_{1-x}Br_x)_3$ (x = 0 to 100 % Br) compounds in the I4/mcm symmetry, calculated at Tred = - 0.08. (b) Evolution of the volumetric thermal expansion coefficient of the cubic phase of $MAPb(I_{1-x}Br_x)_3$ (x = 0 to 100 % Br) at 350 K.

Finally, we extracted the volumetric thermal expansion coefficient (CTE) αV of the different MAPb($I_{1-x}Br_x$)$_3$ compounds, which we calculated using the following equation:

$$\alpha_V = \frac{1}{V}\frac{\delta V}{\delta T} \tag{5.4}$$

We report here only the CTEs in the cubic phase, at 350 K, for the different compounds to avoid any considerations about the precision determination of the tetragonal lattice parameters for some compounds. The results are displayed in Figure 5.10.b, showing that $MAPbBr_3$ exhibits slightly smaller volumetric CTE then $MAPbI_3$, and that increasing contents of Br in the sample induces a gradual decrease in the expansion coefficient. This tuning of volume expansion through composition is a highly interesting property to consider when selecting a material for its integration in a device. It is even more critical when the device is destined to be exposed to a large temperature range and if its configuration consists in a stacking of different thin layers which can exhibit different volume expansion coefficients. However, it is important to highlight the fact that these volumetric CTEs values are quite high. For example, volumetric CTE of crystalline Si is $0.08 \times 10^{-4}\,K^{-1}$,[13] for $BaTiO_3$, the CTE is found to be $0.06 \times 10^{-4}\,K^{-1}$,[14] which is more than one order of magnitude lower than $MAPbBr_3$ ($1 \times 10^{-4}\,K^{-1}$).

5.3. Temperature behavior of FA-based compounds

5.3.1. Structural phase transitions in $FAPbI_3$

In contrast to MA-based halide perovskite, FA-based compounds have been less investigated, despite their promises. In the case of $FAPbI_3$, it is mainly because of the unstable character of the perovskite phase and its spontaneous evolution into its so-called yellow hexagonal polymorph (δ-phase), which has made the studies delicate.

We start this study by first inspecting the temperature behavior of the yellow δ-phase of $FAPbI_3$, which at RT, adopts a hexagonal $P6_3/mmc$ symmetry. By lowering the sample's temperature from RT to 90 K, additional diffraction peaks appear between 173 and 153 K, indicating a phase transition between these two temperatures. In agreement with the literature, the pattern recorded at 93 K was refined using the hexagonal $P6_3/m$ space group, as shown in Figure 5.11 with lattice parameters of a = 8.537(3)Å and c = 7.944(3)Å.[15] We should precise that upon cooling and as we approached the phase transition, the diffraction peaks became broader. For time reasons, we performed scans on a reduced 2θ range, thus, we could not evaluate the strain values arising as the sample approached the phase transition.

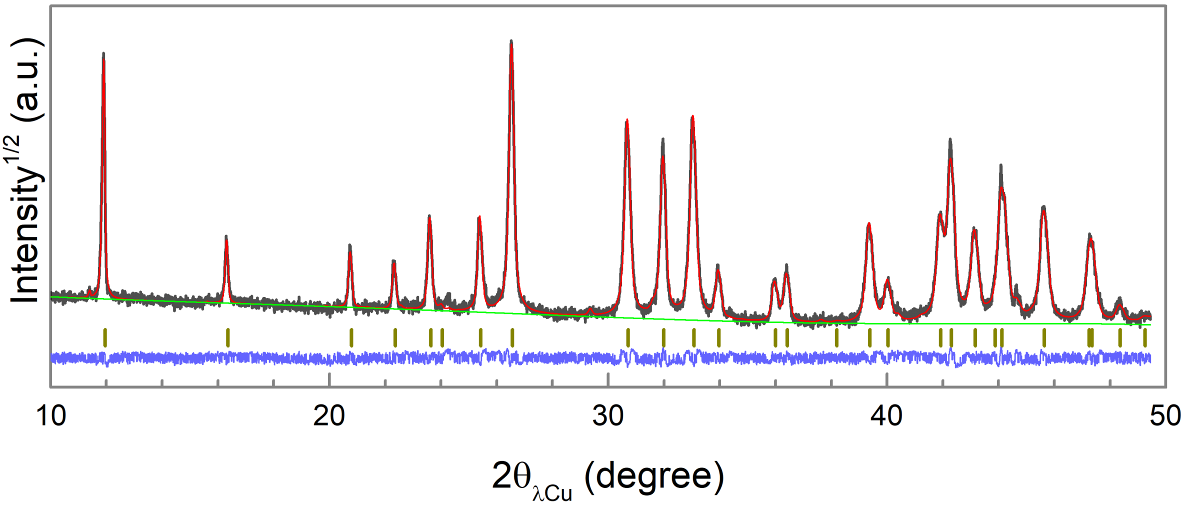

Figure 5.11: LeBail refinement of the low temperature (90 K) phase of hexagonal δ-FAPbI3 in P63/m space group, with a = 8.537(3) $\AA$ and c = 7.944(3) $\AA$.

Thereafter, the temperature behavior of the metastable cubic $FAPbI_3$ is studied. This structure can be kinetically trapped at RT after heat treatment of the sample above 150 °C and subsequent cooling down. Here, after 1h at 160 °C, $FAPbI_3$ was cooled down to RT, and the cubic phase was studied. A temperature range from 93 to 383 K was probed, and data was collected with 15 K steps, using the same counting statistics as before (cf section 5.1 of this chapter). Upon cooling, this cubic Pm-3m phase becomes tetragonal around 270 K, as can be seen on Figure 5.12.a where the (210) and (211) line appears, characteristic of the tetragonal structure. In agreement with the literature, the tetragonal lattice was refined in the P4/mbm space group. It is worth noting that the space group of this tetragonal phase is different from the I4/mcm symmetry adopted by MA-based compounds. When comparing empirical observations, Butler found that I4/mcm tetragonal crystals are more likely found in halide perovskites. By running interatomic potential simulations, he found that larger A cations will favor P4/mbm over I4/mcm (ionicity of the structure also plays a role, P4/mbm is more easily found in bromide and iodine based than in fluoride perovskites), which is in agreement with the larger cation size FA-based samples adopting the P4/mbm symmetry.[16] P4/mbm space group corresponds to $a^0a^0c^+$ symmetry in Glazer's notation. In this symmetry, two adjacent octahedra layers along c tilt in the same direction, leading to similar packing. Hence, there is no need to double the lattice along the c axis in this structure in comparison to the cubic lattice and c^T can be directly compared to a^C.

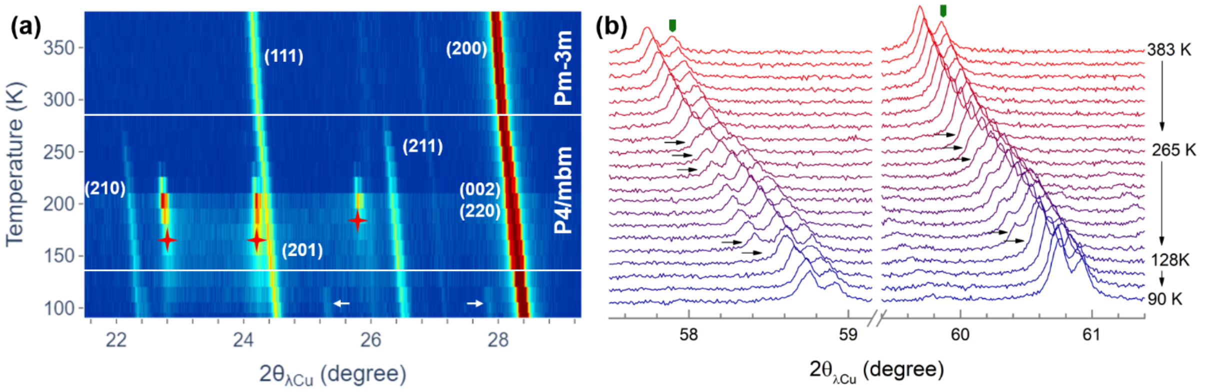

Figure 5.12: Temperature behavior of $FAPbI_3$. (a) contour plot of a selected 2θ region, showing the cubic (Pm-3m) tetragonal (P4/mbm) phase transition expressed by the growth of tetragonal (210) and (211) reflections between 278 and 263 K. The white horizontal line indicates this transition. A third temperature domains is indicated by the low temperature white line, where the tetragonal (002)/(220) peak sharpens. The white arrows indicate peaks appearing at low temperatures and red stars marks the ice peaks positions. (b) XRD patterns on a selected 2θ region stacked to show the splitting of the Bragg peaks between 278 and 263 K, indicating the cubic – tetragonal phase transitions. It is followed by a sharpening of these same peaks at lower temperatures, between 143 and 128 K. Black arrows are a guide for the eye to observe the peak splitting and sharpening as the temperature decreases. The green symbols indicate the Kα2 diffraction lines.

Interestingly, below 143 K and as showed on Figure 5.12.b, the peak splitting disappears, which would indicate a reentrant tetragonal-cubic phase transition at low temperatures, however, Figure 5.12.b shows that the distinctive peaks of the tetragonal phase remain present. Moreover, additional peaks are observed at low temperature (LT), indicated by the white arrows in Figure 5.12.a. Such unusual behavior has already been observed on $FAPbI_3$ in the literature.[17,18] Two strategies have been employed in the literature to describe this low temperature phase. The first consists in considering a tetragonal P4/mbm super cell, multiplying the lattice 6-fold along the c direction. While this solution allows to refine all the peaks, even the additional ones observed at LT, many calculated peaks have to be attributed zero intensity which is not satisfying. The fact that this super-cell helps to refine the additional peaks falls under statistical chances of finding a peak at a given angle rather than real physical meaning behind the used model.

The second strategy, which is the one we adopted, is to refine the pattern with close a and c lattice metrics and P4/mbm space group, allowing to refine the major features of the pattern. Comparison of the best refinements obtained at 218 K (before the second phase transition) and 90 K (after the second phase transition) is shown in Figure 5.13. Table 5.1 summarizes the peak positions not met by the P4/mbm symmetry and observed under 140 K. Some of these peak positions are in agreement with the ones observed by Weber *et al.*.[18]

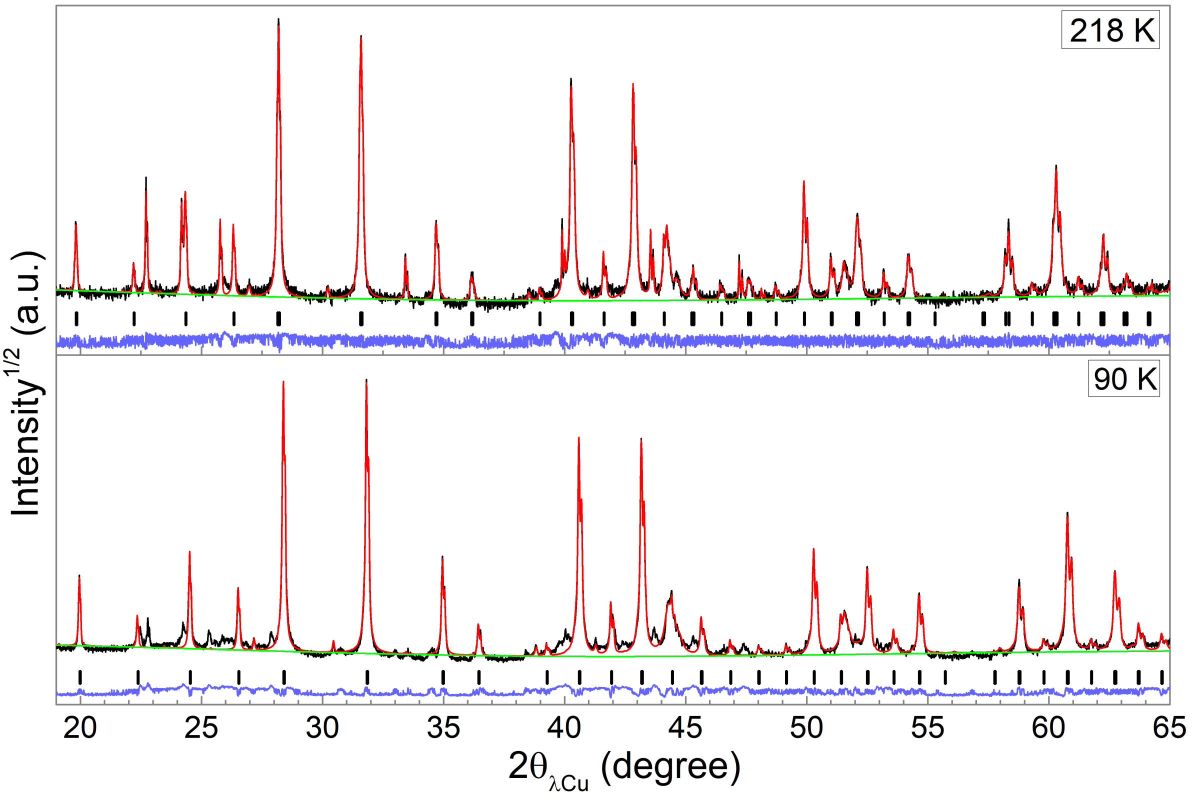

Figure 5.13: LeBail refinement of XRD pattern of $FAPbI_3$ measured at 218 (top panel) and 90 K (bottom panel), using, for both, P4/mbm space group. While the refinement matched all observed lines at 218 K, additional peaks at 90 K are not met by the P4/mbm space group.

2θ (°)	22.47(2)	25.31(3)	27.87(2)	38.39(2)	43.70(1)	45.31(1)	47.39(1)	51.99(2)	52.91(2)
d (Å)	3.953(2)	3.516(5)	3.197(2)	2.343(2)	2.070(2)	2.000(1)	1.917(1)	1.757(1)	1.729(1)

Table 5.1: Additional Bragg lines appearing at T < 140 K and not explained by P4/mbm space group.

We should highlight that no tetragonal space group allowed refining the additional peaks. Moreover, using an orthorhombic symmetry does not seem appropriate when considering the narrow peak widths and the small number of observed Bragg lines. Finally, these additional peaks do not correspond to diffraction lines observed for the low temperature δ-FAPbI3 polymorph. The lattice parameters obtained from our refinement using P4/mbm space group from 90 to 270 K are displayed in Figure 5.14.a. In the tetragonal phases, pseudo-cubic a^T_{pC} lattice parameter was used for clarity (cf. Equation 5.2). We calculated the tetragonal factor defined as a^T_{pC}/c^T for all phases and the result is shown in Figure 5.14.b. It appears that after the cubic-tetragonal phase transition, the tetragonal factor gradually deviates from 1, indicating a higher tetragonal distortion. The tetragonal factor abruptly increases, retrieving a value close to 1 (smaller tetragonal distortion) as the second phase transition happens and as can be expected from the disappearance of the peak splitting (Figure 5.12.b and the close a^{T}_{pC} and c^{T} values (Figure 5.14.a. These results are in good agreement with the reports from the literature.[17,18] In the following, the first tetragonal phase (between 270 and 135 K) will be referred to as β and the low temperature tetragonal phase will be called β'.

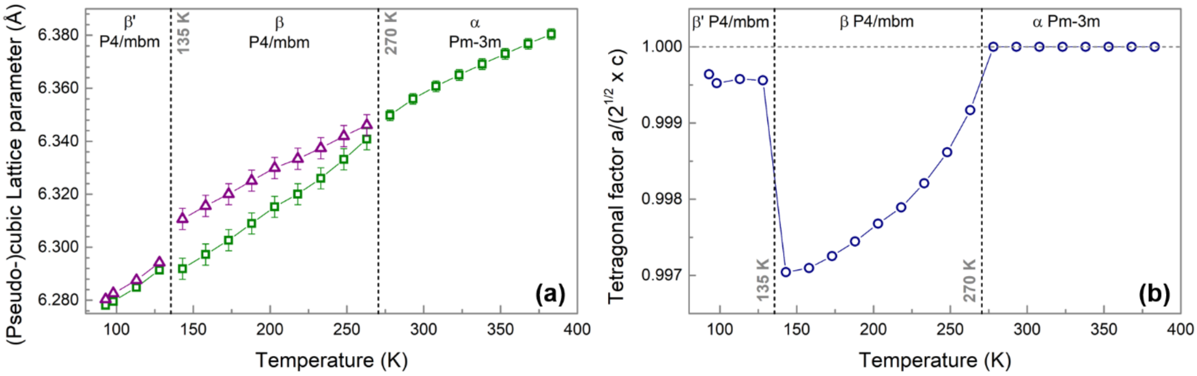

Figure 5.14: (a) Pseudo-cubic lattice parameters evolution over the whole measured temperature range for FAPbI$_3$. The low temperature region shows close values for a and c lattice metrics, in agreement with the thinner Bragg lines observed. (b) Evolution of the tetragonal lattice ratio over temperature, showing an increasing deviation from 1 (ideal cubic) in the first β phase (between 170 and 135 K), before an abrupt increase to a value close to 1 as the sample transits to its low temperature phase.

These observations give rise to many questions about the mechanism behind such an unusual behavior at low temperatures. A close inspection of our data revealed another interesting feature by comparing peak areas. On the one hand, Bragg lines which are present over the whole temperature range, for instance peak at $2\theta \sim 28$ ° ((200) and (002)/(220) reflections in the cubic and tetragonal structures, respectively) display an increase of their areas while cooling, as expected. On the other hand, peaks which are characteristic of the tetragonal symmetry (such as (210) and (211), Figure 5.12.a and (410)) display a noticeable decrease of their intensity when lowering the temperature and entering the low temperature β' phase. These observations are displayed in Figure 5.15.

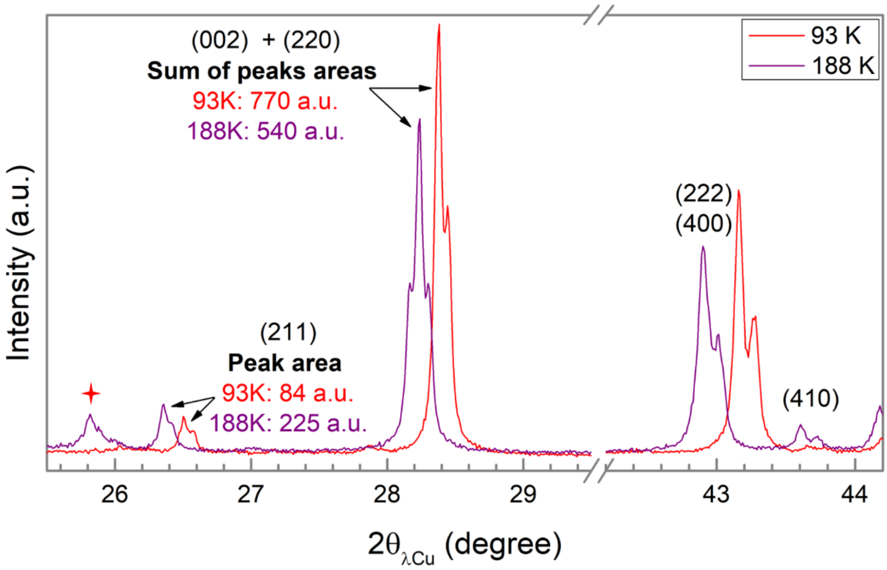

Figure 5.15: Comparison of peak areas at 93 (β' phase) and 188 K (β phase), showing a decrease of the area of the peaks characteristic of the tetragonal phase while the other Bragg lines display an increased peak area as the temperature is lowered

Precious elements of understanding are given in Fabini's *et al.* work.[19] The authors compared activation barriers for molecular rotation of FA^+ obtained from solid-state proton NMR and DFT calculations. They found good agreement between the experimental and calculated values for both α (cubic Pm-3m) and β (tetragonal P4/mbm) phases, yet noticeable discrepancies were observed in the low temperature phase (β'). For the LT phase simulations, the authors used the structure extracted from scattering measurements (X-ray and neutrons) which suggest small octahedral tilting ($a^T_{pC} \approx c^T$). They explained that the discrepancy may thus arise from local octahedra tilts, not taken into account in the simulation but which are known to greatly impact the properties of the perovskites. A random distribution of these tilts would explain the features displayed by the diffraction measurements. Being random, the tilt could "cancel" themselves at the long range, thus leading to what would appear as $a^T_{pC} \approx c^T$. However, these tilts, which are not negligible as they impact the cation dynamics, would break the cubic symmetry, probably explaining why distinctive tetragonal peaks are observed on the XRD patterns, but also why these same peaks exhibit lower intensities than in a long-range ordered tetragonal phase. Thus, the β' phase can be qualified as disordered pseudo-cubic phase.

In the same paper, Differential Scanning Calorimetry (DSC) measurements were performed, showing that the $\beta \rightarrow \beta'$ phase transition is not a first order transition, nor a full order-disorder transition, but mostly a cascade of multiple events before the phase transitions (Figure 5.16.b). Moreover, solid-state proton NMR showed that while MA^+ and FA^+ exhibit the same reorientation times at RT, reorientation dynamics of FA^+ present a weaker dependence with temperature. Combining these two observations lead the authors to state that, upon cooling, incompatibility between the organic cation geometry and the inorganic framework tilting arises, leading to frustrated FA^+ cage interactions.

The organic cations were found to retain considerable motion in the β' phase until 100 K. Interestingly, below 100 K, solid-state proton NMR, calorimetry and dielectric constant measurements showed a gradual loss of motion of the cations. Here again, rather than being an abrupt order-disorder transition, this transition was found to correspond to a glassy freezing of the organic motion (Figure 5.16.b, c and d). Neutron scattering experiment did not exhibit any additionnal crystallographic phase transition below 140 K until 5 K.[19]

All the features explained above seem to indicate that the frustration of the FA^+ cation–inorganic cage interaction causes the formation of two independent sublattices below 140 K. On the one hand, around 140 K, the inorganic sublattice, which adopted $a^0a^0c^+$ tilting at higher temperatures (up to 270 K) becomes randomly tilted as frustration happens, thus appearing more symmetric on the long range. On the other hand, FA^+ which is less impacted by temperature lowering, keeps its motion freedom until 100 K (causing the frustration) before experiencing a glassy freezing around 60 K.

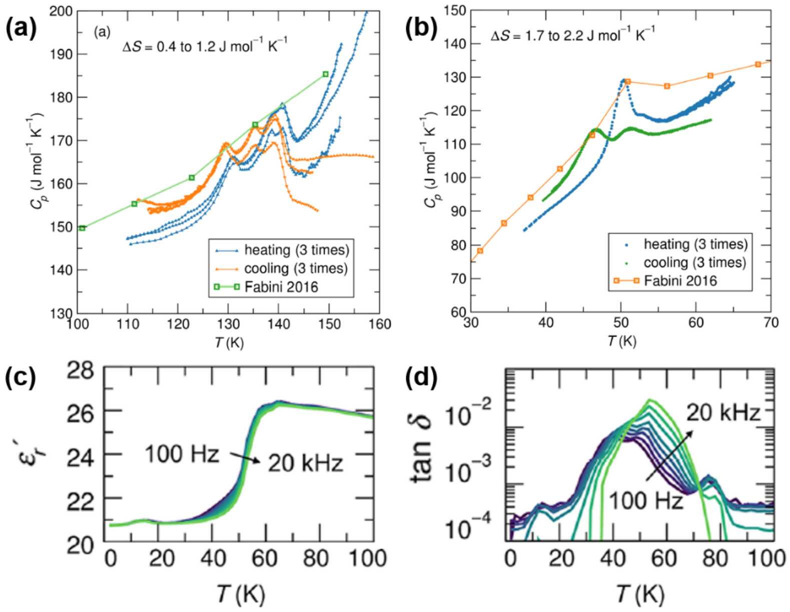

Figure 5.16: (a) Heat capacity in the vicinity of the $\beta \rightarrow \beta'$ phase transition, showing a cascade of events, with a total transition entropy ($< 1.2\,\mathrm{J\,mol^{-1}\,K^{-1}}$) significantly lower than in an order-disorder phase transition ($5.8\,\mathrm{J\,mol^{-1}\,K^{-1}}$). b) Heat capacity under 100 K, showing at least two events, with, here again, a total transition entropy ($\sim 2\,\mathrm{J\,mol^{-1}\,K^{-1}}$) significantly lower than in an order-disorder phase transition. From dielectric constant measurements, real permittivity showed an abrupt drop, thus indicating a restriction in the motion of the organic cation around 60 K (c) and the dielectric tangent loss tan δ showed a frequency modulated peaks around the same temperature, which indicates a glassy freezing of the dipoles (d). Adapted from Fabini *et al.*[19]

Such complex behavior is to be related to the plastic crystal nature of hybrid halide perovskite. A plastic crystal exhibits translational periodicity but orientational disorder. Hybrid halide perovskites can be qualified as plastic crystals because of the organic cation disorder. As the temperature is lowered, frustration and the strengthening of the hydrogen bonds (negligible at RT but not when T is lowered), leading to the features highlighted above. Further investigation concerning the dynamics of the cations and the cation-inorganic cage interactions is required, as it appears to be more complex than in $MAPbI_3$. It is worth mentioning however that the nature of the organic cation is not the only parameter to take into account as it was reported that $FASnI_3$ (same organic cation, smaller B cation) do not show such reentrant phase transition.[20] Fortunately for us researchers, a lot remains to be understood in this field.

5.3.2. STRUCTURAL PHASE TRANSITIONS IN $FAPbBr_3$

Similarly to $FAPbI_3$, fewer studies have been performed on $FAPbBr_3$ in comparison to its MA-based counterpart. Figure 5.17 displays our XRD data, measured between 90 and 380 K with data collection every 15 K, using the same counting statistics as before (cf section 5.1 of this chapter). A first observation from the inspection of the contour plot in Figure 5.17.a is the relatively small changes in the peaks width and intensities across the measured range, in comparison to what is observed on $MAPbBr_3$ for instance (Figure 5.4.a.). In agreement with the literature, this denotes tetragonal and orthorhombic lattices rather close to the cubic arrangement, expressing a pseudo-cubic symmetry even at low temperature. We refined the high temperature phase with the Pm-3m space group and reached satisfying agreement. When cooling the sample from RT, reflection around $2\theta = 28°$ (d = 3.18Å) appears between 120 and 135 K, indicating the apparition of the tetragonal phase which is refined in the P4/mbm space group, similarly to $FAPbI_3$.

By further cooling the sample, the (201) tetragonal peak splits, as well as (211), indicating a tetragonal-orthorhombic phase transition between 255 and 270 K. The low temperature pattern was successfully refined using the Pnma space group, as already reported in the literature. In their group theory based study, Howard and Stokes showed that P4/mbm and Pnma are related by the group-subgroup relationship,[6] indicating that a smooth second order phase transition is possible in this case, as opposed to what was observed for MA-based samples. Through DSC, Schueller *et al.* noted that the cubic-tetragonal phase transition is of second order while they observed a complex cascade of events near the tetragonal-orthorhombic transition.[20] These observations were later confirmed by heat capacity measurements[21] and dilatometry,[22] identifying a total number of 5 transitions among which only 2 are observed in scattering (cubic Pm-3m - tetragonal P4/mbm - orthorhombic Pnma). This cascade of events resembles what was observed on $FAPbI_3$ and described earlier.

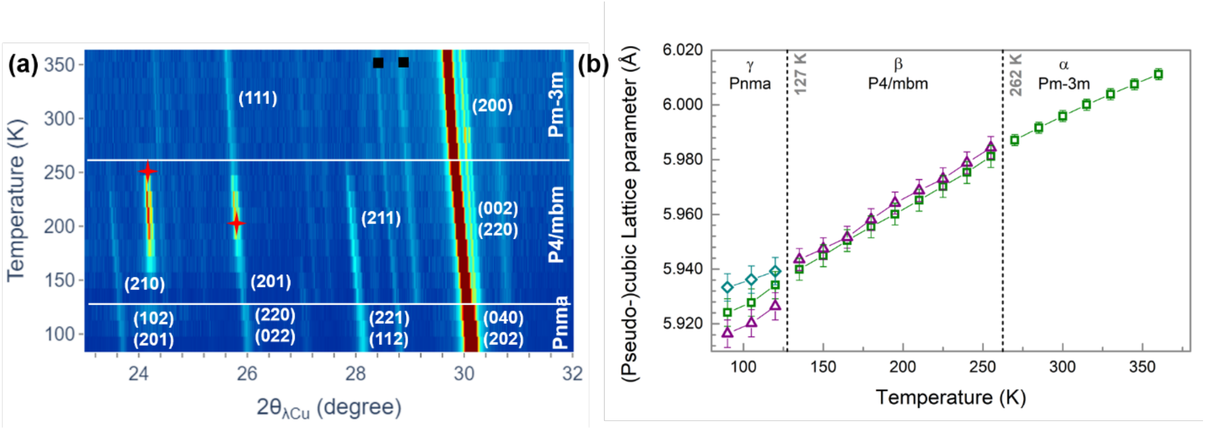

Figure 5.17: Temperature behavior of $FAPbBr_3$. (a) contour plot of the temperature evolution of $FAPbBr_3$ showing a first transition from cubic Pm-3m to tetragonal P4/mbm at 127.5 ± 7.5 K and a second transition from tetragonal to orthorhombic at 262.5 ± 7.5 K. The red stars represent the ice peak positions and the black squares peaks of a parasitic phase which is identified as PbBr2. (b) shows the evolution of the (pseudo-)cubic lattice parameters over the probed temperature range for all three crystallographic phases.

Moreover, at $T < 100$ K, Schueller *et al.* observed the same frequency dependence of the dielectric tangent loss as in $FAPbI_3$ (Figure 5.16.d), proving, here again, a glassy freezing of the FA^+ molecular motion which happens in the same temperature range (~60 K). Poorly understood as of now, these intriguing features need further investigations as Mozur *et al.* showed the influence of these changes in molecular motion on the photoconductivity of $FAPbBr_3$, which are most likely also observed for other hybrid lead halide perovskites.[21]

Finally, we would like to point out to an interesting feature arising from the comparison of FA and MA-based pure compounds. The tetragonal distortion is lower in FA-based than in MA-based: as shown in Figure 5.10, the tetragonal factor for $MAPbI_3$ and $MAPbBr_3$ is 0.991 and 0.993 respectively, at $T_{red} = -0.08$. At the same reduced temperature, tetragonal factor for $FAPbI_3$ and $FAPbBr_3$ is 0.998 and 0.999, considerably closer to 1. Phase transition to tetragonal symmetry in FA-based compounds lead to pseudo-cubic lattice parameters. This observation could be related to the high tolerance factor of these phases (cf section 4.1) and the large A-site cation which prevents the structure from exhibiting pronounced octahedral tilting.

As mentioned earlier, for both $FAPbI_3$ and $FAPbBr_3$ despite these complex molecular dynamic behavior, only three distinct crystallographic phases are observed. This thesis being mainly focused of the crystallographic changes in the perovskite, we will not be addressing the fascinating aspects of the organic cation dynamics in the following. In the same fashion as for MA-based compounds, before starting the investigation of the structural phase transition in mixed halide samples, Figure 5.18 below summarizes the phase transitions in FA-based end compounds.

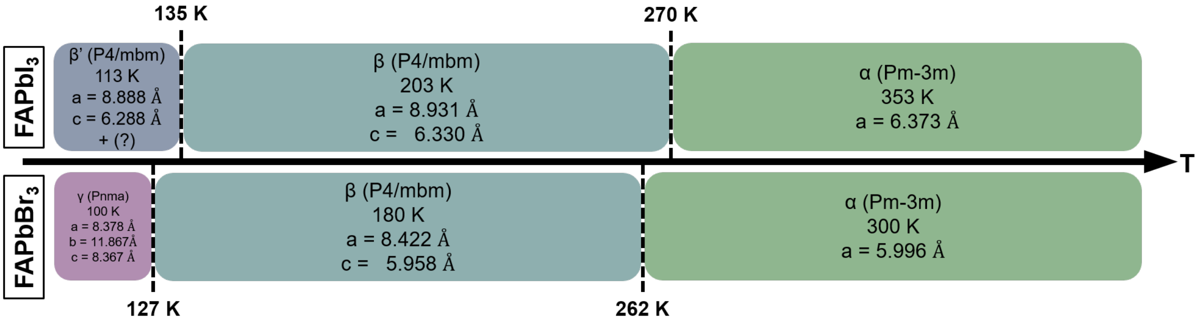

Figure 5.18: Summary of the temperature-induced phase transitions in both $FAPbI_3$ and $FAPbBr_3$ between 100 and 400 K. All reported lattice parameters values were taken from our experiments. The temperatures indicated inside the different boxes correspond to the temperatures at which the indicated lattice parameters were extracted. The temperatures indicated between the boxes are the phase transition temperatures we found.

5.3.3. PHASE DIAGRAM OF $FAPb(I_{1-x}Br_x)_3$ SOLID SOLUTIONS

Before establishing the phase diagram of $FAPb(I_{1-x}Br_x)_3$ solid solution family, we start by examining the temperature behavior of the compound containing 10 % of Br closely. The raw data of the temperature dependent XRD measurement, presented in Figure 5.19.a show that as the temperature drops, the peak broaden. Further cooling induces subsequent peak narrowing. The exact temperatures of the onset of these features will be determined in the following. We can however say at this stage that the same reentrant phase transition as with $FAPbI_3$ happens here. The same peaks as in Figure 5.12.b are displayed in Figure 5.19.a. Observing that at 90 K (lowest probed temperature) the peaks have been noticeably narrowing when compared with the higher temperature ones, we can safely assume that the sample is in its β' phase.

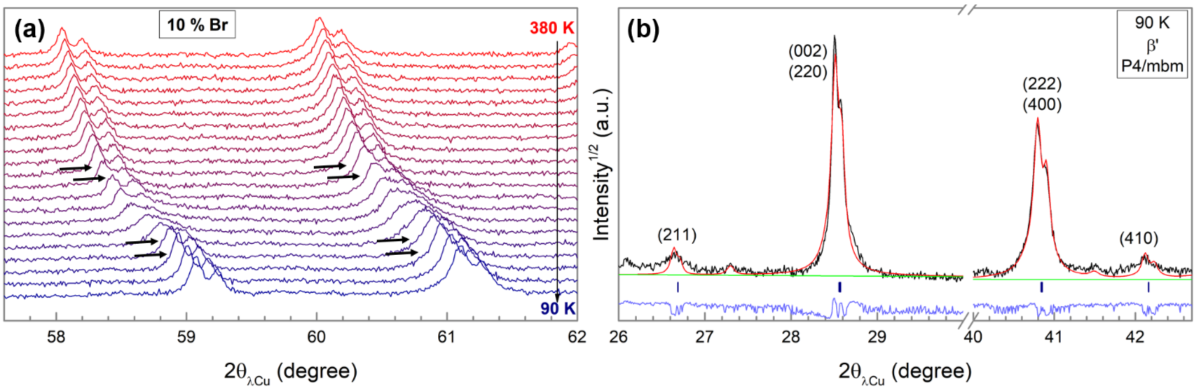

Figure 5.19: (a) Temperature behavior of FAPb$(I_{1-x}Br_x)_3$ containing 10 % Br showing a broadening on the peaks as temperature decreases before narrowing again at the lowest temperatures. Black arrows are a guide for the eye to identify the changes in the peak widths. The same peaks as in Figure 5.12.b are displayed. (b) Example of LeBail refinement performed on the sample containing 10 % Br at the lowest temperature we measured, 90 K, using P4/mbm space group, and assuming, from the narrowing of the peaks that the sample is in the β' phase, similarly to pure $FAPbI_3$ after the disappearance of the peaks splitting. The red curve, which represents the calculated data, shows that while the refinement agrees successfully with the peaks present at all temperatures ((002)/(220) and (222)/(400)), it fails to reproduce the shape (mainly the FWHM) of the peaks distinctive of the tetragonal phase.

Closely inspecting the pattern at 90 K, two main features are observed. First of all, the additional peaks which we could not explain in $FAPbI_3$ (cf. Table 5.1) are not present in this sample. Next, it appears that the additional peaks that appear when transiting into the tetragonal phase P4/mbm ((210), (211), (410)...) are noticeably wider than the peaks present at all temperatures. This observation is confirmed when performing the LeBail refinement, which succeeds to reproduce the shape of the "main" peaks but fails to reproduce the shape of the "sur-structure" peaks. This last feature correlates nicely with the observation about the evolution of the area of these tetragonal peaks we highlighted earlier (cf subsection 5.3.1 and Figure 5.15) on $FAPbI_3$ and further hints to more disordered tetragonal tilts in the low temperature phase.

To date and to the best of our knowledge, no work has been published establishing the phase diagram of FAPb$(I_{1-x}Br_x)_3$ solid solutions. We investigated the temperature dependent behavior of all bromide compositions where the cubic structure was obtained at RT in the previous chapter, namely 10, 15, 20, 60, 70, 80 and 90 % Br (cf. section 4.4).

It appears that locating the temperature of the phase transitions is hard from visual inspection. As shown in the previous chapter, as the bromide content increase in the FAPb$(I_{1-x}Br_x)_3$, compounds, the intrinsic strain increases accordingly, as is attested by the noticeable broadening of Bragg peaks. As observed in Figure 5.19.b which displays the low temperature pattern of the sample containing 10% Br, tetragonal peaks are wide and have small intensities, making their apparition as the temperature is lowered, hard to observe. This sample is the one exhibiting the lowest intrinsic strain at RT, and it can be expected that increasing intrinsic strain (wider peaks) will render the noticing of peak apparition even harder. Figure 5.20.a and b confirm this point: from visual inspection solely, it is difficult to precisely determine the onset of phase transition-induced peak broadening (and peak narrowing at low temperature in case of a reentrant phase transition).

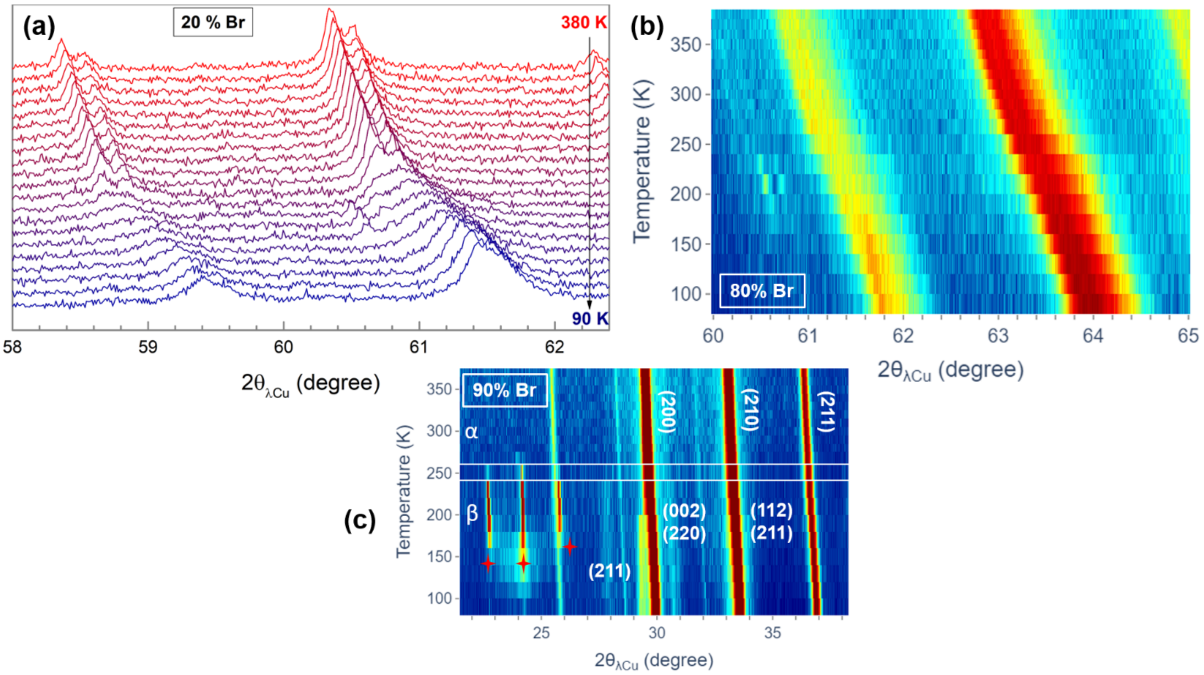

Figure 5.20: Temperature behavior of $FAPb(I_{1-x}Br_x)_3$ samples containing 20 % (a), 80 % (b) and 90 % (c) of bromide and illustrating the difficulty to determine through sole visual inspection the transition temperatures.

To determine these transition temperatures, we decided to investigate the evolution of the FWHM of the peaks with temperature. We focused on the peak at $2\theta \approx 61°$ (the peak at higher angle displayed in Figure 5.12.b, Figure 5.19.a and Figure 5.20.a which is attributed to (400) planes in the cubic Pm-3m phase and (004)/(440) planes in the tetragonal P4/mbm phase. The splitting of this line when going through the cubic – tetragonal phase transition will appear as peak broadening when bromide is introduced in the sample, as can be seen in Figure 5.19.a and Figure 5.20.a. This diffraction line was chosen instead of the $(200)_C$ because, despite the higher intensity of the latter, the former leads to better precision thanks to its position at higher diffracting angle. Moreover, its intensity is high enough to extract reliable values. In addition to help identifying the cubic-tetragonal phase transition, this method will also allow to differentiate whether the sample displays, at low temperatures, a reentrant phase transition like $FAPbI_3$ or a tetragonal-orthorhombic phase transition as it is the case in $FAPbBr_3$. The former will induce peak narrowing after its broadening when the temperature is decreased while the latter will lead to continuous peak broadening as the sample is cooled down. The FWHM values corrected for the instrumental resolution where obtained using the same method as previously (cf subsection 4.2.2). The results are displayed in Figure 5.21.a and b for high and low bromide contents, respectively.

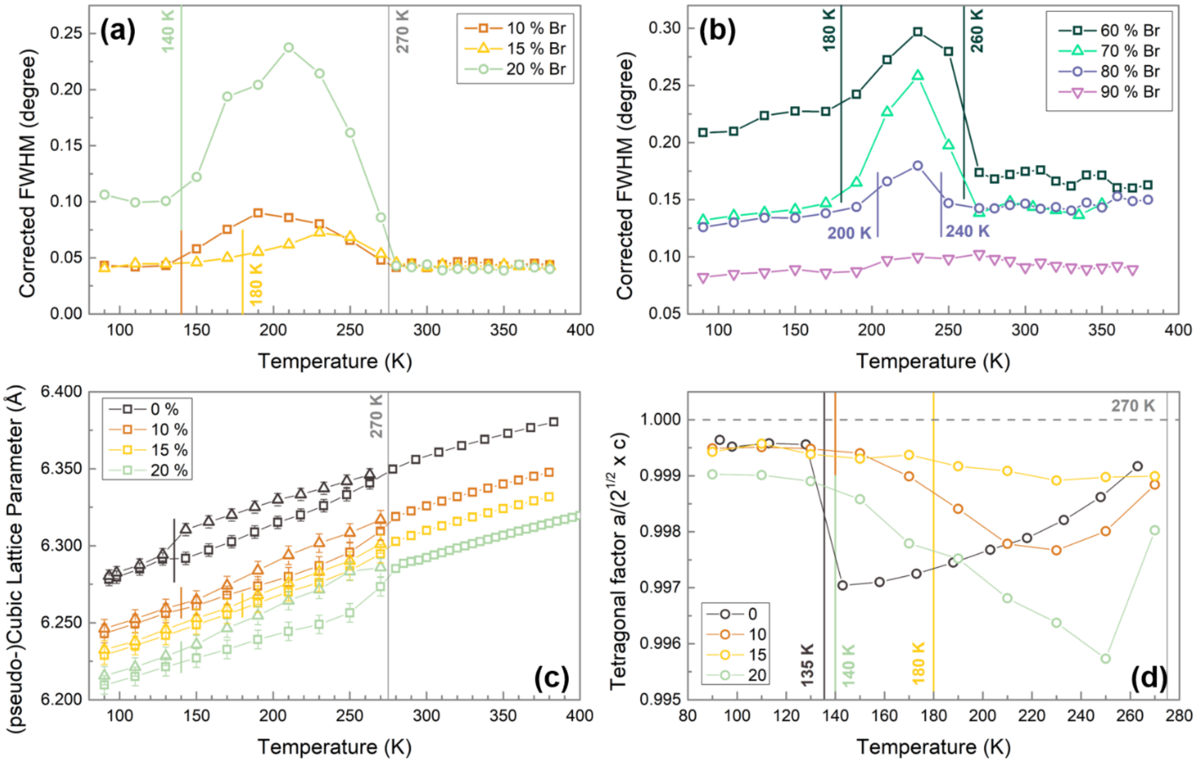

Figure 5.21: (a) and (b) evolution of the FWHM of the diffraction line associated with the (400)C/(002)T/(440)T planes in high and low bromide content respectively, allowing to locate the phase transitions. (c) Evolution of the (pseudo-) cubic lattice parameters for low-content bromide samples over the whole probed temperature range. (d) Evolution of the tetragonal factor calculated for low bromide content samples.

Low bromide content (10, 15 and 20 % Br) : Figure 5.21.a shows a plateau of close FWHM values for all three samples at high temperatures. When the samples are cooled under 270 K, the FWHM starts increasing, thus determining the cubic-tetragonal phase transition to be 270 K ± 10 for all three samples. Interestingly, the sample containing 20 % Br shows the steeper increase of the three samples. Initially displaying the same increasing slope, the FWHM of sample containing 15 % starts decreasing earlier than the sample containing 10 % Br. The former is, of the three samples in Figure 5.21.a, the one exhibiting the smaller increase in the FWHM value. It is visible for all these samples, that after increasing, the FWHM starts decreasing, which indicates a reentrant phase transition similar to what is observed for $FAPbI_3$. The transition temperature can be determined as the temperature at which the FWHM starts decreasing or the temperature at which the FWHM reaches again a plateau. We chose the second option, as we believe that the phase transition is complete when the FWHM is stable, the decrease of its value indicates that the sample becomes closer to the transition, not that it happened. These considerations lead us to determine the transition temperatures displayed in Figure 5.21.a. While the cubic-tetragonal phase transition temperature is obvious from the steep increase of the FWHM, the temperature at which the reentrant transition happen can be a matter of debate, especially for the sample containing 15 % Br where the evolution of the FWHM is the smoothest and shows some asymmetry.

To confirm the temperatures determined from Figure 5.21.a, we refined the patterns for all the temperatures below 270 K using the P4/mbm space group and plotted the extracted pseudo-cubic lattice parameter in Figure 5.21.c. We represented, on this figure, the transition temperature extracted from the FWHM plot as continuous lines and added, for comparison, the evolution of the pseudo cubic lattice parameters of end compound $FAPbI_3$. On this graph, the reentrant phase transition temperature will be found as the temperature at which the difference between a and c becomes constant, as it is the case for $FAPbI_3$.While for 10 and 20 % Br the temperature determined through FWHM analysis seem to correctly match this later analysis, the transition temperature when the sample contains 15 % Br is still hard to be precisely determined. It is striking to note that the difference between a and c lattice metrics in this sample is the smallest one.

Also, one observes that, while for $FAPbI_3$ the difference between a and c increases as the temperature decreases before abruptly converging, mixed halide samples exhibit different behavior. For these samples, the difference between a and c starts to slowly increase on a relatively reduced temperature range, before decreasing gradually and slowly converging to similar values. No more abrupt change is observed, and this behavior is well translated by the evolution of tetragonal factor presented in Figure 5.21.d. This observation indicates a difference in the mechanism of this reentrant transition which is abrupt in the end-compound and becomes more gradual when incorporating small amounts of Br in the compounds. Further calorimetry measurements may bring more insights into the transition mechanisms in these compounds. Concerning the sample containing 15 % Br, it seems that the transition is less marked for this sample than for the others, and repeating the measurement in addition to the calorimetry experiments would allow to settle if this observation arises from experimental bias or if it has physical meaning. For now, the phase transition temperature for this compound will be indicated with a bigger bar error.

High bromide content (60, 70, 80, and 90 % Br) : surprisingly, the FWHM plot for these compositions represented in Figure 5.21.b also displays the features of a low temperature reentrant phase transition for the samples containing 60 to 80 % Br. After a high temperature plateau in the cubic phase, the FWHM starts increasing, indicating the cubic-tetragonal phase transition which temperature has been indicated for each sample on the graph. After reaching a maximum, the FWHM starts decreasing, before reaching a plateau at low temperature, thus indicating the reentrant phase transition temperature (also indicated on the graph). For these high Br content samples, refining the low temperature phases using a tetragonal symmetry did not seem achievable in a reliable manner. These compounds exhibit high intrinsic strain values, as reminded earlier, as proved by the large Bragg peaks. When increasing the temperature, the peak broadening is noticeable but the weak intensity of the tetragonal characteristic peaks makes the tetragonal lattice parameters determination weakly reliable, and we decided not to extract these values for which the error bars will be greater than the evolution amplitude. However, we demonstrated above that the FWHM plot allows to extract reliable transition temperatures, and we will use these values in the following. Finally, concerning the sample containing 90 % Br, the FWHM remained stable over the whole temperature range. Figure 5.20.c shows that a weak diffraction line that could be attributed to tetragonal (211) reflection appears around 230 K upon cooling, but it is hard to determine precisely at which temperature this peak appear because of its low intensity. A higher error bar will thus be used for this compound in this phase diagram. No additional phase transition seems to happen when further lowering the temperature.

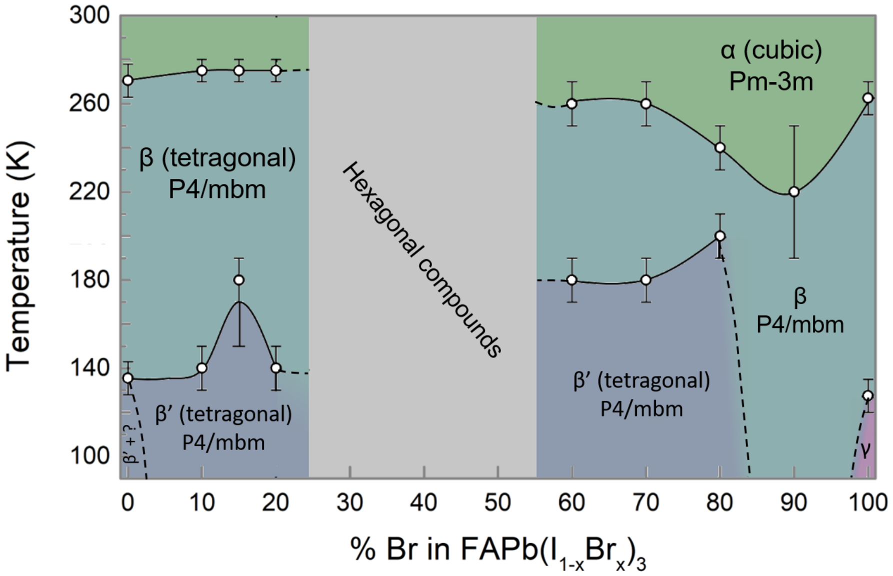

Figure 5.22: Phase diagram of FAPb(I$_{1-x}$Br$_x$)$_3$ solid solutions showing the phase transitions observed between 90 and 380 K.

The results are gathered in Figure 5.22 which is, to our knowledge, the first phase diagram of the FAPb(I$_{1-x}$Br$_x$)$_3$ solid solutions family. The temperature of the cubic – tetragonal phase transition seems poorly impacted by the composition. The phase diagram reveals large temperature and composition ranges of stability for the disordered tetragonal phase β'. The temperature-composition phase diagram of FA$_{1-x}$MA$_x$PbI$_3$ established by Fransisco-Lopez *et al.* revealed also large temperature and composition domains of existence of this latter phase in the mixed organic cation compounds.[2] This observation stresses again the importance of understanding the low temperature behavior of FA-based (and majorly FA-containing) compounds. The stability of the orthorhombic phase, which is observed with the end compound $FAPbBr_3$, seems to be highly impacted by the halide mixing, which does not favor its formation. A similar observation was made for $MAPb(I_{1-x}Br_x)_3$ solid solutions.

Finally, the evolution of the cubic lattice parameter for all $FAPb(I_{1-x}Br_x)_3$ is displayed in Figure 5.23.a, showing similar increase for all compositions. Figure 5.23.b shows the evolution of the volumetric CTE of these compounds, calculated at 350 K. First of all, $FAPbI_3$ and $FAPbBr_3$ exhibit close values of CTE at 350 K, both being larger than $MAPbBr_3$'s and close to the value calculated for $MAPbI_3$. The same scale as in Figure 5.10 is used, showing close values for all compositions.

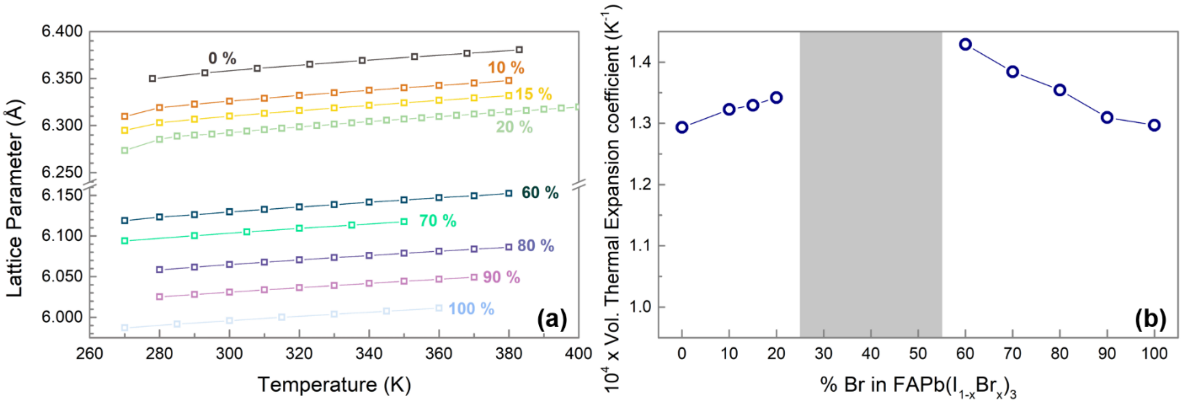

Figure 5.23: (a) Evolution of the cubic lattice parameter for all $FAPb(I_{1-x}Br_x)_3$, compounds. The error bars being smaller than the markers, they have been neglected. (b) Evolution of the volumetric thermal expansion coefficient of the cubic phase of $FAPb(I_{1-x}Br_x)_3$ (x = 0 to 20 % and 60 to 100 % Br) compounds at 350 K.

5.4. TEMPERATURE BEHAVIOR OF A MIXED-CATIONS MIXED-HALIDES PEROVSKITE

Finally, following the same logic as in the previous chapter, we inspected the temperature behavior of the sample where two different organic cations and two different halogens coexist: $FA_{0.85}MA_{0.15}Pb(I_{0.15}Br_{0.85})_3$; which we will call FAMAPbIBr henceforth for clarity. As explained in chapter 4, this sample and its composition was chosen for its excellent performances when used in solar devices. A working device can be exposed to various temperature, ranging from 85 °C (358 K) down to −40 °C (233 K) in extreme cases.

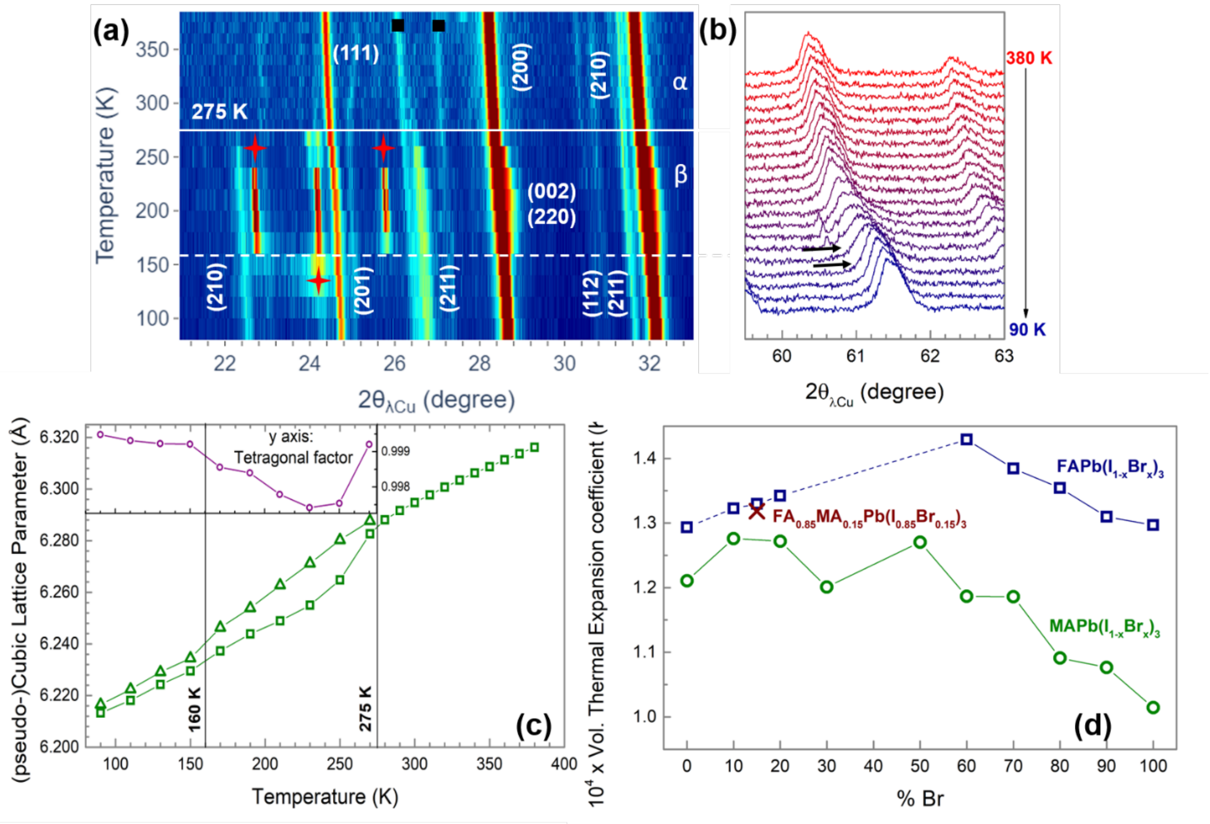

Figure 5.24: (a) contour plot of the temperature evolution of FAMAPbIBr sample showing the formation of tetragonal P4/mbm characteristic reflections (210) and (211) between 280 and 270 K, thus signing a cubic-tetragonal phase transition at 275 K. Cubic (220) and (210) lines broaden below this temperature, before narrowing again at lower temperature. (b) Temperature dependent XRD raw data, confirming the sharpening of the peak at $2\theta = 61°$ at low temperature after initial broadening. (c) Evolution of FAMAPbIBr lattice parameters through the measured temperature range. LeBail refinement was performed on all patterns, using Pm-3m cubic symmetry above 275 K and tetragonal P4/mbm symmetry below, which shows a reentrant phase transition around 160 K with a pseudo-cubic symmetry below. Insert shows the evolution of the tetragonal facto with temperature; the same x axis as the main graph is used. (d) Cubic lattice volumetric CTE of FAMAPbIBr at 350 K with, for comparison, the volumetric CTE of the quaternary compounds studied earlier.

As a reminder, this compound was found in the previous chapter to adopt a cubic Pm-3m symmetry at RT. Figure 5.24.a shows the evolution of the Bragg peaks upon cooling. Between 280 and 270 K, characteristic diffraction lines of tetragonal P4/mbm reveals a cubic-tetragonal phase transition. The sample, in which the majority of the cations are FA$^+$ adopts the tetragonal symmetry of FA-based compounds. As expected, the cubic (200) and (210) line broaden when below the phase transition, as they respectively split into (002)/(220) and (112)/(221) tetragonal reflections. However, upon cooling, these lines become sharper between 170 and 150 K (white dashed line), indicating what would seem to be a reentrant phase, as was observed in pure $FAPbI_3$ and most of the perovskite $FAPb(I_{1-x}Br_x)_3$ solid solutions. This last feature is also observed on Figure 5.24.b, which shows an enlarged view of the evolution of the (400) cubic peak, which broadens in the tetragonal phase as splits into (004) and (440) reflections, before becoming sharper again at low temperature. As we do not observe any additional peak or increased peak broadening at low temperature, we can exclude a tetragonal – orthorhombic phase transition happening at low temperatures. We performed LeBail refinement on our data and the patterns measured at temperatures lower than 275 K were refined using a tetragonal P4/mbm space group while cubic Pm-3m symmetry was used for temperature higher than 275 K. The extracted lattice parameters are shown in Figure 5.24.c where, after increasing, the differences between pseudo-cubic a and c lattice parameters decrease again, before becoming almost negligible. The evolution of the lattice parameters confirms the second phase transition at 160 K, from β (long range tilting of the octahedra) to β' (random and disordered octahedra titling) phases. The two phase transition temperature (275 ± 5 K for the cubic - tetragonal and 160 ± 10 K for the $\beta \to \beta'$ phase transitions) are fairly close to the transition temperature observed in $FAPb(I_{1-x}Br_x)_3$ solid solutions with low Br content, showing little impact of the introduction of MA^+ in the material. The tetragonal factor calculated from the lattice parameters is displayed in the insert in Figure 5.24.c (displayed with the same x axis), showing a behavior closer to the evolution displayed by $FAPb(I_{1-x}Br_x)_3$ solid solutions with low Br content rather than pure $FAPbI_3$. The tetragonal $\beta \to \beta'$ phase transition appears more gradual in FAMAPbIBr than it is in $FAPbI_3$.

Observed in at least one of the compositions of the 5-components hybrid halide perovskite compounds used in high efficiency solar cells, dedicating efforts to understand this reentrant phase transition seems of paramount importance, together with understanding the cation dynamics in such complex materials during such intriguing process and the seemingly predominant role of the complex organic cation – inorganic cage interaction.

Finally, the cubic lattice volumetric CTE calculated at 350 K is displayed in Figure 5.24.b together with the expansion coefficient of the quaternary compounds studied in the previous sections. Here again, FA^+ being in majority proportions, it seems to impose its characteristic features to FAMAPbIBr which exhibits high expansion coefficient. Hence, MA^+ cation, which is present in a small amount in the material seems to play little role in the temperature behavior of this 5-component $FA_{0.85}MA_{0.15}Pb(I_{0.85}Br_{0.15})_3$ perovskite material.

5.5. Conclusion

After establishing the intrinsic properties of the mixed ions hybrid perovskites at RT in the previous chapter, this chapter was dedicated to the study of the temperature behavior of the mixed halide perovskites $MAPb(I_{1-x}Br_x)_3$ and $FAPb(I_{1-x}Br_x)_3$ solid solutions in the 90 − 380 K temperature range.

Concerning the MA-based compounds, both end compounds $MAPbI_3$ and $MAPbBr_3$ follow the cubic Pm-3m ↔ tetragonal I4/mcm ↔ orthorhombic Pnma structural transition path. While the temperature-dependent behavior of $MAPbI_3$ is now relatively well understood, un-answered questions remain in the case of $MAPbBr_3$. An additional phase is reported to form in the latter between the tetragonal and orthorhombic phases over a reduced temperature range of 5 K, the nature of which is still under debate to date. In the case of $MAPbI_3$, this phase transition was proved to be first order as both tetragonal and orthorhombic phases were observed to coexist over a 5 K range.

By conducting temperature dependent XRD measurements, we established the first complete phase diagram of the $MAPb(I_{1-x}Br_x)_3$ solid solutions. We observed that the introduction of bromide induces a lowering of the cubic – tetragonal phase transition temperature, which reaches its minimum value for compounds containing 50 to 70 % Br. The tetragonal- orthorhombic phase transition was even more impacted by the halide mixing. The temperature range of phase coexistence is extended to 40 K when introducing 20 % of Br and for higher bromide content, no orthorhombic phase is observed for temperatures as low as 90 K. The orthorhombic phase is later retrieved when the sample contains 90 % Br, but due to intrinsic high and anisotropic strain at low temperature on this sample, we could not determine if there was tetragonal – orthorhombic phase coexistence in this compound. The main features were however attributed to the orthorhombic phase. The data were collected every 20 K, and considering the small temperature range stability of the unknown phase that is formed in $MAPbBr_3$, we do not exclude the possible formation of this structure in the compound containing 90 % Br. Finally, we observed in these samples the tuning of the volume lattice expansion coefficients between the high expansion of $MAPbI_3$ and the lower expansion of $MAPbBr_3$ when introducing increasing bromide content. This latter observation can be quite interesting for device applications.

The temperature-dependent behavior of FA-based halide perovskite was examined, which showed more surprising behavior. As the temperature decreases, $FAPbI_3$ experiences a cubic Pm-3m – tetragonal P4/mbm phase transition just below 270 K. Further cooling of the compound reveals what was qualified as a reentrant phase transition, still refined as P4/mbm but where the ratio between a and c lattice metrics brutally change to become closer to a pdeuso-cubic symmetry. $FAPbBr_3$ follows the cubic Pm-3m – tetragonal P4/mbm – orthorhombic Pnma transition pathway, but the cell keeps a pseudo-cubic symmetry, as lattice expressed by the patterns which hardly change upon cooling. Still poorly understood, the complex molecular dynamics of FA^+ are proved to be completely different from MA-based compounds. Recent studies are hinting to a frustration of the organic cation – inorganic cage that causes the intriguing behavior of these compounds, and efforts are still needed to reach an enhanced understanding of the mechanisms at play.

Temperature-dependent XRD measurements on $FAPb(I_{1-x}Br_x)_3$ solid solutions allowed to extract the first phase diagram of these family of compounds. We observed, for almost all samples, the same reentrant phase transition as in $FAPbI_3$, but the evolution of the tetragonal lattice metrics is different when mixed halides are introduced. In $FAPbI_3$ the reentrant phase transition is characterized by an abrupt change in the lattice parameters, while in mixed halides, this transition appears to be smoother. This observation hints to a modification of the mechanism behind the phase transition and more studies are needed to extract quantitative information. The volume thermal expansion coefficient was extracted for these compounds, showing slightly higher values when mixing halides in comparison to end-compounds which have close expansion coefficient. This expansion coefficient values appeared, for $FAPb(I_{1-x}Br_x)_3$ solid solutions to have little dependence on the sample's composition.

Finally, by studying the behavior of the 5 components $FA_{0.85}MA_{0.15}Pb(I_{0.85}Br_{0.15})_3$ sample presented in the previous chapter, we observed a temperature behavior close to the one characteristic of FA-based samples, with a transitions temperatures and mechanisms close to $FAPb(I_{1-x}Br_x)_3$ with low bromide content. The thermal expansion coefficient was poorly impacted by the ion mixing, showing close values to $FAPbI_3$ and $FAPbBr_3$, proving that the MA^+ introduced have little impact on the structural changes when varying the temperature of this compound.

References

[1] O. J. Weber, B. Charles, and M. T. Weller. "Phase behaviour and composition in the formamidinium–methylammonium hybrid lead iodide perovskite solid solution". en. In: *J. Mater. Chem. A* 4.40 (2016), pp. 15375–15382. DOI: `10.1039/C6TA06607K`.

[2] A. Fransisco-Lopez et al. "Phase Diagram of Methylammonium/Formamidinium Lead Iodide Perovskite Solid Solutions from Temperature-Dependent Photoluminescence and Raman Spectroscopies". en. In: *J. Phys. Chem. C* 124.6 (2020), pp. 3448–3458. DOI: `10.1021/acs.jpcc.9b10185`.

[3] S. Yamamoto, Y. Suematsu, and Y. Shinnaka. "X-Ray Study of Phase Transition in $RbNO_3$". en. In: *J. Phys. Soc. Jpn.* 43.6 (1977), pp. 1962–1967. DOI: `10.1143/JPSJ.43.1962`.

[4] F. Lehmann et al. "The phase diagram of a mixed halide (Br, I) hybrid perovskite obtained by synchrotron X-ray diffraction". en. In: *RSC Adv.* 9.20 (2019), pp. 11151–11159. DOI: `10.1039/C8RA09398A`.

[5] P.S. Whitfield et al. "Structures, Phase Transitions and Tricritical Behavior of the Hybrid Perovskite Methyl Ammonium Lead Iodide". In: *Sci Rep* 6 (2016), p. 35685. DOI: `10.1038/srep35685`.

[6] C. J. Howard and H. T. Stokes. "Group-Theoretical Analysis of Octahedral Tilting in Perovskites". en. In: *Acta Crystallographica Section B* 54.6 (1998), pp. 782–789. DOI: `10.1107/S0108768198004200`.

[7] I.P. Swainson et al. "Phase transitions in the perovskite methylammonium lead bromide, $CH_3ND_3PbBr_3$". en. In: *Journal of Solid State Chemistry* 176.1 (2003), pp. 97–104. DOI: `10.1016/S0022-4596(03)00352-9`.

[8] S. Govinda et al. "Critical Comparison of $FAPbX_3$ and $MAPbX_3$ (X = Br and Cl): How Do They Differ?" en. In: *J. Phys. Chem. C* 122.25 (2018), pp. 13758–13766. DOI: `10.1021/acs.jpcc.8b00602`.

[9] C. Chen et al. "Elucidating the phase transitions and temperature-dependent photoluminescence of $MAPbBr_3$ single crystal". en. In: *J. Phys. D: Appl. Phys.* 51.4 (2018), p. 045105. DOI: `10.1088/1361-6463/aaa0ed`.

[10] A. Poglitsch and D. Weber. “Dynamic disorder in methylammoniumtrihalogenoplumbates (II) observed by millimeter-wave spectroscopy”. en. In: *The Journal of Chemical Physics* 87.11 (1987), pp. 6373–6378. DOI: `10.1063/1.453467`.

[11] C. A. López et al. “Elucidating the Methylammonium (MA) Conformation in $MAPbBr_3$ Perovskite with Application in Solar Cells”. en. In: *Inorg. Chem.* 56.22 (2017), pp. 14214–14219. DOI: `10.1021/acs.inorgchem.7b02344`.

[12] M. T. Weller et al. “Complete structure and cation orientation in the perovskite photovoltaic methylammonium lead iodide between 100 and 352 K”. en. In: *Chem. Commun.* 51.20 (2015), pp. 4180–4183. DOI: `10.1039/C4CC09944C`.

[13] D. H. Fabini, R. Seshadri, and M. G. Kanatzidis. “The underappreciated lone pair in halide perovskites underpins their unusual properties”. en. In: *MRS bulletin* 45 (2020), pp. 467–477. DOI: `10.1557/mrs.2020.142`.

[14] V. Srikant et al. “Crystallographic orientation of epitaxial $BaTiO_3$ films: The role of thermal-expansion mismatch with the substrate”. en. In: *Journal of Applied Physics* 77.4 (1995), pp. 1517–1522. DOI: `10.1063/1.358902`.

[15] T. Chen et al. “Entropy-driven structural transition and kinetic trapping in formamidinium lead iodide perovskite”. en. In: *Sci. Adv.* 2.10 (2016), e1601650. DOI: `10.1126/sciadv.1601650`.

[16] K. T. Butler. “The chemical forces underlying octahedral tilting in halide perovskites”. en. In: *J. Mater. Chem. C* 6.44 (2018), pp. 12045–12051. DOI: `10.1039/C8TC02976H`.

[17] D. H. Fabini et al. “Reentrant Structural and Optical Properties and Large Positive Thermal Expansion in Perovskite Formamidinium Lead Iodide”. en. In: *Angew. Chem.* 128.49 (2016), pp. 15618–15622. DOI: `10.1002/ange.201609538`.

[18] O. J. Weber et al. “Phase Behavior and Polymorphism of Formamidinium Lead Iodide”. en. In: *Chem. Mater.* 30.11 (2018), pp. 3768–3778. DOI: `10.1021/acs.chemmater.8b00862`.

[19] D. H. Fabini et al. “Universal Dynamics of Molecular Reorientation in Hybrid Lead Iodide Perovskites”. en. In: *J. Am. Chem. Soc.* 139.46 (2017), pp. 16875–16884. DOI: `10.1021/jacs.7b09536`.

[20] E. C. Schueller et al. “Crystal Structure Evolution and Notable Thermal Expansion in Hybrid Perovskites Formamidinium Tin Iodide and Formamidinium Lead Bromide”. In: *Inorg. Chem.* 57.2 (2018), pp. 695–701. DOI: `10.1021/acs.inorgchem.7b02576`.

[21] E. M. Mozur et al. “Dynamical Phase Transitions and Cation Orientation-Dependent Photoconductivity in $CH(NH_2)_2PbBr_3$”. en. In: *ACS Materials Lett.* 1.2 (2019), pp. 260–264. DOI: `10.1021/acsmaterialslett.9b00209`.

[22] M. Keshavarz et al. “Tracking Structural Phase Transitions in Lead-Halide Perovskites by Means of Thermal Expansion”. en. In: *Advanced Materials* 31.24 (2019), p. 1900521. DOI: `10.1002/adma.201900521`.

Conclusions on the impact of ion mixing on hybrid lead halide perovskites

The second part of the manuscript is dedicated to the study of the impact of ion mixing on hybrid lead halide perovskites. An important number of samples with different ions and different compositions where studies at different temperatures. Namely, three family of solid solutions were synthesized and characterized: $\mathrm{MAPb(I_{1-x}Br_x)_3}$, $\mathrm{FAPb(I_{1-x}Br_x)_3}$ and $\mathrm{FA_{1-x}MA_xPbI_3}$. We conclude this part with a short summary of the main results extracted from this study.

- Polymorphism in FA-based compounds. We studied the polymorphic behavior of $\mathrm{FAPbI_3}$ which is known to spontaneously evolve into a photo-inactive hexagonal phase. We investigated the impact of halide and cation substitution on this polymorphism. Our results show that the electrostatic repulsion plays a major role in the stabilization of the perovskite phase, thus showing that geometrical considerations cannot solely help predicting the formability of organic lead halide perovskites. This same study rationalized the reasons behind the impossibility of forming a cubic structure of $\mathrm{FAPb(I_{1-x}Br_x)_3}$ compounds with intermediate bromide content (30 to 50 %), as observed in the literature.
- To obtain $\mathrm{MAPb(I_{1-x}Br_x)_3}$ samples containing high amounts of Br, we used additional high temperature annealing step, allowing us to obtain compositions that were not stabilized in the literature. Despite the high level of crystal defects presents in these samples, the evolution of the intrinsic properties evaluated here (band gap and lattice parameter) with the percentage of halide substituted followed Vegard's law. This result is coherent the now well-established defect tolerant nature of these compounds
- Our room temperature investigation revealed that all three of our solid solutions shows an evolution of the lattice parameters with composition following Vegard's Law. Mixed halide compounds showed high intrinsic strain values, increasing in a non-symmetrical way with the amount of bromine inserted. Lower levels of intrinsic strain were observed when mixing $\mathrm{FA^+}$ and $\mathrm{MA^+}$, however, anisotropic strain is

observed when both cations are inserted in equal proportions. Halide mixing allows bandgap tuning while the bandgap evolution when substituting the organic cations have a reduced range.

- We established the temperature-composition phase diagrams of $\mathrm{MAPb(I_{1-x}Br_x)_3}$ and $\mathrm{FAPb(I_{1-x}Br_x)_3}$ which were not or only partially reported in the literature.
- Nourished from all these information, we studied the intrinsic strain and the phase behavior of the mixed cations mixed halides lead perovskite compound $\mathrm{FA_{0.85}MA_{0.15}Pb(I_{0.85}Br_{0.15})_3}$, which composition was chosen to match that of the material leading to the highest performance photovoltaic cells in our team.

All these results are tentatively summarized in Figure 5.25.

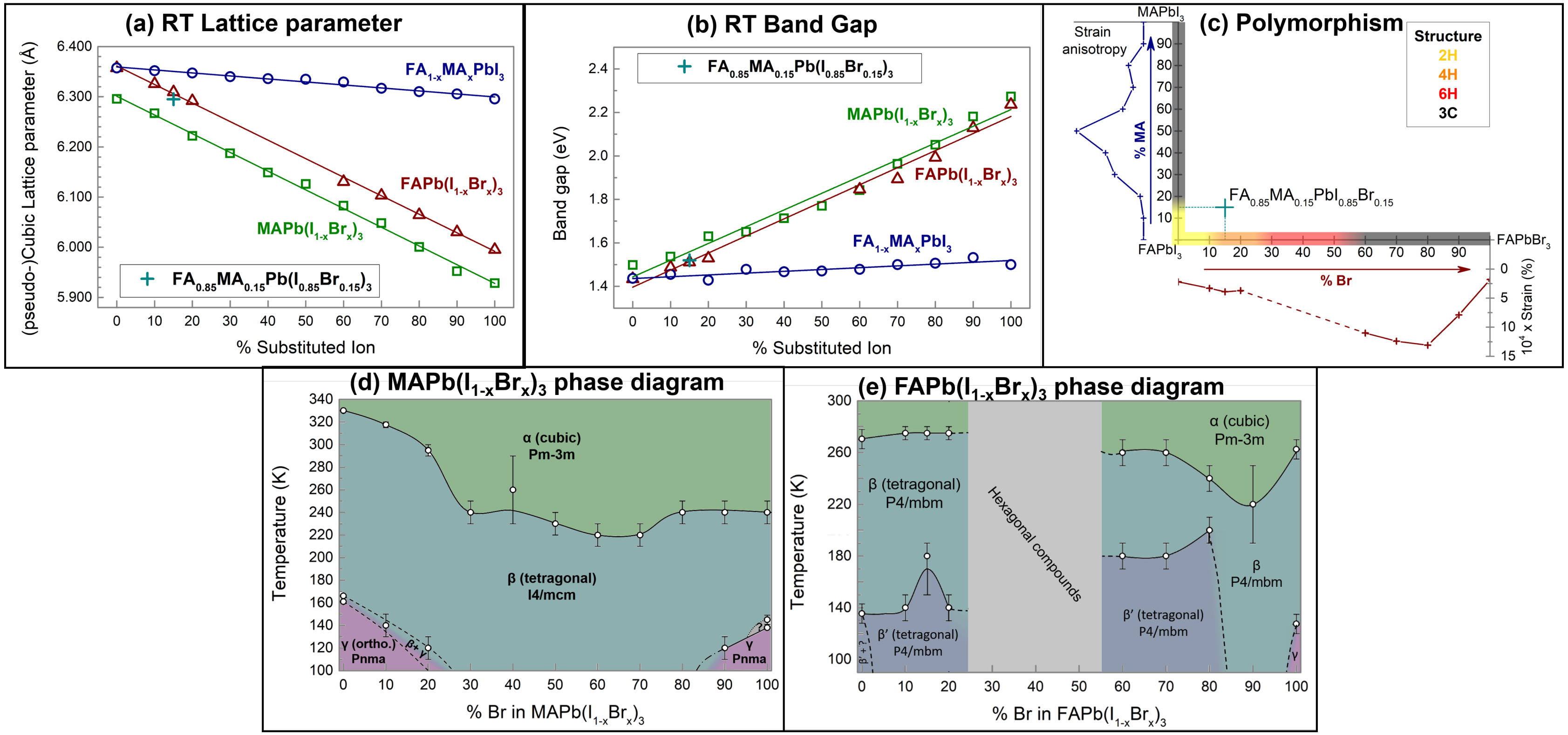

Figure 5.25: Main results of the second part of the thesis. (a) and (b) Evolution of the (pseudo-)cubic lattice parameter (a) and the bandgap (b) as function of the inserted ion at RT for the three solid solution families studied: $MAPb(I_{1-x}Br_x)_3$, $FAPb(I_{1-x}Br_x)_3$ and $FA_{1-x}MA_xPbI_3$ and for the 5-component sample $FA_{0.85}MA_{0.15}Pb(I_{0.85}Br_{0.15})_3$. (c) Representation of the polymorphism observed in FA-based compounds. (d) and (e) Established temperature – composition phase diagram of $MAPb(I_{1-x}Br_x)_3$ (e) and $FAPb(I_{1-x}Br_x)_3$ (f) between 90 and 400 K.

General conclusion and outlooks

This thesis focuses on the structural properties of hybrid lead halide perovskite compounds used in solar cells. It is divided into two parts.

The first part is dedicated to the study of $MAPbI_3$ thin layers.

In a chapter 2, we conducted a detailed investigation of one possible path for the crystallization of these layers in presence of chlorine. We demonstrated that $MAPbCl_3$ can spontaneously form in solution when introducing $PbCl_2$ into a solution of pre-solubilized MAI in DMF. We conducted an in-situ XRD study which allowed us to demonstrate the crystallization of $MAPbI_3$ from $MAPbCl_3$ through halogen exchange, despite the large lattice mismatch between these two crystalline phases. We identified the three stages of this mechanism and we highlighted the high strain level in the $MAPbI_3$ crystalline phase formed through this path. This eventually leads to its degradation and the formation of PbI_2 before the end of the crystallization process. The formation of the latter is accompanied by a gradual relaxation of the strain and the complete disappearance of $MAPbCl_3$ leads to an abrupt strain relaxation of $MAPbI_3$ and stops its degradation into PbI_2. Probing the relative distribution of the different phases led us to conclude that the conversion process starts from the top part of the layer before spreading in its thickness. Finally, we highlighted a correlation between the annealing time of the perovskite layer and the efficiencies of the solar cells obtained with these types of layers.

The second chapter of this part (chapter 3) detailed our investigation of the microstructure of $MAPbI_3$ thin layers. When crystallized in the presence of chlorine, a preferential orientation along the [hh0] tetragonal (I4/mcm) direction is observed. However, some layers exhibit additional texture along [00l]. Using the FFDXM technique developed at ESRF, we provided the proof that [hh0] and [00l]-oriented grains are twin domains and we reported the ferroelastic twin domains switching.

$MAPbI_3$ thin layers are obtained by annealing at 100 °C, and as they are cooled down after crystallization, they experience a cubic Pm-3m - tetragonal I4/mcm phase transition, which is known to be ferroelastic. Hybrid perovskites are characterized by remarkably large values of their thermal expansion coefficients. By following the evolution of out-of-plane lattice parameters of a sample as it is cooled down and assuming a bi-axial stress resulting from the high film/substrate CTE mismatch, we estimated the in-plane lattice parameters before the cubic-tetragonal phase transition. This allowed us to explain the formation of [hh0] texture as a consequence of the tensile in-plane stress.

Concerning the highly strained layers studied in Chapter 2, we demonstrated that [00l]-domains form in the upper part of the layer, in opposition to the layers discussed above. In the latter, when observed, [00l]-oriented domains as well as [hh0] are both coherent over the whole sample layer. In the case of highly strained layers, the bi-axial stress applied by the interaction with the substrate is not the driving force behind the formation of [00l]-domains. Here, these domains might appear as a response of the system to lower the elastic energy associated to the highly distorted perovskite crystalline lattice induced by the ion exchange mecanism.

The second part of this thesis details the impact of ion mixing on the hybrid halide perovskite structure. We synthesized different solid solutions, by substituting in turn the halogen site or the organic cation site, generating 3 families of compounds: $\mathrm{MAPb(I_{1-x}Br_x)_3}$ and $\mathrm{FAPb(I_{1-x}Br_x)_3}$ and $\mathrm{FA_{1-x}MA_xPbI_3}$.

Chapter 4 is devoted to the properties of these compounds at RT. Two mains results were reported. $\mathrm{FAPbI_3}$ is known to adopt a hexagonal yellow phase at RT, and the cubic black phase is stable above 150 °C. Our study strongly suggests that electrostatic repulsion might be the reason behind the transformation of the hexagonal structure into the cubic structure. This repulsion might also help to explain the stability of the cubic phase of $\mathrm{FAPbBr_3}$. Thermal treatment helps to stabilize the cubic phase at RT but for few hours only. One of the strategies developed to stabilize cubic $\mathrm{FAPbI_3}$ at RT more permanently is through ion mixing. Our results demonstrated that the partial substitution I/Br of the halogens leads to the formation of different hexagonal polytypes and the cubic phase is stable only for Br contents higher than 60 % in $\mathrm{FAPb(I_{1-x}Br_x)_3}$ solid solutions. Furthermore, this study provided an explanation to the reported difficulties for obtaining a cubic structure for intermediary Br contents in $\mathrm{FAPb(I_{1-x}Br_x)_3}$ solid solutions ($\mathrm{x_{Br}}$ = 30 to 60%). Finally, in agreement with the literature, we observed that the $\mathrm{FAPbI_3}$ cubic phase can be stabilized by substituting 20 % of $\mathrm{FA^+}$ by $\mathrm{MA^+}$ cations.

Moreover, we observed the chemical tuning of the band gap through composition. In agreement with the literature, halide mixing allows to modulate the band gap between 1.4 and 2.3 eV while organic cation alloying modifies its value on a much reduced range, between 1.4 and 1.6 eV. All the studied solid solutions followed Vegard's law in terms of RT lattice parameters and accordingly, the band gap evolved linearly. However, we observed that despite the formation of solid solutions, halogen mixing in hybrid lead halide compounds results in high intrinsic strain levels.

Finally, the last chapter of this manuscript (chapter 5) allowed us to establish the temperature - composition phase diagrams of the different mixed halides families. Moreover, we investigated the structural properties of a mixed organic cation and mixed halide compound, $FA_{0.85}MA_{0.15}Pb(I_{0.85}Br_{0.15})_3$, the composition of which was optimized for solar devices. The results were commented regarding the ones obtained on the quaternary solid solutions.

This work opens a number of perspectives and outlooks for future work.

In the frame of the efforts towards more efficient and more stable devices, it seems important to assess the effect of strain on the latter. We highlighted in chapter 2 the degraded thermal stability of $MAPbI_3$ thin layers when highly strained. Our study of the solid solutions revealed high distortion levels when introducing mixed halogens in the material. We showed even higher strain level when both the cation and halogen were substituted. An interesting study would be to assess the effect of such distortion of the long-term and thermal stability of devices containing the solid solution compounds.

The introduction of Cs^+ in the perovskite structure is now largely used in thin layers designed for solar cells as it helps reaching higher efficiencies and improved stability. Applying the same methodology as the one we developed in chapters 4 and 5 could be highly beneficial for understanding the impact of this cation on the intrinsic properties of the material, in term of stabilization against polymorphism, strain, lattice distortion, phase behavior…

In the frame of the efforts towards better understanding of the intrinsic properties of this class of materials, a number of perspectives open. Directly following the work of this PhD, investigating temperatures lower than 90 K would help enriching the phase diagrams established in chapter 5. Particularly in the case of $MAPb(I_{1-x}Br_x)_3$ family, where the orthorhombic phase was not observed in the probed temperature range for intermediate compositions. Moreover, scattering experiments are needed to confirm the temperature-composition phase diagram of $FA_{1-x}MA_xPbI_3$ compounds since the published one to date was established solely from photoluminescence and Raman spectroscopy.

Moreover, the general picture drawn in this thesis highlights one major observation. These hybrid halide compounds adopt the perovskite structure, which has been known and studied for several decades, and still continues to attract a lot of interest because of the complex interactions taking place in the materials and leading to an impressive number of properties. In the case of hybrid halide perovskites, a number of intriguing phenomena have been reported. To cite a few, chapter 5 reported the observation of a peculiar reentrant phase transition in $FAPbI_3$ at low temperature, as already mentioned in the literature. Recent reports start to point to a frustration of the organic cations in the inorganic lead-halide cage, which was also invoked for $FAPbBr_3$ at low temperature. Also, several reports in the literature highlight an important different between the long-range and the local symmetry in a number of different hybrid halide materials. Finally, our results indicate that the properties of these compounds are maintained despite the important disorder (high strain levels) they can experience.

All of the features above point to complex and multiple interactions raising and competing in this class of ”plastic crystals”, where the disorder might play an important role. Disentangling and understanding the interplay between these different interactions is complex and can be the object of a number of fascinating studies, combining classical solid states characterization techniques with tools to better understand the intrinsic disorder of these compounds

In this thesis, we developed and followed a methodology in order to help to better understand observations reported in the literature and the intrinsic behavior of this new class of compounds. We sincerely hope that our contribution will be helpful to the scientific community.

Appendix A

Materials

Contents

A.1. THIN LAYERS FABRICATION

$MAPbI_3$ and $MAPbI_3(Cl)$ thin layers were deposited by spin coating on glass/FTO/TiO_2 or glass/ITO/SnO_2 substrate and subsequent thermal annealing was performed.

Most of H.C., L.C. $MAPbI_3(Cl)$ and $MAPbI_3$ thin layers were deposited on glass/FTO/TiO_2 substrate. The Fluorine-doped tin oxide (FTO) coated glass (7 Ω/sq, thickness of ∼3 mm with ∼500 nm of FTO) were purchased from Pilkington. The substrates were cleaned by ultrasonication sequentially in detergent solution, deionized water, acetone, and ethanol for 10 min each. Preceding a UV/ozone treatment of 20 min, the substrates were died by Ar gas. The TiO_2 was deposited by spin-coating a precursor solution of 1 mL of ethanol, 76 µL of acetyl acetonate and 130 µL of Ti(IV) isopropoxide. 60 µL of the solution was spin-coated on 1 x 1 cm cleaned (FTO) covered glass substrates at 3000 rpm for 30 s. The substrates were afterwards annealed in the oven at 500 °C for 30 min.

D.O thin layers were deposited in glass/ITO/SnO_2 substrates which were fabricated at INES, and the procedure is reported in Pia Dally's thesis.[1] The perovskite thin layers were deposited by spin coating and annealed in the glovebox and Table A.1 summarizes the experimental parameters for the deposition of the perovskite layers.

Thin layer	Organic cation precursor	Lead precursor	Solution fabrication	Solution concentration	Spin coating parameters	Annealing time and temperature
MAPbI3 (no Cl^-)	MAI 243 mg	PbI2 706 mg	Simultaneous dissolution in DMF - Clear solution	1.5 M 1 MAI : 1 PbI_2	5000 rpm 30 s + 150 µL chlorobenzene dropped after 7 s of spin coating	100 °C for 10 min
MAPbI3(Cl) L.C.	MAI 360 mg	PbCl2 207 mg	Simultaneous dissolution in DMF - Clear solution	0.8 M 3 MAI : 1 $PbCl_2$	5000 rpm 30 s + 150 µL chlorobenzene dropped after 7 s of spin coating	110 °C for 30 min
MAPbI3(Cl) H.C.	MAI 720 mg	PbCl2 414 mg	Simultaneous dissolution in DMF - Turbidsolution, heated to 70 °C	1.6 M 3 MAI : 1 $PbCl_2$	5000 rpm 30 s + 150 µL chlorobenzene dropped after 7 s of spin coating	110 °C for 30 min
MAPbI3(Cl) D.O.	MAI 3.8 g dissolved in 5 mL DMF	PbCl2 751 mg	Addition of $PbCl_2$ and DMF (1.7 mL) to 1.305 mL) of pre-solublized MAI in DMF - Turbid solution, filtrated using a 0.4 µm PTFE filter	0.8 M 3 MAI : 1 $PbCl_2$	1200 rpm for 1 s followed by 2400 rpm for 1 s followed by 4000 rpm for 40 s No anti-solvent dripping is used here	100 °C for 35 min

Table A.1: Experimental parameters for the deposition of the various perovskite thin layers studied here

A.2. POWDER SAMPLES FABRICATION

Figure A.1 illustrates the retrograde solubility of $MAPbBr_3$ in NMP as an initially clear solution precipitates when heated. The orange precipitate dissolves back after cooling down to room temperature.

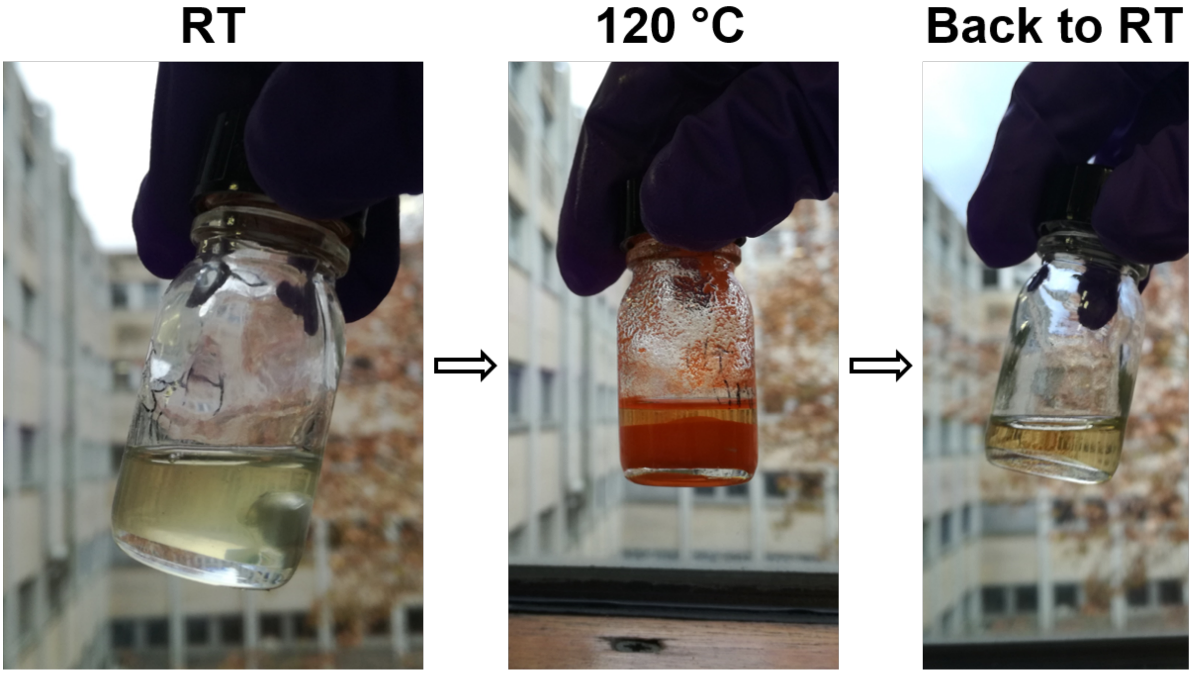

Figure A.1: Photographs illustrating the retrograde solubility of $MAPbBr_3$ in NMP : at RT, the solution is clear. Heating the solution to 120 °C causes precipitation of an orange powder ($MAPbBr_3$) which dissolves when the temperature is lowered.

The following tables (A.2, A.3, A.4 and A.5) gather the synthetic parameters for obtaining mixed ion perovskite powders for all the samples presented in chapter 4 and chapter 5. The table presents, for each compounds, the nature and the quantities of the powder precursors used to obtain 2 mL of a 1M solution in the solvent indicated. The synthesis temperature is indicated and, when required, the temperature and duration of the addition thermal annealing is specified. As a reminder, these powder samples are obtained by pouring the solution into a petri dish and evaporating the solvent at high temperature. When dry, the powder is further ground to ensure homogeneous grain sizes in the sample.

Compound Family	**Composition**	**Precursor MAI (g)**	**Precursor MABr (g)**	**Precursor PbI_2 (g)**	**Precursor $PbBr_2$ (g)**	**Solvent**	**Synthesis temperature**	**Annealing temperature**	**Annealing duration**
$MAPb(I_{1-x}Br_x)_3$	0 % Br	0.318	-	0.922	-	GBL	100 °C	-	-
	10 % Br	0.224	0.067			NMP	140 °C	-	-
	20 % Br	0.127	0.134						
	30 % Br	0.032	0.201						
	40 % Br	-	0.224	0.830	0.070				
	50 % Br	-	0.224	0.692	0.180			150 °C	2h30
	60 % Br	0.318	-	0.092	0.660				4h
	70 % Br	0.283	0.022	-	0.730				4h
	80 % Br	0.191	0.089						4h
	90 % Br	0.095	0.157						2h
	100 % Br	-	0.224			DMF	100 °C	-	-

Table A.2: Synthesis parameters of the powders of mixed ions perovskites for $MAPb(I_{1-x}Br_x)_3$: precursors natures and quantities for 2 mL of a 1 M solution; solvent, synthesis temperature and when required, annealing temperature and duration.

Compound Family	**Composition**	**Precursor FAI (g)**	**Precursor FABr (g)**	**Precursor PbI_2 (g)**	**Precursor $PbBr_2$ (g)**	**Solvent**	**Synthesis temperature**
$FAPb(I_{1-x}Br_x)_3$	0 % Br	0.344	-	0.922	-	GBL	100
	10 % Br	0.241	0.075				120
	15 % Br	0.189	0.112				
	20 % Br	0.138	0.149				
	30 % Br	0.034	0.225			GBL or DMF or NMP	140
	40 % Br	0.344	-	0.369	0.44		
	50 % Br	0.344	-	0.230	0.550		
	60 % Br	-	0.250	0.553	0.29	NMP	
	70 % Br	-	0.250	-	0.730		
	80 % Br	0.206	0.100				
	90 % Br	0.103	0.015				
	100 % Br	-	0.250			DMF	100

Table A.3: Synthesis parameters of the powders of mixed ions perovskites for $FAPb(I_{1-x}Br_x)_3$: precursors natures and quantities for 2 mL of a 1 M solution; solven and synthesis temperature.

Compound Family	**Composition**	**Precursor MAI (g)**	**Precursor FAI (g)**	**Precursor PbI_2 (g)**	**Solvent**	**Synthesis temperature**
$FA_{1-x}MA_xPbI_3$	10 % MA	0.310	0.032	0.922	GBL	120 °C
	20 % MA	0.276	0.064			
	30 % MA	0.240	0.096			
	40 % MA	0.206	0.128			
	50 % MA	0.172	0.160			
	60 % MA	0.138	0.190			
	70 % MA	0.104	0.222			
	80 % MA	0.068	0.254			
	90 % MA	0.034	0.286			

Table A.4: Synthesis parameters of the powders of mixed ions perovskites for $FA_{1-x}MA_xPbI_3$: precursors natures and quantities for 2 mL of a 1 M solution; solvent and synthesis temperature.

Composition	**Precursor MAI (g)**	**Precursor FAI (g)**	**Precursor FABr (g)**	**Precursor PbI_2 (g)**	**Solvent**	**Synthesis temperature**
$FA_{0.85}MA_{0.15}Pb(I_{0.85}Br_{0.15})_3$	0.050	0.138	0.113	0.922	GBL	120 °C

Table A.5: Synthesis parameters of $FA_{0.85}MA_{0.15}Pb(I_{0.85}Br_{0.15})_3$ powder: precursors natures and quantities for 2 mL of a 1 M solution; solvent and synthesis temperature.

Appendix B

X-ray diffraction

In 1895, Röntgen reported the discovery of a new type of radiation, which he labelled as "X-rays". Since then, great advances have been achieved and a number of Nobel prices have been awarded for discoveries in the field of X-rays. X-rays have established themselves as powerful tool in medical applications as well as in physical, chemical and biological sciences.

X-rays are electromagnetic radiations, with wavelengths ranging from 0.1 to 100 Å, leading to corresponding energies from 100 keV to 100 eV. Such wavelengths, close to the characteristic lengths of atomic and molecular arrangements, make the X-rays an ideal tool for resolving atomic and molecular structures. During its interaction with the matter, an X-ray beam can be either absorbed or scattered. During the former, the absorption of the X-ray photon leads to a photoelectric event as a core electron is ejected. Studying the absorption and emission spectra informs, respectively, about the electronic and chemical state of a given material (techniques such as EXAFS, XANES, XPS...). On the other hand, scattering can be inelastic (loss of energy after the interaction of the X-ray beam with the matter, resulting in a scattered beam with a lower frequency than the incident beam) or elastic. X-ray diffraction (XRD) experiments rely on this elastic scattering between a crystal and an incident X-ray beam.

Contents

B.1. CRYSTAL DEFINITION AND RECIPROCAL SPACE

A crystal is a three-dimensional periodic repetition of a unit cell. A unit cell is described by **a**, **b** and **c** vectors and α, β and γ angles between these base vectors. In a crystal, each unit cell can be located in the direct space using the formula:

$$\mathbf{R_m} = x_m\mathbf{a} + y_m\mathbf{b} + z_m\mathbf{c} \tag{B.1}$$

Where $\mathrm{x_m}$, $\mathrm{y_m}$ and $\mathrm{z_m}$ are integers and $\mathbf{R_m}$ is the position of the vector associated to the unit cell m. The atomic positions within a unit cell can be described as:

$$\mathbf{r_n} = x_n\mathbf{a} + y_n\mathbf{b} + z_n\mathbf{c} \tag{B.2}$$

Where $\mathrm{x_n}$, $\mathrm{y_n}$ and $\mathrm{z_n}$ are factional numbers between 0 and 1 and $\mathbf{r_n}$ is the position of the vector of atom n inside the unit cell.

The atomic packing in a crystal can be considered as the packing of equidistant planes and different atomic plane families can be defined, as shown in Figure B.1.a. A convenient way to characterize and refer to these planes is through their Miller indices (h, k, l) defined as follows: let us consider the plane which is the closest to the origin without containing it. This plane intercepts the three x, y, z axis of the lattice at positions which by definition are considered as equal to a/h, b/k and c/l, thus defining the integer values of the h, k and l Miller indices, as can be seen in Figure B.1.b.

An important notion in diffraction is the reciprocal space, or reciprocal lattice, which is defined by its vectors **a***, **b*** and **c*** as follows:

$$\mathbf{a}^* = 2\pi \frac{\mathbf{b} \times \mathbf{c}}{\mathbf{a} \cdot \mathbf{b} \times \mathbf{c}} \tag{B.3}$$

$$\mathbf{b}^* = 2\pi \frac{\mathbf{c} \times \mathbf{a}}{\mathbf{a} \cdot \mathbf{b} \times \mathbf{c}} \tag{B.4}$$

$$\mathbf{c}^* = 2\pi \frac{\mathbf{a} \times \mathbf{b}}{\mathbf{a} \cdot \mathbf{b} \times \mathbf{c}} \tag{B.5}$$

Where the product $\mathbf{a} \cdot \mathbf{b} \times \mathbf{c}$ defines the lattice volume. Let us now define the reciprocal lattice vector $\mathbf{Q_{hkl}}$:

$$\mathbf{Q_{hkl}} = h\mathbf{a}^* + k\mathbf{b}^* + l\mathbf{c}^* \tag{B.6}$$

One of the main interests of the reciprocal space defined here relies in the fact that whatever the crystallographic system, $\mathbf{Q_{hkl}}$ is perpendicular to the (hkl) plane family it characterizes.

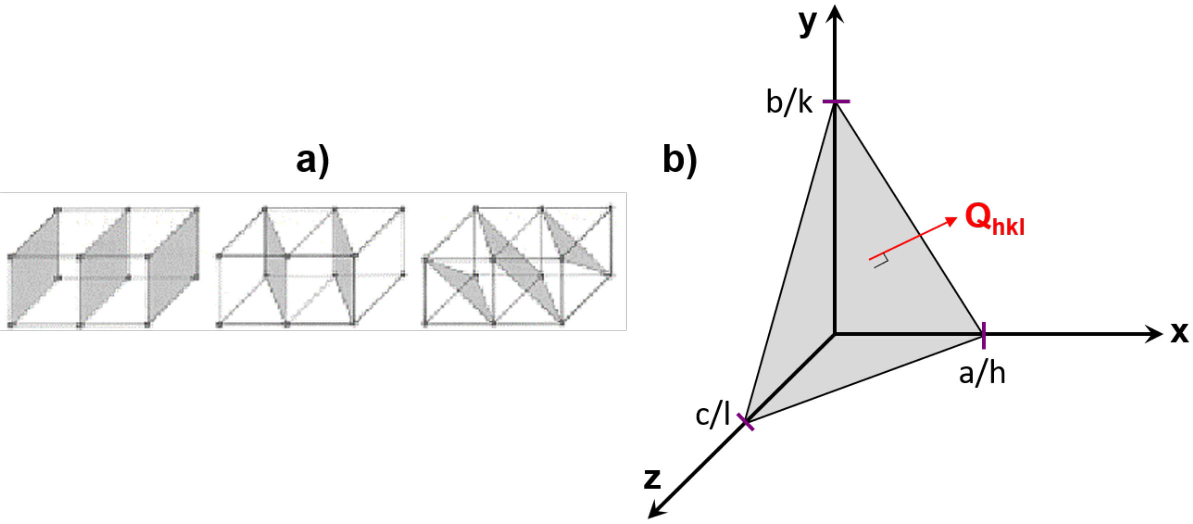

Figure B.1: (a) Illustration of the different parallel and equidistant planes describing the crystal packing (b) Illustration of an (hkl) plane, its intersection with the x, y and z axis at, respectively a/h, b/k and c/l, thus defining the h, k and l Miller indices. Illustration of the reciprocal lattice vector Q_{hkl} which is perpendicular to the plane.

The spacing between two parallel planes, called interreticular distance d_{hkl}, which is the perpendicular distance between the two planes can thus be defined as :

$$d_{hkl} = \frac{2\pi}{|\mathbf{Q_{hkl}}|} \tag{B.7}$$

Hence, the interreticular distance is directly related to the lattice parameters through the previous relationship. For cubic and tetragonal systems, this relationship can be simplified and expressed in the direct space as follows:

- For a cubic system: $\mathrm{d_{hkl}} = \frac{\mathrm{a}}{\sqrt{\mathrm{h^2+k^2+l^2}}}$
- For tetragonal system: $\mathrm{d_{hkl}} = \frac{\mathrm{a}}{\sqrt{\mathrm{h^2+k^2+\frac{a^2}{c^2}l^2}}}$

B.2. DIFFRACTION CONDITION : BRAGG'S LAW AND EWALD'S SPHERE

The famous Bragg's law is the expression of the condition for constructive interference of the X-rays incident beam waves to a set of (hkl) lattice planes, which is written as:

$$\theta_i = \theta_d = \theta \tag{B.8}$$

$$n\lambda = 2d_{hkl}\sin\theta \tag{B.9}$$

Where λ is the X-rays wavelength, $\mathrm{d_{hkl}}$ the interreticular distance defined earlier and θ is half of the angle between the incident angle and the exit wave, as shown in Figure B.2.a.

Equation B.8 places us in a symmetric configuration. Equation B.9, known as the Bragg's law, reflects the fact that the path difference for waves coming from different planes must be an integer number of wavelengths. When applying Bragg's law, it is usual to consider the multiples of the (hkl) Miller indices, which contradicts the initial definition of these indices given above but allows to ignore the n value which can be tricky to define.

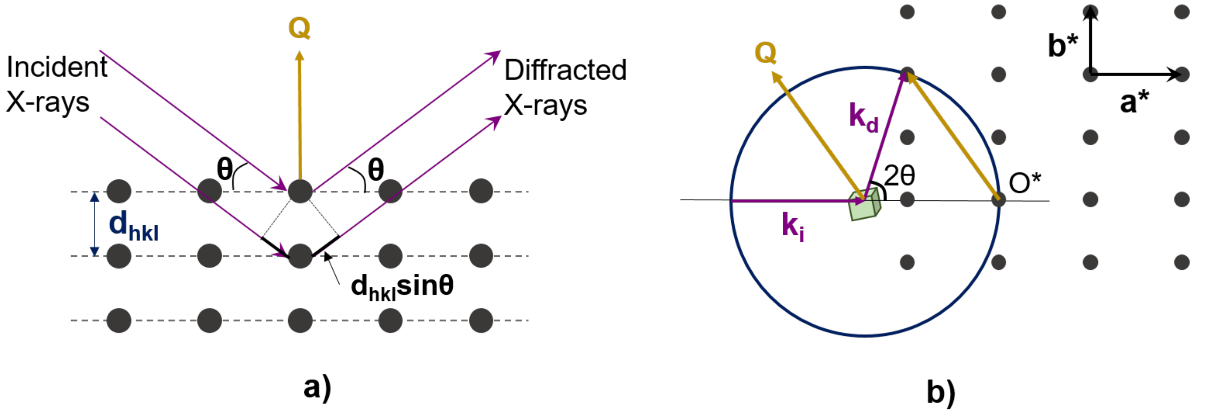

Figure B.2: (a) Illustration of Bragg condition of diffraction during a $\theta/2\theta$ experiment. (b) Scheme in 2D of Ewald's construction and illustration of the diffraction condition in this representation: every time a node of the reciprocal lattice intersects Ewald's construction

However, this law only contains scalar information, and the directional information can be found by introducing the wavevector transfer $\mathbf{Q^i}$ which is expressed as $\mathbf{Q^i} = \mathbf{k_d} - \mathbf{k_i}$ where $\mathbf{k_i}$ and $\mathbf{k_d}$respectively, the incident and the diffracted wavevectors. The $\mathbf{Q^i}$ vector defined here is purely instrumental as it only depends on the position of the X-ray source and the detector.

A useful tool to visualize the diffraction condition in the reciprocal space is by using Ewald's sphere, which is represented in 2D in Figure B.2.b. For this representation, a sphere (or a circle in 2D) centered on the crystal is constructed, with a $2\pi/\lambda$ radius. The incident and the diffracted wavevectors, ki and kd respectively, are equal in norm to the radius. The origin of the reciprocal space (O* in Figure B.2.b) is defined as the intersection of the sphere and the $\mathbf{k_i}$. Diffraction is observed when the instrumental $\mathbf{Q^i}$ vector equals one of the reciprocal lattice vector $\mathbf{Q_{hkl}}$ defined earlier, in other words:

$$Q^i = Q_{hkl} = k_d - k_i = Q = h\mathbf{a}^* + k\mathbf{b}^* + l\mathbf{c}^* \tag{B.10}$$

B.3. DIFFRACTION FROM POLYCRYSTALLINE POWDER SAMPLES

Polycrystalline samples can be regarded as an assembly of a great number of small crystals with random orientations. Diffraction from a powder sample generates concentric cones, as shown in Figure B.3. The intersection of these cones with a perpendicular 2D plane gives concentric rings. When intercepted with a detector along one direction, the rings translate into the classical diffractograms showing the diffracting intensity as function of the diffraction angle 2θ.

Multiple configurations are possible when measuring powder samples. The most common configuration and the one used in our experiments is the Bragg-Brentano configuration. Here, the powder is pressed onto a flat sample holder and positioned in the center of the goniometer. Two types of Bragg-Brentano diffractometers exist: in $\theta/2\theta$ diffractometers, the X-ray source is fixed and both the sample and the detector circle around the goniometer circle, the detector moving two times faster than the sample. With the second type, called θ/θ, the sample is fixed and it is the source and the detector that rotates around the sample in opposite directions at equal speed. Both these type of measurements are labelled symmetric or $\theta/2\theta$ scans, as the scattering vector $\mathbf{Q}$ remains perpendicular to the sample's surface; only its norm varies during the measurement. Due to the random orientation of the crystallites, all the possible orientations of the crystallites are found in the probed volume of the sample, and, statistically, the diffraction condition will be satisfied for all lattice planes of the crystal.

As explained earlier, the goniometer circle is defined by the movement of the detector (and the source in the case of θ/θ geometry) with the sample positioned at the center of the goniometer. Due to the geometric property of circles, when using a divergent incident X-ray beam, the diffracted beam converges in one same point of the circle, thus allowing to achieve good resolution despite the initial divergence. This configuration is particularly adapted for the measurement of powder samples, and high intensity can be reached. However, because of the same property that allows to work with a divergent beam, it is highly sensitive to the position of the sample, and the symmetric geometry is the only one possible.

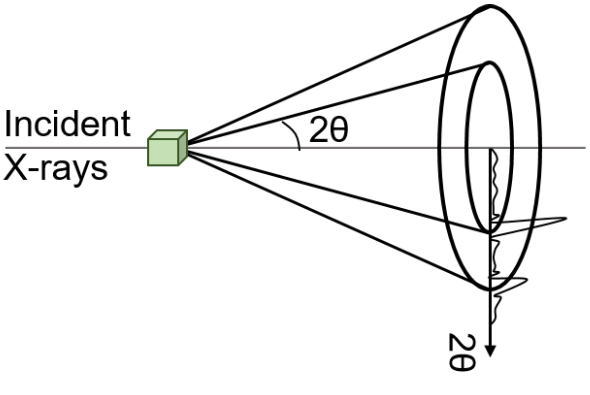

Figure B.3: Illustration of concentric diffraction cones.

DIFFRACTION PATTERNS AND DATA TREATMENT

From classical powder diffraction, the following structural information of the crystal can be obtained.

The peak position in 2θ allows to identify the cell symmetry and extract lattice parameters by combining Bragg's Law and the relationship between the interreticular distance and the lattice parameters.

The peak profile, in other words, the peaks shape and full-width at half-maximum (FWHM) informs about the microstructure of the sample in terms of distortion, crystallite sizes… One common model used to extract these information is through Williamson-Hall model. In this method, that peak broadening over the whole 2θ measurement range is assumed to arise from size and strain effects. The FWHM of the peaks and these microstructural features are related through the following equation in Williamson-Hall model :

$$FWHM_{corr} = \frac{K\lambda}{L\cos\theta} + \epsilon\tan\theta \tag{B.11}$$

Where the FWHM is expressed in radians, K is the Scherrer constant, which depends on the crystal shape; an approximated value of 0.9 is often used, λ begin the X-ray wavelength (in Å), L the crystallite size (in Å), $\epsilon = \Delta\mathrm{d}/\mathrm{d}$ which is the strain, characterizes the percentage of deviation from nominal d value, and θ is the half value of the diffracting angle of the considered peak. The above equation can we rewritten as :

$$FWHM_{corr}\cos\theta = \frac{K\lambda}{L} + \epsilon\sin\theta \tag{B.12}$$

The results are often shown as a graph, where, as expressed by the above equation, the product of the corrected FWHM by the cosine of the angle θ evolves linearly with the sine of θ. The obtained lines allow to identify the origin of the peak broadening: the intercept at the origin of the line would be inversely proportional to the crystallite size while its slope would be proportional to the intrinsic strain. One effect can be predominant with respect to the other or both effects can arise in a sample. The famous Scherrer formula, used to estimate the crystallite sizes, is contained in the Williamson-Hall model (Equation B.11) and obtained by neglecting the strain effects in the FWHM broadening.

The values of the FWHM (in radian) need to be corrected from the instrumental broadening, particularly in the case of narrow peaks. To obtain corrected FWHM in chapter 4, we used the TOPAS software. By indicating the measurement configuration (geometry, optic elements defining the beam divergence, distance of the sample from the X-ray tube and the detector... etc), the software calculates the resolution function of the diffractometer and convolutes the fitted peaks parameters by this resolution function. Single peak fitting is performed, and the peak shape function was selected to be the one imposed by the resolution, allowing us to obtain the corrected FWHM.

Finally, the peak intensity of a given reflection depends on the nature of the atoms and their position in the crystal unit cell. The intensity of the diffractions lines is directly impacted by the amount of crystalline material measured, and to mathematically describe these peak intensities, two cases have to be considered. In the first case, a powder sample of volume V is bathed in an incident beam of intensity $\mathrm{I_0}$. The intensity of a given (hkl) reflection is then:

$$I_{hkl} = I_0 \frac{V \lambda^3 m_{hkl} F_T^2}{v_a^2} LP(\theta) \tag{B.13}$$

Where $\mathrm{m_{hkl}}$ is the multiplicity of the considered reflection and $\mathrm{v_a}$ the volume of the unit cell. The volume of the unit cell. LP(θ) is the Lorentz-Polarization factor which depends on the measurement configuration. For the Bragg-Brentano configuration, for example, it is defined as:

$$LP(\theta) = \frac{1 + \cos^2 2\theta}{\sin\theta \sin 2\theta} \tag{B.14}$$

In Equation B.13, $\mathrm{F_T}$ is the structure factor of the reflection, which is defined as follows:

$$F_T = \sum_1^N f_n(\mathbf{Q}) e^{2\pi i \mathbf{Q}\cdot\mathbf{r_n}} e^{-B_n \frac{\sin^2\theta}{\lambda^2}} Occ \tag{B.15}$$

Where $\mathrm{f_n}$is the atomic scattering factor which is specific to each element and depends on the X-ray wavelength λ and the diffracted angle 2θ; the scalar product $\mathbf{Q} \cdot \mathbf{r_n}$ where $\mathbf{Q}$ is the wavevector and $\mathrm{r_n}$ the vector defining the position of the atoms in the lattice, describe the atoms contributing to the considered reflection (hkl). Bn is the Debye-Weller factor which characterize the temperature induced vibration of the atom. Finally, Occ is the site occupancy. The summation is made on all the N atoms of the unit cell.

This first definition is valid when performing the measurement in a Debye-Scherrer configuration, that is for example, when using capillaries where the volume of the probed sample is small.

Measurements where the powder sample is pressed onto a flat sample holder to form a dense, thick and uniform sample, are also widely used, and the volume of the powder is considered to be infinite relatively to the volume probed by the primary beam. The definition of the peak intensity is then defined as:

$$I_{hkl} = I_0 \frac{\lambda^3 m_{hkl} F_T^2}{2\mu v_a^2} LP(\theta) \tag{B.16}$$

Where μ is the absorption coefficient. Here, the volume is no longer needed as it is considered to be infinite in regards to the X-ray beam. However, correction from the beam absorption, which depends on the atoms constituting the sample, its density and the wavelength is needed in this configuration, to take into account the part of the sample which is probed.

The data recorded during an XRD experiment can be analyzed following different procedures: single peak fitting in which the diffraction lines are considered independently or whole pattern refinement. The latter can be divided into two categories : profile refinement, which refines the peak position and shape over the whole measurement range, allows to extract the information about the crystal lattice and the sample microstructure. During such refinement, the peak intensities are left as free parameters and not refined. The introduction of the atomic positions into the refinement leads to perform Rietveld analysis, which allows to refine the peak intensities by refining the atomic positions, site occupancies, thermal agitations… in agreement with the definition of the peak intensity and the structure factor

EVALUATING THE GOODNESS OF THE REFINEMENT

During data refinement, LeBail or Rietveld, the refined parameters selected by the user are varied to obtain the calculated curve that describes the best the measured data. In most cases, the model is optimized by minimizing the weighted sum of the squared difference between the observed and the calculated intensity on each data point of the pattern.[2] Various discrepancy indexes are defined, the most straightforward being the weighted profile R-factor, labeled R_{wp} and defined as follows:

$$R_{wp}^2 = \frac{\sum_m w_m (Y_{0,m} - Y_{c,m})^2}{\sum_m w_m Y_{0,m}} \tag{B.17}$$

Where w_m is a weighting factor given to data point m evaluated from the counting statistics, $Y_{0,m}$ and $Y_{c,m}$ are the observed and calculated data at data point m respectively. The numerator is the weighted sum described earlier which is divided by the weighted intensity the of the corresponding data point.

Another useful index is the expected R-factor, R_{exp}, which evaluates the best possible refinement:

$$R_{exp}^2 = \frac{M - P}{\sum_m w_m Y_{0,m}} \tag{B.18}$$

Where M and P are, respectively, the number of data points and P the number of refined parameters. Some argue that as usually M is notably larger then P, the subtraction can be ignored and only M is used in the numerator.

The most largely used factor, called the "chi squared" factor χ^2, is defined from the two previous factors and allows to evaluate the goodness of the fit relatively to the best fit that could be obtained:

$$\chi^2 = \frac{R_{wp}^2}{R_{exp}^2} = \frac{\sum w_m (Y_{0,m} - Y_{c,m})^2}{M - P} \tag{B.19}$$

B.4. DIFFRACTION FOR TEXTURED THIN LAYERS

Thin layers can be polycrystalline, but they also can exhibit preferential orientation along one direction (Figure B.4.a), as it is the case for most of $MAPbI_3$ thin layers studied here. As explained earlier, during a classical θ-2θ measurement, the direction of the wavevector transfer **Q** is not varied and kept perpendicular to the sample's surface (Figure B.4.c). During these measurements, and because of the preferential orientation of the thin layers, only one family of diffracting planes will be observed.

In these cases, different types of measurements are needed, often in a non-symmetric configuration and the Bragg-Brentano geometry cannot be used anymore. Parallel beams are used, usually achieved in laboratory diffractometers by using a parabolic mirror. Another advantage of this configuration is the little influence of the sample's height, and samples with irregular surfaces can be measured.

As illustrated in Figure B.4.a, the crystallites have a preferential orientation, but can exhibit more or less important tilting around this main direction. Such tilting, called mosaicity, is evaluated by measuring "rocking curves". During these measurements, the modulus of the scattering vector is fixed and its direction is varied, as illustrated in Figure B.4.b. By doing so, as the norm is fixed, the same planes are probed (same d_{hkl} probed, see Equation B.7), but the change in the direction allows to evaluate the tilting angle of the crystallites from the main perpendicular orientation. The obtained curve, represented in Figure B.4.b), shows the evolution of the intensity in function of the incident angle ω, describing a peak positioned at $\omega = 2\theta/2$, where 2θ is diffracting angle of the probed direction. The FWHM of this peak characterizes the mosaicity of the sample : for a Si wafer for example, the FWHM of the peak will correspond to the instrumental resolution as the sample is a perfect single crystal with no tilting. A powder sample will lead to a flat curve with a high background because of the random orientation of the crystallites. Textured thin layers are in between these two extreme cases, and the narrower the FWHM, the less tilting in the crystal.

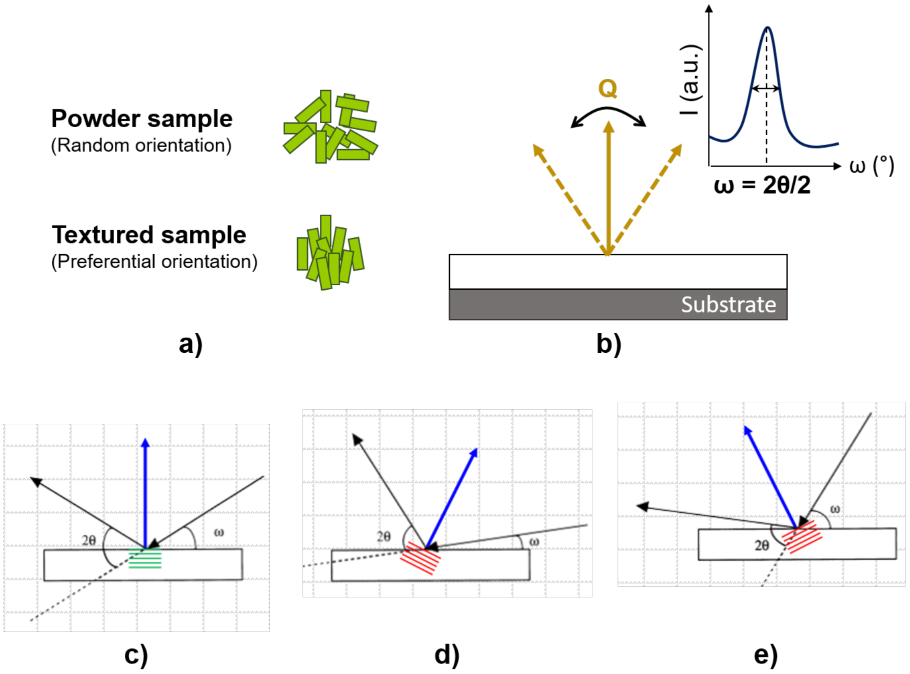

Figure B.4: (a) Schematic representation of a powder sample with random orientation of the crystallites, in opposition with a textured sample, where the crystallites present a preferential orientation. (b) Direction of the scattering vector Q during a rocking curve measurement and schematic representation of a rocking curve (c) Reminder of the planes probed during an out-of-plane $\theta/2\theta$ measurement. (d) and (e) Illustration of the planes probed during an asymmetric measurement, with the condition $\omega = \theta - \alpha$ (d) and $\omega = \theta + \alpha$.

Measuring planes which are not perpendicular to the surface can be achieved by performing asymmetric scans, where the condition $\omega = \theta \pm \alpha$ is imposed, where ω is the incident angle, θ half of the diffraction angle on the plane of interest and α is the angle between the plane to be probed and the planes parallel to the surface. Such measurements, illustrated in Figure B.4.d and e allow to access to out-of-plane as well as in-plane lattice parameters, which can be different in the case of thin layers due to the interaction with the substrate.

One final measurement configuration will be presented here: in-plane measurements.

Here, the probed direction is no longer perpendicular to the sample surface but parallel to it, as shown in Figure B.5.b. For these measurements, specific diffractometers are needed, as the detector needs additional degrees of freedom to rotate around the sample in the sample's plane and not only perpendicularly. Here again, such measurements allow to access to the in-plane lattice parameters. However, these measurements suffer from lower angular resolution because of the axial divergence of the primary parallel beam. Increasing beam collimation by using optical elements increases the resolution but lowers the incident beam intensity, and these measurements are often preferentially conducted on diffractometers equipped with rotating anodes as the X-ray source to ensure higher intensity.

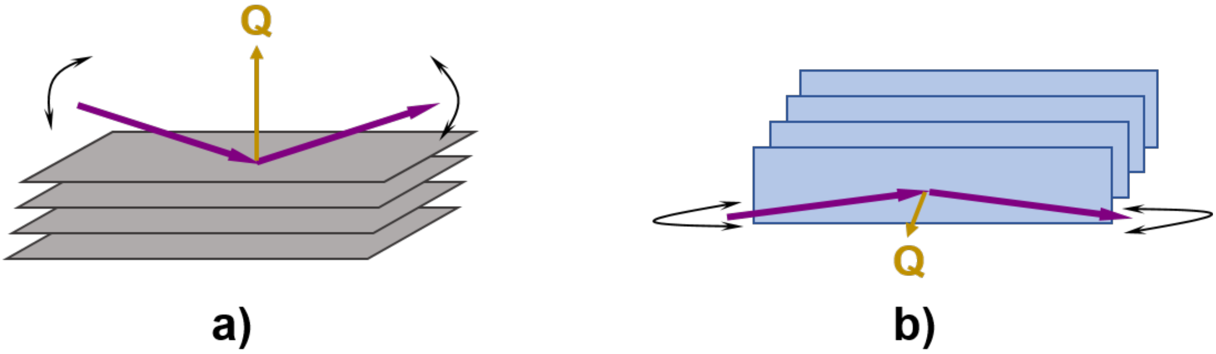

Figure B.5: (a) Planes probed during an out-of-plane $\theta/2\theta$ measurement. (b) Illustration of the planes probed during an in-plane measurement

In plane measurement are performed by fixing the incident angle ω at a small value, usually < 1, during the whole measurement, and the detector arm is moved to measure the diffracted intensity in the sample's plane. The choice of the incident angle ω is however not arbitrary, as will be explained now.

As an electromagnetic wave arrives at an interface between two different propagation media, refraction phenomenon can be expected. To describe it, we will consider the following approximations known as Fresnel's approach: the media are homogeneous with sharp interface between them, and each media is characterized by its refractive index n. This last parameter characterizes the interaction of the wave with the medium. The refractive index of X-rays can generally be expressed as

$$n = 1 - \delta + i\beta \tag{B.20}$$

Where typical values of δ and β are of the order 10^{-5} and 10^{-6} - 10^{-7} for X-rays, respectively, making the refractive index of X-rays slightly smaller than unity. Snell's law links the incident grazing angle ω to the refracted angle ω' as follows:

$$\cos \omega = n \cos \omega' \tag{B.21}$$

As, for X-rays n < 1, there is a critical angle ωc below which X-ray undergoes total external reflection. This critical angle, which depends on the atomic density and the X-rays wavelength, is expressed as follows

$$\omega_c = \lambda \sqrt{r_e p_e} \tag{B.22}$$

Where r_e is the classical radius of the electron and p_e the average electronic density.

Measurements performed with incident angles just above the critical angle allow to probe the surface of the sample, and thus avoiding diffraction pattern arising from the substrate. Moreover, by tuning the incident angle, one may vary the probed depth in the layer thickness. The penetration depth p of the X-ray in the material, which depends on the material density, the atoms in the structure and the wavelength of the X-ray allows to evaluate the probed depth h when varying the incident angle ω using the following equation:

$$\sin \omega = \frac{h}{p} \tag{B.23}$$

The probed depth can be calculated or estimated using the Laurence Berkley Laboratory website (`https://henke.lbl.gov/optical_constants/atten2.html`).

B.5. A FEW WORDS ABOUT SYNCHROTRON RADIATION

Since their discovery in 1895, tremendous advances on the understanding of X-rays and how to use their interaction with matter have been achieved. Meanwhile, X-rays sources remained the main limitation. In 1912, the Coolidge tube was developed to product X-rays: a tungsten filament is heated and produces electrons. Application of a high voltage accelerates the electrons towards a water-cooled metal anode (usually Copper). As the electrons hit the metallic plate, they transmit their energy to the atoms of the target, causing the promotion of electrons of the target atoms to excited states. As the electrons return to the ground state, X photons are emitted. The main limitation of this technique comes from the energy loss in form of heat that results from the bombarding of the electrons of the metallic plate. The introduction of the rotating anode in the 1960 s allowed to increase the intensity of the X-ray beam thanks to the better heat dissipation resulting from spinning the anode.

Synchrotron radiation installations remain the most intense source of X-rays. When electrons accelerated to move at relativistic speed are forced to follow curved trajectories by magnetic field, they emit a tangential radiation, known as synchrotron radiation. This emission was first unwanted, as it represented the major energy loss in high energy particle accelerators, but synchrotron radiation was quickly established as a highly interesting source of X-rays.

The first synchrotron radiation facilities were installed as “parasitic” experimental benches on existing particle accelerators. Dedicated infrastructures, the 2$^{\text{nd}}$ generation facilities, allowed to generate beams about one million times more brilliant then laboratory rotating anode sources. The brilliance is defined as the factor of the number of photons emitted per second by the angular divergence, the size of the beam source and the beam spectral distribution (relative energy bandwidth):

$$Brilliance = \frac{Photons/second}{(mrad)^2(mm)^2(0.1\%\ BW)} \tag{B.24}$$

The third generation synchrotron facilities allowed to reach a brilliance 10 orders of magnitude higher then rotating anodes. These facilities introduced the use of wigglers and undulators, also called insertion devices, which are period magnetic elements which force the electrons to undergo oscillations additionally to their curved trajectory, leading to more intense X-rays emission. Hence, synchrotron radiation facilities allow faster acquisition times and better resolution, but also allows experiments which cannot be performed otherwise because of the low intensity of the sources, such as absorption experiments…

More information on the general aspects of XRD can be found in the books by Warren,[3] Als-Nielsen and McMorrow[4] and Guinebretière.[5]

B.6. LABORATORY DIFFRACTOMETERS

We performed our experiments on the different diffractometers present in the laboratory, depending on the information we were looking for.

Thin films $\theta/2\theta$ and rocking curves were measured on a Empyrean Panalytical diffractometer (Figure B.6.a), equipped with an X-ray tube with a Cobalt anode ($\lambda_{\mathrm{K}\alpha1} = 1.789\,\text{Å}$). For the sake of clarity, all the diffractograms measured on this equipment were converted to cupper wavelength. A parabolic Goebel mirror was mounted in the primary optics to insure a parallel beam. The detector used for our measurements is a 2D Pixcel detector (255x255 px) which can be used as a punctual (0D) or a linear detector (1D). The sample stage is motorized, allowing for sample alignment, and different types of measurements in addition to classical θ-θ.

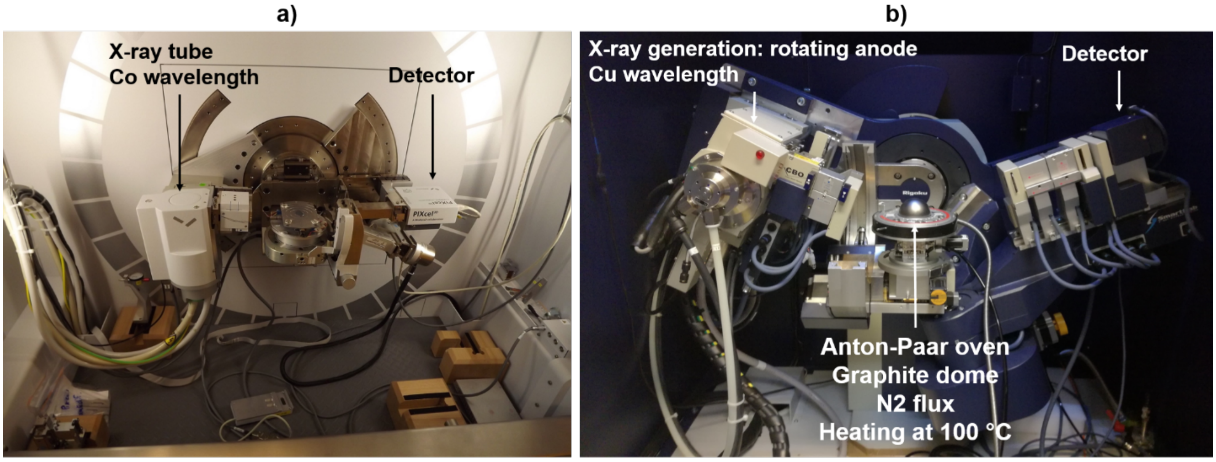

Figure B.6: (a) Panalytical Empyrean diffractometer used here for measuring thin films. (b) Rigaku SmartLab's diffractometer equipped with the Anton-Paar oven and the graphite dome, allowing to perform in-situ experiments under controlled atmosphere.

For in-situ measurements (chapter 2), the measurements were performed on the Rikagu SmartLab diffractometer (Figure B.6.b) equipped with an Anton Parr oven (up to 1100 °C) and a graphite dome to insure controlled atmosphere. Thanks to its rotating Cupper anode ($\lambda_{\mathrm{K}\alpha 1} = 1.5406\,\text{Å}$), the incident beam is more intense, and, as seen in Figure B.7, the two motion axis of the detector arm (2θ and $2\theta\chi$) allows out-of-plane measurements ($\theta/2\theta$, rocking curves and grazing incident) as well as in-plane measurements (chapter 2 and chapter 3). For our measurements, collimators were used and average angular resolution was reached, but the diffractometer can be equipped with monochromators to reach higher resolution. Both these diffractometers have been used with a parallel beam thanks to a parabolic Goebel mirror.

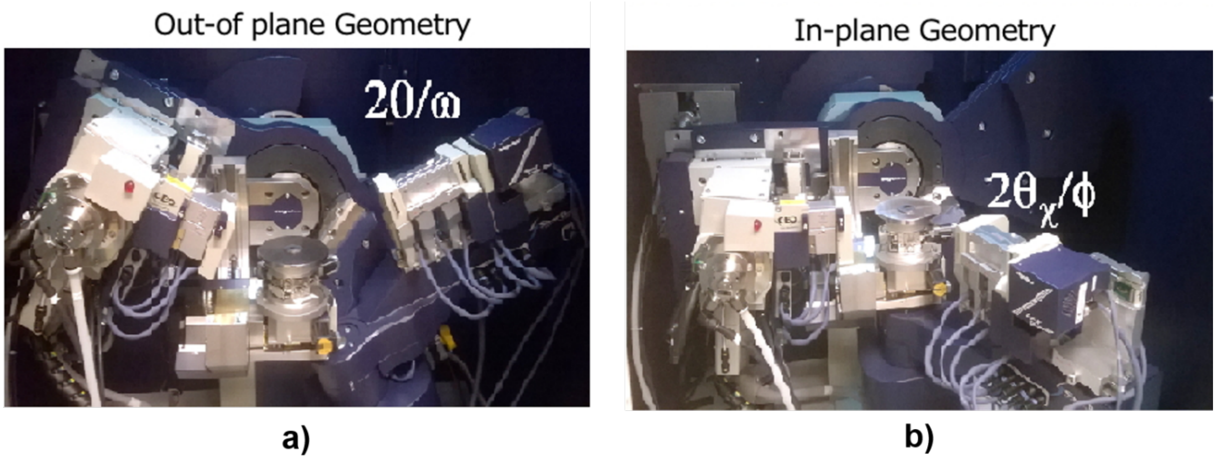

Figure B.7: Illustration of the degrees of freedom of the detector arm on Smartlab diffractometer: (a) out-of-plane (2θ axis) measurement and (b) in-plane ($2\theta\chi$ axis) measurement

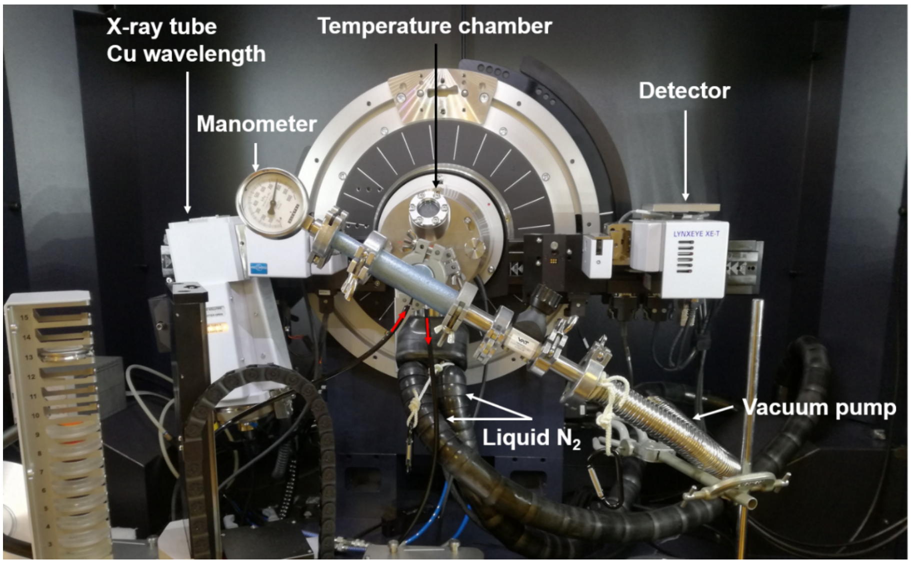

Figure B.8: Bruker D8 advanced diffractometer, equipped with the temperature chamber and the atmosphere control tubes. the red arrows identify the inert gas flow tubes.

Most of the powder diffractograms showed in chapter 4 and chapter 5 were measured using a Bruker D8 advanced diffractometer, equipped with an X-ray tube with a Cupper anode. The detector is a Lynxeye XE-T. The incident beam is divergent, and automatic divergence slits were used to ensure the same irradiated length on the same over the whole measurement range. For temperature dependent measurements, the diffractometer can be equipped with an Anton-Parr TTK600 temperature chamber, with an accessible temperature range from 90 K (liquid N_2 cooling system) to 873 K. The measurement can be performed under vacuum or under inert atmosphere.

Appendix C

Complementary characterization techniques

Contents

C.1. OPTICAL BAND-GAP MEASUREMENT: UV-VIS ABSORPTION

UV-visible absorption spectroscopy was performed on a Perkin Elmer Lambda 650 spectrometer and an integration sphere were used. The measurement was performed on a 300 – 1100 nm range. A deuterium lamp was used for UV light and a tungsten one for the visible-IR region. In the UV-visible region, the detection was performed by a photomultiplier tube (PMT) and an InGaAs detector was used for IR-detection. The sample was prepared for measurement by spreading evenly a small quantity of powder between two microscopy glasses. The absorption spectra of the microscopy glasses was measured and subtracted from the spectra of the sample. As the quantity of powder used for each sample preparation is hard to control, the absorption spectra of all the samples were normalized to display the same absorbance at 400 nm, were no signal is observed. To extract the Bandgap, the Tauc plot method was used. To do so, the wavelength λ is converted into energy E using the formula:

$$E(eV) = \frac{hc}{\lambda} = \frac{1241}{\lambda(nm)} \tag{C.1}$$

Were h is Planck constant and c the speed of light. To obtain the $\alpha h\nu^2$ value used in the y axis of the Tauc plot, the absorbance is converted into the optical absorption coefficient α using Beer-Lambert relation:

$$I = I_0 e^{-\alpha l} \Rightarrow \frac{I_0}{I} = e^{\alpha l} \Rightarrow \ln\left(\frac{I_0}{I}\right) = \alpha l \tag{C.2}$$

Where l is the absorption path. The definition of the absorbance being:

$$A = \log_{10}(\frac{I_0}{I}) \; and \; \log_{10}(x) = \frac{\ln(x)}{\ln(10)} \tag{C.3}$$

We can write

$$A = \frac{\ln(\frac{I_0}{I})}{\ln(10)} \approx \frac{\ln(\frac{I_0}{I})}{2.303} \approx \frac{\alpha l}{2.303} \Rightarrow \alpha \approx \frac{2.303A}{l} \tag{C.4}$$

Here, we consider the absorption path to be the same for all samples as it is set by the spacing between the two microscopy glasses. For all measurements, these microscopy glasses were separated by a the thickness of the duct tape glued between the glasses.

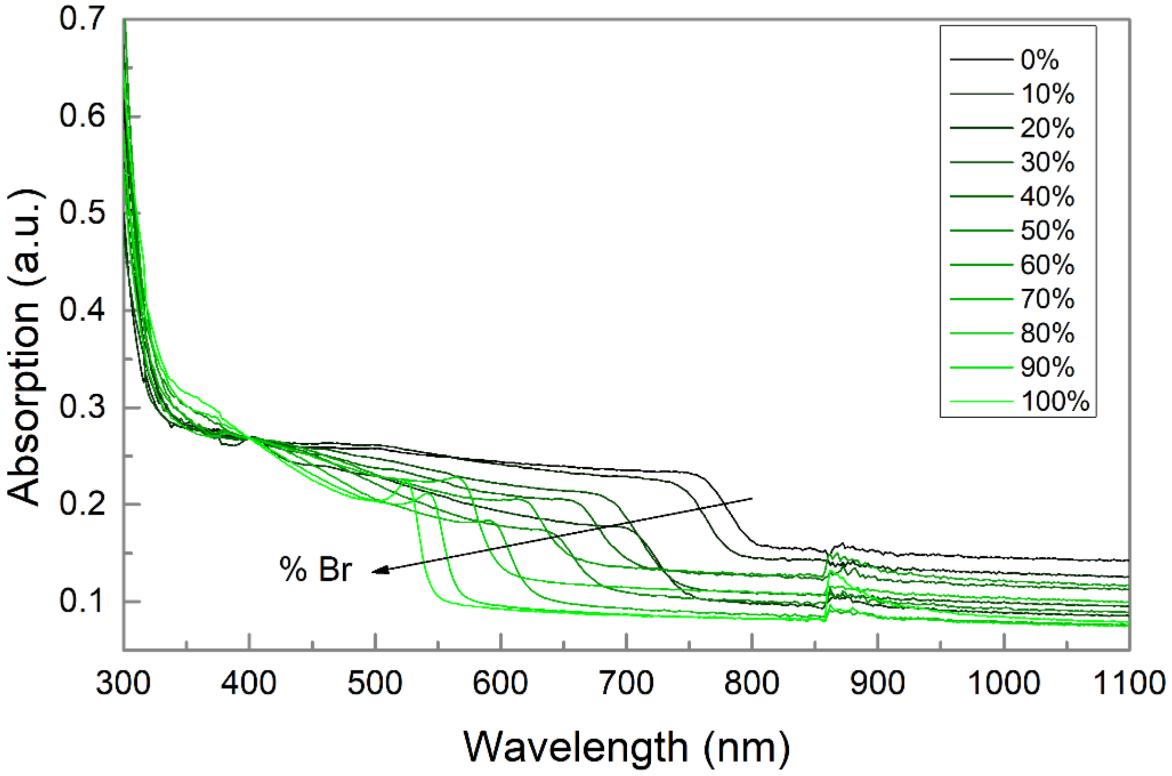

Figure C.1: UV-vis absorption spectra of $\mathrm{MAPb(I_{1-x}Br_x)_3}$ powder samples.

C.2. SCANNING ELECTRON MICROSCOPY (SEM) AND ENERGY DISPERSIVE X-RAY ANALYSIS (EDX)

The SEM microscopy images of the thin films were acquired on a ZEISS-ultra 55 scanning electron microscope. The same microscope is equipped with an EDX probe, allowing us to determine the elemental composition of the powders with mixed halogens. The elemental composition was determined using Esprit software.

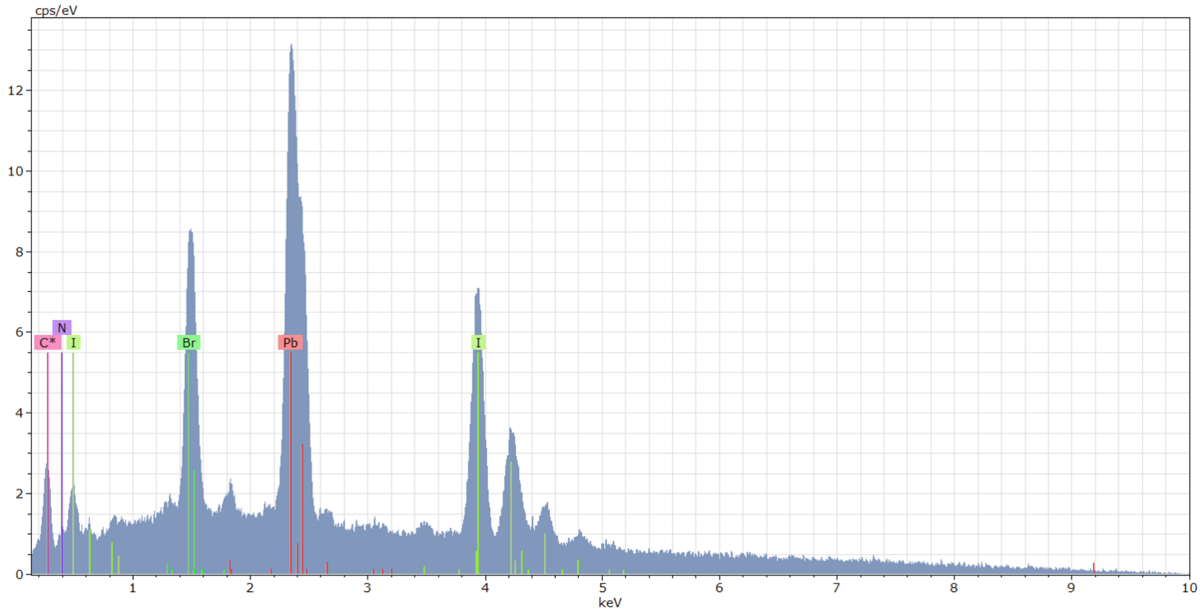

Figure C.2: Example of an EDX spectra measured on $MAPb(I_{0.70}Br_{0.30})_3$.

C.3. NUCLEAR MAGNETIC RESONANCE (NMR)

The proportions of FA^+ and MA^+ cations in the $FA_{1-x}MA_xPbI_3$ were determined by proton Nuclear Magnetic resonance, inspired by the report of Weber et al..[6] Around 10 mg of sample were dissolved in deuterated DMSO prior to the experiment. The spectra were recorded using Bruker AC400 (or AC500) spectrometers and the cations proportions were calculated from the integration of the signal of each of the cations.

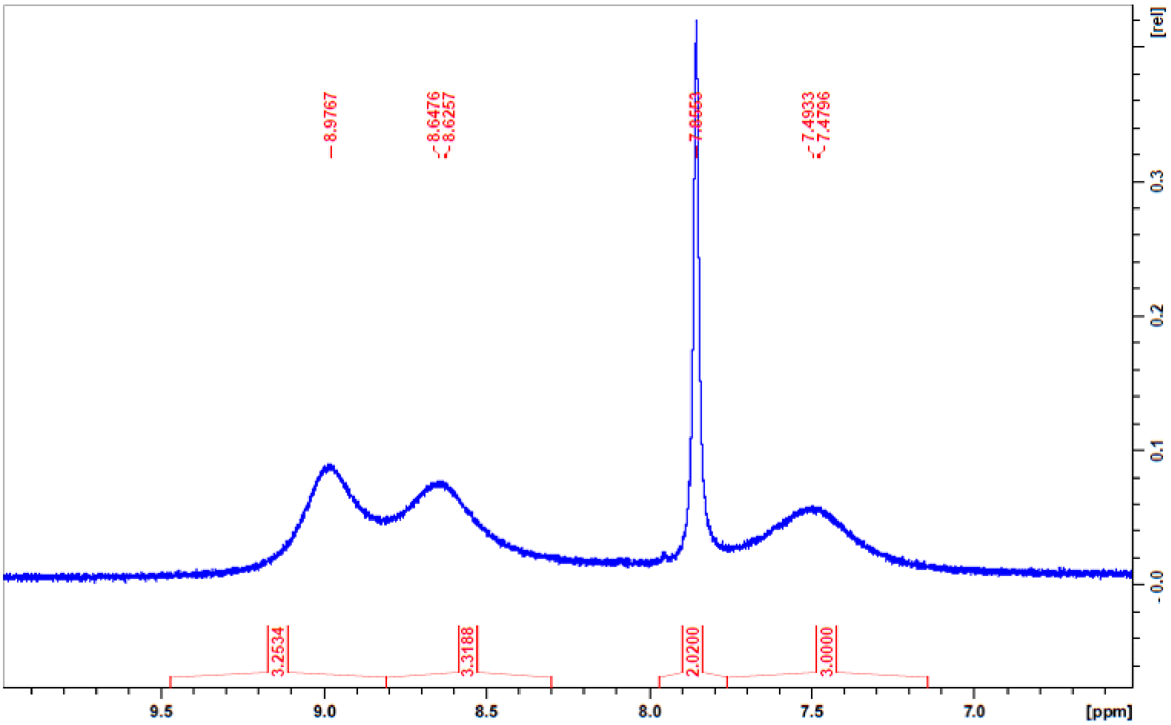

Figure C.3: Enlarged view of an NMR spectra measured on a sample with a $FA_{0.60}MA_{0.40}PbI_3$ sample. Assignments for the protons were used as reported by Weber et al.[6] as for MA^+ : 1H NMR δ 7.46 ppm (3H, NH3). FA^+ : ^1H NMR δ 7.83 ppm (1H, CH), δ 8.63 ppm (2H, NH_2) and δ 8.98 ppm (2H, NH_2)

References

[1] P. Dally. “Cellules Solaires à base de Pérovskites : De la caractérisation des matériaux à l’amélioration des rendements et de la stabilité”. PhD thesis. 2019.

[2] B. H. Toby. “R factors in Rietveld analysis: How good is good enough?” In: *Powder Diffraction* 21.1 (2006), pp. 67–70. DOI: `10.1154/1.2179804`.

[3] B. E. Warren. *X-ray diffraction*. Dover. 1990.

[4] J. Als-Nielsen and D. McMorrow. *Elements of Modern X-ray Physics, 2nd edition*. John Wiley & Sons, Ltd. 2011. ISBN: 78-0-470-97395-0.

[5] R. Guinebretière. *X-ray Diffraction by Polycrystalline Materials*. ISTE Ltd. 2007. ISBN: 978-1-905209-21-7.

[6] O. J. Weber, B. Charles, and M. T. Weller. “Phase behaviour and composition in the formamidinium–methylammonium hybrid lead iodide perovskite solid solution”. en. In: *J. Mater. Chem. A* 4.40 (2016), pp. 15375–15382. DOI: `10.1039/C6TA06607K`.

List of Figures

List of Tables

Abstract

The intense human activity during the last three centuries is now showing its consequences, and climate change is now an undisputable truth. Developing efficient technologies to allow the broad use of low-carbon energy sources is vital to limit our impact on the environment and working on restoring the balance. Photovoltaics constitute one promising path to achieve this goal, as the sun constitutes a very powerful and sustainable source of energy. Silicon-based modules are predominant in the market, but alternative and complementary technologies are developed in research laboratories. During the last decade, a new technology appeared, generating tremendous interest in the scientific community: the hybrid halide perovskite solar cell.

Perovskite designates a structural family, which constitutes one of the most important classes of materials in solid-state sciences, due to their very versatile properties, which can be tuned through chemical engineering. The introduction of an organic cation inside an inorganic lead-halide cage gave rise to semi-conducting perovskite materials with impressive optoelectronic properties. The first material of this family to be used in photovoltaic devices was $MAPbI_3$ ($MA = CH_3NH_3$). Research solar cells using such hybrid perovskite materials as light absorber have seen a steep rise of their efficiency. In only ten years, they reached more than 25 % conversion effiency, challengin silicon-based devices. However, the in-depth understanding of the fundamental properties of these compounds and their origin is still lacking far behind the more empirical technological advances.

It is with the aim of enhancing our understanding of the structural features of these compounds that this PhD project was constructed. Mainly using X-Ray diffraction techniques, we investigated different systems. The first part of this work is dedicated to the structural investigation of $MAPbI_3$ thin layers. By means of in-situ experiments, we identified the different steps of the crystallization mechanism through ion exchange which occur in the presence of chlorine in the precursors, under specific conditions. These results allowed to rationalize observed performances in solar cells based on similar $MAPbI_3$ thin films. We then focused on the $MAPbI_3$ thin films microstructure and more particularly on the peculiarity and variability of the observed texture. This behavior is shown to be related to the ferroelastic nature of the $MAPbI_3$ cubic-tetragonal structural phase transition..

The second part of this work is dedicated to the study of the impact of ion mixing on the perovskite structure. High efficiencies and long-term stability of solar cells have been achieved in recent years by using hybrid halide perovskite materials constituted of different organic cations and different halide anions. However, the effect of each substitution on the structure is not well understood, as most of the work is performed on compounds in which two different ions are substituted simultaneously. We therefore decided to study the structure of compounds where only one ion is substituted at a time, generating three families of solid solutions: $\mathrm{FA_{1-x}MA_xPbI_3}$ ($\mathrm{FA = CH(NH_2)_2}$), $\mathrm{MAPb(I_{1-x}Br_x)_3}$ and $\mathrm{FAPb(I_{1-x}Br_x)_3}$. The room temperature properties of these compounds as well as their temperature-dependent structural behavior were studied. Finally, we used the structural behavior of the mixed organic cation mixed halide compound $\mathrm{(FAPbI_3)_{0.85}(MAPbBr_3)_{0.15}}$ with a composition optimized for photovoltaic applications is discussed at the light of the results obtained with the quaternary compounds.

Résumé

Les conséquences de l'intense activité humaine des trois derniers siècles se font aujourd'hui ressentir et le dérèglement climatique est indéniable. Le développement de l'exploitation des sources d'énergies à faible empreinte carbone est une condition sine qua non pour limiter notre impact sur l'environnement. Dans ce contexte, convertir l'énergie solaire en électricité est une solution de choix pour atteindre cet objectif. Les panneaux solaires en silicium représentent la technologie dominante sur le marché, mais des technologies alternatives et complémentaires sont développées en laboratoire depuis plusieurs dizaines d'années. La dernière en date a grandement attisé l'intérêt de la communauté scientifique : les cellules solaires à base de pérovskites hybrides et halogénées.

Le nom pérovskite désigne une famille structurale qui constitue l'une des catégories de matériaux les plus importantes de la matière condensée. Ces matériaux pérovskites possèdent une grande variété de propriétés, qui peuvent être adaptées en modifiant leur composition chimique. Lorsqu'un cation organique est inséré au centre d'une cage inorganique plomb-halogène, un matériau pérovskite semi-conducteur présentant des propriétés optoélectroniques impressionnantes est obtenu. Le premier matériau de ce type employé comme couche active de cellule solaire a été $MAPbI_3$ ($MA = CH_3NH_3$). Durant les dix dernières années, l'efficacité des dispositifs à base de ces matériaux pérovskite a fortement augmenté, passant des 10 % initiaux en 2012 à 25.5 % aujourd'hui, concurrençant ainsi de près les efficacités des cellules solaires à base de silicium. Cependant, la compréhension des propriétés intrinsèques de ces matériaux reste limitée.

C'est dans le but d'approfondir nos connaissances sur les propriétés structurales de ces composés que ces travaux ont été menés. Nous avons ainsi étudié différents systèmes, en employant principalement sur des mesures de diffraction des rayons X. La première partie de ce travail a été consacrée à l'étude structurale des couches minces de $MAPbI_3$. Au moyen d'expériences in situ, nous avons identifié les différentes étapes du mécanisme de cristallisation par échange ionique qui se produit en présence de chlore dans les précurseurs, dans certaines conditions spécifiques. Ces résultats ont permis d'expliquer les performances de cellules solaires réalisées à partir de couches minces $MAPbI_3$ similaires. Nous nous sommes ensuite focalisés sur la microstructure des couches minces $MAPbI_3$ et plus particulièrement sur la variabilité surprenante observée de la texture des couches $MAPbI_3$.

Nous montrons que ce comportement est lié à la nature ferroélastique de la transition de phase structurale cubique-tétragonale $MAPbI_3$ qui survient vers 60 °C, en mettant en évidence l'influence de la déformation subie par le matériau à haute température sur la microstructure des couches à température ambiante.

La seconde partie de cette thèse porte sur l'étude de solutions solides de pérovskite hybrides halogénées. De plus hautes efficacités et une meilleure stabilité des dispositifs ont été atteintes lorsque des solutions solides multi-cations et multi-halogènes sont utilisées. Cependant, l'effet de chaque substitution sur la structure pérovskite est encore mal compris, la plupart des études portant sur des composés où plusieurs ions sont substitués simultanément. Notre but a donc été de substituer un ion à la fois, générant ainsi trois familles à étudier : $FA_{1-x}MA_xPbI_3$ ($FA = CH(NH_2)_2$), $MAPb(I_{1-x}Br_x)_3$ et $FAPb(I_{1-x}Br_x)_3$. La structure de ces composés a été systématiquement étudiée à température ambiante ainsi qu'en fonction de la température pour établir le diagramme de phase de ces matériaux. Pour finir, le comportement structural du composé multi-cations organiques et multi-halogènes $(FAPbI_3)_{0.85}(MAPbBr_3)_{0.15}$ qui présente une composition chimique optimisée pour l'application en cellules solaires, est discuté à la lumière des résultats obtenus avec les composés quaternaires.